Solar-driven reduction of CO_2: From homogeneous to heterogeneous catalytic systems

THÈSE N^{O} 7754 (2017)

PRÉSENTÉE LE 10 MAI 2017

À LA FACULTÉ DES SCIENCES DE BASE
LABORATOIRE DE PHOTONIQUE ET INTERFACES
PROGRAMME DOCTORAL EN CHIMIE ET GÉNIE CHIMIQUE

ÉCOLE POLYTECHNIQUE FÉDÉRALE DE LAUSANNE

POUR L'OBTENTION DU GRADE DE DOCTEUR ÈS SCIENCES

PAR

Marcel Roland SCHREIER

acceptée sur proposition du jury:

Prof. U. A. Hagfeldt, président du jury
Prof. M. Graetzel, Prof. K. Sivula, directeurs de thèse
Prof. M. Kanan, rapporteur
Prof. W. Smith, rapporteur
Prof. S. Haussener, rapporteuse

ÉCOLE POLYTECHNIQUE
FÉDÉRALE DE LAUSANNE
Suisse
2017

Eine Wissenschaft, die sich nur um sich selbst dreht, ist ein Verwaltungsbetrieb. - NZZ

Abstract

Rapidly increasing levels of atmospheric carbon dioxide and their damaging impact on the global climate system raise doubts about the sustainability of the fossil resource based energy system. Meanwhile, raising living standards and increasing global population lead to an ever growing need for energy. Renewable energy sources are believed to present a solution to these problems with the sheer abundance of solar energy showing particular promise to fulfill the world's energy needs. However, for large scale application of solar energy to be possible, the problem of its storage has to be addressed. The insufficient flexibility of present-day storage technologies has led to the quest for producing solar fuels, centering on hydrogen as a fuel in a prospective hydrogen economy. Nevertheless, the gaseous state, low volumetric energy density and explosive nature of hydrogen makes it a challenging fuel for practical applications and establishing a hydrogen economy will require trillions of dollars of investments. Using solar energy to produce carbon-based liquid fuels solves these challenges, closes the anthropogenic carbon cycle and allows for the continued utilization of existing infrastructures.

A promising method for the production of such fuels consists in the photoelectrochemical and electrochemical conversion of carbon dioxide. In this thesis, I investigate both methods using molecular homogeneous catalysts and heterogeneous systems.

The photoelectrochemical reduction of carbon dioxide on TiO_2-protected Cu_2O photocathodes was investigated using a rhenium bipyridyl catalyst in solution. Important charge transport limitations were encountered, which could be overcome by the addition of protic additives to the electrolyte. The selective light-assisted photoelectrochemical production of CO was thus achieved for the first time on this type of low-cost photoelectrode. Investigations into the charge transfer limitations discovered a changed catalytic pathway in the presence of protic additives which was hypothesized to avoid passing by a negatively charged intermediate experiencing repulsion at the negatively charged TiO_2 surface.

Improving on this result, the molecular catalyst was covalently immobilized on the TiO_2 surface of the photocathode by modifying the bipyridyl ligand with a

phosphonate binding group. A nanostructure of TiO_2 was needed to support sufficient catalyst to sustain the photocurrent generated by the Cu_2O photoelectrode while thermal stability limitations of the photoelectrode materials required the development of a low-temperature process for the deposition of mesoporous TiO_2. The complete device showed photocurrents exceeding 2.5 mA cm^{-2} and large faradaic efficiency for the production of CO. Deactivation was found to occur and was attributed to likely changes in the catalyst structure.

Moving toward heterogeneous catalysis, the promotion of the CO_2 to CO conversion reaction on silver surfaces by imidazolium cations was investigated. Previous research pointed to the imidazolium C2 proton playing a crucial role, which was not confirmed in our studies. Instead, replacing the C2 proton with a phenyl substituent led to a substantial enhancement as compared to the commonly reported $EMIM^+$. Replacing the C4 and C5 protons with methyl groups, however, suppressed the catalysis-promoting effect of the imidazolium salt for different C2 substituents.

As one of the first examples, the unassisted solar-driven splitting of CO_2 into CO and O_2 was demonstrated using water as electron source. This was achieved by the use of a porous gold cathode and an IrO_2 anode, driven by three methylammonium lead iodide perovskite solar cells in series. Extended operation of this perovskite-driven system over 18 h was shown, achieving a solar to CO efficiency exceeding 6.5 %.

The atomic layer deposition (ALD) modification of CuO nanowire cathodes with SnO_2 was investigated, leading to striking impacts on the catalytic selectivity of this system. In an aqueous electrolyte, bare CuO led to the production of a wide spectrum of products, which was modified to the production of CO with high selectivity over an extended potential range upon ALD modification. By conducting partial current and chemisorption analyses, this change was attributed to a suppression of the hydrogen evolution reaction due to a decreased hydrogen binding strength on modified samples. By exploiting the oxygen evolving activity of SnO_2-coated CuO, a bifunctional system was constructed using the same material both as a selective CO_2 reducing cathode and oxygen evolving anode. To sustain different electrolytes and pH values in the anode and cathode compartment and to achieve

product separation, a bipolar membrane was employed. Driving this system with a 3-junction photovoltaic achieved a solar to CO efficiency peaking at 13.4%.

The studies presented herein represent important advancements both in the field of photoelectrochemical CO_2 reduction by molecular catalysts and in the field of unassisted solar-driven reduction of CO_2. At the time of their respective publication, both solar to CO efficiencies were world records and have contributed to the solar fuels community which aims to push toward higher efficiencies in these conversion processes.

Résumé

La croissance rapide de la concentration atmosphérique de dioxyde de carbone et l'impact néfaste de ce gaz sur le climat terrestre soulève des doutes quant au bien-fondé du système énergétique basé sur les ressources fossiles. Par ailleurs, l'amélioration du niveau de vie et la croissance de la population mondiale conduisent à un besoin croissant d'énergie. Les sources d'énergie renouvelables présentent une solution à ces défis et l'énergie solaire, en particulier, permettrait de répondre aux besoins énergétiques mondiaux. Cependant, pour une application à grande échelle de la production d'énergie solaire, il est nécessaire de traiter le problème de son stockage. L'insuffisante flexibilité des technologies de stockage actuelles a incité à la recherche sur la production de combustibles solaires, dont principalement l'hydrogène, considéré comme le combustible central d'une future économie basée sur l'hydrogène. Néanmoins, l'état gazeux, la faible densité d'énergie volumétrique et l'explosivité de l'hydrogène en font un combustible exigent dans le cadre des applications pratiques. L'établissement d'une économie basée sur l'hydrogène nécessitera, de plus, des milliards de dollars d'investissements pour la mise en place d'une infrastructure de distribution. L'utilisation d'énergie solaire pour produire des combustibles liquides à base de carbone présente une solution alternative intéressante, puisqu'elle permet de fermer le cycle anthropique de carbone et permet l'utilisation des infrastructures existantes.

Un procédé prometteur pour la production de tels combustibles consiste en la conversion photoélectrochimique et électrochimique du dioxyde de carbone. Dans cette thèse, j'étudie ces deux approches en utilisant d'une part des catalyseurs moléculaires homogènes et d'autre part des systèmes hétérogènes.

La réduction photoélectrochimique du dioxyde de carbone sur des photocathodes en Cu_2O protégées par du TiO_2 a été étudiée en utilisant un catalyseur de bipyridyle de rhénium en solution. D'importantes limitations de transport de charges ont initialement été observées et ont été dans un deuxième temps surmontées par l'addition de composés protiques dans l'électrolyte. La production photoélectrochimique et sélective de CO, assistée par la lumière, a ainsi été réalisée pour la première fois sur ce type de photoélectrodes, caractérisées par un faible coût.

Des études sur les limitations du transfert de charges ont mené à la découverte d'un mécanisme catalytique modifié en présence d'additifs protiques. Il a été supposé que contrairement au mécanisme observé en l'absence d'additifs protiques, la formation d'un intermédiaire négativement chargé qui subirait une répulsion à la surface de TiO_2, elle aussi chargée négativement, est ici évitée.

Dans le but d'améliorer ce premier résultat, le catalyseur moléculaire a ensuite été immobilisé par covalence sur la surface de TiO_2 de la photocathode. A cette fin, le ligand bipyridyle du catalyseur a été modifié avec un groupe phosphonate qui sert de groupe de liaison. De plus, une nanostructuration du TiO_2 a été implémentée. Elle est nécessaire afin de lier suffisamment de catalyseur pour convertir l'intégralité du photocourant généré par la photoélectrode de Cu_2O. Il est à noter que du fait de la stabilité thermique limitée des matériaux qui composent la photoélectrode, le développement d'un procédé à basse température pour la déposition du TiO_2 mésoporeux a été mis en place. Le produit final de cette recherche a permis d'obtenir des photocourants supérieurs à 2.5 mA cm^{-2} et une grande efficacité faradique pour la production de CO. Une désactivation a néanmoins été observée et a été attribué à des changements potentiels dans la structure du catalyseur.

Concernant la catalyse hétérogène, la promotion de la réaction de conversion électrochimique de CO_2 en CO par des cations imidazole a été étudiée sur des surfaces en argent. Des recherches antérieures ont montré que le proton C2 de l'imidazole jouait un rôle crucial pour permettre la promotion de cette reaction. Ceci n'a pas été confirmé dans nos études. Au lieu de cela, le remplacement du proton C2 par un substituant phényle a conduit à une amélioration substantielle de la promotion de la conversion de CO_2 en CO sur des surfaces en argent, en particulier par rapport à la référence, $EMIM^+$. Cependant, un remplacement des protons C4 et C5 par des groupes méthyle a supprimé l'effet promoteur de l'imidazole pour les différents substituants en C2.

Dans l'étude suivante, pionnière dans le domaine, l'électrolyse solaire non assistée du CO_2 en CO et en O_2 a été démontrée en utilisant l'eau comme source d'électrons. Ceci a été réalisé par l'utilisation d'une cathode en or poreux et d'une anode en IrO_2, l'énergie nécessaire au procédé étant fournie par trois cellules solaires de perovskite

méthylammonium d'iodure de plomb, connectées en série. Le fonctionnement prolongé de ce système basé sur des perovskites a été démontré pour une durée de 18 heures et a mené à un rendement lumière–CO supérieur à 6,5%.

Finalement, la modification par ALD de cathodes en nanofils de CuO avec du SnO_2 a été étudiée, et a montré un effet important sur la sélectivité catalytique de ce système. En effet, dans un électrolyte aqueux, le CuO conduit à la production d'un large spectre de produits. Par contre, après la modification par ALD une sélectivité élevée en CO sur une large plage de potentiel a été observée. En effectuant des analyses de courant partiel et de d'adsorption chimique, cette différence a été attribué à une suppression de la réaction d'évolution de l'hydrogène suite à une diminution de la force de la liaison de l'hydrogène à la surface des échantillons modifiés. De plus, en exploitant l'activité catalytique des échantillons de CuO recouverts de SnO_2 pour la réaction l'évolution de l'oxygène, un système bifonctionnel a été construit, qui utilise le même matériau à la fois comme cathode réductrice de CO_2 et comme anode évoluant l'oxygène. Pour maintenir les concentrations des électrolytes et les valeurs de pH dans les compartiments anodique et cathodique constantes, et afin de séparer les produits de l'électrolyse, une membrane bipolaire a été utilisée. En ajoutant une cellule photovoltaïque à 3 jonctions comme source d'énergie, un rendement lumière–CO maximal de 13,4% a été atteint.

Les études présentées ici représentent des progrès importants dans les domaines de la réduction photoélectrochimique du CO_2 par des catalyseurs moléculaires et de la réduction non assistée du CO_2 par l'énergie solaire. Au moment de leur publication respective, les rendements solaires étaient des records mondiaux et ont ainsi apporté leur contribution à la communauté scientifique qui vise à accroître l'efficacité de ces processus de conversion.

Zusammenfassung

Schnell ansteigende Mengen von atmosphärischem Kohlendioxid und ihre schädlichen Auswirkungen auf das globale Klimasystem führen zu Zweifeln an der Nachhaltigkeit des fossilen Energiesystems. Gleichzeitig führen die weltweite Verbesserung des Lebensstandards und die zunehmende Weltbevölkerung zu einem ständig wachsenden Energiebedarf. Erneuerbare Energiequellen versprechen eine Lösung für diese Probleme. Ganz speziell die Sonnenenergie könnte, dank ihrer ausserordentlich grossen Energiemenge, den weltweiten Energiebedarf decken. Die großflächige Anwendung von Solarenergie bedarf jedoch ihrer Speicherung, wobei die unzureichende Flexibilität der heutigen Speichertechnologien zur Erforschung von sogenannten Solarkraftstoffen geführt hat. Diese Arbeit konzentriert sich auf Wasserstoff, welcher als Brennstoff in einer zukünftigen Wasserstoffwirtschaft eingesetzt werden soll. Dieser Brennstoff hat jedoch verschiedene Nachteile, ganz speziell sein gasförmiger Zustand, seine geringe volumetrische Energiedichte und seine Explosionsgefahr. Ausserdem wird die Schaffung einer Wasserstoffwirtschaft ausserordentliche Investitionen benötigen. Die Nutzung von Solarenergie zur Herstellung von kohlenstoffbasierten flüssigen Brennstoffen löst diese Probleme, kann den anthropogenen Kohlenstoffkreislauf schliessen und ermöglicht die Nutzung bestehender Infrastrukturen.

Eine vielversprechende Methode zur Herstellung solcher Kraftstoffe besteht in der photoelektrochemischen und elektrochemischen Umwandlung von Kohlendioxid. In dieser Arbeit untersuche ich beide Methoden, wobei ich sowohl homogene molekulare Katalysatoren wie auch heterogene Systeme einsetze.

Die photoelektrochemische Reduktion von Kohlendioxid auf TiO_2-geschützten Cu_2O-Photokathoden wurde unter Verwendung eines im Elektrolyt gelösten Rhenium-Bipyridyl-Katalysators untersucht. Es wurden starke Ladungs-Übergangsbeschränkungen entdeckt, die durch die Zugabe von protischen Additiven zum Elektrolyten überwunden werden konnten. Dadurch wurde erstmals die selektive und lichtunterstützte photoelektrochemische Herstellung von CO auf dieser Art von kostengünstigen Photoelektroden erreicht. Untersuchungen an den Ladungs-Übergangsbeschränkungen führten zur Entdeckung einer Veränderung

des katalytischen Mechanismus in Gegenwart von protischen Additiven. Es wird vermutet, dass dieser Mechanismus die Bildung eines negativ geladenen Zwischenstadiums verhindert, welches in der Abwesenheit von protischen additiven von der ebenfalls negativ geladenen TiO_2-Oberfläche abgestossen wird.

Aufbauend auf diesen Ergebnissen wurde der molekulare Katalysator auf der TiO_2-Oberfläche der Photokathode kovalent immobilisiert, indem der Bipyridyl-Ligand mit einer Phosphonat-Bindungsgruppe modifiziert wurde. Eine Nanostruktur aus TiO_2 war nötig, um genügend Katalysator zu binden, so dass der gesamte von der Cu_2O-Photoelektrode erzeugte Photostrom umgesetzt werden konnte. Beschränkungen der thermischen Stabilität der Photoelektroden erforderte aber die Entwicklung eines Tieftemperaturprozesses für die Abscheidung von mesoporösem TiO_2. Die schlussendliche Struktur führte zu Photoströmen von über 2.5 mA cm^{-2} und zu einer hohen Faraday Effizienz für die CO-Produktion. Eine graduelle Deaktivation des Photostroms wurde festgestellt und auf mögliche Veränderungen in der Struktur des Katalysators zurückgeführt.

In einem Schritt in Richtung der Untersuchung von heterogenen Katalyseprozessen wurde die Co-Katalyse der Umwandlung von CO_2 zu CO mittels Imidazol-Kationen auf Silberoberflächen untersucht. Bisherige Berichte deuteten darauf hin, dass das Proton an der Imidazol C2-Position eine entscheidende Rolle spielt. Dies wurde in unserer Studie allerdings nicht bestätigt. Stattdessen führte das Ersetzen des C2-Protons durch einen Phenylsubstituenten zu einer wesentlichen Verstärkung der co-katalytischen Wirkung im Vergleich zum klassischen $EMIM^+$. Interessanterweise unterdrückte das Ersetzen der C4- und C5-Protonen mit Methylgruppen jedoch die katalysefördernde Wirkung des Imidazol-Salzes für verschiedene C2-Substituenten.

Als eines der ersten Beispiele wurde die selbstständige solargetriebene Aufspaltung von CO_2 in CO und O_2 ohne Zuhilfenahme einer zusätzlichen Energiequelle, unter Verwendung von Wasser als Elektronenquelle, demonstriert. Dies wurde mittels Verwendung einer porösen Goldkathode und einer IrO_2-Anode erreicht, die von drei seriegeschalteten Methylammonium-Blei-Iodid-Perovskit-Solarzellen angetrieben wurde. Dieses System wurde kontinuierlich während 18 h betrieben und zeigte

einen Wirkungsgrad für die Umwandlung von Solarenergie in CO von mehr als 6.5%.

Die ALD-Modifikation von CuO-Nanodraht-Kathoden mit SnO_2 wurde untersucht, was zu markanten Auswirkungen auf die katalytische Selektivität dieses Systems führte. Unmodifiziertes CuO zeigte ein breites Produktspektrum in einem wässerigen Elektrolyten. Im Gegensatz dazu produzierte ALD-modifiziertes CuO praktisch ausschliesslich CO und dies mit hoher Selektivität über einen erweiterten Potentialbereich. Teilstrom- und Chemisorptionsanalysen führten diese Änderung auf eine Unterdrückung der Wasserstoffentwicklungsreaktion aufgrund einer verminderten Wasserstoffbindungsstärke an modifizierten Proben zurück. Durch die Nutzung der Aktivität zur Sauerstoffproduktion von SnO_2-beschichtetem CuO wurde ein bifunktionelles System aufgebaut, welches das gleiche Material sowohl als selektive CO_2-reduzierende Kathode wie auch als Sauerstoff produzierende Anode einsetzt. Um die benötigten unterschiedlichen Elektrolyte und pH-Werte im Anoden- und Kathodenraum zu erhalten und um eine Produkttrennung zu erreichen, wurde dabei eine Bipolarmembran eingesetzt. Beim Betrieb dieses System mittels einer 3-fachen Stapelsolarzelle wurde ein Solar-CO-Wirkungsgrad von bis zu 13.4% erreicht.

Die hier vorgestellten Studien stellen wichtige Fortschritte sowohl im Bereich der photoelektrochemischen CO_2-Reduktion durch molekulare Katalysatoren als auch im Bereich der selbstständigen solar-getriebenen Reduktion von CO_2 dar. Zum Zeitpunkt ihrer jeweiligen Publikation waren die hier präsentierten Solar zu CO-Effizienzen Weltrekorde und leisteten einen Beitrag zur wissenschaftlichen Solarkraftstoffgemeinschaft, die eine immer höhere Effizienz bei diesen Umwandlungsprozessen anstrebt.

Contents

1 Introduction

Solar irradiation is earth's most important primary energy source, giving rise to the biological processes taking place on the planet. In a complex cycle of events, solar energy is absorbed by chlorophyll molecules in plants and used to drive the transformation of carbon dioxide and water into sugars, which serve as the source of energy for all life. In this process, called *photosynthesis*, oxygen is released as a byproduct, allowing for aerobic life forms to exist. Residues of previous biological life, transformed into hydrocarbons over millions of years under heat and pressure, serve as the backbone of the present day fossil-fuel driven energy system, providing a stark reminder that the essence of the energy on earth originates from the sun.

In the sun's core, energy is predominantly released by nuclear fusion of approximately 670 million tons of hydrogen per second to yield helium.[1] Sunlight, is subsequently generated in the outer layers as electromagnetic radiation, roughly corresponding to the spectrum emitted by a black body at 5'800 Kelvin,[2] compounded with absorption lines due to elements present in the cooler outer layers of the sun.[3] When passing through the earth's atmosphere, Rayleigh Scattering and absorption by water vapor and other species modify the spectrum as illustrated in **Figure 1-1**.[4,5]

Despite losing intensity in the atmosphere, the amount of solar energy that reaches the earth's surface is astonishing. On average, this value amounts to a power of 120'000 TW, which contrasts with an average worldwide consumption of 12.5 TW in 2014, almost 90% of which came from non-renewable resources.[6]

Solar Energy

Faced with an increasing human population and raising living standards, the world's energy consumption is projected to increase by 30% to 16.3 TW until 2040.[8]

At the same time, research showing that overreliance on fossil energy sources leads to adverse effects on the climate,[9] provides motivation to decrease the use of fossil energy and draws the attention to renewable sources. The potential for expanding

traditional renewable resources are limited, however. For example, hydropower has a maximum additional global capacity of only 0.5 TW. The same is true for geothermal energy, where from the 12 TW available over the entire land mass not enough can effectively be extracted to meet the global energy demand. Wind power has been estimated to supply a maximum of 4 TW, which will also not suffice to satisfy a significant part of the required energy.[10] In contrast to these small scale sources, the 120'000 TW of renewable solar radiation hitting the earth's surface makes it a very attractive candidate as a future source of primary energy.

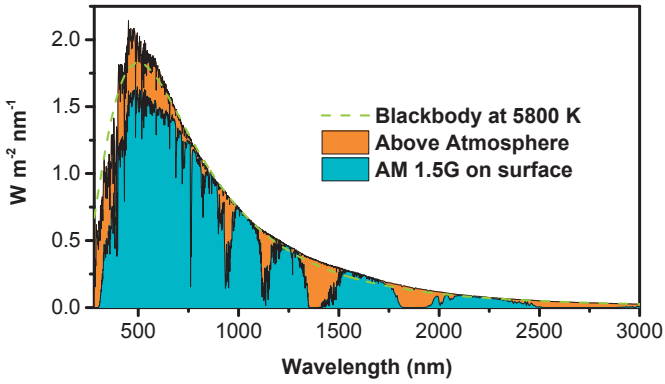

Figure 1-1: **Spectrum of solar radiation.** The solar spectrum roughly corresponds to a black body at 5'800 K, compounded by absorption due to elements present in the outer layers. After passing the atmosphere, the spectrum is significantly modified. The black body spectrum was normalized to the flux of the extraterrestrial spectrum. Data from NREL.[7]

Substantial progress has been made in increasing the efficiency[11] and reliability of photovoltaic cells for the generation of electricity and on solar-thermal installations for the production of heat, electricity or both. For example, 38.8 % solar to electrical power conversion efficiency can be reached using non-concentrated light. This value increases to 46 % if concentrated light is used. Despite the ever increasing harvesting efficiencies, solar energy suffers from its intrinsic intermittency and unpredictable nature (**Figure 1-2**). This has the consequence that it can only be used when the sun is shining, a limitation which becomes unpractical when large amounts of solar power are to be used in an energy system. Due to its intermittency and insufficient concentration, solar energy also cannot be used as a direct power source for transportation, which accounts for no less than 23% of the global energy consumption.[6]

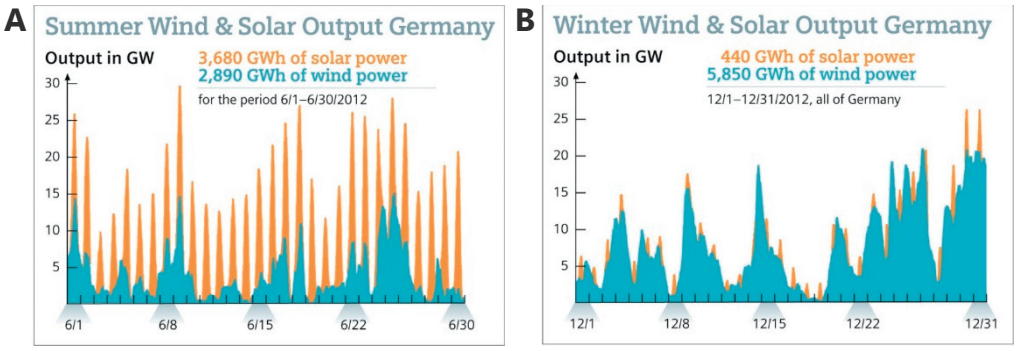

Figure 1-2: **Fluctuation of German wind and solar production.** (A) June and (B) December 2012. Source: Siemens.[12]

For solar energy to become a viable source of power, the problem of storing it efficiently has to be solved. A number of solutions are available for storing electricity, including but not limited to the large scale use of pumped hydroelectric storage, redox flow batteries, pressurized gases, flywheels and other battery technologies such as Li-Ion batteries. All of these technologies, however, present limitations when it comes to storing energy over longer timescales. They may also not be suitable for transport applications, where fast transfer of considerable amounts of energy are required. This is well visible at gas stations, where, at the time of writing, proud owners of battery electric vehicles have to take an extended coffee break for battery charging to take place. It takes 40 minutes to reach 80 % charge on a Tesla Model S car, when using a 120 kW power socket.[13] The question can be asked if the necessary balancing energy can be supplied and if the electric grid will be able to support the power required to fast-charge large quantities of vehicles without requiring costly intermediate storage. In addition to these problems, present day batteries still suffer from low gravimetric and volumetric energy densities, in the range of 10^2 Wh kg^{-1}.[14]

Solar fuels

An alternative solution to the above mentioned problems consists in the production of *solar fuels*. In such a scenario, solar energy is used to drive a chemical reaction, thereby storing solar energy in chemical species. In analogy with nature, this process is therefore called *artificial photosynthesis*.[15]

Significant efforts have gone toward producing hydrogen from sunlight to serve as the fuel in a hydrogen-based energy system, which has been coined the *hydrogen*

economy.[16] Progress in the field was fueled by the relatively well understood electrochemical hydrogen evolution reaction and progress on electrochemical oxygen evolution. This approach, to which I have also contributed in a number of co-authored publications (see publication list), has led to efficiencies for the generation of hydrogen from sunlight as high as 30%.[17] However, some points of criticism can be brought to using hydrogen as a fuel. The most important of them being the fact that the world's energy system is currently based on hydrocarbons as energy carriers and shifting it to hydrogen would require tremendous investments.[18,19] Other criticism has mentioned the volatility of hydrogen, its low volumetric energy density of 1.25 kWh L^{-1} at 690 bar and its explosive nature.[20] While many of these problems are being addressed by academia and industry alike,[21] they could be mitigated altogether by the production of carbon-based fuels from sunlight. As a comparison, a typical carbon-based solar fuel would be ethanol, which has a volumetric and gravimetric energy density of 6.5 kWh L^{-1} and 7.5 kWh kg^{-1},[22] respectively. The gravimetric energy density of ethanol is therefore around a factor 50 larger than lithium ion batteries and its volumetric energy density exceeds the one of heavily compressed hydrogen by a factor of 5.3. **Figure 1-3** makes the stunning differences between the different fuels visible and clearly illustrates the strong case for the production of carbon-based liquid fuels, the renewable synthesis of which is, in principle, feasible by using solar energy to reduce CO_2.

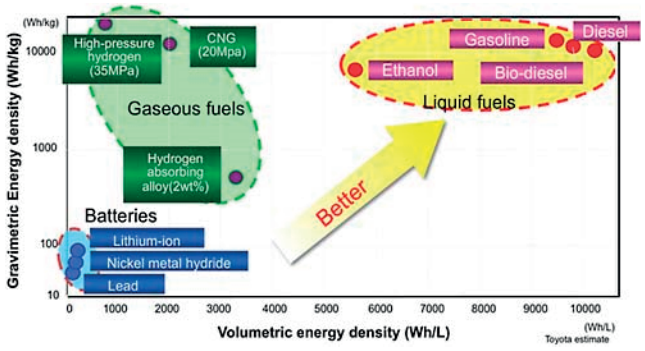

Figure 1-3: **Gravimetric and volumetric energy densities of various energy storage media.** Source: Toyota.[23]

Before investigating the details of the corresponding transformation processes, the role of carbon dioxide in the natural and anthropogenic carbon cycle will briefly be described.

Carbon Dioxide

Natural carbon cycle

The natural carbon cycle, driven by sunlight, is, together with the water and nitrogen cycle, one of the main processes allowing for biological life to take place. On earth, carbon exists in various reservoirs. The main atmospheric reservoir is in the form of gaseous CO_2. But carbon is also bound on land in living vegetation, in soils and in carbon containing minerals, whereas in the oceans, carbon exists in an equilibrium between dissolved CO_2, bicarbonate and carbonate. The carbon cycle links these reservoirs by various fluxes, as shown in **Figure 1-4**.

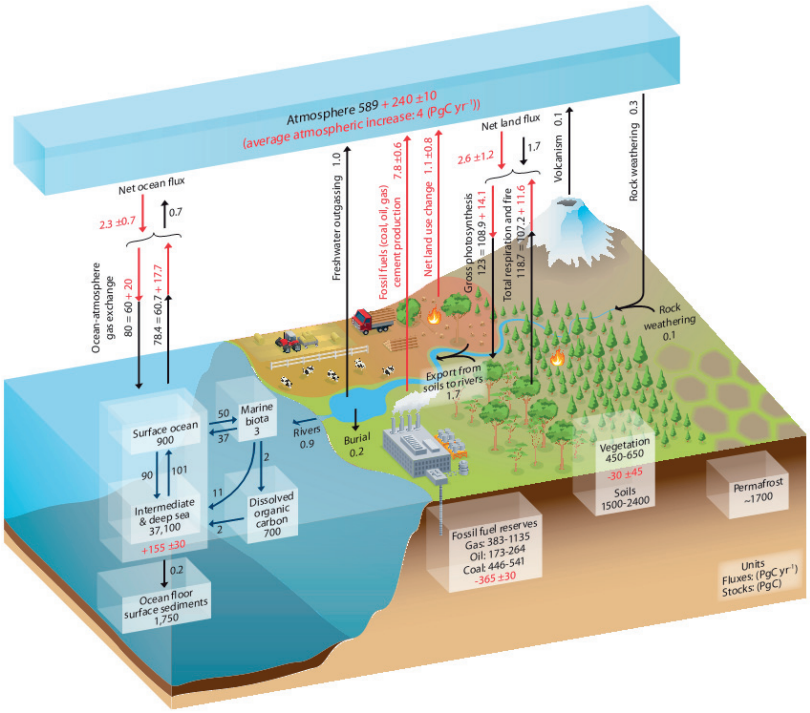

Figure 1-4: **Natural and Anthropogenic Carbon Cycle.** Fluxes and reservoirs are given PgC yr^{-1} and PgC. Source: IPCC.[24]

For example, carbon dioxide is released into the atmosphere by respiration from organisms on land and in the oceans, by combustion of organic matter, by geological processes such as volcanic eruptions and by release of CO_2 from the carbonate equilibrium in the oceans. In the presence of sunlight, plants, on the other hand, fix carbon from the atmosphere by photosynthesis and the partial pressure difference of CO_2 between the atmosphere and the sea drives the dissolution of

massive quantities of atmospheric CO_2 into the oceans, of which a small fraction forms mineral sediments which persist over millennia. These processes are normally in equilibrium with each other and carbon concentrations in the different reservoirs are constant, as was the case before the year 1750, i.e. before the onset of the industrial period.[24]

Anthropogenic carbon use and cycle

Since the beginning of the industrial revolution, mankind has relied on fossil fuel resources as the main energy source for driving human progress. Their combustion has led to the release into the atmosphere of large amounts of carbon which had been stored on earth for millions of years. At the same time, large forest surfaces were removed to make space for productive land. Both of these developments impacted the fluxes in the earth's carbon cycle and have thereby significantly disturbed its equilibrium. This can be seen by the red numbers in **Figure 1-4**. Neither photosynthesis nor the oceans are currently able to compensate the excess carbon released into the atmosphere by human action. As a result, 4.4 Gt (4'400'000'000'000 kg) of carbon are accumulating in the atmosphere each year, primarily in the form of carbon dioxide.[24] This has increased atmospheric carbon dioxide levels from 275 ppm in pre-industrial times to more than 400 ppm today.

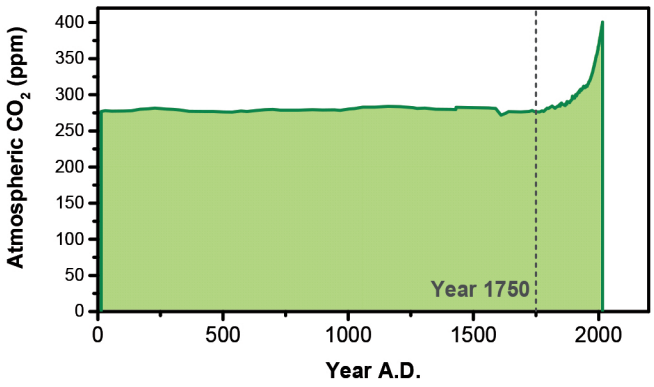

Figure 1-5: **Atmospheric arbon dioxide concentration since 13 A.D.** An extraordinary increase can be observed starting from 1750, coinciding with the onset of industrialization. The y-axis has on purpose been scaled from 0 ppm. Data from Scripps Research Institute.[27]

Due to its optical properties, CO_2 is able to reflect a part of the heat dissipated by earth back to its surface, causing the surface temperature of the planet to correlate

with the CO_2 concentration. This has led the average global temperature to increase by almost 1°C in the same timeframe,[25] which in turn is impacting a number of parameters of the world's climate system, leading to potentially nefarious challenges to the human habitat.[26]

Anthropogenic carbon use causes these modifications because it does not form a closed cycle and instead simply consists in the rapid depletion of fossil carbon reservoirs. If the same fuels, however, had been generated by fixing carbon from the atmosphere, no net increase in atmospheric carbon concentration would occur, rendering the system entirely carbon neutral.

The production of fuels from CO_2 and water is practically feasible but requires energy. If the invested energy derives from renewable resources, however, the production of fuels from CO_2 opens the door to a closed and sustainable anthropogenic carbon cycle, the Holy Grail to solving the world's climate issues.

Carbon-based solar fuels

Carbon based solar fuels can be produced in a number of ways, including the use of organisms which generate biofuels and biomass. However, these approaches normally hover around 1% solar to fuel efficiency and compete for land mass with food crops.[28]

This thesis focusses on yet another approach: the direct electrochemical conversion of CO_2. In this process, electrical energy is used to drive the conversion of CO_2 and H_2O into fuel products at electrocatalytic materials, establishing a bi-directional link between the electrical energy system and the carbon-based value chain, the two main energy flows in the human sphere. Achieving the capability to interconvert electricity and carbon fuels introduces substantial flexibility in the energy system by not only allowing for the production of fuels but also to produce, for example, ethylene, a key commodity in the chemical industry. In addition to its promising industrial applications, the electroreduction of CO_2 is a highly interesting academic problem involving a wide number of fields of study, some of which still lack thorough understanding.

Electrochemical reactions

Electrochemistry links chemical reactions with electrical current. Such a link is typically achieved by spatially separating the oxidation and reduction part of a redox reaction and passing the exchanged electrons through an external circuit (**Figure 1-6**). This setup gives the operator control over both the thermodynamics and kinetics of a reaction by varying the electrical potential between the two compartments.

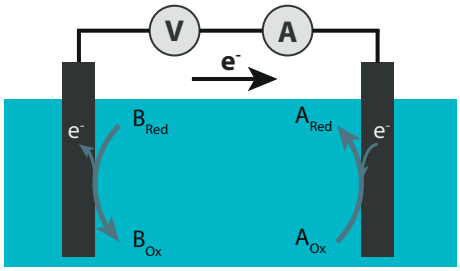

Figure 1-6: **Electrochemical cell.** The oxidation and reduction parts of the reaction happen at distinct places and exchanged electrons are forced through an external circuit. By this setup, a chemical reaction is linked with electrical potential and current.

$$
\begin{aligned}
A_{Ox} + e^- &\rightarrow A_{Red} \\
B_{Red} &\rightarrow B_{Ox} + e^- \\
\hline
A_{Ox} + B_{Red} &\rightarrow A_{Red} + B_{Ox}
\end{aligned}
$$

Equation 1-1: **Generic electrochemical reaction.** The total reaction, shown below the line, can be decomposed into a reduction (top) and oxidation half reaction (top). "*Red*" designates the reduced form of a species, "*Ox*" designates its oxidized form.

A generic electrochemical reaction, wherein an electron is transferred from species B_{Red} to species A_{Ox}, yielding A_{Red} and B_{Ox}, is shown in **Equation 1-1**. Notably, this equation can be decomposed into its two half reactions, the reduction part (top) and oxidation part (bottom). The Gibbs Free Energy change of a reaction directly expresses electron work and is therefore proportional to the electrochemical potential difference and the exchanged charge according to:

$$\Delta G = -n \cdot F \cdot \Delta E$$

Equation 1-2: **Relationship between chemical gibbs energy difference (ΔG) of a reaction and the electrochemical potential difference (ΔE).** ΔG expresses the change in Gibbs Free energy [J mol^{-1}] between the initial and final state of the

reaction, n expresses the number of exchanged electrons in the reaction, F the Faraday constant (96485 C mol^{-1}) and ΔE expresses the electrochemical potential difference in [V].

By changing the applied electrochemical potential at the surface of the electrodes, the operator can therefore freely decide on the driving force, e.g. the Gibbs Free Energy change, of the reaction and also choose the direction (forward, backward) it takes. Like for classical reactions, this thermodynamic description has to be extended by kinetic considerations. Changing the electrochemical potential shifts the relative energetic position of the initial and final state of the reaction, as is illustrated schematically in **Figure 1-7a**. But as can be seen from the same figure, this also impacts the relative position of the activation barriers. At the thermodynamic equilibrium potential, both activation energies have the same magnitude and the reaction will therefore happen with the same rate in both directions. No change in reactants and products will be observed. If the potential is moved away from the equilibrium, one activation energy will become larger, while the one corresponding to the opposite reaction decreases, therefore inducing a net transformation starting from the state experiencing the lower activation energy.

A linearized form of this relationship has been expressed mathematically in the Butler-Volmer model, **Equation 1-3**. Therein, the total current density corresponds to the difference between the forward and the backward reaction, both of which are defined by an Arrhenius type behavior, while the activation energy is influenced by the applied electrochemical potential. In this model, the kinetics of an electrochemical reaction are defined by j_0, the exchange current density, describing the overall height of the activation barrier, and α, the transfer coefficient, which expresses their relative slopes, **Figure 1-7b**.

For an electrochemical process to take place, the activation energy has to be lowered such that it can be overcome by the thermal energy available in the environment. The required electrochemical energy to achieve this will, by nature of the system, exceed the energy required for the electrochemical transformation to become thermodynamically feasible. However, this excess energy, which is also called *overpotential*, is not being stored in the chemical species created in the process and will therefore be lost in the form of heat. In order to be able to run electrochemical

processes efficiently, *electrocatalysts* have to be developed which minimize the activation barriers required for the reaction to take place and, as a consequence, decrease the overpotential losses.

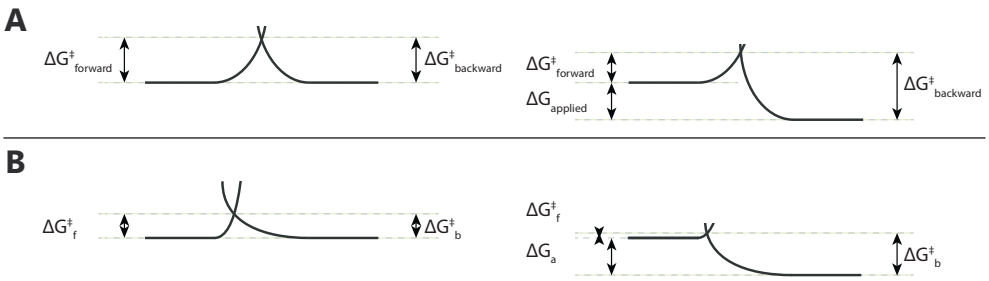

Figure 1-7: **Kinetic processes in electrocatalytic reactions.** (A) Schematic representation of the change in activation barrier upon the application of an electric field. (B) For a transfer coefficient $\alpha \neq 0.5$, the activation barrier becomes asymmetric, leading to a different kinetic behaviour in the anodic and cathodic direction.

$$j = j_0 \cdot \left(e^{\left(\frac{\alpha n F}{RT} \cdot (E - E^0) \right)} - e^{\left(-\frac{(1-\alpha) n F}{RT} \cdot (E - E^0) \right)} \right)$$

Equation 1-3: **Butler-Volmer equation.** j expresses the current density, j_0 the exchange current density at equilibrium, α the transfer coefficient (the symmetry of the energy barrier), R the ideal gas constant (8.314 J mol^{-1} K^{-1}), T the temperature in Kelvin, E the applied electrochemical potential and E^0 the thermodynamic equilibrium potential of the reaction.

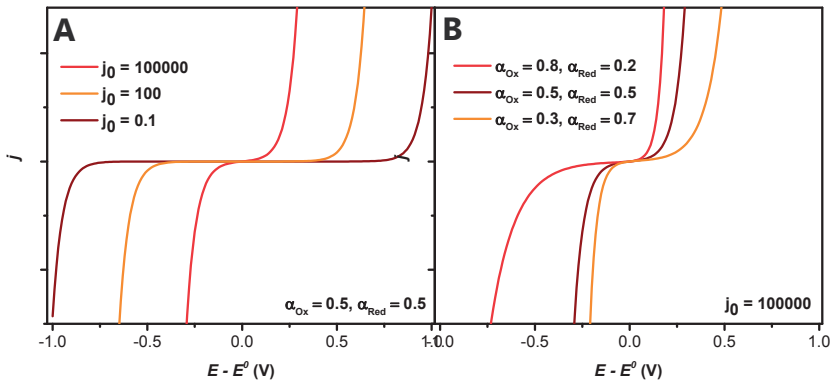

Figure 1-8: **Illustration of Butler-Volmer characteristics.** (A) Impact of exchange current density and (B) impact of the transfer coefficient.

In terms of a Butler-Volmer description, good fuel-forming catalysts will have a large exchange current density and small transfer coefficients (**Figure 1-8**). This description becomes more complicated when multi-electron systems are being considered. The same is true for homogeneous systems, since the electrochemical

signal includes catalyst diffusion. For a treatment of this problem, see the Perspective by Kubiak et al.[29]

Like classical catalysts, electrocatalysts operate by stabilizing intermediates of the reaction cycle and thereby shifting the reaction pathway to lower activation energies. A delicate balance has to be reached to minimize the activation potentials in each reaction step. This is exemplified in **Figure 1-9** for the stabilization of a H* intermediate on different materials. If the intermediate is bound too weakly, the activation energy to generate H* is large, whereas if the intermediate is bound too strongly, forming dihydrogen requires a prohibitive amount of energy. Only an intermediate binding strength leads to efficient catalysis and correspondingly large currents. This becomes particularly challenging for complex multistep reactions such as the ones involved in forming hydrocarbons and oxygenates from CO_2 and water, where dozens of sequential steps are involved.

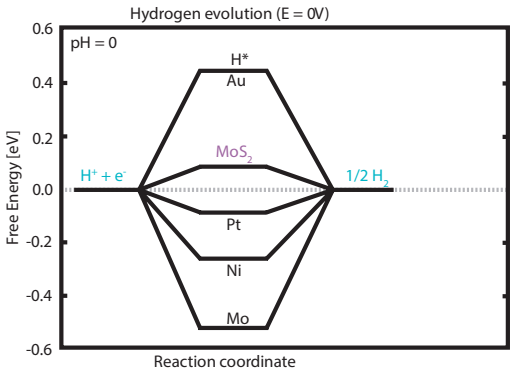

Figure 1-9: **Energy diagram of hydrogen binding on different hydrogen evolution catalyst materials.** An intermediate binding strength is required for the hydrogen evolution reaction to be most efficient. Adapted from Jaramillo.[30]

In addition to their intrinsic activity, electrocatalysts are also defined by a number of extrinsic factors. These include the conductivity of the catalyst material[31] and mass transport considerations.[32] Last but not least, a catalyst has to be stable under extended operation, which specifically also concerns the stability of any catalytically active crystal facets.

With homogeneous and heterogeneous systems, two broad classes of electrocatalysts can be distinguished.[33] Homogeneous catalysts, as distinguished from simple redox shuttles, are commonly molecular metalorganic complexes.

They show well defined chemical structure, allowing for the application of the whole toolbox of chemical synthesis and characterization techniques. This makes them readily amenable to in-depth mechanistic studies both by structure modification and analysis. These catalysts are typically dissolved in an electrolyte and get reduced at the surface of an electrode, which is itself inert to the desired electrochemical reaction.[34] The catalytic operation commonly follows an "inner sphere" mechanism on the metal center of an organometallic complex, which takes up reactants into its coordination sphere and stores charges obtained from the electrode. If present, redox-active ligands may also participate in storing charge. Once the catalytic cycle has been completed and the product released, the catalyst finds itself in its original configuration, leading into the next catalytic cycle. An excellent review on the workings and the design of molecular electrocatalysts for energy applications has been provided by DuBois.[35]

Heterogeneous electrocatalysts are commonly metals, or metal-based solids such as oxides, sulfides, phosphides, etc., with different exposed crystal facets and surface nanostructures. In most cases, these structures are more disordered than their molecular counterparts and therefore more difficult to study.[36] However, due to their complex surface chemistry, they are, in the field of CO_2 reduction, able to promote more complex reactions, leading to interesting products such as hydrocarbons and oxygenates.[37,38]

Hybrid molecular-heterogeneous systems can also be designed, as will be discussed in **Chapter 3**.[39]

CO_2 Reduction Electrocatalysts

Homogeneous

A large number of homogeneous electrocatalysts, based on numerous metal centers (mostly Re, Ru, Pd, Fe, Ni, Mn) and ligands (polypyridyl, phosphines, porphyrins) have been investigated for the CO_2 reduction reaction in aqueous and nonaqueous electrolytes and have been reviewed elsewhere.[34] It is notable that apart from a small number of exceptions,[40] only 2-electron reduction products such as CO and $HCOO^-$ were observed with molecular catalysts. As noted by Savéant, no clear trends between catalytic activity and molecular structure can be derived as of yet between the different catalyst groups, despite the large body of work on these systems.[34]

A notable group of molecular catalysts for CO_2 reduction is based on rhenium-bipyridyl complexes which operate in nonaqueous solvents and were originally introduced by Lehn and co-workers, **Figure 1-10**.[41] These catalysts are highly selective for the production of carbon monoxide, even in presence of substantial amounts of protons.[42,43] Their mechanism of operation will be discussed in the introduction to **Chapter 2**.

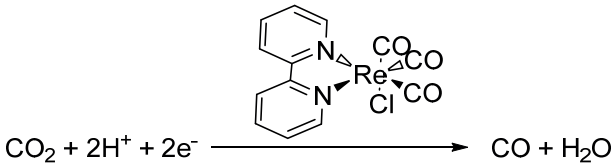

Figure 1-10: **Molecular rhenium catalyst for CO_2 reduction.** In this example, H^+ is designated as oxide acceptor. Voyame has shown that CO_3^{2-} formation is also possible.[44]

Heterogeneous

A minor part of this paragraph was adapted from a section I wrote for publication in reference 45.

Virtually all successful examples of heterogeneous CO_2 electroreduction have been shown on catalysts which are either metallic from the start or have been derived from metal oxide precursors, reduced *in-situ* to the respective metal. Seminal work by Hori has classified the transition metals in four different groups, distinguished by their predominant product: Metals producing hydrogen, metals producing CO and metals producing formate. Gold and silver have been found to be the most efficient and selective catalysts in producing CO.[38,46] Copper, on the other hand, stood out due to its unique activity toward producing hydrocarbons at significant yields and is therefore the only metal in the fourth group.[38,47] An overview of the relevant metals is shown in **Table 1-1**. The most notable products observed from copper were found to be CO, formate, methane, ethylene and ethanol. But more recent work was able to show that a much wider range of different products are produced on copper, albeit at lower concentration.[48] This work led to the discovery of 16 different species, which were hypothesized to have been produced by successive dehydroxylation and gave a glimpse at the complicated chemistry happening on copper surfaces.

Predominant Product	Metal Catalyst	Equilibrium potential (V vs. RHE)
Carbon Monoxide	Au, Ag, Zn, Pd, Ga	- 0.11
Formate	Pb, Hg, In, Sn, Cd, Tl	- 0.20 + 0.059 (pH - 4)
Hydrogen	Ni, Fe, Pt, Ti	0
Hydrocarbons, Alcohols	Cu	0.09 (Ethanol) 0.08 (Ethylene) 0.17 (Methane)

Table 1-1: **Common products observed from the electrochemical reduction of CO_2, related to the metals that predominantly produce them.** Adapted from [38].

The special role of copper was ascribed to its intermediate binding strength for CO, allowing it to be further reduced before desorbing. This was supported by the discovery that the product distribution was similar when CO was used as starting material, indicating its role as a key intermediate in the process.[49] Interestingly, other metals were also found to lead to more reduced products, albeit at very low selectivities.[46] This report, too, assigned a crucial role to the binding strength of CO, which was suggested to act as an intermediate. Cu single crystal experiments showed that on {100} facets, ethylene was formed with good selectivity at low overpotentials, whereas on {111} facets, methane was produced, albeit at larger overpotentials. {110} facets were found to lead to the production of more reduced species at even higher overpotentials.[49,50] With the exception of the role of CO as an intermediate, the mechanism of CO_2 reduction on copper is still poorly understood. Evidence can be found, pointing out that the production of formate versus CO takes a different path right from the step of binding CO_2 to the copper surface.[51] The production of methane is proposed to pass through a *CHO intermediate and is dependent on the pH on the SHE scale.[49] On the other hand, ethylene is proposed to pass through the coupling of two *CO intermediates in a pH-independent process. However, a second mechanism for ethylene formation is proposed to be in play, passing through a shared, pH dependent, *CHO intermediate with methane and appearing at larger overpotentials.[52,53]

A very interesting avenue has emerged in the use of oxidized precursors to catalysts.[54] Particularly the work by Kanan and co-workers is notable in which the oxides of copper, gold and lead were electrochemically reduced *in-situ* to act as catalysts.[55–58] Compared to bare surfaces of the same metal, the performance enhancement observed from these catalysts was striking. Oxide-derived copper electrodes showed a maximum selectivity for CO at almost 400 mV less overpotential than on bare copper foil, while also showing significantly larger current densities.[55] With CO as starting material, the same authors reached high faradaic efficiencies in ethanol and acetate.[59] A significant body of subsequent literature found that these further reduced products also appeared when CO_2 was used as substrate.[60–63] Oxide-derived gold also showed a substantial improvement over metallic gold, achieving 0.3 mA cm^{-2} and 60 % selectivity in CO at only 140

mV of overpotential.[56] Kanan and co-workers have subsequently investigated the origin of the improved performance. By carefully studying highly strained gold and copper nanoparticles, which were subsequently annealed at different temperatures, evidence was found pointing toward a specific activity of grain boundaries in these catalytic processes.[64,65] The improved activity of oxide-derived catalysts was therefore ascribed to their increased density of grain boundaries. In a separate work, the same group used temperature programmed desorption (TPD) of CO to investigate the CO binding strength on different catalyst samples. In this study, the presence of a distinct and strong binding mode of CO was found to correlate with the amount of grain boundaries in the sample.[66]

In an effort to increase the catalytic performance, nanostructuring of metal catalysts has been investigated. This has led to the discovery of a number of different effects, all of which are still under active investigation. Nanostructuring led to the appearance of effects associated with mass transport, leading to increased selectivity of CO_2 reduction on gold and silver catalysts, by suppressing the hydrogen evolution reaction.[67,68] In other systems, mass transfer limitations were suggested to change the product selectivity by influencing the local pH at the electrode surface.[61,69] Nanostructuring not only changes the diffusion in a catalyst but also its surface facets. In this context, it was found that nanostructured catalysts may not be as universally beneficial for CO_2 reduction catalysis, as they are for the hydrogen evolution reaction. Decreasing the feature size was found to expose low-coordinated surface facets of copper and gold nanoparticles, increasing the activity and therefore selectivity of the hydrogen evolution reaction.[70–74] In a recent study, it was suggested that features introduced by nanostructuring gold catalysts lead to an increase in local electric fields, attracting electrolyte cations which in turn increase the concentration of CO_2 at the electrode surface and consequently lead to an improved catalytic activity.[75]

Process conditions were found to be crucial for the activity and selectivity of electrochemical CO_2 reduction systems. Pressure was found to have a large impact on selectivity for copper catalysts, with the production of ethylene being significantly enhanced with increasing pressure up to 9 atm.[61] Increases in pressure above 10 atm lead to more formation of CO and formate, which keep increasing as

the pressure goes up,[49] an effect which was attributed in changes in the hydrogen concentration at the catalyst surface. Similarly, it was found that on Cu catalysts, decreasing the temperature of the CO_2 reducing medium led to a decrease in the selectivity for hydrogen but also for ethylene, while the methane selectivity increases.[49] Cell design and macroscopic transport phenomena involving electrolyte and substrate concentration also have an important impact on the activity and selectivity observed from catalysts. These effects have been investigated in detail by Bell and co-workers.[76,77]

A further parameter used for tuning catalysts for CO_2 reduction consists in the formation of alloys and mixed-metal catalysts. Few studies exist to date on this topic which is still under investigation by a number of groups. In one highly publicized report, the formation of alloys between Au and Cu led to a slightly improved mass activity for CO production, albeit at decreased selectivity.[78] One report combining Au and Pd,[79] as well as another one combining Ni and Ga,[80] found the appearance of products which were not observed on either metal individually. In both cases, however, the selectivity remained very small. More successful in changing the selectivity, albeit from further reduced products to CO, was the electrochemical reduction of copper oxide in the presence of In and Sn.[81,82]

Changes in the activity of catalysts were also observed by changing the composition of the employed electrolyte. Alkali cations were found to have a substantial impact on the electrocatalysis of CO_2 reduction.[83] This effect was attributed to their hydration shell acting as a buffer, stabilizing the local pH at the electrode surface, and thereby stabilizing the local concentration of CO_2. In other studies, the concentration of bicarbonate electrolyte was investigated, finding that higher concentrations led to an increased current but to lowered selectivity for CO_2 reduction.[61,69] A special role has been attributed to electrolyte additives such as ionic liquids, which were shown to enhance the electrocatalytic reduction of CO_2 on silver electrodes.[84] It was suggested that they lead to an improved solubility of CO_2.[85] However, research also shows that the imidazolium cation plays a special role in enhancing the electrocatalysis of CO_2 on silver electrodes.[86] This effect is still poorly understood and while it is possible that imidazolium cations interact

specifically with the electrode surface,[87–89] some groups suggest that non-specific ionic interactions may also be the underlying cause of the observed effects.[90]

This overview makes it clear that substantial work is still needed to gain significant understanding of the processes that govern electrochemical CO_2 reduction on both molecular and heterogeneous catalysts. Specifically, the reduction of CO_2 to hydrocarbons and oxygenates is only insufficiently understood and does not operate in a stable manner.

Solar energy harvesting and fuel generation

Photovoltaic effect

To couple solar energy with an electrochemical process, sunlight has to be transformed into an electromotive force. This can be achieved by exploiting the properties of semiconductors. Semiconductors are materials with an electrical conductivity between metals (> 10^2 S cm^{-1}) and insulators (< 10^{-8} S cm^{-1}),[91] with an electronic structure characterized by the presence of an intermediate energy gap between their valence and conduction bands. In 1939, E. A. Becquerel discovered that two platinum electrodes, immersed in an acidic solution containing silver chloride – a semiconductor - led to the appearance of a photovoltage, hence creating the first solar cell.[92] While Becquerel only reported his phenomenological observation, nowadays the underlying principles of this effect are understood as will be explained next.

The energy of light is related to its wavelength according to **Equation 1-4**.

$$E_{light} = \frac{hc}{\lambda} > E_{BG}$$

Equation 1-4: **Energy of light as a function of wavelength.** h is Planck's constant, c is the speed of light, λ is the wavelength of the light, E_{BG} denotes the bandgap energy which has to be smaller than the energy of light if absorption is to happen.

When light of energy equal or larger than the bandgap is shone on a semiconductor, electrons gain energy by absorbing the radiation and are excited from the semiconductor valence band to a higher energy level in the conduction band (**Figure 1-11**). This leads to an excess of negative charge (electrons) in the

conduction band and an excess of positive charge (holes) in the valence band. If no further action is taken, the two *charge carriers* will simply recombine over time and in most cases release heat.

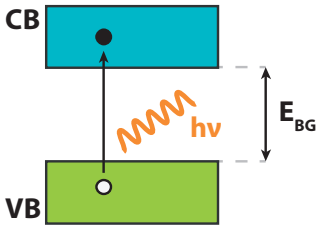

Figure 1-11: **Semiconductor band structure.** Illustration of charge carrier excitation by light absorption.

To extract electric work from excited electrons, light *absorption* has to be followed by a *separation* step. The most prominent consists in creating a p-n junction. Semiconductors can be doped, e.g. excess negative (n-doped) or positive (p-doped) charge can be introduced into the conduction or valence band. This can happen by the intentional or unintentional introduction of impurities, as well as anion or cation vacancies into the semiconductor crystal lattice. The energy level of these impurities lie close to the respective bands allowing for thermal excitation of the respective electrons or holes into the conduction or valence band, respectively (**Figure 1-12a**).

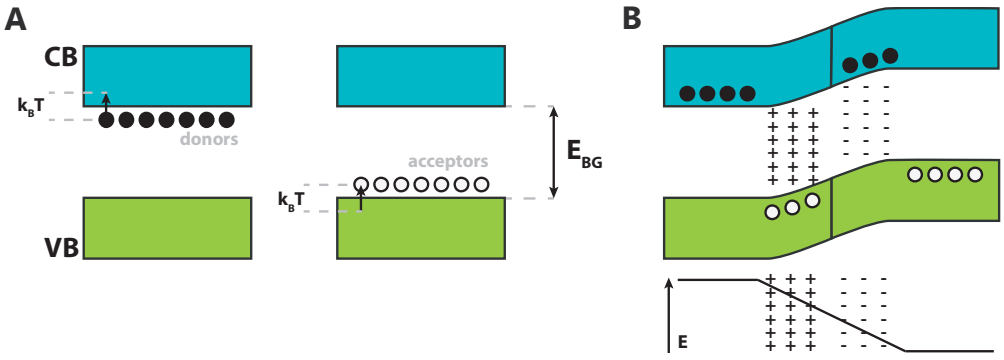

Figure 1-12: **Junction formation.** (A) Illustration of impurity donor and acceptor states, leading to n and p doped semiconductors, respecitvely. (B) Very simplified illustration of a p-n junction after equilibration.

If two semiconductor materials with opposite doping are brought in contact with each-other, the excess electrons of the n-type semiconductor will flow into the p-type semiconductor and holes will flow in the other way. Since there are no mobile

charges of opposite polarity present in the semiconductors, this process introduces a built-in electric field in the junction (**Figure 1-12b**). If a pair of negative and positive charge carriers are photogenerated within the junction or diffuse into it, they will experience an electric field, be separated into opposite directions and thereby build up a spatial voltage difference. The device thus works as a solar cell and provides an electromotive force.

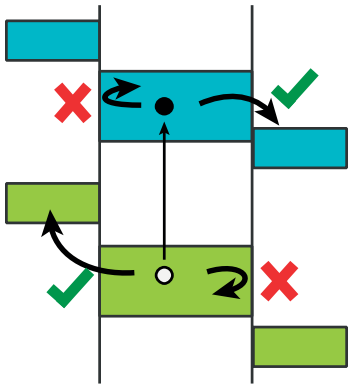

Figure 1-13: **Illustration of the working of charge selective contacts.** Negative charges can flow to the right side of the device while positive charges are reflected and vice-versa.

Charges can equally be separated by carrier selective contacts. For electrons, as an example, this is achieved by contacting the light absorbing semiconductor with a n-type material, which has a slightly lower conduction band, allowing for electrons to flow, and a valence band which lies below the valence band of the absorber, thereby blocking the transport of holes, which always move "up" in energy. In analogy a hole-selective contact can be generated. An illustration is shown in **Figure 1-13**. Light-generated charge carriers thus diffuse to one of both sides and are then extracted by the respective contact, thereby accumulating in the charge selective contact.

Another method concerns charge separation by kinetic competition, an effect which is in play in dye sensitized solar cells but is beyond the scope of this thesis.[93]

Photoelectrochemical cells

Generating and separating photoexcited electrons does not yet make a device to produce fuels from solar energy. The electrons also have to be channeled in a way such as to lead to the reduction of carbon dioxide, hence coupled with an electrocatalyst.

One way of achieving this consists in integrating the different functions - light absorption, charge separation and catalysis - onto a single device. From this results an *artificial leaf*,[94] inspired by nature's implementation of photosynthesis. Such *photoelectrodes* are employed in *photoelectrochemical cells (PEC)*.[95] It is argued that by integrating the different functions a simple system design is achieved, which can potentially lead to a low cost solar fuel conversion device. This approach has received substantial attention both in the scientific community and in mainstream media. A large number of photoelectrodes have been demonstrated in practice. Different categories can be distinguished.[96] Some examples are typical photovoltaic devices, incorporating p-n junctions, which are coated with a catalyst and immersed into an electrolyte to operate.[97]

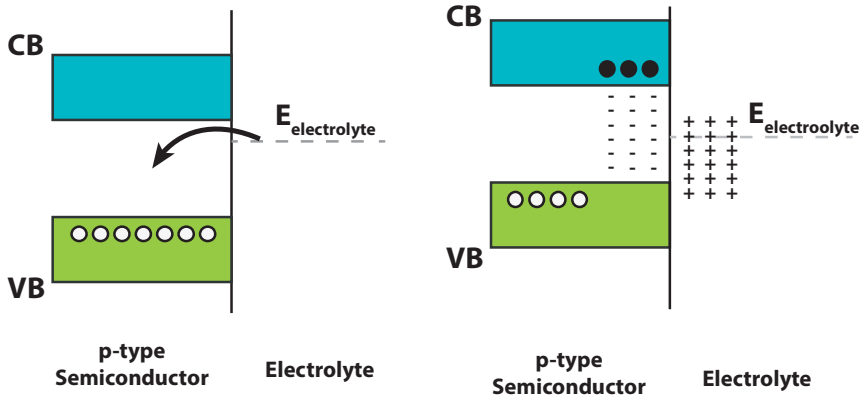

Figure 1-14: **Schematic of the formation of a p-type semiconductor-electrolyte junction.** The equilibration between the semiconductor and the electrolyte leads to a junction which separates photoexcited charges and drives the electrons toward the electrolyte, where they contribute to reduction reactions.

Lewis and co-workers classify this type of device as "PV-biased photoelectrosynthetic cell".[96] Another type of photoelectrode does not require a built-in p-n junction and instead forms a charge extracting junction by equilibrating with the electrolyte. Thereby, upon contacting a p-type semiconductor with a

suitable electrolyte, electrons from the electrolyte flow into the semiconductor, generating a built-in field which pushes photogenerated electrons to the photoelectrode surface (**Figure 1-14**). This type of device has been classified as "Photoelectrosynthetic cell".[96] An industrial implementation of this approach would see large fields of electrolyte-filled panels containing photoelectrochemical cells.[98] The electrolyte would continuously be replenished and the products collected over the extended surface of the PEC field.

Despite its elegant nature and potentially low cost, the approach of building an integrated artificial leaf faces a number of disadvantages. In the opinion of the author, the most important impediment is the requirement to handle large amounts of pressurized multiphase fluids in a large plant, spanning kilometers. A viable alternative consists in using photovoltaic cells to generate electrical current, which is converted to a solar fuel in a separate and specialized electrolysis device. As a key difference, while for the artificial leaf chemical products have to be transported from the solar absorber to the storage site, in a PV-coupled system electrons are being transported. A PV-coupled system allows for concentrating the generated current and therefore may require a smaller amount of catalyst, membranes and other balance of system components. Keeping the solar absorber materials out of the electrolyte also automatically removes impediments due to their corrosion. To date, no clear conclusion on the preferred approach exists and there are only insufficient technoeconomic studies which could provide answers. One notable example by Lewis, McFarland et al. finds the integrated artificial leaf to be less costly, citing that transporting fluids is cheaper than transporting electrical power.[99] Further investigations are needed to get a more in-depth analysis of the important question of large scale solar fuel production.

A number of studies have shown the coupling of CO_2 reduction with solar light by the means of photoelectrodes. Initial work focused of the investigation of the intrinsic activity of p-type semiconductors in contact with an electrolyte. The first report by Halmann in 1978, described the use of Zn-doped p-GaP cathodes in a pH 6.8 phosphate buffer solution containing CO_2. A photocurrent of up to 6 mA cm^{-2} was achieved and the production of formate, formaldehyde and methanol was reported. The same author also reported on the unassisted production of

formaldehyde and methanol when combining p-GaP electrodes with n-Si electrodes in a lithium carbonate electrolyte.[100] Unfortunately, a number of control experiments are missing in that study. Subsequent work investigated the activity of p-GaAs and p-InP toward the photoelectrochemical reduction of CO_2 and found the production of CO and formate with a maximum total yield exceeding 80%.[101] Notably, Hinogami and co-workers modified p-Si electrodes with Au, Ag and Cu particles. By carrying out product analysis at different biases and by comparing the performance of the modified photocathodes with simple metal electrodes, the authors found that the presence of the photocathode shifts the product spectrum to less negative bias by the magnitude of the voltage generated by the photocathode.[102–104] Recently, Yang and co-worker have demonstrated the deposition of Au_3Cu nanoparticles on p-Si nanowire photocathodes, leading to CO production with 80% faradaic efficiency at -0.2 V vs. RHE.

Examples have also been shown, where molecular catalysts were operated with photoelectrodes. A number have investigated cyclams, particularly of Ni, on various photocathodes. Bradley and co-workers have investigated these complexes on p-Si photocathodes, observing a 400 to 600 mV shift in onset potential for the production of a CO and H_2 mixture.[105] Chartier and Petit investigated Ni cyclam at p-GaAs and p-GaP electrodes.[106] Examples have also been shown of polymerized catalysts on photoelectrode surfaces. These will be covered in detail in **Chapter 3**.[107] Kubiak and co-workers showed the operation of $Re(bipy\text{-}Bu^t)(CO)_3Cl$ at p-Si, observing a 600 mV photovoltage shift.[108]

Despite these examples, the field of solar-driven reduction of CO_2 is at the very beginning of its development. A large number of processes remain poorly understood and the catalysts used in the few existing examples are either expensive or non-selective. This is very well illustrated by the record efficiency for unassisted solar CO_2 reduction which, at the start of my thesis work, was at 0.04 %.[109]

The importance of carbon monoxide

As described above, a large number of products can be synthesized by the electrochemical reduction of CO_2. This thesis predominantly pursues the production of carbon monoxide (CO). The electrochemical catalysis of products

other than CO and formic acid remains poorly understood and shows challenges with respect to stability. Striking a balance between the need for catalysis research and the desire to push the envelope of the solar-driven reduction of CO_2 led to the choice of CO as product.

Despite its (justified) reputation as a toxic gas, carbon monoxide is a chemical of considerable importance in the chemical industry where it serves as the starting point for several value chains, the most significant of which are briefly discussed here. CO finds application in the large scale production of methanol,[110] the production of acetic acid and in the production of synthetic hydrocarbon fuels. All of these processes lead to important commodity chemicals and derivatives, as is shown in **Figure 1-15**.

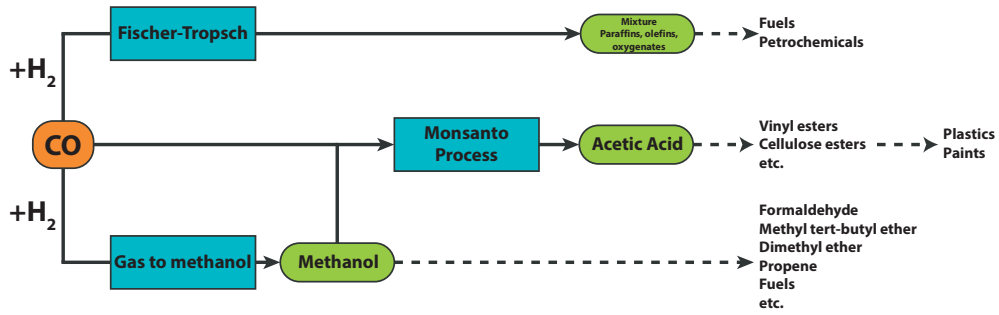

Figure 1-15: **Simplified CO value chain.** The main products synthesized from carbon monoxide are methanol, acetic acid and synthetic fuels, leading to a very large number of derivative chemicals.

Methanol is produced from synthesis gas, a mixture of CO and hydrogen, in the gas-to-methanol process.[111] In 2016, its worldwide production amounted to 80 million tons.[112] Methanol itself has a considerable value chain and serves as a starting point for the production of a large number of derivative chemicals, including formaldehyde, acetic acid and olefins.[112]

Acetic acid was produced at a capacity of 12 million tons in 2014[113]. The majority of acetic acid produced at the large scale comes from methanol carbonylation, where it is synthesized from methanol and CO. Acetic acid finds large scale application in the production of Vinyl and Cellulose ester polymers (65 % of the acetic acid goes toward this application),[114] among a number of other derivatives.

By reacting synthesis gas in the Fischer-Tropsch process, the non-selective production of fuel mixtures, as well as a large amount of olefins, paraffins and oxygenates can be realized. This process was originally developed to transform coal into liquid fuels and, together with other hydrogenation methods, played an important role in Germany during the 2nd world war because of the limited availability of indigenous fuels.[115] Political tension was again the driver for another large scale implementation in South Africa during Apartheid in the 2nd half of the 20th century. The country was under sanctions and therefore forced to derive its fuel from its abundant coal reserves.[116] Today, the South African company Sasol is still the world leader in the production of synthetic fuels,[117] with its three domestic plants producing 82'000 barrel per day.[118] The process is energy intensive, however, with ratios of 3.24 tons of CO_2 emitted per ton of fuel produced.[119]

At the start of all these processes lies the production of carbon monoxide, which is traditionally achieved by gasification of coal or by the reformation of methane or crude oil fractions.[115] In Fischer-Tropsch plants, the preparation of syngas is the most expensive part, accounting for a majority of the capital cost.[120,121] The processes introduced above have therefore the potential to run in a more sustainable way and at substantially decreased cost using renewably sourced CO and H_2. This integration of well-established chemical methods with solar precursors allows for the production of a wide spectrum of chemicals and fuels, making CO a key target for solar-fuel devices.

Motivation

Despite the bright prospects of generating carbon-based solar fuels, both the electrocatalysis as well as the integration of electrocatalysts with solar absorbers is still substantially lagging behind the astonishing progress that has been achieved for the production of hydrogen from solar energy.

The goal of this thesis is to narrow this gap by contributing to both the development of CO_2 reduction catalysts and to their integration with solar absorbers. Based on continuous learning and improvements, the work moved from hybrid inorganic-molecular studies in nonaqueous solutions as inspired by Dye Sensitized Solar Cell (DSSC) technology to unassisted solar-driven systems using heterogeneous electrocatalysts in aqueous electrolytes.

In **Chapter 2**, the integration of a solution borne molecular catalyst with a low-cost TiO_2-protected Cu_2O photoelectrode has been investigated and the ensuing charge transfer limitations, as well as a strategy to overcome them, have been studied.

In **Chapter 3**, the surface of TiO_2-protected Cu_2O photoelectrodes was modified with nanostructured TiO_2 in a low-temperature process, allowing for the covalent immobilization of a molecular rhenium catalyst. Thereby a hybrid heterogeneous-molecular photoelectrochemical system was created, leading to the effective production of carbon monoxide under illumination at 600 mV decreased potential.

Moving toward heterogeneous catalysts, the promotion of the reduction of carbon dioxide on silver electrode surfaces by imidazolium cations was investigated as described in **Chapter 4**. Nonaqueous electrolytes were chosen for this work to allow for meaningful electrochemical studies to be conducted by eliminating the possibility of hydrogen evolution to take place. In contrast to previous reports, the C2 proton was not found to be crucial, whereas the replacement of the C4 and C5 protons led to the suppression of the promoting effect.

Improving on the previous studies, which involve uncontrolled anodic reactions, entails the integration of a sustainable electron source. With the goal of achieving the sustainable and efficient photo-driven reduction of CO_2 coupled with the evolution of oxygen, the reduction of CO_2 to CO in aqueous solution, driven by perovskite photovoltaics was investigated in **Chapter 5**. In this work, porous Au

was used as cathode, whereas IrO_2 served as an oxygen evolving anode. This system operated for 18 h and reached efficiencies exceeding 6.5%.

In **Chapter 6**, CuO nanowires were investigated to serve as CO_2 reduction catalysts. It was discovered that ALD modification of CuO nanowires with minimal amounts of SnO_2 changed the CuO selectivity from a wide range of products to the predominant production of CO. This astonishing effect was investigated in detail by partial current analysis and chemisorption measurements, indicating a suppressed hydrogen evolution reaction and a decreased binding strength for both H_2 and CO after SnO_2 modification. The activity of SnO_2-coated CuO toward both the selective CO_2 reduction and oxygen evolution led to the design of a bifunctional electrolysis cell, separated by a bipolar membrane. This design enabled achieving a new record efficiency for the solar conversion of CO_2 to CO at up to 13.4% using an electrolysis system solely involving earth-abundant elements.

Methods

Simulated solar light

The solar radiation intensity and spectrum vary during the day, during the year and depending on the latitude of the observer. To enable the benchmarking of solar energy converters across different laboratories, standards for simulated solar light are needed. Widely accepted reference spectra have been published the American Society of Standards and Measurements (ASTM). At 1 AU (Astronomic Unit) – the distance between earth and the sun – the light intensity reaching the earth's atmosphere amounts to 1353 W m^{-2} according to ASTM E 490-73a.[3] The amount of solar energy reaching the outer surface of the atmosphere is commonly called "1 sun". When the light travels through the atmosphere, the spectrum is modified. Depending on the position on earth, different lengths of the atmosphere layer stand between the observer and the sun. In this thesis the AM1.5G spectrum is used as reference. This spectrum, according to ASTM G173,[122] was chosen to represent average conditions over all states in the US. It describes a surface, tilted at 37° relative to the normal and considers a spectrum of light which has travelled through 1.5 atmosphere layers. Importantly, this spectrum also includes a contribution of reflected light from the earth's surface, the so-called albedo.[3] In this work, AM1.5G at 1 sun refers to the AM1.5G spectrum at 100 mW cm^{-2}.

Xenon arc discharge lamps were used as laboratory light sources in this thesis. These show a relatively good match with the solar spectrum but exhibit intense lines in the range from 800 – 1100 nm.[123] To transform the spectrum to closer resemble AM 1.5G and to attenuate the intense plasma lines, filters are used. In this work, both Schott KG-3 filters, as well as a proprietary AM1.5 filter from Newport were applied. The light intensity of the xenon arc lamp was subsequently adjusted to 1 sun using a calibration diode.

Three-electrode electrochemical measurements

A key measurement technique in this thesis are three-electrode electrochemical measurements, used to characterize the performance of a single electrochemical half-cell reaction. As described above, an electrochemical reaction always entails

both an oxidation and a reduction process. If an electrochemical reaction is studied by a two-electrode setup, the observed current-voltage response will be a convolution of both the anode and cathode performance curves. In order to study an individual electrode, the contribution of the other half cell has to be removed. This can be achieved by introducing a third electrode, the *reference electrode* (RE), measuring the potential of the electrolyte, relative to the electrode of interest, designated herein as the *working electrode* (WE). In this setup, a potentiostat is used to fix the potential of the working electrode relative to the solution potential. A feedback loop now varies the potential applied between the working electrode and a *counter electrode* (CE), to establish the requested potential difference between the working and the reference electrode, thus solely characterizing the electrode of interest. A schematic of the design is shown in **Figure 1-16**.

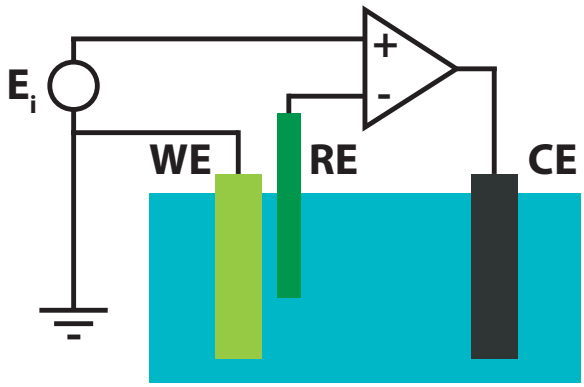

Figure 1-16: **Electronic diagram of a potentiostat connected to an electrochemical cell.** WE, RE and CE designate the working, reference and counter electrodes, respectively. E_i defines the desired potential between working and reference electrode.

Many electrochemical characterization techniques are trivial and simply involve biasing the working electrode at a given potential or current. More information can be obtained by techniques which change the potential at the working electrode in a time-dependent manner. Cyclic Voltammetry, for example, a technique based on sweeping the potential in a cyclic manner, yields a convoluted signal of redox and diffusion processes. If a redox active species is contained in an electrolyte solution and the potential is swept past its oxidation or reduction, a current will appear in the cyclic voltammogram and this current will increase with increasing potential. However, as all of the species close to the electrode are transformed, fresh

molecules have to diffuse from the bulk of the solution, leading to a decrease in the current, until a steady diffusion-controlled regime is attained. This effect leads to the appearance of peaks in classical cyclic voltammograms, as shown in **Figure 1-17**.

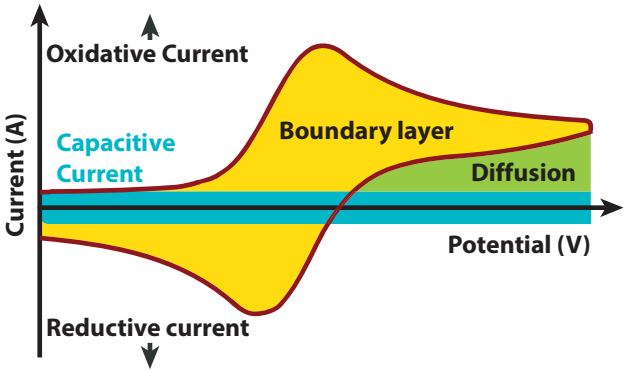

Figure 1-17: **Classical cyclic volatmmogram.** A capacitive region, as well as faradaic processes are shown. The current in the green region is related to diffusion of electroactive species toward the electrode.

Upon the reverse potential sweep, the species which previously has been brought into its reduced or oxidized state will experience the inverse reaction, leading to the fresh appearance of a peak of the opposite current. However, irreversible transformations of species after a redox event change this shape, shedding light on more complex phenomena taking part. A background current, generated by the charging and discharging of the electrochemical double layer capacitance is also observed in CV experiments.

Electrochemical test cell design

As described above, CO_2 reduction processes lead to the appearance of gas and liquid phase species. The details of their characterization are given in the respective chapters. However, in order to be able to recover the products, gastight test cells had to be designed for different applications. In some cases, accommodating a working, a reference and a counter electrode was sufficient. However, in other cases light has to be supplied to the working electrode or a membrane has to be used to separate the working from the counter electrode. To fulfill all these requirements, a highly versatile photoelectrochemical test cell was designed. This cell is characterized by a quartz window, a port accommodating a ceramic diaphragm to

serve as a separator of the counter electrode against the working electrode compartment and a port for a reference electrode. Two feedthroughs for electrodes in the working electrode compartment were integrated, whereas one is designed for the working electrode itself and the other for an auxiliary electrode used to measure the potential of the pseudo reference electrode against an internal standard. This cell design is shown in **Figure 1-18**. The transparent back window allows for spectroelectrochemical measurements to be carried out in transmission mode, for which a special setup was designed using fiber optic cables to transport the signal to a photodiode array. The quartz window can be replaced with any kind of membrane and an attachment serves as container for the counter electrode electrolyte. Gas is sparged into the cell through the lid, from where product gas is also continuously removed for analysis in a gas chromatograph which has been purchased at the beginning of my thesis work.

A second cell design was developed for large-scale two electrode measurements with electrodes of 20 cm^2 area. This design, as shown in **Figure 1-19**, features short distances for ionic transport, thereby minimizing resistive losses in the electrolyte. It also allows for the integration of a membrane and an independent reference electrode into each compartment.

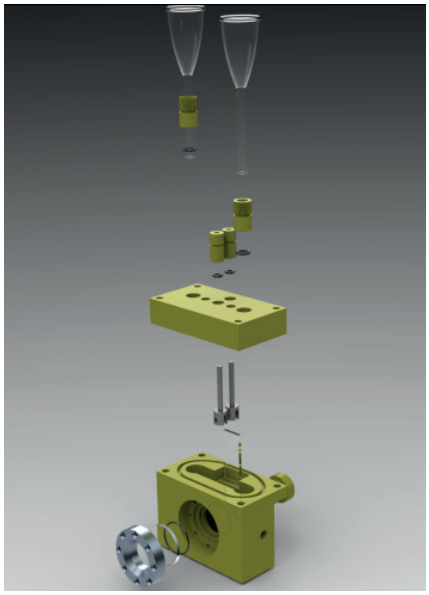

Figure 1-18: CAD drawing of the gastight photoelectrochemical cell design.

Figure 1-19: **CAD Drawing of large scale cell.** The copper plates represent the electrodes, whereas the green sheet represents the membrane.

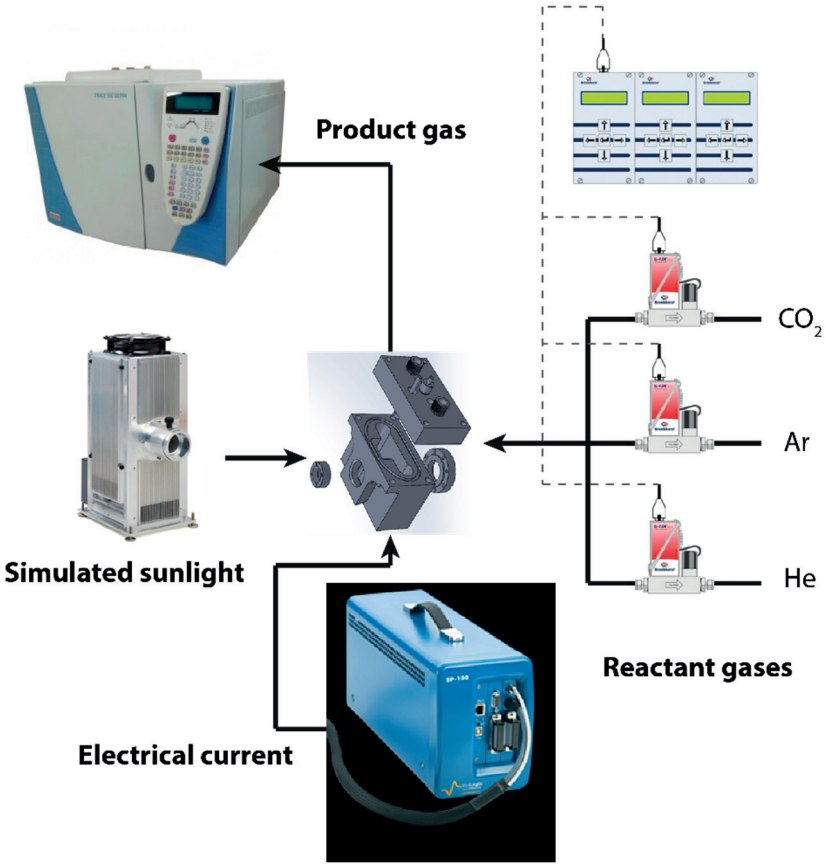

Figure 1-20: **Illustration of the setup for gas analysis.** Three mass flow controllers supply CO_2, Ar and He, whereas the controller for He can also supply CO. These gases then pass into the test cell containing the sample, to which a poteniostat provides current. All the gases then flow out of the cell into the sampling loop of a gas chromatograph and are periodically injected ont the column. If light energy is needed, it is supplied to the cell by an Oriel Xe-Arc solar simulator through a KG3 filter.

Gas analysis setup

A setup was built to allow for the on-line analysis of the gases generated in the electrochemical and photoelectrochemical reduction of CO_2. This setup consisted of mass flow controllers for the desired carrier gases (Bronkhorst), a potentiostat from BioLogic, a solar simulator from LOT Oriel and a GC bought from Thermo Scientific. The gases were passed in the test cell described above, which contains the sample. Subsequently, they flow out of the cell into the sampling loop of the gas chromatograph. The chromatograph is programmed to start a new injection each time it has completed the previous run. Thereby a maximum number of gas measurements are collected. The GC was equipped with a ShinCarbon column, able to achieve the separation of all the products involved in the reaction, except nitrogen and oxygen. A pulse discharge detector was chosen for its universal response. If illumination was involved in the measurement, light was supplied by the solar simulator through the quartz window in the test cell. A schematic of the installation is shown in **Figure 1-20**.

References

1. http://www.kcvs.ca/martin/astro/au/unit3/72/chp7_2.html. (Accessed: 3rd February 2017)
2. http://solarsystem.nasa.gov/planets/sun/facts. (Accessed: 22nd January 2017)
3. https://www.newport.com/t/introduction-to-solar-radiation. (Accessed: 22nd January 2016)
4. McClatchey, R. A., Fenn, R. W., Selby, J. A., Volz, F. E. & Garing, J. S. *Optical properties of the atmosphere*. (DTIC Document, 1972).
5. Bird, R. E., Hulstrom, R. L. & Lewis, L. J. Terrestrial solar spectral data sets. *Sol. Energy* **30,** 563–573 (1983).
6. *Key world energy statistics*. (International Energy Agency, 2016).
7. http://rredc.nrel.gov/solar/spectra/am1.5/. (Accessed: 22nd January 2017)
8. IEA. Key World Energy Statistics. (2012).
9. *Climate change 2014: synthesis report*. (Intergovernmental Panel on Climate Change, 2015).
10. Lewis, N. S. & Crabtree, G. *Basic Research Needs for Solar Energy Utilization: report of the Basic Energy Sciences Workshop on Solar Energy Utilization, April 18-21, 2005*. (US Department of Energy, Office of Basic Energy Science, 2005).
11. http://www.nrel.gov/pv/assets/images/efficiency-chart.png. (Accessed: 21st January 2017)
12. http://www.siemens.com/innovation/en/home/pictures-of-the-future/energy-and-efficiency/sustainable-power-generation-neural-networks.html. (Accessed: 2nd January 2017)
13. https://www.tesla.com/supercharger. (Accessed: 23rd January 2017)
14. http://batteryuniversity.com/learn/archive/whats_the_best_battery. (Accessed: 23rd January 2017)
15. Graetzel, M. Artificial photosynthesis: water cleavage into hydrogen and oxygen by visible light. *Acc. Chem. Res.* **14,** 376–384 (1981).
16. Bockris, J. O. A Hydrogen Economy. *Science* **176,** 1323–1323 (1972).
17. Jia, J. *et al.* Solar water splitting by photovoltaic-electrolysis with a solar-to-hydrogen efficiency over 30%. *Nat. Commun.* **7,** 13237 (2016).
18. *The hydrogen economy: a non-technical review*. (United Nations Environment Programme, 2006).
19. http://www.bccresearch.com/market-research/energy-and-resources/hydrogen-economy-opportunities-report-egy055c.html. (Accessed: 23rd January 2017)
20. Lalwani, S., Mitra, P., Ranjan, V., Tiwari, R. & Dewangan, A. K. Hydrogen Boosting In Single Cylinder Carborated Vehicle. *Ratio* **364,** 8
21. Durbin, D. J. & Malardier-Jugroot, C. Review of hydrogen storage techniques for on board vehicle applications. *Int. J. Hydrog. Energy* **38,** 14595–14617 (2013).
22. Alternative Fuels Data Center, US Department of Energy. Fuel Properties Comparison. (2014).
23. National Research Council of the National Academies, *Assessment of Fuel Economy Technologies for Light-Duty Vehicles.* Available at: https://www.nap.edu/read/12924/chapter/1 (Accessed: 3rd February 2017)
24. Ciais, P. *et al.* in *Climate change 2013: the physical science basis. Contribution of Working Group I to the Fifth Assessment Report of the Intergovernmental Panel on Climate Change* 465–570 (Cambridge University Press, 2014).
25. http://www.metoffice.gov.uk/research/news/2015/global-average-temperature-2015. (Accessed: 22nd January 2017)
26. Field, C. B. *et al.* in *Climate change 2014: impacts, adaptation, and vulnerability. Part A: global and sectoral aspects. Contribution of Working Group II to the Fifth Assessment Report of the Intergovernmental Panel on Climate Change* 1–32 (Cambridge University Press, 2014).
27. http://scrippsco2.ucsd.edu/data/atmospheric_co2/icecore_merged_products. (Accessed: 26th January 2017)
28. http://www.berkeleybiodiesel.org/efficiency-biodiesel-fuel.html. (Accessed: 24th January 2017)

29. Sathrum, A. J. & Kubiak, C. P. Kinetics and Limiting Current Densities of Homogeneous and Heterogeneous Electrocatalysts. *J. Phys. Chem. Lett.* **2,** 2372–2379 (2011).
30. http://jaramillogroup.stanford.edu/catalysis.html. (Accessed: 26th January 2017)
31. Trotochaud, L., Young, S. L., Ranney, J. K. & Boettcher, S. W. Nickel–Iron Oxyhydroxide Oxygen-Evolution Electrocatalysts: The Role of Intentional and Incidental Iron Incorporation. *J. Am. Chem. Soc.* **136,** 6744–6753 (2014).
32. Bard, A. J. & Faulkner, L. R. *Electrochemical methods: fundamentals and applications*. (Wiley, 2001).
33. Bertini, I. *Inorganic and Bio-Inorganic Chemistry - Volume II*. (EOLSS Publications, 2009).
34. Savéant, J.-M. Molecular Catalysis of Electrochemical Reactions. Mechanistic Aspects. *Chem. Rev.* **108,** 2348–2378 (2008).
35. DuBois, D. L. Development of Molecular Electrocatalysts for Energy Storage. *Inorg. Chem.* **53,** 3935–3960 (2014).
36. Bard, A. J. Inner-Sphere Heterogeneous Electrode Reactions. Electrocatalysis and Photocatalysis: The Challenge. *J. Am. Chem. Soc.* **132,** 7559–7567 (2010).
37. Appel, A. M. *et al.* Frontiers, Opportunities, and Challenges in Biochemical and Chemical Catalysis of CO_2 Fixation. *Chem. Rev.* **113,** 6621–6658 (2013).
38. Hori, Y. in *Handbook of Fuel Cells* (John Wiley & Sons, Ltd, 2010).
39. Windle, C. D. & Reisner, E. Heterogenised Molecular Catalysts for CO_2 Conversion. *Chimia* **69,** 435-441 (2015).
40. Shen, J. *et al.* Electrocatalytic reduction of carbon dioxide to carbon monoxide and methane at an immobilized cobalt protoporphyrin. *Nat. Commun.* **6,** 8177 (2015).
41. Hawecker, J., Lehn, J.-M. & Ziessel, R. Electrocatalytic reduction of carbon dioxide mediated by $Re(bipy)(CO)_3Cl$ (bipy = 2,2′-bipyridine). *J. Chem. Soc. Chem. Commun.* **6,** 328–330 (1984).
42. Smieja, J. M. *et al.* Kinetic and structural studies, origins of selectivity, and interfacial charge transfer in the artificial photosynthesis of CO. *Proc. Natl. Acad. Sci.* **109,** 15646–15650 (2012).
43. Keith, J. A., Grice, K. A., Kubiak, C. P. & Carter, E. A. Elucidation of the Selectivity of Proton-Dependent Electrocatalytic CO_2 Reduction by fac-$Re(bpy)(CO)_3Cl$. *J. Am. Chem. Soc.* **135,** 15823–15829 (2013).
44. Voyame, P. Photocatalytic and Electrocatalytic Reduction of Carbon Dioxide in Pressurized Systems. (2016). doi:10.5075/epfl-thesis-6985
45. Luo, J., Schreier, M., Mayer, M. T. & Grätzel, M. The quest for solar fuel. *Chem* (in preparation).
46. Kuhl, K. P. *et al.* Electrocatalytic Conversion of Carbon Dioxide to Methane and Methanol on Transition Metal Surfaces. *J. Am. Chem. Soc.* **136,** 14107–14113 (2014).
47. Hori, Y., Wakebe, H., Tsukamoto, T. & Koga, O. Electrocatalytic process of CO selectivity in electrochemical reduction of CO_2 at metal electrodes in aqueous media. *Electrochimica Acta* **39,** 1833–1839 (1994).
48. Kuhl, K. P., Cave, E. R., Abram, D. N. & Jaramillo, T. F. New insights into the electrochemical reduction of carbon dioxide on metallic copper surfaces. *Energy Environ. Sci.* **5,** 7050–7059 (2012).
49. Gattrell, M., Gupta, N. & Co, A. A review of the aqueous electrochemical reduction of CO_2 to hydrocarbons at copper. *J. Electroanal. Chem.* **594,** 1–19 (2006).
50. Hori, Y., Takahashi, I., Koga, O. & Hoshi, N. Electrochemical reduction of carbon dioxide at various series of copper single crystal electrodes. *J. Mol. Catal. Chem.* **199,** 39–47 (2003).
51. Kortlever, R., Shen, J., Schouten, K. J. P., Calle-Vallejo, F. & Koper, M. T. M. Catalysts and Reaction Pathways for the Electrochemical Reduction of Carbon Dioxide. *J. Phys. Chem. Lett.* **6,** 4073–4082 (2015).
52. Goodpaster, J. D., Bell, A. T. & Head-Gordon, M. Identification of Possible Pathways for C–C Bond Formation during Electrochemical Reduction of CO_2: New Theoretical Insights from an Improved Electrochemical Model. *J. Phys. Chem. Lett.* **7,** 1471–1477 (2016).
53. Schouten, K. J. P., Qin, Z., Gallent, E. P. & Koper, M. T. M. Two Pathways for the Formation of Ethylene in CO Reduction on Single-Crystal Copper Electrodes. *J. Am. Chem. Soc.* **134,** 9864–9867 (2012).

54. Le, M. *et al.* Electrochemical Reduction of CO_2 to CH_3OH at Copper Oxide Surfaces. *J. Electrochem. Soc.* **158,** E45–E49 (2011).
55. Li, C. W. & Kanan, M. W. CO_2 Reduction at Low Overpotential on Cu Electrodes Resulting from the Reduction of Thick Cu_2O Films. *J. Am. Chem. Soc.* **134,** 7231–7234 (2012).
56. Chen, Y., Li, C. W. & Kanan, M. W. Aqueous CO_2 Reduction at Very Low Overpotential on Oxide-Derived Au Nanoparticles. *J. Am. Chem. Soc.* **134,** 19969–19972 (2012).
57. Chen, Y. & Kanan, M. W. Tin Oxide Dependence of the CO_2 Reduction Efficiency on Tin Electrodes and Enhanced Activity for Tin/Tin Oxide Thin-Film Catalysts. *J. Am. Chem. Soc.* **134,** 1986–1989 (2012).
58. Lee, C. H. & Kanan, M. W. Controlling H^+ vs CO_2 Reduction Selectivity on Pb Electrodes. *ACS Catal.* **5,** 465–469 (2015).
59. Li, C. W., Ciston, J. & Kanan, M. W. Electroreduction of carbon monoxide to liquid fuel on oxide-derived nanocrystalline copper. *Nature* **508,** 504-507 (2014).
60. Kas, R. *et al.* Electrochemical CO_2 reduction on Cu_2O-derived copper nanoparticles: controlling the catalytic selectivity of hydrocarbons. *Phys. Chem. Chem. Phys.* **16,** 12194-12201 (2014).
61. Kas, R., Kortlever, R., Yılmaz, H., Koper, M. T. M. & Mul, G. Manipulating the Hydrocarbon Selectivity of Copper Nanoparticles in CO_2 Electroreduction by Process Conditions. *ChemElectroChem* **2,** 354–358 (2015).
62. Chen, C. S. *et al.* Stable and selective electrochemical reduction of carbon dioxide to ethylene on copper mesocrystals. *Catal Sci Technol* **5,** 161–168 (2015).
63. Ren, D. *et al.* Selective Electrochemical Reduction of Carbon Dioxide to Ethylene and Ethanol on Copper(I) Oxide Catalysts. *ACS Catal.* **5,** 2814–2821 (2015).
64. Feng, X., Jiang, K., Fan, S. & Kanan, M. W. Grain-Boundary-Dependent CO_2 Electroreduction Activity. *J. Am. Chem. Soc.* **137,** 4606–4609 (2015).
65. Feng, X., Jiang, K., Fan, S. & Kanan, M. W. A Direct Grain-Boundary-Activity Correlation for CO Electroreduction on Cu Nanoparticles. *ACS Cent. Sci.* **2,** 169–174 (2016).
66. Verdaguer-Casadevall, A. *et al.* Probing the Active Surface Sites for CO Reduction on Oxide-Derived Copper Electrocatalysts. *J. Am. Chem. Soc.* **137,** 9808–9811 (2015).
67. Hall, A. S., Yoon, Y., Wuttig, A. & Surendranath, Y. Mesostructure-Induced Selectivity in CO_2 Reduction Catalysis. *J. Am. Chem. Soc.* **137,** 14834–14837 (2015).
68. Yoon, Y., Hall, A. S. & Surendranath, Y. Tuning of Silver Catalyst Mesostructure Promotes Selective Carbon Dioxide Conversion into Fuels. *Angew. Chem. Int. Ed.* **55,** 15282–15286 (2016).
69. Varela, A. S., Kroschel, M., Reier, T. & Strasser, P. Controlling the selectivity of CO_2 electroreduction on copper: The effect of the electrolyte concentration and the importance of the local pH. *Catal. Today* **260,** 8–13 (2016).
70. Reske, R., Mistry, H., Behafarid, F., Roldan Cuenya, B. & Strasser, P. Particle Size Effects in the Catalytic Electroreduction of CO_2 on Cu Nanoparticles. *J. Am. Chem. Soc.* **136,** 6978–6986 (2014).
71. Mistry, H. *et al.* Exceptional Size-Dependent Activity Enhancement in the Electroreduction of CO_2 over Au Nanoparticles. *J. Am. Chem. Soc.* **136,** 16473–16476 (2014).
72. Zhu, W. *et al.* Monodisperse Au Nanoparticles for Selective Electrocatalytic Reduction of CO_2 to CO. *J. Am. Chem. Soc.* **135,** 16833–16836 (2013).
73. Zhu, W. *et al.* Active and Selective Conversion of CO_2 to CO on Ultrathin Au Nanowires. *J. Am. Chem. Soc.* **136,** 16132–16135 (2014).
74. Back, S., Yeom, M. S. & Jung, Y. Active Sites of Au and Ag Nanoparticle Catalysts for CO_2 Electroreduction to CO. *ACS Catal.* **5,** 5089–5096 (2015).
75. Liu, M. *et al.* Enhanced electrocatalytic CO_2 reduction via field-induced reagent concentration. *Nature* **537,** 382–386 (2016).
76. Lobaccaro, P. *et al.* Effects of temperature and gas–liquid mass transfer on the operation of small electrochemical cells for the quantitative evaluation of CO_2 reduction electrocatalysts. *Phys. Chem. Chem. Phys.* **18,** 26777–26785 (2016).

77. Singh, M. R., Clark, E. L. & Bell, A. T. Effects of electrolyte, catalyst, and membrane composition and operating conditions on the performance of solar-driven electrochemical reduction of carbon dioxide. *Phys. Chem. Chem. Phys.* **17,** 18924–18936 (2015).
78. Kim, D., Resasco, J., Yu, Y., Asiri, A. M. & Yang, P. Synergistic geometric and electronic effects for electrochemical reduction of carbon dioxide using gold–copper bimetallic nanoparticles. *Nat. Commun.* **5,** 4948 (2014).
79. Kortlever, R. *et al.* Palladium–gold catalyst for the electrochemical reduction of CO_2 to C1–C5 hydrocarbons. *Chem. Commun.* **52,** 10229–10232 (2016).
80. Torelli, D. A. *et al.* Nickel–Gallium-Catalyzed Electrochemical Reduction of CO_2 to Highly Reduced Products at Low Overpotentials. *ACS Catal.* **6,** 2100–2104 (2016).
81. Rasul, S. *et al.* A Highly Selective Copper–Indium Bimetallic Electrocatalyst for the Electrochemical Reduction of Aqueous CO_2 to CO. *Angew. Chem. Int. Ed.* **54,** 2146–2150 (2015).
82. Sarfraz, S., Garcia-Esparza, A. T., Jedidi, A., Cavallo, L. & Takanabe, K. Cu–Sn Bimetallic Catalyst for Selective Aqueous Electroreduction of CO_2 to CO. *ACS Catal.* **6,** 2842–2851 (2016).
83. Singh, M. R., Kwon, Y., Lum, Y., Ager, J. W. & Bell, A. T. Hydrolysis of Electrolyte Cations Enhances the Electrochemical Reduction of CO_2 over Ag and Cu. *J. Am. Chem. Soc.* **138,** 13006–13012 (2016).
84. Rosen, B. A. *et al.* Ionic Liquid–Mediated Selective Conversion of CO_2 to CO at Low Overpotentials. *Science* **334,** 643–644 (2011).
85. Klähn, M. & Seduraman, A. What Determines CO_2 Solubility in Ionic Liquids? A Molecular Simulation Study. *J. Phys. Chem. B* **119,** 10066–10078 (2015).
86. Zhao, S.-F., Horne, M., Bond, A. M. & Zhang, J. Is the Imidazolium Cation a Unique Promoter for Electrocatalytic Reduction of Carbon Dioxide? *J. Phys. Chem. C* **120,** 23989–24001 (2016).
87. Wang, Y. *et al.* Activation of CO_2 by ionic liquid EMIM–BF_4 in the electrochemical system: a theoretical study. *Phys. Chem. Chem. Phys.* **17,** 23521–23531 (2015).
88. Rosen, B. A. *et al.* In Situ Spectroscopic Examination of a Low Overpotential Pathway for Carbon Dioxide Conversion to Carbon Monoxide. *J. Phys. Chem. C* **116,** 15307–15312 (2012).
89. Urushihara, M., Chan, K., Shi, C. & Nørskov, J. K. Theoretical Study of $EMIM^+$ Adsorption on Silver Electrode Surfaces. *J. Phys. Chem. C* **119,** 20023–20029 (2015).
90. Chen, L. D., Urushihara, M., Chan, K. & Nørskov, J. K. Electric Field Effects in Electrochemical CO_2 Reduction. *ACS Catal.* **6,** 7133–7139 (2016).
91. Stiny, L. *Aktive elektronische Bauelemente: Aufbau, Struktur, Wirkungsweise, Eigenschaften und praktischer Einsatz diskreter und integrierter Halbleiter-Bauteile.* (Springer-Verlag, 2016).
92. Becquerel, E. Mémoire sur les effets électriques produits sous l'influence des rayons solaries. *Comptes Rendus Hebd. Séances Académie Sci.* 561 (1839).
93. Listorti, A., O'Regan, B. & Durrant, J. R. Electron Transfer Dynamics in Dye-Sensitized Solar Cells. *Chem. Mater.* **23,** 3381–3399 (2011).
94. Nocera, D. G. The Artificial Leaf. *Acc. Chem. Res.* **45,** 767–776 (2012).
95. Grätzel, M. Photoelectrochemical cells. *Nature* **414,** 338–344 (2001).
96. Nielander, A. C., Shaner, M. R., Papadantonakis, K. M., Francis, S. A. & Lewis, N. S. A taxonomy for solar fuels generators. *Energy Env. Sci* **8,** 16–25 (2015).
97. Reece, S. Y. *et al.* Wireless Solar Water Splitting Using Silicon-Based Semiconductors and Earth-Abundant Catalysts. *Science* **334,** 645–648 (2011).
98. Pinaud, B. A. *et al.* Technical and economic feasibility of centralized facilities for solar hydrogen production via photocatalysis and photoelectrochemistry. *Energy Environ. Sci.* **6,** 1983–2002 (2013).
99. Shaner, M. R., Atwater, H. A., Lewis, N. S. & McFarland, E. W. A comparative technoeconomic analysis of renewable hydrogen production using solar energy. *Energy Environ. Sci.* **9,** 2354–2371 (2016).
100. Halmann, M. Photoelectrochemical reduction of aqueous carbon dioxide on p-type gallium phosphide in liquid junction solar cells. *Nature* **275,** 115–116 (1978).

101. Yoneyama, H., Sugimura, K. & Kuwabata, S. Effects of electrolytes on the photoelectrochemical reduction of carbon dioxide at illuminated p-type cadmium telluride and p-type indium phosphide electrodes in aqueous solutions. *J. Electroanal. Chem. Interfacial Electrochem.* **249,** 143–153 (1988).
102. Hinogami, R., Nakamura, Y., Yae, S. & Nakato, Y. An Approach to Ideal Semiconductor Electrodes for Efficient Photoelectrochemical Reduction of Carbon Dioxide by Modification with Small Metal Particles. *J. Phys. Chem. B* **102,** 974–980 (1998).
103. Hinogami, R., Mori, T., Yae, S. & Nakato, Y. Efficient Photoelectrochemical Reduction of Carbon Dioxide on a p-Type Silicon (p-Si) Electrode Modified with Very Small Copper Particles. *Chem. Lett.* **23,** 1725–1728 (1994).
104. Hinogami, R., Nakamura, Y., Yae, S. & Nakato, Y. Modification of semiconductor surface with ultrafine metal particles for efficient photoelectrochemical reduction of carbon dioxide. *Appl. Surf. Sci.* **121–122,** 301–304 (1997).
105. Bradley, M. G., Tysak, T., Graves, D. J. & Viachiopoulos, N. A. Electrocatalytic reduction of carbon dioxide at illuminated p-type silicon semiconduccting electrodes. *J. Chem. Soc. Chem. Commun.* **7,** 349–350 (1983).
106. Petit, J.-P., Chartier, P., Beley, M. & Deville, J.-P. Molecular catalysts in photoelectrochemical cells: Study of an efficient system for the selective photoelectroreduction of CO_2: p-GaP or p-GaAs/Ni(cyclam)$^{2+}$, aqueous medium. *J. Electroanal. Chem. Interfacial Electrochem.* **269,** 267–281 (1989).
107. Cabrera, C. R. & Abruña, H. D. Electrocatalysis of CO2 reduction at surface modified metallic and semiconducting electrodes. *J. Electroanal. Chem. Interfacial Electrochem.* **209,** 101–107 (1986).
108. Kumar, B., Smieja, J. M. & Kubiak, C. P. Photoreduction of CO_2 on p-type Silicon Using Re(bipy-But)$(CO)_3$Cl: Photovoltages Exceeding 600 mV for the Selective Reduction of CO_2 to CO. *J. Phys. Chem. C* **114,** 14220–14223 (2010).
109. Sato, S. *et al.* Selective CO_2 Conversion to Formate Conjugated with H_2O Oxidation Utilizing Semiconductor/Complex Hybrid Photocatalysts. *J. Am. Chem. Soc.* **133,** 15240–15243 (2011).
110. http://www.chemie.de/lexikon/Methanol.html#Herstellung. (Accessed: 25th January 2017)
111. Ott, J. *et al.* in *Ullmann's Encyclopedia of Industrial Chemistry* (Wiley-VCH Verlag GmbH & Co. KGaA, 2000).
112. http://www.chemweek.com/lab/The-changing-face-of-the-global-methanol-industry_80172.html. (Accessed: 25th January 2017)
113. http://www.prnewswire.com/news-releases/global-acetic-acid-market---segmented-by-application-and-geography---trends-and-forecasts-2015-2020---reportlinker-review-300145381.html. (Accessed: 25th January 2017)
114. Le Berre, C., Serp, P., Kalck, P. & Torrence, G. P. in *Ullmann's Encyclopedia of Industrial Chemistry* (Wiley-VCH Verlag GmbH & Co. KGaA, 2000).
115. Kaneko, T. *et al.* in *Ullmann's Encyclopedia of Industrial Chemistry* (Wiley-VCH Verlag GmbH & Co. KGaA, 2000).
116. http://www.handelsblatt.com/unternehmen/industrie/petrochemie-konzern-sasol-der-heimliche-oelkonzern-aus-suedafrika/2699502.html. (Accessed: 25th January 2017)
117. http://www.sasol.com/extras/sasol-facts-pres-2/. (Accessed: 25th January 2017)
118. Hilyard, J. *2008 International Petroleum Encyclopedia*. (PennWell Books, 2008).
119. http://www.news24.com/scitech/news/sasols-co2-emissions-down-20091120. (Accessed: 25th January 2017)
120. *Annual Energy Outlook 2006 - Issues in Focus*. (US Energy Information Administration, 2006).
121. Shuster, E. *FY14 Analysisof Natura lGas-to-Liquid Transportation Fuels via Fischer-Tropsch*. (National Energy Technology Laboratory, US Department of Energy, 2013).
122. https://compass.astm.org/EDIT/html_annot.cgi?G173+03(2012). (Accessed: 25th January 2017)
123. Simulation of Solar Irradiation. Available at: https://www.newport.com/n/simulation-of-solar-irradiation. (Accessed: 4th February 2017)

2 Reduction of CO_2 to CO on Cu_2O Photoelectrodes using a Molecular Catalyst

This chapter is adapted with permission from the peer-reviewed publication:
***Marcel Schreier**, Peng Gao, Matthew T. Mayer, Jingshan Luo, Thomas Moehl, Mohammad K. Nazeeruddin, S. David Tilley, Michael Grätzel. Energy Env. Sci., 2015, vol. 8, 855.*
Reproduced with permission from the Royal Society of Chemistry.

With the aim of producing carbon monoxide by the photoelectrochemical reduction of CO_2 on the surface of a TiO_2 protected Cu_2O photocathode, the operation of a rhenium polypyridyl catalyst at the surface of such photocathodes is being investigated. Important charge transfer limitations are discovered, investigated and overcome, leading to the efficient sunlight-assisted production of CO for several hours.

Introduction

In addition to Dye Sensitized Solar Cells, which became a flagship project,[1] previous research at LPI has strongly focused on the development of sunlight-driven water splitting devices.[2] Among others, this work has led to the development of Cu_2O-based photocathodes for water splitting applications. Cu_2O is a semiconductor with a nominal direct bandgap of 2.0 eV, the transition of which is parity forbidden and therefore only leads to weak absorption. Parity allowed transitions set in from 2.5 eV.[3] The main advantage of Cu_2O as a light absorber is its low-cost and the possibility to prepare it in a scalable electrochemical solution process. While this material has therefore been used to fabricate early solar cells,[4] it cannot be readily applied as a photoelectrode since both its oxidation and reduction potential lie within its bandgap.[5] This has the consequence that, in presence of water, Cu_2O will corrode as soon as it being exposed to light (**Figure 2-1**).

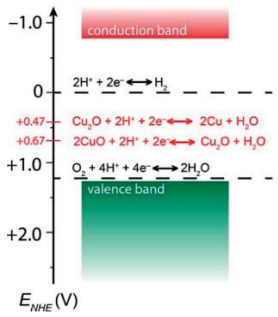

Figure 2-1: **Band positions and corrosion potentials of Cu_2O.** Theoretically the semiconductor is able to achieve unassisted water splitting. However, its corrosion potentials lie within the bandgap. Reprinted with permission from Tilley et al.[3] Copyright 2015 American Chemical Society.

This problem has been addressed by the deposition of wide bandgap semiconductor overlayers, which prevent the Cu_2O from contacting the electrolyte.[6] The most successful implementation of this approach was achieved by electrodeposition of Cu_2O, followed by atomic layer deposition (ALD) of TiO_2, a wide bandgap n-type semiconductor, which by its conformal nature allowed for stable operation of Cu_2O photoelectrodes to take place.[5] In order for a good contact to be established between TiO_2 and Cu_2O, an intermediate layer of aluminum doped zinc oxide (Al:ZnO) was

introduced, which also forms a p-n junction with Cu_2O, thereby improving charge extraction from the light absorber. With Pt deposited on the surface as catalyst, this multilayer architecture achieved a maximum photocurrent of 7.6 mA cm^{-2} at 0 V vs. RHE under 1 sun AM 1.5G illumination in a pH 5 phosphate buffer.[5]

Taking advantage of the excellent performance of protected Cu_2O photoelectrodes and with the goal of extending their spectrum of photoelectrochemical products, it was sought to replace the Pt catalyst with a catalyst capable of reducing CO_2 instead of water. Approaches toward the photoelectrochemical reduction of CO_2, meanwhile, have been mostly limited to expensive III-V semiconductors and crystalline silicon photocathodes, and only a few reports have studied the interaction between photoelectrodes and molecular catalysts.[7–11] In this chapter the photoelectrochemical reduction of CO_2 using TiO_2-protected Cu_2O is investigated, in an effort to demonstrate a low-cost approach to CO_2 reduction while achieving for the first time such a reaction on this type of electrode.

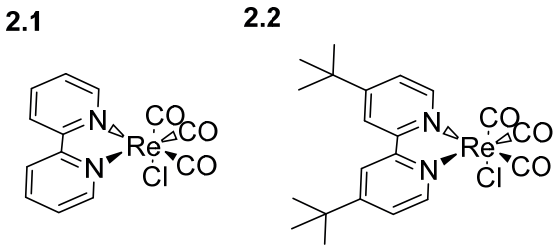

Figure 2-2: **Molecular structures of rhenium catalysts.** Catalyst **2.1** was introduced by Lehn et al. in 1984, whereas Catalyst **2.2** was introduced by Kubiak et al. upon the investigation of different ligand modifications.

Drawing from experience with the preparation of metalorganic complexes to serve as sensitizers in Dye Sensitized Solar Cells, it was decided to use a molecular catalyst, based on a rhenium polypyridyl complex (Molecule **2.1, Figure 2-2**). This type of catalyst was first introduced by Lehn et al. in 1984[12] and shown to selectively reduce CO_2 to CO, even in the presence of large amounts of protons.[8,13] Subsequent research led to insights into the catalytic mechanism and to the investigation of ligand modifications.[8,13–21] As a notable example, Kubiak et al. introduced a tertio-butyl substituent on the bipyridyl ligand of the catalyst and thereby obtained a catalyst which showed a higher activity and decreased

propensity to deactivate through dimer formation, albeit at the expense of a 100 mV delayed onset (Molecule **2.2**, **Figure 2-2).**[17]

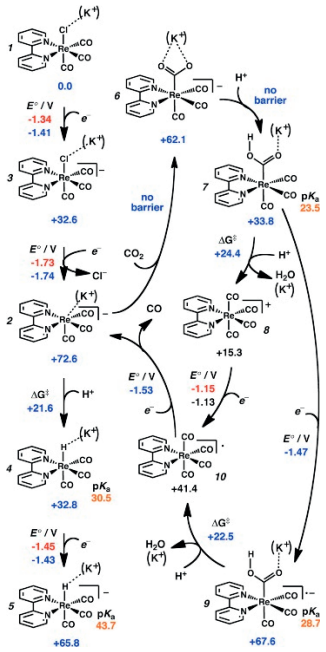

Figure 2-3: **Mechanistic proposal for Re(bpy) based CO_2 reduction catalysts.** This mechaism is based on DFT calculations by Carter and Kubiak. Numbers in red derive from experimental data, numbers in blue have been calculated. It has to be kept in mind that a number of competing mechnistic proposals exist in the literature. Reprinted with permission from Carter et al.[13] Copyright 2013 American Chemical Society.

Mechanistic studies have led to a number of competing mechanistic hypotheses. A notable and complete example for operation in MeCN is the mechanism for Catalyst **2.1** obtained from DFT calculations by Carter and Kubiak shown in

Figure 2-3. The authors propose that the complex enters the catalytic cycle after being reduced once to form a negatively charged anion radical and subsequently a second time during which the catalyst loses Cl^- to form a negatively charged undercoordinated intermediate. This intermediate readily binds CO_2, which immediately gets protonated by a proton source. The catalyst is subsequently reduced again, followed by protonation, in the rate-determining step, and elimination of water to form a metastable radical containing 4 carbonyl radicals. After reduction, this complex readily releases CO to return to the beginning of the catalytic cycle. As can be seen, a proton donor is involved in the rate determining step. It could indeed be observed by experiments that the presence of proton donors

in the electrolyte has a substantial impact on the turnover cycle of the catalyst.[8,13,18] Interestingly, however, the impact of proton donors on the catalyst activation step, which is the potential determining step here, has not received much attention from the community, as will be discussed later in this chapter.

In this chapter, the pairing of Re(tBu-bipy)(CO)$_3$Cl (Catalyst **2.2**, **Figure 2-2**), introduced by Kubiak *et al.*,[17] with a TiO_2-protected Cu_2O photocathode is investigated in CO_2-saturated acetonitrile electrolyte as illustrated schematically in **Figure 2-4**. At the time these experiments were carried out, this was the first study on the combination of a molecular CO_2 reduction catalyst with an oxide photocathode and led to interesting observations pertaining to charge transfer dynamics in such systems.

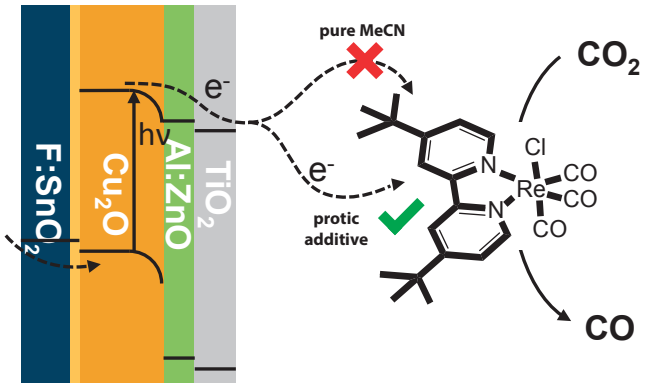

Figure 2-4: **Schematic of the investigated device.** Photo-electrochemical CO_2 reduction process involving protected Cu_2O photocathodes and a Re-based molecular catalyst. Source: Schreier et al.[22]

Results and Discussion

Charge transfer measurements

Photocathodes used in this study were prepared as previously reported, wherein a crystalline cuprous oxide film (500 nm), grown by electrodeposition onto a fluorine-doped tin oxide (F:SnO_2, FTO) substrate, is covered by sequential atomic layer deposited (ALD) films of aluminium-doped zinc oxide (Al:ZnO; 20 nm) and titanium oxide (TiO_2; 100 nm), resulting in the conformal heterojunction device depicted by the cross-section micrograph in **Figure 2-5**.

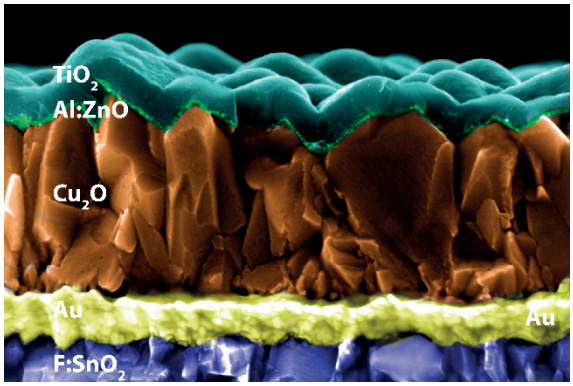

Figure 2-5: **SEM cross section of protected Cu_2O photocathode.** The TiO_2 protection layer on top of Cu_2O can clearly be distinguished. Source: Schreier et al.[22]

Fabrication of the device is carried out by electrodeposition and at temperatures below 150 °C, while ALD uses only moderate vacuum. This leads to a low cost and easy to produce photoelectrode which is readily scalable, representing the main advantages of this material.

To examine the CO_2 reduction activity of this device, photoelectrochemical experiments were carried out using simulated solar light (AM 1.5G at 1 sun) in anhydrous acetonitrile solution containing 0.1 M of Bu_4NPF_6 as supporting electrolyte. The solutions contained 2 mM of Re(tBu-bipy)$(CO)_3Cl$ as catalyst and were saturated with either argon or carbon dioxide to distinguish between electrochemical catalyst reduction under argon and the resulting catalytic current under CO_2.

In cyclic voltammetry experiments on glassy carbon electrodes (**Figure 2-6**), the catalyst showed a typical behavior, characterized by a quasi-reversible wave,

followed by an irreversible catalytic wave, which is only observed under CO_2 but not under Ar.[17]

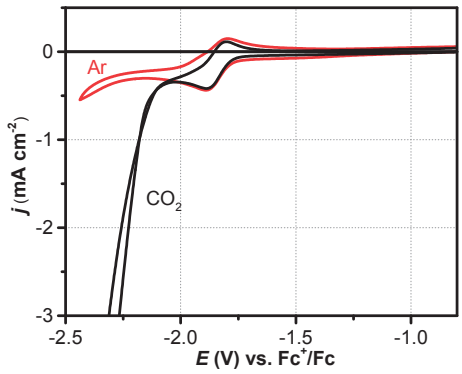

Figure 2-6: **Cyclic voltammograms of catalyst 2.2 at glassy carbon.** Scans under argon and CO_2 are markedly different, with a catalytic current only observed under CO_2.

When exchanging the glassy carbon electrode with a protected Cu_2O photocathode under illumination, the same cyclic voltammetry scans lead the first reductive wave to appear at 500 mV decreased overpotential, which demonstrates the voltage-generating nature of the Cu_2O photocathode. Remarkably, however, in contrast to CV scans on glassy carbon, no subsequent onset of catalytic current could be observed in this configuration (**Figure 2-7a**). To investigate whether this problem is caused by light absorption by the yellow colored catalyst solution, which could lead to insufficient light intensity at the cathode to sustain enough current, voltammetry experiments with varying incident light intensities were carried out (**Figure 2-7b**).

Surprisingly, a proportionality between the photocurrent and incident light intensity was not observed. The observed photocurrent saturated for light intensities beyond 0.14 sun, whereas the quasi Fermi level of the electrons continued to rise with increasing light intensity, as indicated by a progressively more positive reduction onset. Although the first catalyst reduction takes place similarly as on glassy carbon, further reductions seem to be severely hindered. This points to a critical interfacial charge transfer limitation which is not related to the photovoltaic efficiency of the photoelectrode.

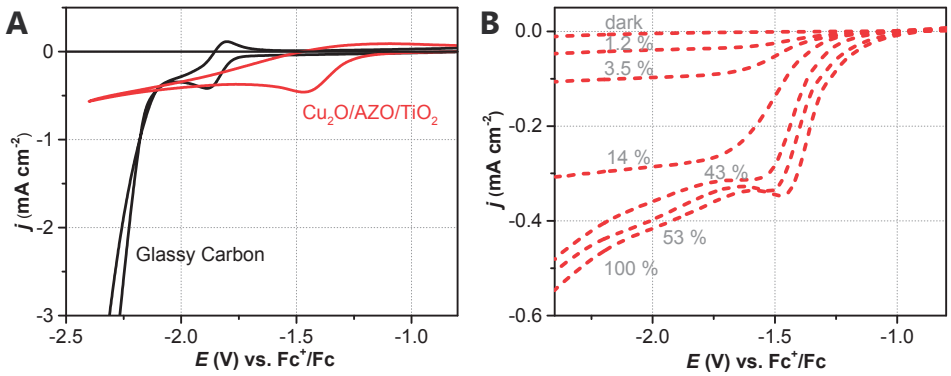

Figure 2-7: **Voltammograms of catalyst 2.2 at protected Cu_2O photocathodes.** (A) CV Scans of the Re catalyst at glassy carbon and on a protected Cu_2O photoelectrode under light. (B) Linear sweep measurements at varying light intensity.

The observation of these charge transfer limitations was unexpected and severe since it essentially precludes the use of Re(bpy) catalysts with protected Cu_2O photocathodes. What is more, the effect is highly intriguing since the first reduction wave of the catalyst could be readily observed. Initial hypotheses were directed toward a mismatch of the TiO_2 conduction band and the catalyst redox potentials. This, however, is unlikely to be the case since the effectiveness of the first reduction should allow for the 2nd one to be able to take place by TiO_2 simply going further into accumulation.[23]

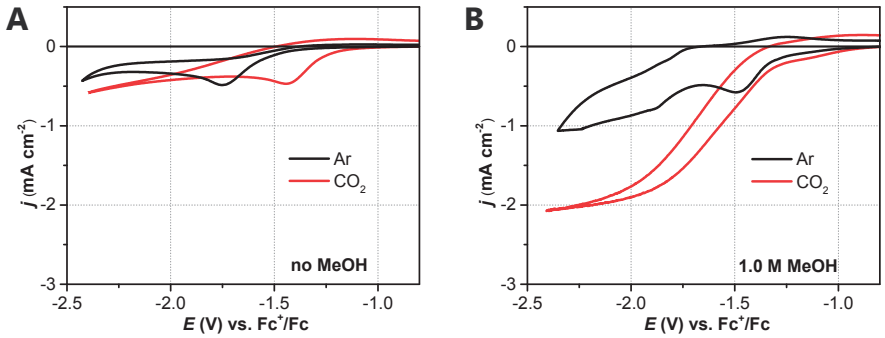

Figure 2-8: **Impact of protic additives on performance.** CV scans under illumination in the absence (A) and in the presence of 1.0 M MeOH (B).

An extensive search for methods to overcome these limitations was therefore carried out. Drawing inspiration from research on the role of proton donors on the catalytic mechanism, as cited above,[8,13] protic additives were added to the electrolytes at large concentrations. Employing an electrolyte containing 1.0 M

methanol (MeOH) as a protic additive, potentiodynamic experiments revealed a strong cathodic photocurrent under CO_2 saturation, as compared to a weaker and unsustained photocurrent response under argon saturation, clearly demonstrating the current flow toward reducing carbon dioxide (**Figure 2-8**).

As seen in **Figure 2-9**, and in its inset showing the plateau photocurrent as a function of light intensity, in the presence of 1.0 M MeOH as additive, it was indeed found that the measured photocurrent varied linearly with the incident light intensity, thus supporting that the photocurrent is solely limited by the photon flux arriving at the photoelectrode under these conditions and that charges are efficiently extracted.

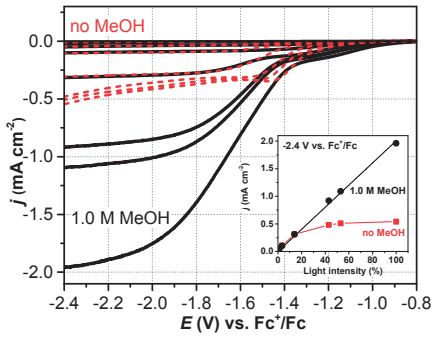

Figure 2-9: **Impact of MeOH at different light intensities.** Linear sweep scans of the Cu_2O photoelectrode with 2 mM of catalyst **2.2** under CO_2 in the absence (red) and presence (black) of 1.0 M MeOH, under 0, 1.2, 3.5, 14, 43, 53 and 100% simulated AM 1.5G illumination at 1 sun. The inset shows the photocurrent at -2.4 V vs. Fc^+/Fc as a function of light intensity. Source: Schreier et al.[22]

The role of protic additives

It is striking that in the absence of MeOH, charge transfer from the photocathode to the molecular catalyst is severely limited and no catalytic onset was observed. This is in contrast to a glassy carbon electrode where, in agreement with the literature, the second reduction of the catalyst happens concomitantly with the onset of catalytic current (**Figure 2-7a**, **Figure 2-10a**).[17] Adding protic solvents allowed for overcoming the observed limitations on the photocathode, which constitutes a new and intriguing finding and warrants further discussion.

The above tests at different light intensities (**Figure 2-9**) suggest that the limitations in current density on Cu_2O photocathodes are due to an interfacial charge transfer

effect, rather than due to the internal photovoltaic activity of the photocathode. Since the interface of the photocathode is defined by the TiO_2 protection layer, the interaction between TiO_2 and the molecular catalyst was suspected to be the culprit in hindering charge transfer.

This hypothesis was confirmed by carrying out cyclic voltammetry experiments on ALD TiO_2 deposited on bare FTO substrates, thereby acting as dark electrodes with surfaces similar to the photocathodes. In CO_2-saturated catalyst solutions (**Figure 2-10b**), these electrodes showed similar charge transfer limitations as the photocathode (**Figure 2-10c**), confirming that its TiO_2 surface is the element hindering charge transfer in the absence of a protic additive. In addition, just as observed on the photocathode, protic additives such as MeOH and n-propanol (**Figure 2-11a**) led to a significant enhancement of electron transfer from the TiO_2 surface, and, most notably, to greater similarity between CVs on TiO_2 and on glassy carbon (**Figure 2-10a** and **b**, red). This effect could be generalized as a comparable behavior was also observed on crystalline anatase TiO_2 electrodes (**Figure 2-11b**).

As a basis for gaining understanding of the process, it is hypothesized that the cause of this effect is found in a changed catalytic pathway at the molecular level. This can be observed on glassy carbon, where the presence of a protic additive led to a significantly changed mechanism as evidenced by the CV plots of **Figure 2-10a**, with the complete loss of reversibility of the first reduction wave pointing to a rapid turnover of the catalyst once it has been reduced. This was accompanied by an earlier onset of catalytic current and a different turnover mechanism when compared to the CV in the absence of a protic additive.

To interpret these observations, one has to take a look at the mechanistic hypotheses of catalyst function. As described above, it is believed that the catalytically active form of the Re(bipy) class of molecules is the doubly-reduced and chloride free $Re(bipy)(CO)_3^-$ intermediate.[24] Nevertheless there remains some uncertainty in the literature regarding the chloride ligand loss, whether it occurs before or after the second reduction.[13,17,25,26] Several reports have suggested that the catalyst activation happens upon loss of Cl^- following the second reduction of the molecule.[13,25] However, the fact that the addition of MeOH led to a pronounced change in the CV on glassy carbon, namely the loss of reversibility of the first reduction and the

absence of a CV crossover indicating that the catalyst turnover potential is higher than the catalyst activation potential (**Figure 2-10a**), suggests a significant mechanistic change. It is therefore proposed that in the presence of a protic species the catalytic pathway is modified to one in which the chloride abstraction precedes the second catalyst reduction.

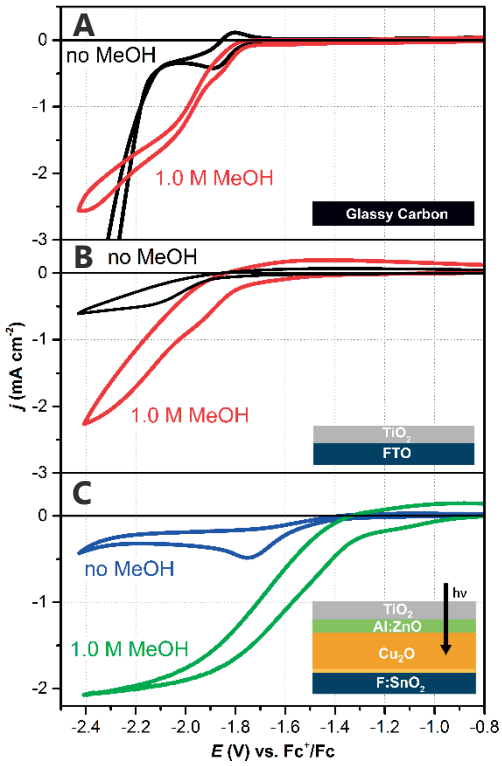

Figure 2-10: **CV scans of catalyst 2.2 under CO_2, in absence and presence of MeOH at different surfaces.** Tested surfaces: (A) glassy carbon in dark, (B) ALD TiO_2 on FTO in dark, and (C) protected photocathode under simulated AM 1.5 illumination. The absence of a catalytic current on the TiO_2 surface in the dark as well as on the TiO_2-terminated photocathode is striking. The limitations can be overcome by adding a protic solvent such as MeOH to the electrolyte. Source: Schreier et al.[22]

The single electron reduction of the catalyst to $Re(tBu\text{-}bipy)(CO)_3Cl^-$ (without loss of the chloride ligand) will produce a charged (anionic) catalyst intermediate as described above.[13,25] It can be proposed that in the presence of protic additives like methanol, abstraction of the chloride ligand from the catalyst (shown to be a crucial step in catalyst activation, as described above) is significantly enhanced, likely through hydrogen bonding of the protic species to chloride,[27] leading to an enhancement of chloride dissociation. This is in agreement with what has recently

been proposed for a similar catalyst in an ionic liquid solvent.[25] If chloride abstraction is enhanced and able to occur after the first electron transfer, a neutral intermediate Re(tBu-bipy)$(CO)_3^{\cdot}$ would form upon first reduction. This would lead to the irreversibility of the first catalyst reduction, as is observed in the CV trace in **Figure 2-10a.**

These observations are very relevant with regards to the reduction behavior observed on TiO_2 surfaces. On an n-type TiO_2 electrode, cathodic current flow requires the semiconductor to go into accumulation, resulting in a buildup of localized electrons through the filling of trap and conduction band states close to the electrode surface.[23,28] This will produce a significant surface charging effect, in contrast to metal-like electrodes which generally exhibit shorter Debye lengths due to more effective charge screening.[29]

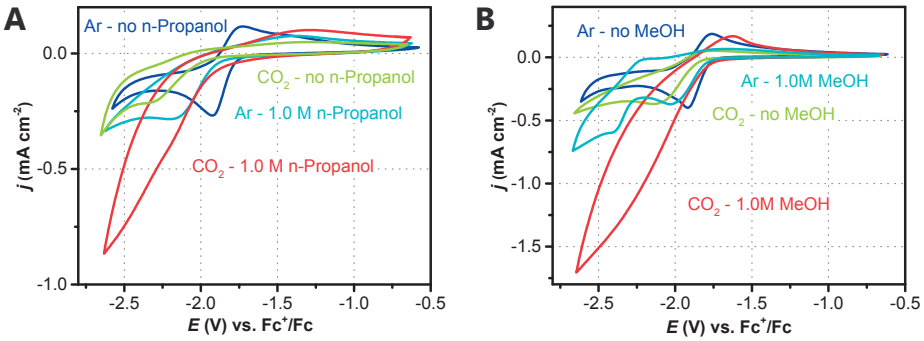

Figure 2-11: **Generalization of the observed effects.** Adding n-Propanol in the case of ALD TiO_2 films led to the same effects as observed with MeOH (A). On crystalline anatase TiO_2 surfaces, the same effect as on ALD TiO_2 films is ovserved (B).

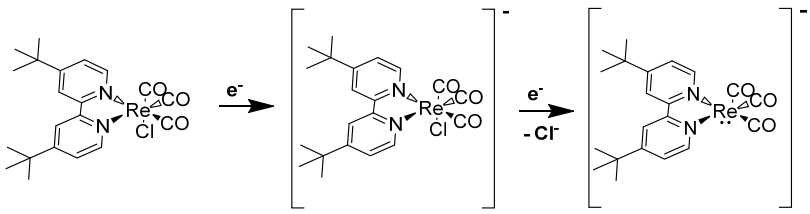

Figure 2-12: **Catalyst activation.** Illustration of the activation process of Re-based bipyridine carbonyl catalysts in the absence of protic additives.

The difference in charging between electrode types is the proposed cause of the disparities observed in the methanol-free CVs of **Figure 2-10**. Formation of the anionic intermediate Re(tBu-bipy)$(CO)_3Cl^-$ in the first reduction (**Figure 2-12**)

leads to coulombic repulsion of this species from the negatively charged semiconductor surface, thereby inhibiting a second reduction from taking place. Meanwhile, the absence of coulombic repulsion on the metal-like glassy carbon surface allows the second reduction and catalyst turnover to occur readily, albeit at a more negative potential.

In contrast, a catalyst pathway avoiding a charged intermediate, like it would result in the case of Cl^- abstraction upon the first reduction, will not experience coulombic repulsion limitations to charge transfer. It therefore should allow the second reduction to occur even on a charged semiconductor surface, thereby enabling the turnover of the catalyst to take place on TiO_2 as was observed in **Figure 2-10**. Improved abstraction of Cl^- thus has significant implications on the catalytic activity of this class of CO_2 reduction catalysts on semiconductor surfaces.

While a number of questions are still to be addressed, the electrochemical data points toward a change in Cl^- abstraction being in play. Further evidence comes from more recent investigations for example by Voyame, who found that when increasing the concentration of a trifluoroethanol (TFE) protic additive, the rate of the 2-electron reduction process got enhanced at low TFE concentrations, whereas a one electron catalytic process became possible at high TFE concentrations, which was suggested to be due to early Cl^- dissociation, followed by stabilization of the formed complex by TFE coordination.[30] This raises an interesting question, on whether after an early Cl^- dissociation in the present system, still a 2-electron mechanism is in play. One electron mechanisms, involving binuclear intermediates, have been reported for Re-based catalysts.[19] In the present study, careful inspection of the catalyst CV at glassy carbon under argon and in presence of MeOH shows the appearance of a second reduction peak at a slightly more negative potential than the first reduction (**Figure 2-13**). Under CO_2, a change in slope can be observed at the same potential, hinting toward a 2^{nd} reduction taking place, albeit at a lower potential than is required in the absence of MeOH.

The mechanistic details observed here shed new light on the complex processes involved in the operation of a seemingly "simple" Re-based CO_2 reduction electrocatalysts. Further investigation is needed and will lead to more insight into their numerous possible pathways. Particular emphasis should be directed to the use

of spectroelectrochemical techniques, which allow for the analysis of the catalyst structure under electrochemical bias.

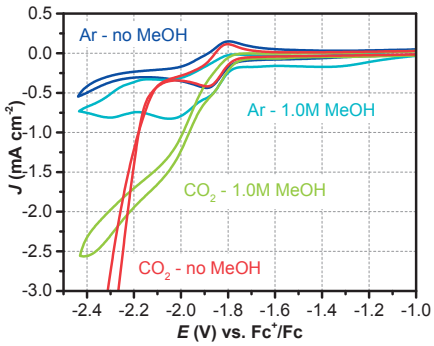

Figure 2-13: **Cyclic voltammetry at glassy carbon.** CV scans are compared in presence and absence of MeOH under CO_2 and Ar.

Photoelectrochemical performance

The prohibitive charge transfer limitations introduced at the onset of the present chapter could be overcome by changing the electrolyte composition, thereby opening a new catalytic pathway and enabling the efficient reduction of the rhenium catalyst on the surface of TiO_2. This was a key requirement for operating the catalyst on protected Cu_2O photoelectrodes. The performance of this system will be investigated next.

Photoelectrochemical measurements under chopped AM 1.5G illumination at 1 sun intensity of the protected Cu_2O photocathode with 2 mM of $Re(tBu\text{-}bipy)(CO)_3Cl$ are shown in **Figure 2-14**. Compared to an amorphous TiO_2 surface in the dark, which is analogous to the surface of the photocathode as described before, a photovoltage shift of 560 mV combined with a good fill factor was observed when operating at the surface of a protected Cu_2O photocathode. A similar photovoltage was found when compared against a glassy carbon electrode, consistent with the photovoltage observed from similar photocathodes in water splitting applications.[31] Additionally, a photocurrent density of 2.1 mA cm^{-2} was observed, which was the largest current density obtained toward CO_2 reduction on an oxide material at the time of publication. In this system, through the photovoltaic activity of the photocathode, an onset of reductive photocurrent was observed positive of the -1.28 V vs. Fc^+/Fc reversible potential of carbon dioxide reduction in acetonitrile.[32]

Additionally, through the use of MeOH as an electrolyte additive, a significantly earlier onset is achieved than shown in previous studies using silicon as photocathodes,[8,9] leading to sustained CO_2 reduction at potentials where those devices do not even reach a catalytic onset.

Over the entire potential range tested, only negligible dark currents were observed, thereby pointing toward excellent performance and stability of the photocathode device, even at potentials significantly more negative than those used in water reduction demonstrations. This is notable since unprotected cuprous oxide devices degrade severely under these conditions, as will be described below.

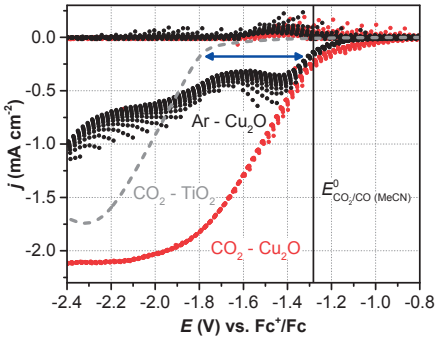

Figure 2-14: **Copped light linear sweep measurements.** Chopped light voltammetry of the Cu_2O photoelectrode with 2 mM of catalyst **2.2** in the presence of 1.0 M MeOH under argon (black curve) or under CO_2 (red curve), compared to the same linear sweep at an FTO-TiO_2 electrode under CO_2 in the dark (grey curve). Adapted from: Schreier et al.[22]

The currents observed in the absence of CO_2 (under argon saturation) correspond to reduction of the catalyst itself but without leading to a catalytic turnover. A number of transient effects are observed which shed light on the dynamics in play in this system. Upon light chopping under argon, transients are observed which originate from the transport-limited diffusion of catalyst molecules toward the electrode surface. Current transients are no longer observed in the presence of CO_2 since as soon as a catalyst molecule has been reduced, it catalyzes the reduction of CO_2 and returns to its oxidized state, allowing its rapid re-reduction by the photocathode and thereby supporting sustained currents. The absence of transients in the presence of carbon dioxide (**Figure 2-14**) suggests that diffusive transport no longer limits the photocurrent, but rather that the incident light intensity becomes the limiting factor, as has indeed been observed above.

Reaching an optimum performance of the photoelectrochemical setup requires optimization of the amount of catalyst used in the test cell. Due to the design of the cell, light must travel through 1 cm of strongly yellow colored catalyst solution which absorbs a non-negligible part of the radiation. A complex relationship exists between catalyst concentration and observed photocurrent since higher catalyst concentrations lead to larger currents but also to increased light absorption. The maximum photocurrent increases with increasing catalyst concentration, plateaus between 2 and 4 mM and subsequently decreases again as the concentration is increased (**Figure 2-15**). To further enhance the photocurrents obtained from this system, the cell design would have to be optimized.

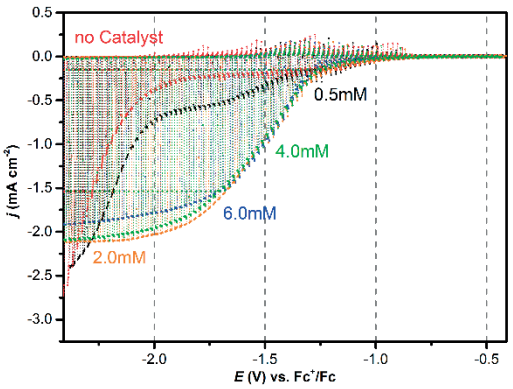

Figure 2-15: **Impact of catalyst concentration on protected Cu_2O photocathode performance.** The concentrationof catalyst **2.2** is varied and chopped light linear sweeps are performed. Source: Schreier et al.[22]

Sustained current stability test

From the above measurements, it can be seen that the energy input from the photocathode, as compared to a bare TiO_2 electrode is maximum just at the onset of the catalytic wave on TiO_2. At lower bias, the current of the photoelectrode is just setting in, whereas at higher bias, the current observed from dark electrodes quickly catches up with the plateau current of the photoelectrode. For this reason, the extended operation and quantitative production of carbon monoxide was investigated at -1.73 V vs. Fc^+/Fc, a potential which is near the onset of the first catalyst reduction on dark electrodes. The current density and faradaic efficiency obtained from these measurements over several hours under CO_2 saturation and periodically chopped illumination are shown in **Figure 2-16a**. The inset details the

absence of dark current, and the small perturbations of the photocurrent can be attributed to accumulated carbon monoxide bubbles releasing from the electrode surface. The generation of CO bubbles could be observed by bare eye, as details the photograph shown in **Figure 2-16b**. During stability tests, interrupting the light source for 2 seconds following each 2 minute period allowed for verification of the continued photoactivity of the device. This is important since it confirms the generation of true photocurrent, rather than corrosion processes which would manifest as an increase in the dark current. The negligible dark current even after 5 hours of testing shows the effectiveness of the protective TiO_2 overlayer and overall stability of the device.

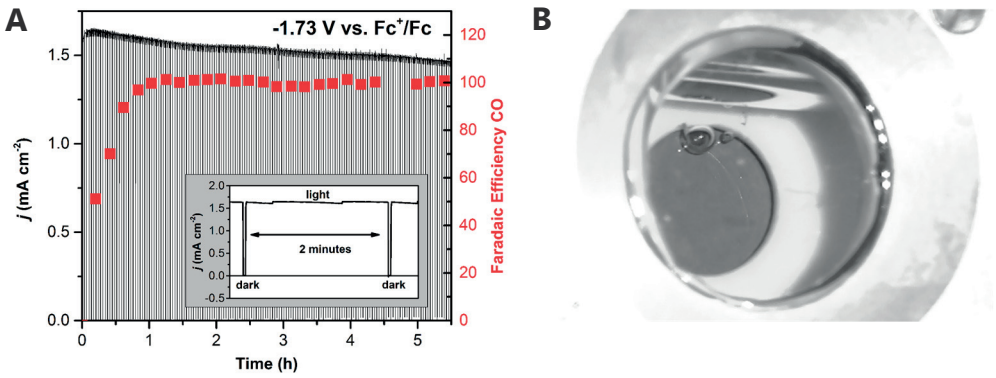

Figure 2-16: **Long term testing of protected Cu_2O photocathode.** (A) Cathodic current density and CO evolution efficiency of the Cu_2O photocathode under chopped light at a constant potential of −1.73 V vs. Fc^+/Fc with 2 mM Re(tBu-bipy)$(CO)_3Cl$ and 7.5 M MeOH under CO_2. Both current density (black line) and Faradaic efficiency toward carbon monoxide (red dots) are reported. The initial increase in CO efficiency is attributed to the gradual saturation of the electrolyte. The inset shows a zoomed view of the recorded current, showing the absence of dark current and the occasional changes in current density due to CO gas bubbles detaching from the electrode surface. Only little performance loss is observed over 5.5 h and can be mainly attributed to increased light absorption by the catalyst due to evaporation of the solvent. (B) Observation of CO bubbles in the test cell. Source: Schreier et al.[22]

For the duration of the test, CO_2 flowed through the headspace of the photoelectrochemical cell and the product gas was analyzed on-line by gas chromatography. From the gas measurements, a strong CO signal developed whereas only trace amounts of hydrogen were observed, confirming that the observed bubbles corresponded to carbon monoxide generation. When related to calibration with a CO standard, a quantitative current yield toward the production

of carbon monoxide was confirmed within experimental error. Over 5.5 hours, only a small decrease of photocurrent was observed. To the best of my knowledge, this represents the longest stability shown for an oxide-based system toward CO_2 reduction. The good performance and quantitative CO yield of this system is notable since it is operating at a potential where previous reports using silicon as photocathodes did not even observe the onset of catalytic currents. The earlier onset results from the combination of the device photovoltage as well as from the earlier onset imparted by the changed catalyst mechanism in the presence of MeOH, as discussed above.

The importance of protective layers

The presence of a TiO_2 surface renders the operation of the molecular rhenium catalyst difficult to achieve, as described before. An interesting simplification of the device would therefore be the use of unprotected Cu_2O as a p-type semiconductor in direct contact with the electrolyte, a configuration which should theoretically be capable of producing cathodic photocurrents in this system.

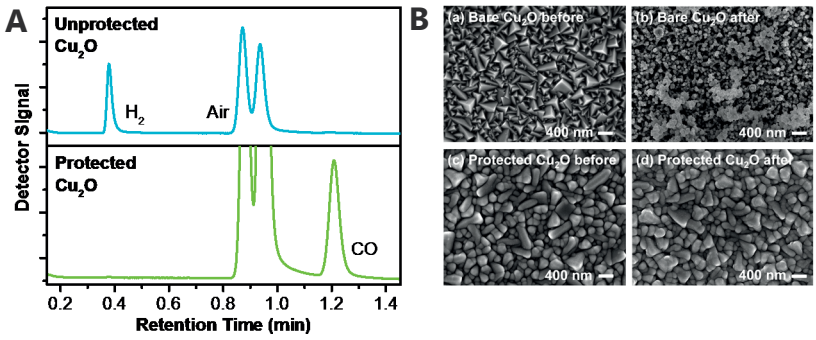

Figure 2-17: **Importance of protective overlayers.** Polarization of unprotected and protected Cu_2O at -1.73 V under AM 1.5G illumination in presence of 2 mM of catalyst **2.2** and 7.5 M MeOH. (A) GC traces of observed gases, (B) SEM micrographs of the electrodes before and after testing. Adapted from: Schreier et al.[22]

To investigate the feasibility of this approach, long-term polarization tests were carried out using unprotected Cu_2O under conditions identical to the stability test described previously. As a result of these tests, it was found that within a few minutes, the photoactivity was lost whereas significant dark currents remained, and the gas analysis showed the production of large amounts of hydrogen but only trace

CO (**Figure 2-17a**), thereby indicating the degraded Cu_2O photocathode acts as a catalyst for hydrogen evolution from non-aqueous acids. Scanning electron microscopy analysis of the bare and protected Cu_2O electrodes before and after the polarization tests showed the emergence of a particulate morphology on the unprotected surface while the morphology of protected Cu_2O photocathodes remained unchanged after several hours of polarization (**Figure 2-17b**). To examine compositional changes in these devices, X-Ray diffraction analysis was performed, revealing that while the protected electrodes experienced no observable changes in diffraction pattern, the unprotected Cu_2O clearly showed the emergence of metallic copper due to corrosion under reaction conditions. It is therefore apparent that TiO_2 protection layers are important for sustained CO_2 reduction to be possible on a Cu_2O photocathode, even in the absence of water.

Conclusion and outlook

By studying the operation of a molecular rhenium catalyst using TiO_2 protected Cu_2O photoelectrodes, the efficient reduction of carbon dioxide to carbon monoxide on an oxide photocathode using a molecular catalyst was demonstrated for the first time. The device produced high photovoltages of 560 mV and a photocurrent density of 2.1 mA cm^{-2}, corresponding to the highest photocurrent observed toward CO_2 reduction on an oxide material. Protection of the Cu_2O photocathode by TiO_2 enabled stable and selective reduction of CO_2 over several hours, and it was found that protic electrolyte additives were needed to overcome the unexpected charge transfer limitations on the protected photocathode surface. From these observations, insight was gained into potential modifications of the catalytic pathway to avoid charged catalyst intermediates. It has to be mentioned that the presence of protic additives also changes the properties of TiO_2 by improved shielding of charges as well as by changing the flatband potential due to the generation of a dipole on the surface.[33] It is likely that several processes are in play, requiring further research to understand the importance of their respective contribution.

The discovery of charge transfer limitations from the surface of TiO_2 to the rhenium-based molecular catalyst and its elimination by the use of protic additives is highly relevant to the field of electrochemistry and photoelectrochemistry, where there is a general trend toward the use of protective overlayers. Furthermore, the types of observations made in this study allow for gaining an understanding of the processes happening upon transferring charges from semiconductors to molecules in solution and further research along this direction is likely to lead to highly relevant insights. Further investigations may also enable a better understanding of the processes taking place in the electrochemical double layer and may potentially represent a new tool for mechanistic study. The findings from this chapter are therefore believed to be broadly applicable and point the way toward a more fundamental understanding of charge transfer in semiconductor – molecular catalyst systems.

Methods

Protected Cu_2O photocathodes were prepared as previously described[31] with the exception that the ALD deposition of aluminum-doped zinc oxide (AZO) was modified. The deposition of AZO was carried out in pulse mode instead of exposure mode. While constantly under vacuum, diethylzinc was pulsed for 15 ms, followed by a 10 second wait time. Subsequently, H_2O was pulsed for 15 ms, also followed by a 10 second wait time. After every 20^{th} cycle, trimethylaluminum was pulsed for 15 ms, followed by 10 seconds wait time, and subsequently H_2O was pulsed for 15 ms, followed by 10 seconds wait time as well. 5 x (20 + 1) cycles were carried out in this manner, leading to 20 nm of aluminium-doped zinc oxide.

Re(tBu-bipy)$(CO)_3Cl$ (Molecule **2.2**) was prepared by Dr. Peng Gao as follows: $Re(CO)_5Cl$ (0.8 g, 2.21 mmol) was dissolved in 150 mL of toluene which was heated to 60°C until the suspension fully dissolved. An equimolar amount of 4,4'-di-tert-butyl-2,2'-bipyridine (0.594 g, 2.21 mmol) was added to the hot solution, and the reaction mixture was stirred under reflux for 2 h. The reaction mixture changed color from colorless, to yellow, and finally to orange. After 2 h of reflux the reaction mixture was removed from heat and cooled in a freezer. A shiny needle-shaped yellow solid precipitated from cold toluene over 24 h. The solid product was isolated by filtration and dried overnight under high vacuum at room temperature. Spectroscopically pure product was obtained from the reaction with an overall yield of 95%. ^1H NMR (acetonitrile-d^3): δ 1.46 (s, 18H, tBu), 7.65 (dd, 2H, 5 and 5' H's), 8.42 (d, 2H, 6 and 6' H's), 8.89 (d, 2H, 3 and 3' H's).

Photoelectrochemical experiments were carried out in a custom gastight photoelectrochemical cell as described in **Chapter 1**. A Gamry Interface 1000 was used as potentiostat. The counter electrode was a Pt wire, separated by a gastight diaphragm (Metrohm, Switzerland). An Ag/AgCl wire, separated by a similar diaphragm, was used as reference electrode, and ferrocene, measured at a secondary Pt working electrode, was used as an internal standard. All compartments were filled with the same electrolyte. For tests with 1.0 M MeOH, 630 µL of MeOH (Sigma Aldrich, >99.8%) were added to 15 mL of cell content. A 450 W Xe arc lamp (Lot Oriel) with a KG3 filter was used to simulate the AM 1.5 G solar

spectrum in the absorption range of Cu_2O, and the intensity was calibrated with a silicon photodiode. For long term stability tests, a collimated LED light source (MCWHL5, Thorlabs, USA) was used, which had previously been calibrated to match the photocurrents that were obtained on Cu_2O photocathodes measured using the simulated AM 1.5 G illumination. This LED light source was interrupted for 2 seconds every 2 minutes in order to verify the absence of dark current. CV experiments were carried out at 100 mV sec^{-1} between 0 and -2.0 V vs. the Ag/AgCl wire, which translates to -0.4 and -2.4 V vs. Fc/Fc^+, whereas linear sweeps were carried out in the same potential range at 50 mV/sec. Chopped light experiments were performed at 10 mV/sec with a chopping frequency of 1 Hz. Experiments at glassy carbon electrodes were performed in an electrochemical cell (Metrohm, Switzerland) using a commercial 3 mm dia. glassy carbon electrode (Metrohm, Switzerland), which had been polished with a slurry of Al_2O_3 powder (Buehler, USA) of subsequently finer particle size down to 0.05 µm. The electrolyte was 0.1 M tetrabutylammonium hexafluorophosphate ($TBAPF_6$, Sigma Aldrich) in anhydrous MeCN (Sigma Aldrich, < 0.001% H_2O). CO_2 (99.998 %) and Ar (99.998 %) were obtained from Carbagas, Switzerland. Before each experiment, the cell was sparged for at least 30 min in order to saturate the liquid with CO_2. For measurements with Ar, the cell was purged for at least 45 min. Gas analysis was carried out using a Thermo Trace Ultra gas chromatograph, equipped with a Pulse Discharge Detector (Vici) and a Shincarbon column (Restek) using He (Carbagas, 99.99990 %) as carrier gas. CO_2 was passed through the headspace of the cell at 7.5 mL/min using a mass flow controller (Bronkhorst, Netherlands), directly transported into the sample loop of the gas chromatograph, and periodically injected onto the column. The resulting data were smoothed using adjacent averaging over 5 points. The gas measurements were corrected for the volume that is added to the effluent stream by the evaporation of the solvent. This error was determined by measuring the drop of concentration in CO when flowing a 500 ppm CO standard through the cell at 7.5 mL/min using a 100 mL/min CH_4 mass flow controller, which was scaled to the standard in He using the gas conversion factors supplied by Bronkhorst. An error of 10% is estimated on the measurement of the faradaic efficiency. XRD Data was recorded using an X'Pert MPD PRO (Panalytical)

equipped with a ceramic tube (Cu anode, λ=1.54060 Å), a secondary graphite (002) monochromator and a RTMS X'Celerator (Panalytical). The measurements were done in the Bragg-Brentano geometry. The samples were mounted without further modification and the automatic divergence slit and beam mask were adjusted to the dimension of the films. A step size of 0.008° was chosen for an acquisition time of 7.5 min deg^{-1}. The data were adjusted for a small angular shift (~0.6°) by aligning the most prominent Cu_2O peak (36.42°) to the standard JCPDS card No. 05-0667. SEM micrographs were taken using a Zeiss Merlin high resolution microscope. Crystalline anatase TiO_2 layers were deposited by Dr. Fabrizio Giordano from a solution of 0.4 mL acetylacetone, 0.6 mL titanium diisopropoxide bis(acetylacetonate) and 9 mL of ethanol which was sprayed onto FTO substrates at 450°C using oxygen as carrier gas. UV-Vis spectra were acquired using a Shimadzu UV-3600 UV-Vis-NIR spectrophotometer (Shimadzu, Japan). XPS measurements were carried out on a ESCA KRATOS AXIS ULTRA system (Kratos, UK).

References

1. O'Regan, B. & Grätzel, M. A low-cost, high-efficiency solar cell based on dye-sensitized colloidal TiO_2 films. *Nature* **353,** 737–740 (1991).
2. Grätzel, M. Photoelectrochemical cells. *Nature* **414,** 338–344 (2001).
3. Wick, R. & Tilley, S. D. Photovoltaic and Photoelectrochemical Solar Energy Conversion with Cu_2O. *J. Phys. Chem. C* **119,** 26243–26257 (2015).
4. Grondahl, L. O. The copper-cuprous-oxide rectifier and photoelectric cell. *Rev. Mod. Phys.* **5,** 141 (1933).
5. Paracchino, A., Laporte, V., Sivula, K., Grätzel, M. & Thimsen, E. Highly active oxide photocathode for photoelectrochemical water reduction. *Nat. Mater.* **10,** 456–461 (2011).
6. Siripala, W., Ivanovskaya, A., Jaramillo, T. F., Baeck, S.-H. & McFarland, E. W. A Cu_2O/TiO_2 heterojunction thin film cathode for photoelectrocatalysis. *Sol. Energy Mater. Sol. Cells* **77,** 229–237 (2003).
7. Kumar, B. *et al.* Photochemical and Photoelectrochemical Reduction of CO_2. *Annu. Rev. Phys. Chem.* **63,** 541–569 (2012).
8. Smieja, J. M. *et al.* Kinetic and structural studies, origins of selectivity, and interfacial charge transfer in the artificial photosynthesis of CO. *Proc. Natl. Acad. Sci.* **109,** 15646–15650 (2012).
9. Kumar, B., Smieja, J. M. & Kubiak, C. P. Photoreduction of CO_2 on p-type Silicon Using $Re(bipy\text{-}Bu^t)(CO)_3Cl$: Photovoltages Exceeding 600 mV for the Selective Reduction of CO_2 to CO. *J. Phys. Chem. C* **114,** 14220–14223 (2010).
10. Barton, E. E., Rampulla, D. M. & Bocarsly, A. B. Selective Solar-Driven Reduction of CO_2 to Methanol Using a Catalyzed p-GaP Based Photoelectrochemical Cell. *J. Am. Chem. Soc.* **130,** 6342–6344 (2008).
11. Liu, R., Stephani, C., Han, J. J., Tan, K. L. & Wang, D. Silicon Nanowires Show Improved Performance as Photocathode for Catalyzed Carbon Dioxide Photofixation. *Angew. Chem. Int. Ed.* **52,** 4225–4228 (2013).
12. Hawecker, J., Lehn, J.-M. & Ziessel, R. Electrocatalytic reduction of carbon dioxide mediated by $Re(bipy)(CO)_3Cl$ (bipy = 2,2′-bipyridine). *J. Chem. Soc. Chem. Commun.* **6,** 328–330 (1984).
13. Keith, J. A., Grice, K. A., Kubiak, C. P. & Carter, E. A. Elucidation of the Selectivity of Proton-Dependent Electrocatalytic CO_2 Reduction by fac-$Re(bpy)(CO)_3Cl$. *J. Am. Chem. Soc.* **135,** 15823–15829 (2013).
14. Benson, E. E., Grice, K. A., Smieja, J. M. & Kubiak, C. P. Structural and spectroscopic studies of reduced $[Re(bpy\text{-}R)(CO)_3]^{-1}$ species relevant to CO_2 reduction. *Polyhedron* **58,** 229–234 (2013).
15. Benson, E. E. & Kubiak, C. P. Structural investigations into the deactivation pathway of the CO2 reduction electrocatalyst $Re(bpy)(CO)_3Cl$. *Chem. Commun.* **48,** 7374–7376 (2012).
16. Agarwal, J., Fujita, E., Schaefer, H. F. & Muckerman, J. T. Mechanisms for CO Production from CO_2 Using Reduced Rhenium Tricarbonyl Catalysts. *J. Am. Chem. Soc.* **134,** 5180–5186 (2012).
17. Smieja, J. M. & Kubiak, C. P. $Re(bipy\text{-}tBu)(CO)_3Cl^-$ improved Catalytic Activity for Reduction of Carbon Dioxide: IR-Spectroelectrochemical and Mechanistic Studies. *Inorg. Chem.* **49,** 9283–9289 (2010).
18. Wong, K.-Y., Chung, W.-H. & Lau, C.-P. The effect of weak Brönsted acids on the electrocatalytic reduction of carbon dioxide by a rhenium tricarbonyl bipyridyl complex. *J. Electroanal. Chem.* **453,** 161–169 (1998).
19. Johnson, F. P. A., George, M. W., Hartl, F. & Turner, J. J. Electrocatalytic Reduction of CO_2 Using the Complexes $[Re(bpy)(CO)_3L]^n$ (n = +1, L = $P(OEt)_3$, CH_3CN; n = 0, L = Cl^-, Otf^-; bpy = 2,2′-Bipyridine; Otf^- = CF_3SO_3) as Catalyst Precursors: Infrared Spectroelectrochemical Investigation. *Organometallics* **15,** 3374–3387 (1996).
20. Christensen, P., Hamnett, A., Muir, A. V. G. & Timney, J. A. An in situ infrared study of CO_2 reduction catalysed by rhenium tricarbonyl bipyridyl derivatives. *J. Chem. Soc. Dalton Trans.* **9,** 1455–1463 (1992).

21. Cosnier, S., Deronzier, A. & Moutet, J.-C. Electrochemical coating of a platinum electrode by a poly(pyrrole) film containing the fac-Re(2,2′-bipyridine)$(CO)_3Cl$ system application to electrocatalytic reduction of CO_2. *J. Electroanal. Chem. Interfacial Electrochem.* **207,** 315–321 (1986).
22. Schreier, M. *et al.* Efficient and selective carbon dioxide reduction on low cost protected Cu_2O photocathodes using a molecular catalyst. *Energy Env. Sci* **8,** 855–861 (2015).
23. Frank, S. N. & Bard, A. J. Semiconductor electrodes. II. Electrochemistry at n-type titanium dioxide electrodes in acetonitrile solutions. *J. Am. Chem. Soc.* **97,** 7427–7433 (1975).
24. Grice, K. A. & Kubiak, C. P. in *Advances in Inorganic Chemistry* (ed. Michele Aresta and Rudi van Eldik) **Volume 66,** 163–188 (Academic Press, 2014).
25. Grills, D. C. *et al.* Electrocatalytic CO_2 Reduction with a Homogeneous Catalyst in Ionic Liquid: High Catalytic Activity at Low Overpotential. *J. Phys. Chem. Lett.* **5,** 2033–2038 (2014).
26. Sampson, M. D. *et al.* Direct observation of the reduction of carbon dioxide by rhenium bipyridine catalysts. *Energy Environ. Sci.* **6,** 3748–3755 (2013).
27. Lam, S. Y., Louis, C. & Benoit, R. L. Thermodynamic study of hydrogen bonding to chloride ions. *J. Am. Chem. Soc.* **98,** 1156–1160 (1976).
28. Tan, M. X. *et al.* in *Progress in Inorganic Chemistry* (ed. Karlin, K. D.) 21–144 (John Wiley & Sons, Inc., 1994).
29. Nozik, A. J. & Memming, R. Physical Chemistry of Semiconductor−Liquid Interfaces. *J. Phys. Chem.* **100,** 13061–13078 (1996).
30. Voyame, P. Photocatalytic and Electrocatalytic Reduction of Carbon Dioxide in Pressurized Systems. (2016). doi:10.5075/epfl-thesis-6985
31. Tilley, S. D., Schreier, M., Azevedo, J., Stefik, M. & Graetzel, M. Ruthenium Oxide Hydrogen Evolution Catalysis on Composite Cuprous Oxide Water-Splitting Photocathodes. *Adv. Funct. Mater.* **24,** 303–311 (2014).
32. Costentin, C., Drouet, S., Robert, M. & Savéant, J.-M. A Local Proton Source Enhances CO_2 Electroreduction to CO by a Molecular Fe Catalyst. *Science* **338,** 90–94 (2012).
33. Enright, B., Redmond, G. & Fitzmaurice, D. Spectroscopic determination of flatband potentials for polycrystalline TiO_2 electrodes in mixed solvent systems. *J. Phys. Chem.* **98,** 6195–6200 (1994).

3 Covalent Immobilization of a Molecular Catalyst on Cu_2O Photocathodes for CO_2 Reduction

The chapter is adapted with permission from the peer-reviewed publication:
***Marcel Schreier**, Jingshan Luo, Peng Gao, Thomas Moehl, Matthew T. Mayer, Michael Grätzel.*
J. Am. Chem. Soc., 2016, vol. 6, 1938.

In Chapter 2, a molecular rhenium catalyst was dissolved in solution and therefore only randomly interacting with the photoelectrode surface, while most of the catalyst in the system remains inactive. Here, improving on this work, the immobilization of a very similar catalyst directly at the surface of the photoelectrode is investigated. It is found that a nanoscaffold is required for sufficient catalyst to be deposited, the integration of which has to be carried out at low temperature to maintain the activity of the Cu_2O photocathode.

Introduction

An attractive approach to driving molecular catalysts using the power of sunlight is to incorporate them into photoelectrochemical systems. As described in **Chapter 2**, catalysts can be incorporated as a homogeneous solution-phase species.[1–3] This, however, requires large amounts of catalyst, most of which is not actively participating in the reaction, and in addition, causes parasitic light absorption, thereby limiting the photocurrent density observed from these systems.[1,4] Furthermore, many molecular catalysts rely on precious metal centers, thus providing incentive for minimizing the amount of required catalyst as much as possible. Both of these challenges can be addressed by binding the molecular catalyst directly to the surface of a photoelectrode, which comes down to "heterogenizing" a homogeneous catalyst. Thereby, the use of catalyst is reduced to an amount which is actively participating in the reaction, and some recent works have demonstrated the ability of this approach to significantly improve catalytic yield in electrocatalytic and photocatalytic systems.[5–8] The immobilization of a molecular catalyst also allows for a different set of electrochemical studies since the catalyst diffusion component of the cyclic voltammetry signal is removed.

However, despite the attractive prospect of decreasing catalyst loading while retaining efficiency, few examples of molecular catalysts linked to surfaces of photoelectrodes have been shown, whereas the only examples of direct linking involve catalysts for hydrogen evolution.[9–11] Notably, Rose and co-workers covalently attached a nickel-phosphine catalyst for hydrogen evolution by the chemical functionalization of a chlorine-terminated p-type silicon surface (**Figure 3-1a**), achieving reductive currents at close to 20 mA cm^{-2} from trifluoro-acetic acid (TFA) in acetonitrile containing 0.2 M $LiClO_4$.[11] This is the only example of direct molecular attachment of a molecular catalyst to a photocathode surface. Other cases relied on nonspecific interactions between catalyst and scaffold[12] or on the polymerization of species onto the photocathode surface.[9,10] In this context, notably, Moore and co-workers immobilized a cobaloxime catalyst on a p-GaP electrode by the means of polymerizing 4-vinylpyridine on the photocathode surface, followed by the immobilization of a catalyst precursor as shown in **Figure 3-1b**. In aqueous

solutions, this device showed hydrogen evolving currents exceeding 2.5 mA cm^{-2} but was characterized by a relatively low stability.[10]

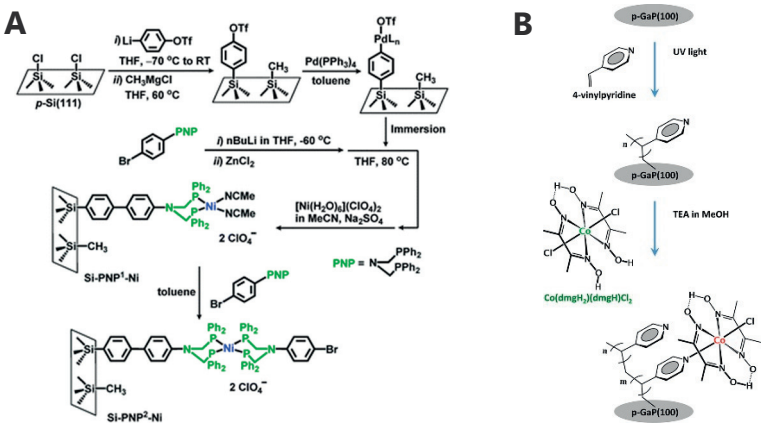

Figure 3-1: **Immobilization strategies.** (A) Nickel phosphine catalyst on p-type silicon electrodes. Adapted from Seo et al.[11] with permission of The Royal Society of Chemistry. (B) Cobaloxime on polyvinylpyridine on p-type GaP electrodes. Adapted with permission from Krawicz et al.[10] Copyright 2013 American Chemical Society.

In the case of CO_2 reduction, all reports on immobilized catalysts have so far focused on immobilized dye-catalyst complexes,[13,14] which are not deposited on light absorbing semiconductors and hence not relevant to this work, and polymer films deposited on substrates.[15–20] The most notable work in this direction was carried out by Arai, Sato and co-workers, whom polymerized a pyrrole-modified ruthenium bipyridyl catalyst on top of a Zn-doped p-InP photoelectrode,[21] achieving photocurrents in the range of 100 µA and a selectivity of 67% for formate (**Figure 3-2**). In several iterations[15,16] of improvements, the same group eventually achieved a device with a silicon-germanium junction as absorber and the same ruthenium bipyridyl polymer catalyst, allowing for reaching a solar-to-fuel efficiency of 4.6%.[17] Furthermore, Fabre, Chardon-Noblat and co-workers have shown the electropolymerization of a manganese bipyridyl catalyst on p-type silicon nanowires.[20] With this setup, the authors reached photocurrents in the range of 1 mA cm^{-2} in the presence of CO_2, however, in the absence of CO_2 the same current density was observed.

Despite these interesting examples, no previous study exists, where a molecular catalyst for CO_2 reduction has been covalently bound directly to the semiconductor

surface of a photocathode. With the aim of achieving this feat and improving on the state of the art in **Chapter 2**, the immobilization of rhenium based catalysts for the solar-driven reduction of CO_2 was investigated here, so as to reach a functional hybrid inorganic photocathode – molecular catalyst design.

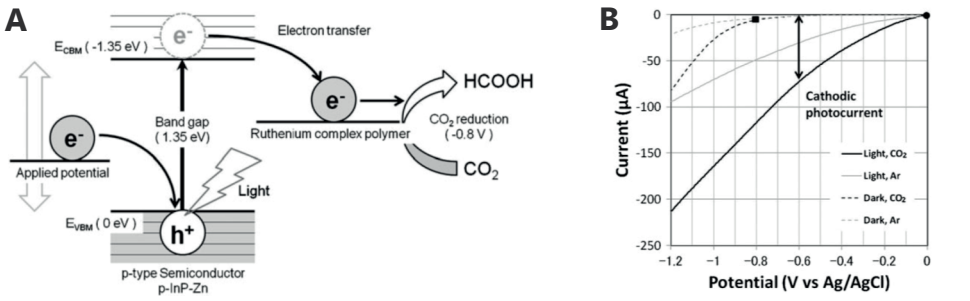

Figure 3-2: **Design by Arai, Sato and co-workers. (A)** Zn-doped p-InP photoelectrode is paired with a polymerized Ru bipyridyl catalyst, leading to the production of formate. **(B)** Observed photocurrents and dark currents in pure water electrolyte. Adapted from: Arai et al.[21] with permission of The Royal Society of Chemistry.

A number of different strategies exist for the immobilization of molecules on inorganic materials. However, the TiO_2 terminated surface of Cu_2O photoelectrodes presents an excellent opportunity to draw inspiration from strategies used in the field of Dye Sensitized Solar Cells (DSSC). As described above, the use of metal oxides, particularly TiO_2, toward the protection of otherwise unstable photoelectrode materials, such as Cu_2O, has drawn much attention in the solar fuels research community.[22–25] TiO_2 is also used as a scaffold for sensitizers in DSSC and represents an ideal substrate for the covalent binding of molecules by the means of molecular linking groups such as carboxylates and phosphonates, the strategy which was thus chosen for this work.[6,26–29]

Results and Discussion

The virtues of a mesoporous scaffold

As could be seen in **Chapter 2**, complexes based on Re, particularly Re(bpy-Bu^t)$(CO)_3Cl$, have shown excellent performance as well as robustness for the use as homogeneous electrocatalysts for the selective conversion of CO_2 to CO in acetonitrile on protected Cu_2O photocathodes.[30–33] To enable covalent binding to the TiO_2 surface protecting the Cu_2O photocathode, the bipyridyl ligand of the original Lehn complex was modified with phosphonate linking groups. Since previous reports have hinted that the introduction of carboxylate groups on the bipyridyl moiety hampers the activity of rhenium based molecular CO_2 reduction catalysts,[32] a methylene bridge was incorporated between the phosphonate and bipyridyl to minimize modification of the electronic structure of the catalyst by the substituent. From research on DSSC, it is known that a direct link between the catalyst and the semiconductor is not a strict requirement for high electron injection efficiency and as a positive side effect, the utilization of a spacer group between the phosphonic acid and the bipyridine ligand allows for positioning the catalytic redox center a considerable distance away from the semiconductor surface, making it more accessible for the reaction to take place. These considerations led to the design of species **3.1** (**Figure 3-3**).

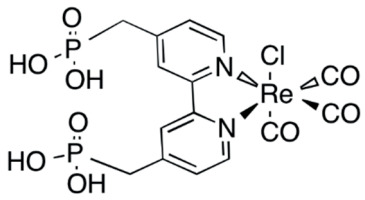

Figure 3-3: Structure of the phosphonate-modified catalyst **3.1**

Cu_2O photocathodes were prepared by electrodeposition followed by atomic layer deposition of 20 nm Al doped ZnO (Al:ZnO) and 100 nm of TiO_2, as described in the previous chapter.[23] The TiO_2 surface was subsequently functionalized with catalyst **3.1** by soaking the device in a 1 mM solution of catalyst in MeCN for 24 hours, followed by copious rinsing with neat MeCN. Interestingly, however, subsequent photoelectrochemical testing in 0.1 M Bu_4NPF_6 under chopped AM 1.5

G, 1 sun illumination showed only very small photocurrents, pointing toward the absence of catalytic activity. The maximum photocurrent densities under CO_2 were found to be merely 65 μA cm^{-2}, which indicated a negligible rate of catalytic charge transfer under these conditions (**Figure 3-4**).[1,23]

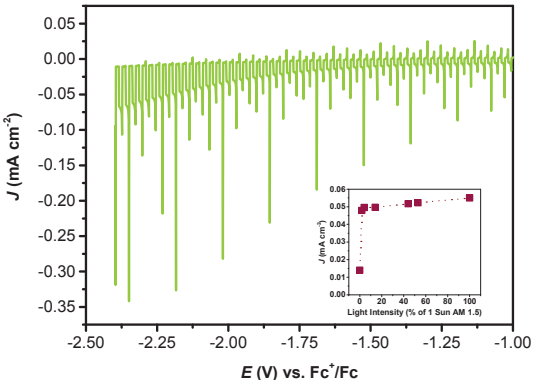

Figure 3-4: **Performance on flat photocathodes.** Chopped light potentiodynamic sweep on a flat protected Cu_2O photocathode surface, modified with rhenium catalyst. Adapted from: Schreier et al.[34]

In addition, measurements with varying light intensities, as described in **Chapter 2** showed a non-linear photocurrent response as shown in the inset of **Figure 3-4**, indicating an impeded charge extraction which leads to major charge recombination within the photoelectrode. Therefore, the simple functionalization of a standard Cu_2O photocathode with catalyst **3.1** was found to be inadequate for achieving significant rates of light-driven CO_2 reduction.

It was hypothesized that the catalyst loading on this flat TiO_2 surface was too low to achieve significant currents, introducing a bottleneck to the flux of photogenerated charge from the photocathode. This was further confirmed by FTIR, showing no signal relative to any bound catalyst. In their early stages of development, dye sensitized solar cells suffered from analogous limitations where the light absorption of a planar device was too low to achieve high efficiency, a problem eventually overcome by loading the dyes onto thick, transparent films of mesoporous TiO_2, which led to the breakthrough of DSSC research.[29] It was theorized that a similar approach might find success here, wherein enhancing the roughness factor and catalyst loading could enable better compatibility with the

photogenerated electron flux from the photocathode, and it was therefore sought to deposit porous films atop the photocathode surface.

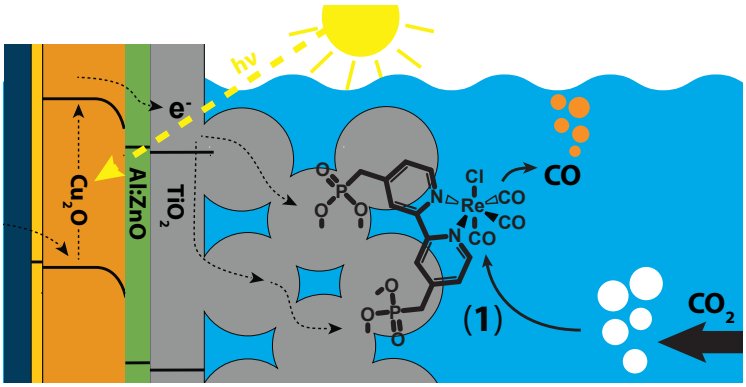

Figure 3-5: **Schematic of the modified photocathode.** The surface was modified with mesoporous TiO_2 and catalyst **3.1** was bound to this enhanced surface. Adapted from: Schreier et al.[34]

Mesoporous TiO_2 films for DSSC applications are traditionally processed at 500 °C in air, a treatment necessary to oxidize the binder material and to sinter the TiO_2 particles.[35] Unfortunately, this method is not compatible with the photocathode employed here since the p–n junction between Cu_2O and AZO has been found to deactivate upon heating beyond 250 °C, thereby precluding any high temperature treatment for protected Cu_2O photocathodes.[36] However, the curing of TiO_2 films under ultraviolet (UV) light has shown promising results as an alternative to high-temperature processing.[37,38] Inspired by these works, mesoporous films of 4.5 to 5 µm thickness with 18 nm TiO_2 particles were deposited onto fluorine-doped tin oxide (FTO) substrates and treated by UV light at room temperature for 48 hours followed by $TiCl_4$ processing at 70 °C. The $TiCl_4$ treatment was found to be the key to achieve films, which were stable under the testing conditions.

Catalyst immobilization on low-temperature mesoporous TiO_2 films

The UV-curing of TiO_2 films proved successful and could be confirmed by FTIR measurements. To serve as a reference, screen-printed TiO_2 films were thermally cured up to 500°C, in a standard ramp devised for the production of films for dye sensitized solar cells.[35]

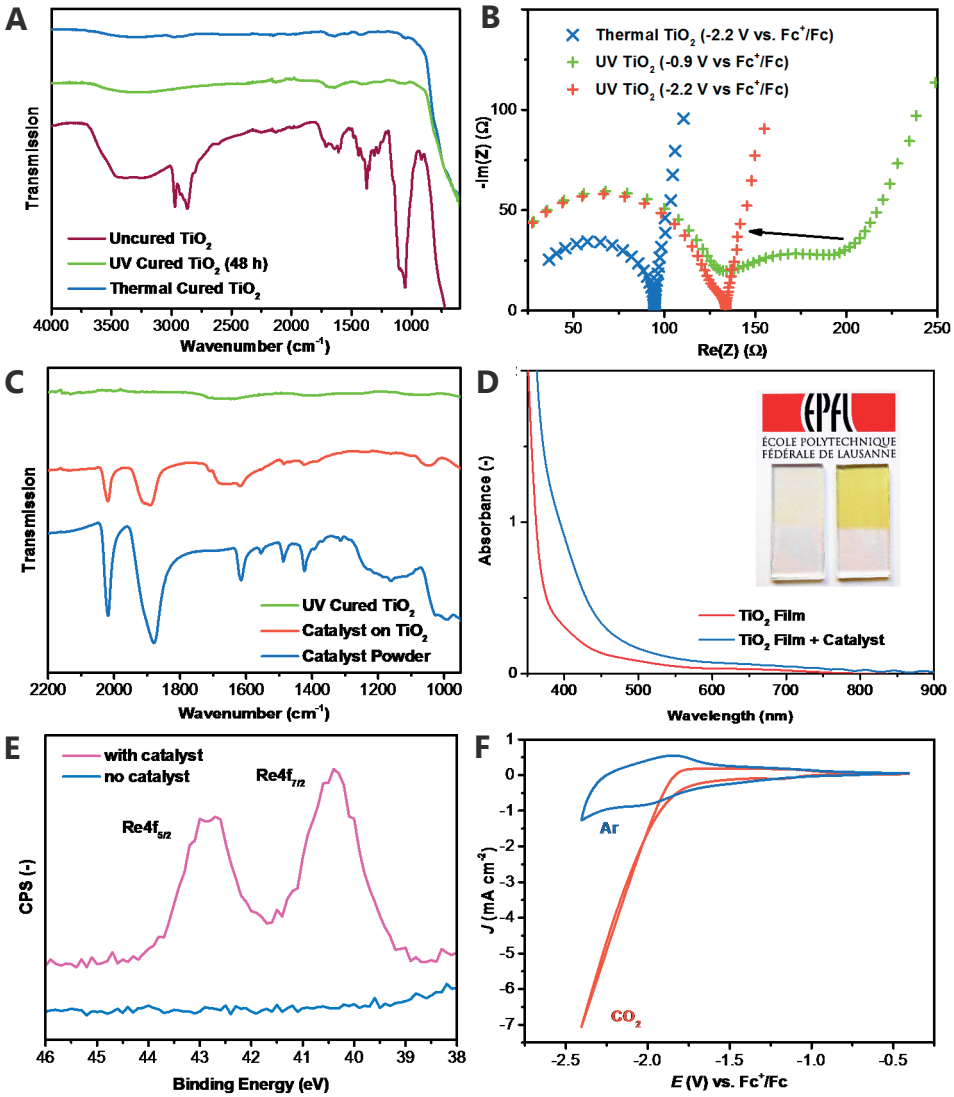

Figure 3-6: **Characterization of TiO_2 samples and catalyst immobilization.** (A) FTIR-ATR measurement of TiO_2 films before curing and after thermal and UV curing. Ethyl cellulose is efficiently eliminated upon UV curing, yielding films which are essentially indistinguishable from thermal processing. (B) EIS Spectra of thermally- and UV cured films. The additional charge transfer resistance which is observed for UV cured films disappears at more negative potentials. (C) FTIR-ATR measurements of films before and after binding of catalyst **3.1**, compared to the catalyst powder spectrum, confirming catalyst binding to the film. (D) Optical absorption spectra of TiO_2 films with and without bound catalyst. The inset shows a photo of a TiO_2 film with and without bound catalyst, as an illustration of the catalyst color. (E) XPS detail spectrum of the Re4f peak, confirming the presence of Re-catalyst on the TiO_2 film surface compared to a UV cured TiO_2 film without catalyst. (F) Cyclic voltammetry of catalyst **3.1** bound to UV cured TiO_2 on FTO. The catalytic onset can be clearly distinguished in the presence of CO_2. Adapted from: Schreier et al.[34]

After 48 h UV treatment, the disappearance of modes associated with ethyl cellulose could be observed by FTIR, leading to a spectrum which closely resembles the one of films which were treated thermally (**Figure 3-6a**). AC-impedance measurements were carried out to investigate the conductivity of the low temperature films, which led to the appearance of an additional RC element for UV treated samples which could be attributed to a contact resistance between individual particles. Interestingly, this element almost completely disappeared at more negative potentials as shown in **Figure 3-6b**, and the films thus behave similar to thermally cured films under these conditions.

To improve adsorption of catalyst molecules, it was sought to remove adsorbed water from the TiO_2 films. This was achieved by heating the films in an ALD chamber to 150 °C under vacuum. The phosphonate-modified rhenium bipyridyl catalyst **3.1** was subsequently applied onto the surface of mesoporous TiO_2 by soaking the substrate in a 1 mM solution of **3.1** for 24 hours. The samples were then copiously rinsed with MeCN to ensure removal of any unbound species. To verify for the presence of bound catalysts, FTIR-ATR measurements were carried out on the sample surface. As shown in **Figure 3-6c**, strong peaks corresponding to the carbonyl vibrations on the Re complex could be observed at 1911 and 2035 cm^{-1}, which are not present on a bare TiO_2 sample before the treatment with catalyst. These peaks are blue-shifted in the bound form as compared to their powder spectrum (1868 and 2012 cm^{-1}), suggesting a decreased electron density on the Re center upon binding to TiO_2. The bound catalyst introduced a slight yellow coloration of the TiO_2 films as can be seen from the photographs and UV-Vis transmission spectra in **Figure 3-6d**. The presence of grafted catalyst was further confirmed by X-ray photoelectron spectroscopy (XPS) measurements on the photocathodes which show the appearance of a clearly visible signal for Re (**Figure 3-6e**) at 40.4 and 42.7 eV, in agreement with previously reported values.[39] The amount of catalyst present on the scaffold was determined by ICP-OES of rhenium after complete dissolution in acid and found to be ~ 85 nmol cm^{-2}.

To prove that binding was mediated by the phosphonate group and indeed covalent, the catalyst binding procedure was repeated using the original Lehn catalyst, consisting of the rhenium bipyridyl complex without any substituent (Species **2.1**,

Figure 2-2, **Chapter 2**).[1,32] After rinsing, no FTIR signal from bound molecules could be observed in this case (**Figure 3-7**), thereby establishing that the phosphonate groups were indeed crucial for achieving catalyst immobilization on the scaffold.

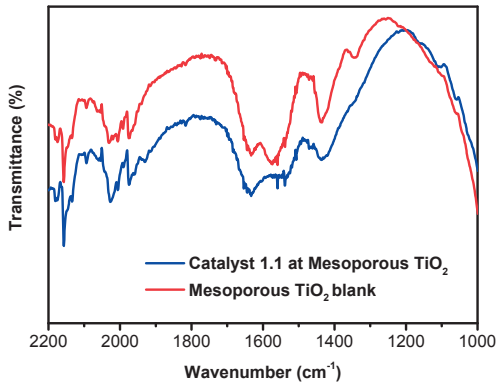

Figure 3-7: **Adsorption of catalyst without binding group.** FTIR spectra of TiO_2 films, treated with catalysts without binding group show that no catalyst is attached to the scaffold. Adapted from: Schreier et al.[34]

Electrochemical characterization of immobilized catalyst

To examine the electrochemical behavior of the unbound catalyst itself, cyclic voltammetry scans were carried out on a MeCN solution of catalyst **3.1** using a Glassy Carbon electrode (**Figure 3-8**).

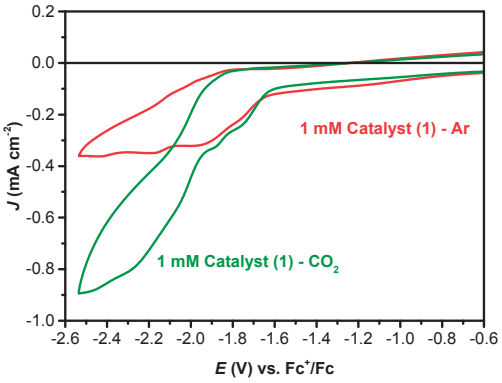

Figure 3-8: **Catalyst 3.1 at glassy carbon electrodes.** Performance of phosphonate-modified catalyst in solution under Ar and CO_2. Adapted from: Schreier et al.[34]

After a first reduction at -1.62 V vs. Fc^+/Fc, two minor reduction peaks could be observed at -1.77 V and -1.88 V. Under CO_2, the second peak leads into a catalytic wave, confirming the activity of the complex toward reducing CO_2. Furthermore,

as a positive side effect of the bipyridine modification, its catalytic onset is shifted 195 mV positive compared to Lehn's $Re(bpy)(CO)_3Cl$ catalyst.[33] Cyclic voltammetry measurements of catalyst **3.1** bound to UV cured TiO_2 films show a strong activity toward the electroreduction of CO_2 (**Figure 3-6f**), exhibiting current densities exceeding 7 mA cm^{-2} at -2.4 V vs. Fc^+/Fc in the presence of CO_2. The onset of current is observed at approximately -1.7 V vs. Fc^+/Fc in only one reduction peak, which is interesting since commonly Re(bpy) catalysts are known to be activated through a 2-step reduction process in systems where homogeneously dissolved catalyst is driven by an inert electrode.[32,40] This raises the question on whether the immobilization of the catalyst changes the way it is being activated.

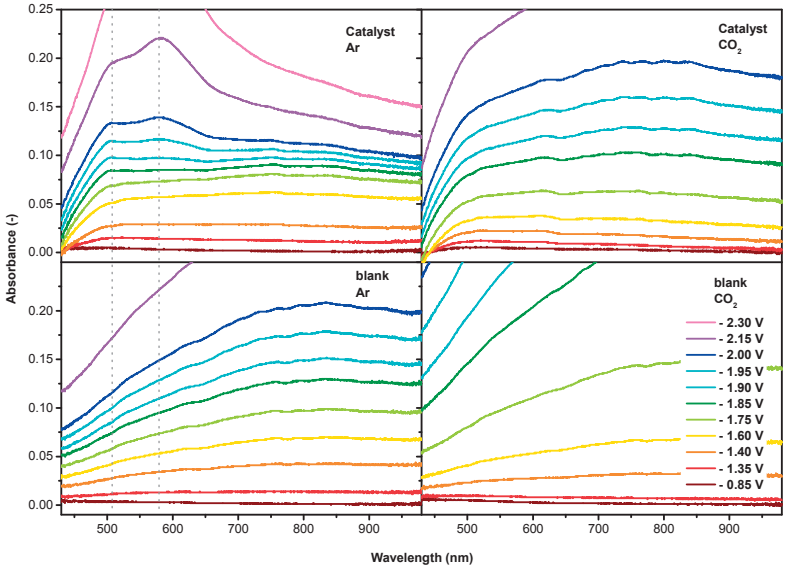

Figure 3-9: **Spectroelectrochemical measurements.** UV-Vis transmission measurements on UV-treated TiO_2 in presence of catalyst **3.1** under Ar (top left) and CO_2 (top right) and in the absence of catalyst under Ar (bottom left) and under CO_2 (bottom right). The presence of a reduced species which is present under Ar but not under CO_2 can be observed from 1.90 V. Potentials are given vs. Fc^+/Fc. Adapted from: Schreier et al.[34]

To investigate this question, the catalytic activation in the present system was analyzed by UV-Vis spectroelectrochemical experiments. The system under study offers a particularly powerful tool for combining electrochemical and spectroscopic study. The scaffold roughness enables the presence of a high density of grafted species, while the semi-transparency of the TiO_2 scaffold allows the use of transmittance-based measurements. From the analysis of potential-dependent light

absorption (**Figure 3-9**), a catalyst transition characterized by two absorption peaks at 507 and 578 nm was observed, appearing at –1.9 V vs. Fc^{+}/Fc when polarized in the absence of CO_2, a potential coinciding with the catalytic onset under CO_2 as shown in **Figure 3-6f**. The spectral change was attributed to the formation of a stable anion of catalyst 1.[40] Furthermore, this absorption was only observed in the presence of Ar, but not under CO_2, indicating that the observed species is being rapidly turned over in the presence of carbon dioxide and suggesting that it corresponds to the catalytically active species. In addition, the onset of catalytic current from the unbound catalyst at glassy carbon (**Figure 3-8**) was observed at the same potential. These data and the spectroelectrochemical observation of a catalytically active intermediate at the potential of the catalytic reduction event at glassy carbon, indicates that the catalytic mechanism remains unchanged by binding the catalyst to the TiO_2 scaffold.

CO_2 reduction photoelectrocatalysis

Having established UV-cured TiO_2 as a viable substrate for active grafted catalysts, this low-temperature process was applied to deposit the mesoporous scaffold onto Cu_2O/AZO/TiO_2 photocathodes.

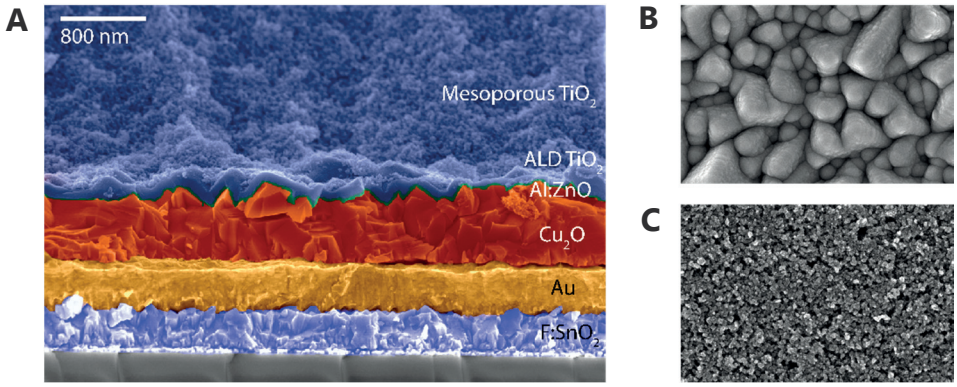

Figure 3-10: **Structure of the low-temperature processed photoelectrode.** (A) SEM cross section of the modified photoelectrode. Layers have been colored for better readability. The device has the following structure: FTO (580 nm), gold (550 nm), Cu_2O (500 nm – 1µm), ALD Al:ZnO (20 nm), ALD TiO_2 (100 nm), mesoporous TiO_2 (4.5 – 5 µm). (B) Top-down view of the unmodified photoelectrode surface (corresponding to the green layer in (A)) exhibiting low roughness, and (C) after adding the mesoporous TiO_2 network which leads to a highly porous structure, exhibiting a large surface area. Adapted from: Schreier et al.[34]

The different layers of the device can be clearly distinguished from the electron micrographs shown in **Figure 3-10**. Layer thicknesses are indicated in the figure caption. The layers fulfill the following functions: Cu_2O serves as photoabsorber and forms a p-n junction with AZO, whereas the ALD TiO_2 layer serves as a protection layer to avoid photocorrosion of Cu_2O as demonstrated in **Chapter 2** and mesoporous TiO_2 serves as a scaffold to support the molecular catalyst.[23] Due to its nature as a buried p-n junction device,[41] the transfer of electrons to the catalyst is dictated by the offset of the conduction band of TiO_2 and the catalyst redox potential. The flatband potential of mesoporous TiO_2 in acetonitrile is known to be in the range of -2.4 V vs. Fc^+/Fc,[42] whereas the onset of catalytic activity of catalyst 1 at glassy carbon is observed at -1.9 V vs. Fc^+/Fc. Thus, a significant driving force can be expected to exist for electron transfer to take place.

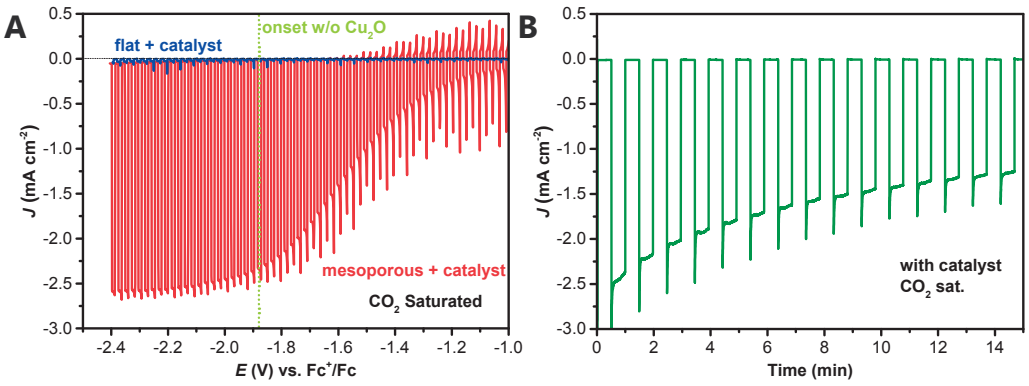

Figure 3-11: **Device performance.** (A) Photoelectrochemical performance under chopped simulated sunlight of Cu_2O photocathodes with (red) and without (blue) a mesoporous TiO_2 layer on the surface, tested under CO_2 with molecular Re catalyst covalently bound to the surface. Linear sweep at 10 mV s^{-1}. (B) Chopped-light polarization test under CO_2 at -1.9 V vs. Fc^+/Fc of mesoporous TiO_2 layer modified Cu_2O photocathode with catalyst. Adapted from: Schreier et al.[34]

A linear sweep voltammogram of the mesoporous TiO_2 modified photoelectrode loaded with catalyst **3.1** is shown in **Figure 3-11a**. Under CO_2, substantial photocurrents exceeding 2.5 mA cm^{-2} were observed. Importantly, the presence of a mesoporous scaffold led to a 40-fold increase in current compared to flat photocathodes. In comparison to the catalyst activity on a dark electrode, i.e. a mesoporous TiO_2 film deposited directly on FTO (**Figure 3-6f**), the catalytic current begins at potentials about 600 mV more positive on the photoelectrode, defining

the photovoltage produced by the electrode. Both the photocurrent density and photovoltage achieved here represent an improvement over the values observed in **Chapter 2** wherein a protected Cu_2O photocathode was immersed in a solution of dissolved catalyst, and the enhancement in photocurrent can be largely attributed to decreased parasitic light absorption by the catalyst when it is selectively grafted onto the electrode surface. As shown in **Figure 3-12**, a linear dependence on incident light intensity was observed for this system, showing that the catalyst is now capable of supporting the flux of photogenerated electrons from the photocathode, enabled by loading onto the high area surface of the mesoporous TiO_2 scaffold.

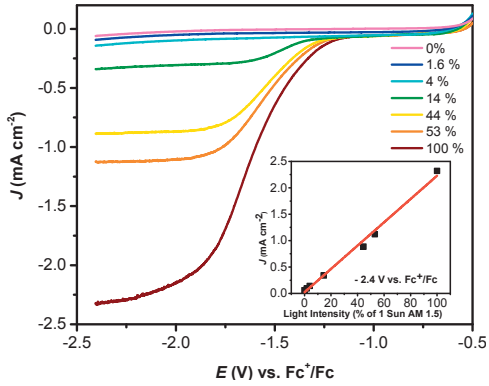

Figure 3-12: **Light intensity dependence of observed photocurrent.** The inset, representing the photocurrent at -2.4 V vs. Fc^+/Fc shows a linear behavior. The red line represents a linear fit of the presented data. Adapted from: Schreier et al.[34]

The observations in **Chapter 2** using a TiO_2 protected Cu_2O photocathode to drive a homogenous catalyst in solution led to the hypothesis that consecutive catalyst reductions were hindered by electrostatic repulsion between the polarized semiconductor electrode and charged catalyst intermediates, inhibiting subsequent CO_2 reduction.[1] In that study, the inhibition could be surmounted by addition of a protic additive to solution. In this chapter, efficient catalyst turnover was accomplished without the need for protic additives, demonstrating how covalently linking the catalyst to the electrode surface is a useful approach toward enabling sequential charge transfer between semiconductor electrode and CO_2 reduction catalyst, in addition to greatly decreasing the required catalyst amount and minimizing its parasitic absorption.

As can be seen in **Figure 3-11b**, potentiostatic testing at -1.9 V vs. Fc^+/Fc under chopped light illumination showed sustained catalytic activity toward the reduction of CO_2, during which a gradual decrease in photocurrent could be observed as will be discussed below.

In order to verify the catalytic activity toward CO_2 conversion, the evolved gases were quantified by gas chromatography during constant polarization of UV cured TiO_2-supported catalyst on FTO. It was found that the sample reached faradaic yields for CO between 80 and 95%, whereas in absence of catalyst, negligible CO was observed (**Figure 3-13a**). Furthermore, when polarized under inert helium saturation, no production of gas-phase species was observed (**Figure 3-13b**).

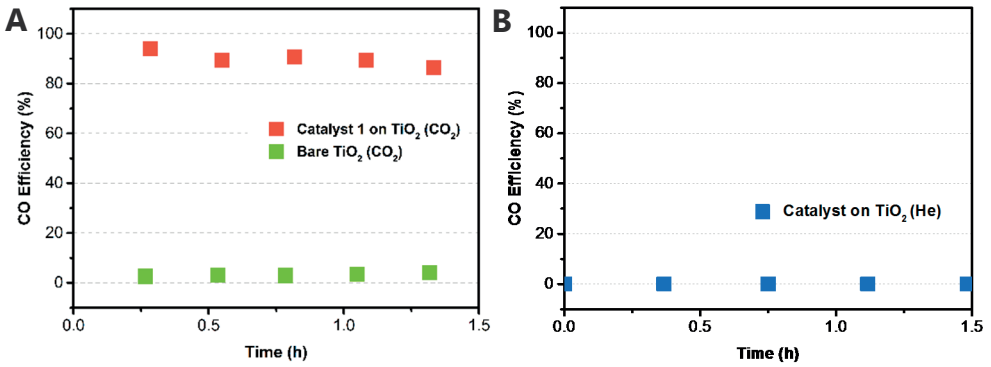

Figure 3-13: **Gas product measurements.** (A) Quantification of the faradaic efficiency of carbon monoxide production by catalyst-modified TiO_2 films polarized at -2.05 V vs. Fc^+/Fc and from a bare TiO_2 film at -2.20 V vs. Fc^+/Fc under CO_2 saturation. The presence of catalyst is necessary for CO_2 to be turned over. (B) If a catalyst-modified TiO_2 film is polarized at -2.20 V vs. Fc^+/Fc under helium, no production of CO is observed, proving that CO does not stem from the decomposition of the catalyst. Adapted from: Schreier et al.[34]

Taken together with the high turnover numbers observed, as estimated below, these experiments demonstrate that the observed carbon monoxide originates from a catalytic reaction of CO_2 rather than from decomposition of the catalyst, and that the molecular catalyst is indeed required for turnover of CO_2 to take place.

Loss of catalytic activity

During potentiostatic testing of the photoelectrode under chopped light, a gradual decrease in photocurrent (**Figure 3-11b**) and in faradaic efficiency for CO (**Figure 3-13a**) was observed over time. To shed light on these processes, a series of techniques were used to determine the changes to the electrodes resulting from

extended operation. After 2 hours of polarization at –1.9 V vs. Fc^+/Fc under chopped light of a catalyst coated photoelectrode followed by rinsing in neat MeCN, surface analysis by XPS confirmed the persistence of the elements attributable to the immobilized catalyst (Re, N, and P), albeit at a slightly lower intensity (**Figure 3-14**).

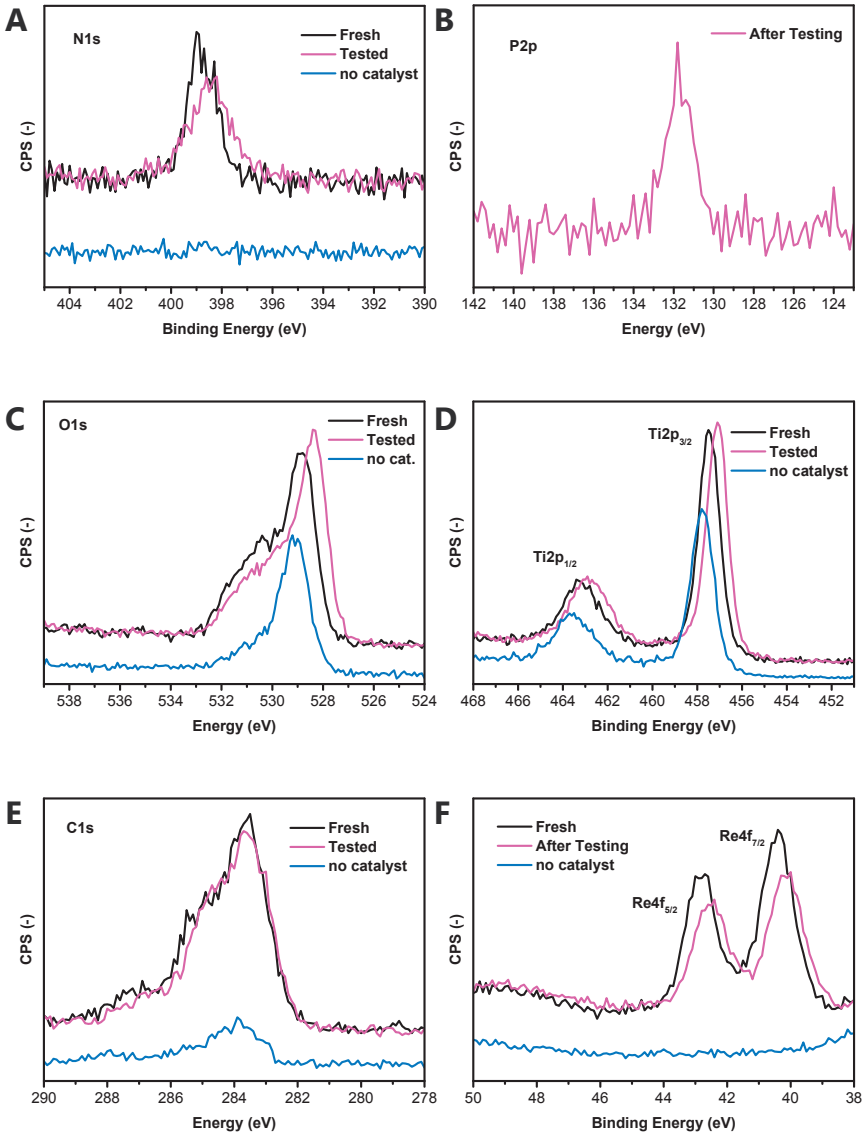

Figure 3-14: **XPS measurement of photocathode with covalently bound catalyst.** (A) Nitrogen 1s, (B) Phosphorus 2p, (C) Oxygen 1s, (D) Titanium 2p, (E) Carbon 1s, (F) Rhenium 4f. Measurements are shown before and after testing under chopped AM 1.5G illumination at 1 sun at -1.9 V vs. Fc^+/Fc for 2h and compared to a UV cured TiO_2 sample without catalyst. In the case of phosphorous, no measurement before testing and in the absence of catalyst is available. Adapted from: Schreier et al.[34]

The peaks associated with Re did not experience a significant shift, indicating no change in oxidation state. From the observation of a decreased signal intensity, one may assume that a part of the catalyst is desorbing which is the most straightforward explanation for the decrease in photocurrent. However, further experiments gave evidence that other processes, such as the structural change of catalysts, are likely to play a role. The results in **Chapter 2** point against instability of the Cu_2O photoabsorber underlayer,[1] so the issue remains on catalyst and TiO_2 mesoporous scaffold. To eliminate contribution from the scaffold, additional experiments were conducted using thermally cured mesoporous TiO_2 films on FTO, where a similar degradation was observed, suggesting that the scaffold does not play a role in the deactivation process. Furthermore, it was found that immersing a completely deactivated sample in a 1 mM solution of catalyst for 24 h led to almost complete recovery of the catalytic activity (**Figure 3-15a**). In contrast, when a deactivated sample was rinsed, dried and subsequently tested in fresh electrolyte, no regain of activity was observed. Despite the loss of catalytic activity, the presence of catalyst was consistently observed by FTIR spectroscopy in between the measurements (**Figure 3-15b**). It is notable that even after 3 h of polarization at -2.2 V vs. Fc^+/Fc, strong signals from the catalyst C-O stretches were visible.

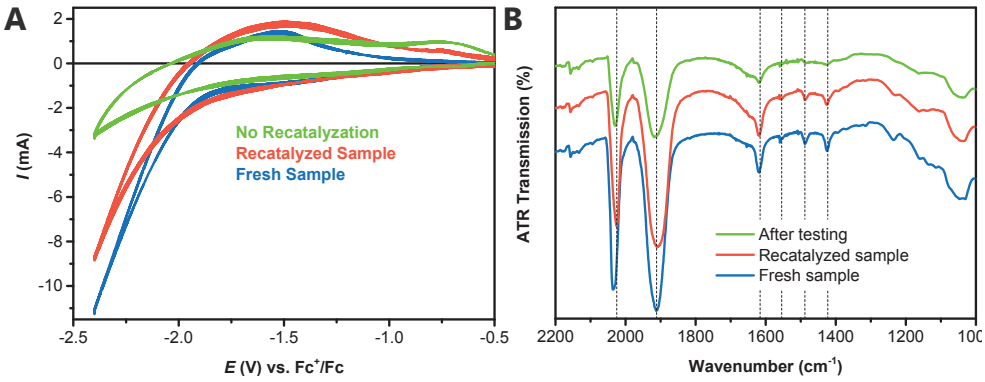

Figure 3-15: **Recatalyzation test.** (A) CV curves recorded from a thermally treated TiO_2 sample at different stages of testing. Re-exposing a deactivated sample to fresh catalyst (red trace) led to a performance comparable to the fresh sample (blue trace). In contrast, the performance of a sample tested for 3 h without recatalyzation (green trace) is significantly lower than of a fresh sample. (B) At each stage of the experiment ATR-FTIR measurements were carried out. The C-O stretches associated with the catalyst are observed at each stage. Adapted from: Schreier et al.[34]

Sample	Rhenium (nmol cm^{-2})
UV Cured TiO_2 + catalyst **3.1**	84.4
UV Cured TiO_2 + catalyst **3.1**	85.8
UV Cured TiO_2 + catalyst **3.1**, -1.65 V vs. Fc^+/Fc for 3h	60.7
UV Cured TiO_2 + catalyst **3.1**, -2.20 V vs. Fc^+/Fc for 3h	51.5

Table 3-1: **ICP-OES analysis of fresh- and tested samples.** Even after extended testing under CO_2, still 60 - 70 % of the initial rhenium is observed. Adapted from: Schreier et al.[34]

Despite being weaker than in the case of a fresh sample, the observation of these signals indicates that loss of catalyst is not the only process leading to the observed decrease in current. Support for this conclusion comes from complete digestion of the samples, followed by ICP-OES analysis, which even after 3 h of continuous polarization still detects between 60 and 70 % of the initial rhenium on the substrates (**Table 3-1**). Structural change of the catalyst molecules themselves is therefore likely to play a significant role as well, as can be seen from the distinct color change of samples after deactivation, as seen in the photograph as well as in the reflectance spectra (**Figure 3-16**).

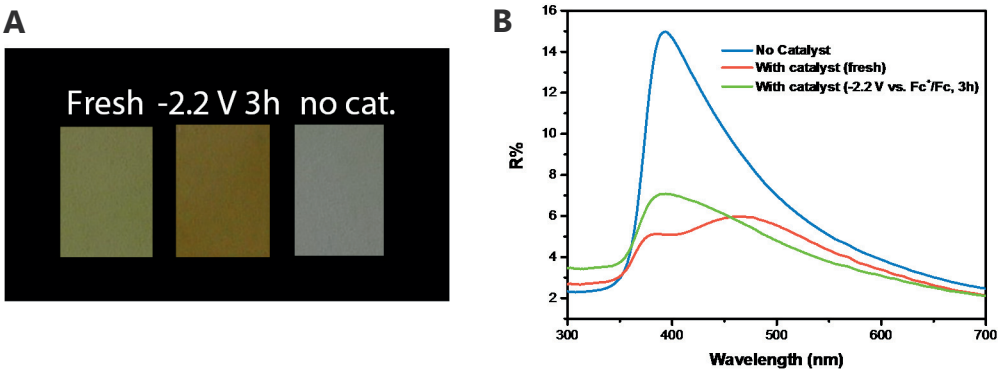

Figure 3-16: **Modification of the catalyst aspect upon testing.** (A) Aspect of samples before testing, after 3h at -2.2 V vs. Fc^+/Fc and without catalyst. Testing leads to a change in color. (B) Diffuse reflectance spectra. The reflectance dip around 400 nm caused by catalyst absorption appears attenuated following extended reaction. Adapted from: Schreier et al.[34]

Previously, the formation of a formato-rhenium complex was suggested as being at the origin of the loss of catalytic activity,[43] however here no evidence for this effect can be obtained from FTIR, where no significant shift of the carbonyl stretches is observed. In contrast, it is found that the vibrations in the region from 1400 to 1600 cm^{-1}, related to the bipyridine group, are bleached after testing, suggesting that a potential structural change of the bipyridine may lead to catalyst deactivation. This effect is likely intensified by the fact that only a very small amount of catalyst is present in the system, which cannot be replenished by diffusion of pristine catalyst from a bulk solution, as it is the case in a homogeneous electrocatalytic system. As an example, from integrating the current toward CO during a 1.5 h test at -2.05 V vs. Fc^{+}/Fc (**Figure 3-13a**), the catalyst molecules exceed 70 turnovers, which is larger than what was achieved in previous reports under similar conditions.[6,7,39,43,44]

Advantages and challenges

The catalyst binding strategy developed here successfully enabled CO_2 reduction to CO while using orders of magnitude smaller quantities of expensive catalyst as compared to systems of homogeneous catalyst solutions, and minimizing parasitic absorption due to the catalyst. Since the covalent linking strategy uses a small amount of catalyst with a high proportion of catalytic participation, in contrast to homogeneous systems where only a miniscule fraction of catalyst is interacting with the electrode at a given moment, each grafted catalyst molecule experiences a significantly higher number of turnovers. Therefore, it is subject to the acceleration of any degradation pathways, as opposed to cases where abundant fresh catalyst molecules are present in solution. This is an advantage of heterogenized homogeneous catalyst systems, since they can provide a more direct picture of catalyst change than is possible in homogeneous systems.

While study relative to deactivation is still needed, the system has been examined by multiple techniques before, during, and after operation. The hybrid heterogeneous system demonstrated here will require further analysis by *in-situ* techniques (optical spectroscopy, transient absorption spectroscopy) to elucidate the mechanisms, kinetics, and deactivation pathways of molecular catalysts with the added benefit of electrochemical control. Binding the catalyst to an electro-active

surface enables biasing all catalyst molecules at the same potential, reduces the influence of diffusion processes, and facilitates the multiple electron transfers necessary for a multi-step reaction like CO_2 reduction. For instance, it has been reported that surface immobilization of catalyst can lead to increased lifetimes of catalyst intermediates.[6] This strategy of using immobilized catalysts on a nanostructured scaffold may prove attractive for diverse electrochemical and photoelectrochemical applications, including but not limited to water splitting, CO_2-reduction and bioelectrochemistry.[45–47]

Since the catalyst itself absorbs light, the question arises whether it serves as a sensitizer, leading to the generation of photocurrent by itself. To verify this hypothesis, a linear sweep scan was carried out on a catalyst-modified mesoporous TiO_2 sample under chopped illumination at 1 sun intensity. As can be seen in **Figure 3-17**, apart from a slight anodic response at very positive bias, likely related to TiO_2, no significant photoresponse was observed, thereby excluding the light absorbing effect of the catalyst itself to serve as a sensitizer.

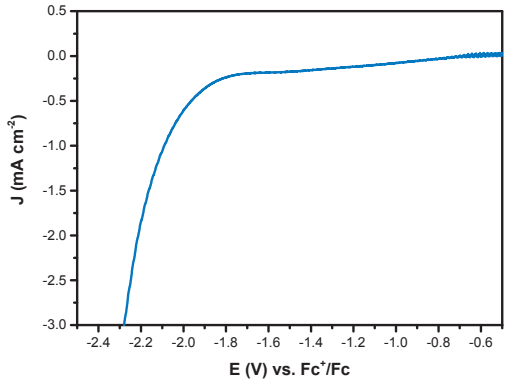

Figure 3-17: **Demonstration of the absence of sensitizing behaviour.** Linear Sweep scan (10 mV s^{-1}) of UV cured mesoporous TiO_2 + catalyst **3.1** on FTO under chopped illumination (0.5 Hz, AM1.5G, 1 sun). No cathodic photresponse was observed. Adapted from: Schreier et al.[34]

Although there are reports of immobilized catalysts for heterogeneous photocatalytic CO_2 reduction on particles in solution,[6–8,26–28] relatively few studies exist where catalysts are grafted onto an electrode surface,[18] and even fewer which report electrochemical characterization. Among these, this work was the first report of examining the potential and the photoelectrochemistry of phosphonate-mediated covalently bound catalysts for CO_2 reduction. While the performance observed with

this system is astonishing and even exceeds the performance recently reported with silicon nanowires,[20] numerous further improvements can be envisioned. Increasing the robustness of the catalyst as well as the binding strategy will improve the stability of the system. Furthermore, the replacement of rhenium with an earth-abundant metal core will lead to a system that is free of precious metals, thereby decreasing the system cost. This will enable another step toward the realization of scalable solar fuels devices, which will be key to achieving an energy system based on renewable resources.

Conclusion and outlook

The light-assisted reduction of carbon dioxide was demonstrated by the use of a covalently bound molecular catalyst on mesoporous TiO_2 modified Cu_2O photocathodes. The observed photocurrents exceed the ones achieved in **Chapter 2**. Furthermore, in addition to being based on a low-cost photoelectrode, the observed photocurrents are comparable to or better than previous reports of immobilized catalysts on photoelectrodes both toward CO_2 reduction and water splitting. This achievement can largely be attributed to the use of a nanostructured photoelectrode surface which has proven necessary to reach large photocurrents with covalently bound catalysts. This work represents the first demonstration of the use of phosphonate linking groups to immobilize a molecular fuel generation electrocatalysts on the surface of a photoelectrode and opens the path toward further research into improving the system stability and efficiency, as well as more detailed investigation of the mechanistic details of molecular electrocatalysts.

As was mentioned in the previous chapters, the use of molecular electrocatalysts enables the application of a number of spectroelectrochemical techniques, opening the path to in-depth study of catalyst activation, turnover and deactivation processes, the study of which is highly relevant and needed for the community to progress further. Notably, progress has to be made on the stability of such molecular systems for them to become viable in industrial applications. Also, improving the activity of the catalyst would allow for decreasing its loading on the photocathode, which would allow for more light to reach the absorber and for decreasing the overall cost of the system. Last but not least, while the overpotential of the catalyst

shown here is already improved over the state of the art Lehn catalyst, substantial efforts are still needed to reduce this parameter, which at the present time still leads to the requirement for large applied biases in order for catalyst turnover to be achieved.

The study conducted here examined a photocathode in three-electrode configuration, where the oxidation of the electrolyte serves as the source of electrons. A complete solar-to-fuel conversion process, however, requires a balanced and sustainable counter electrode oxidation process, such as oxygen evolution from water, to supply electrons for the CO_2 reduction reaction.[17,22] The design of such a device will therefore be discussed in later chapters.

Methods

Synthesis of catalyst 2.1

Re(I) complexes derived from diethylmethylphosphonate-bipyridine were synthesized by Dr. Peng Gao as follows:

4,4'-Bis(hydroxymethyl)-2,2'-bipyridine (3.2). 8.2 g of sodium borohydride was added in one portion to a suspension of 4,4'-Bis(methyl carboxylate)-2,2'-bipyridine (3.0 g, 10.0 mmol) in 200 mL of absolute ethanol. The mixture was refluxed for 3 h and cooled to room temperature, and then 200 mL of an ammonium chloride saturated water solution was added to decompose the excess borohydride. The ethanol was removed under vacuum and the precipitated solid dissolved in a minimal amount of water. The resulting solution was extracted with ethyl acetate (5 × 200 mL) and dried over sodium sulfate, and the solvent was removed under vacuum. The desired solid was obtained in 79% yield and was used without further purification.

^{1}H NMR (400 MHz, CD_3OD, δ): 4.75 (4H, s, CH_2); 7.43 (2H, d, J = 5.5 Hz, aryl H on C5 and C5'); 8.25 (2H, s, aryl H on C3 and C3'); 9.00 (2H, d, J = 5.5 Hz, aryl H on C6 and C6').

4,4'-Bis(bromomethyl)-2,2'-bipyridine (3.3). The bipyridine **3.2** (1.06 g, 4.9 mmol) was dissolved in a mixture of 48% HBr (30 mL) and concentrated sulfuric acid (10 mL). The resulting solution was refluxed (135 °C) for 6 h and then allowed to cool to room temperature, and 40 mL of water was added. The pH was adjusted to neutral with NaOH solution and the resulting precipitate filtered, washed with water (pH = 7), and air-dried. The product was dissolved in chloroform (40 mL) and filtered. The solution was dried over magnesium sulfate and evaporated to dryness, yielding 1.42 g of **2.3** (85% yield) as a white powder.

^{1}H NMR (400 MHz, $CDCl_3$, δ): 4.50 (4H, s, CH2); 7.38 (2H, d, J = 5 Hz, aryl H on C5 and C5'); 8.45 (2H, s, aryl H on C3 and C3'); 8.68 (2H, d, J = 5 Hz, aryl H on C6 and C6').

4,4'-Bis(diethylmethylphosphonate)-2,2'-bipyridine (3.4). A chloroform (8 mL) solution of **2.3** (1.1 g, 3.2 mmol) and 12 mL of triethyl phosphite was refluxed (156

°C) for 3 h under nitrogen. The excess phosphite was removed under high vacuum, and then the crude product was purified by column chromatography on silica gel (eluent ethyl acetate/methanol 80/20) yielding 1.17 g (80%) of **2.4**.

^{1}H NMR (300 MHz, $CDCl_3$, δ): 1.29 (12H, t, J = 7 Hz, CH_3); 3.23 (4H, d, J = 22 Hz, CH_2P); 4.09 (8H, apparent quintet, J = 7 Hz, OCH_2); 7.35−7.38 (2H, m, aryl H on C5 and C5‘); 8.34−8.37 (2H, m, aryl H on C3 and C3‘); 8.62 (2H, d, J = 5 Hz, aryl H on C6 and C6‘).

^{31}P NMR (81 MHz, $CDCl_3$, δ): 25.37.

[Re(4,4’-diethylmethylphosphonate-2,2’-bipyridine)$(CO)_3$Cl] (3.5).

$Re(CO)_5Cl$ (0.5 g, 1.38 mmol) was dissolved in 50 mL of hot toluene. An equimolar amount of 4,4‘-Bis(diethylmethylphosphonate)-2,2‘-bipyridine (0.630 g, 1.38 mmol) was added to the hot solution, and the reaction mixture was stirred with reflux for 1 h. Once the solution reached reflux the mixture began to change color from clear, to yellow, and finally to orange. After 1 h of reflux the reaction mixture was removed from heat and cooled in a freezer. A solid precipitate was obtained from cold toluene. The yellow solid was dried overnight in a vacuum oven at 90 °C. Spectroscopically pure product was obtained from the reaction with an overall yield of 90 %. ^{1}H NMR (400 MHz, Chloroform-d, δ): 8.95 (d, J = 5.7 Hz, 2H), 8.22 (t, J = 2.1 Hz, 2H), 7.45 (dt, J = 5.6, 2.0 Hz, 2H), 4.20 – 4.06 (m, 8H), 3.33 (s, 2H), 3.27 (s, 2H), 1.33 (td, J = 7.1, 1.7 Hz, 12H).

[Re(4,4’-dimethylphosphonic acid-2,2’-bipyridine)$(CO)_3$Cl] (Catalyst 3.1). 200 mg (0.252 mmol) of **5** was added to 1 M HCl (5.0 mL) and the mixture was kept at 70 °C for 6 h. Upon cooling to room temperature, the precipitate formed was collected by vacuum filtration and washed with cold methanol and water. Drying first in air and then in vacuum gave catalyst **2.1** as a yellow solid. ^{1}H NMR (400 MHz, Acetonitrile-d3, δ): 8.93 – 8.80 (m, 2H), 8.41 (s, 2H), 7.52 – 7.41 (m, 2H), 3.44 – 3.27 (m, 4H).

Synthesis of catalyst 1.1

Catalyst **1.1** was synthesized by Dr. Peng Gao as described in the previous chapter.[1]

Fabrication of photoelectrodes and reference samples

30 nm of Cr, followed by 450 nm (nominal) of Au were deposited on FTO glass (TEC-15, Solaronix, Switzerland) by sputter deposition. The deposition was carried out using an Alliance Concept DP650 Sputtering system (AllianceConcept, France). Cu_2O thin films were deposited onto the gold layer by electrodeposition from a copper lactate solution as described previously[35] for 105 minutes under a galvanostatic current density of 0.1 mA cm^{-2}. A Pt mesh was used as counter electrode. The copper lactate solution was prepared by dissolving 7.58 g of $CuSO_4$ (Sigma Aldrich), 67.5 g of lactic acid (Fluka), and 21.77 g of K_2HPO_4 (Sigma Aldrich) in 250 ml H_2O. 2 M KOH (Reactolab) was slowly added to the reaction mixture to reach pH 12. During this step, the color of the solution changed from dark blue to light blue, and finally to dark blue again. Precise adjustment of the pH was achieved using small amounts of KOH and lactic acid.

Atomic Layer Deposition of the Al:ZnO and TiO_2 layers was carried out on a Savannah 100 system (Cambridge Nanotech, USA) as described previously.[1] Al:ZnO was deposited at 200 °C, whereas the precursors, diethylzinc (ABCR), trimethylaluminum (ABCR), and H_2O (18 MΩ) were kept at room temperature. Under constant vacuum, the precursor was pulsed for 15 ms, followed by a 10 s wait time. Subsequently, H_2O was pulsed using the same sequence. After 20 cycles of ZnO, 1 cycle of Al_2O_3 was deposited using the same pulse sequence. This was repeated for 5 times, which led to the deposition of 20 nm of Al:ZnO. TiO_2 was deposited under constant vacuum at 150 °C using tetrakis (dimethylamino) titanium, TDMAT (99%, Sigma Aldrich) at 75 °C, and H_2O_2 (50%, Sigma Aldrich) at room temperature, using a pulse length of 10 ms, followed by 10 s wait time. 1500 cycles were carried out to yield a TiO_2 film of 100 nm thickness.

After ALD deposition of overlayers, the surface of the photoelectrode was subjected to a $TiCl_4$ chemical bath treatment. This was achieved by incubating the samples in 150 mL of 40 mM $TiCl_4$ solution for 30 minutes at 70 °C. The samples were subsequently rinsed with water and dried in an air stream.

Crystalline mesoporous TiO_2 was deposited onto the surface of the cathodes by screen printing. Commercial 18-NRT TiO_2 paste (Dyesol) was deposited by

carrying out 2 printing steps using a 61T (30.4 cm^3 m^{-2}) screen. The thus-formed films were analyzed by profilometry to exhibit a thickness of 4.5 to 5 μm.

Curing of the films was carried out at room temperature for 48 hours by keeping the film under UV irradiation at 1 mm distance from the lamp (GPH 369T5VA/4 18 W, 253.7 nm peak, Heraeus). Subsequently, the $TiCl_4$ treatment was repeated as described above.

Before catalyst immobilization, water was removed from the mesoporous scaffold by treating the electrode for 30 minutes at 150 °C under vacuum. Subsequently, the catalyst was immobilized by immersing the electrode for 24 h in a 1 mM solution of catalyst in acetonitrile, followed by copious rinsing with dry acetonitrile.

Reference samples of mesoporous TiO_2 films were prepared directly on FTO glass. UV treated samples were prepared as follows: FTO glass was pretreated with $TiCl_4$, followed by deposition of the mesoporous scaffold and subsequent treatment steps as described above.

Thermally cured samples were prepared as follows: FTO glass was pretreated with $TiCl_4$ and subsequently mesoporous TiO_2 was deposited as above. In the next step, the films were cured according to a well-established thermal procedure.[35] $TiCl_4$ post treatment was carried out as above, followed by heating to 500 °C in a hot air stream for 30 minutes. If catalyst was deposited on the sample, it was immersed in catalyst solution as above while still in a warm state.

Device characterization

Scanning electron microscopy was carried out using a Zeiss Merlin microscope. FTIR-ATR measurements were carried out using a Spectrum GX system (Perkin Elmer), equipped with an ATR extension (MIRacle, Pike Technologies). Each spectrum consists of 50 scans at 4 cm^{-1} resolution. Catalyst loading onto the TiO_2 films were determined by Karine Vernez and Sylvain Coudret as follows: After determination of the surface area, each sample was introduced in a 100 mL Erlenmeyer flask. Subsequently, 2 – 3 mL of Milli-Q water, 7.5 mL HCl (Merck 318, Suprapur) and 2.5 mL HNO_3 (Merck 441, Suprapur) were added. After standing overnight, the mixture was refluxed for 2 h and 20 mL of Milli-Q water was added. The solution was subsequently filtered and the filter washed 5 times

with 2.0 M HNO_3. Subsequently, the volume was completed to 50.0 mL with 2.0 M HNO_3 and analyzed by ICP-OES. Profilometry of TiO_2 films was carried out using an Alpha-Step 500 profilometer. XPS measurements were carried out using a PHI VersaProbe II Scanning XPS Microprobe.

Electrochemical testing

Solar simulation was carried out using a LOT Oriel light source, equipped with a 450 W Xe arc lamp (Ozone Free, Osram). The light intensity was reduced by a metal grid which served as a neutral density filter, followed by a KG3 filter (Edmund Optics). The system was tuned to 1 sun intensity using a calibration diode. Light chopping was carried out using an electromechanical chopper at a frequency of 1 Hz. Samples were tested in a custom-built gastight PEC test cell as described in **Chapter 1**. The test solution was dry acetonitrile (Sigma Aldrich) with 0.1 M Bu_4NPF_6 (tetrabutylammonium hexafluorophosphate, Sigma Aldrich). Electrochemical measurements were performed using a Gamry Interface 1000 and a BioLogic SP-300 potentiostat. An Ag/AgCl wire, separated from the cell by a porous diaphragm, was used as a pseudo reference electrode and its potential was calibrated to ferrocene. A Pt wire in the same compartment was used as counter electrode. A 3 mm diameter Glassy Carbon rotating disk electrode (Metrohm) was used for electrochemical characterization of catalysts in solution. In all cases, the solution was saturated either with Ar (Carbagas, 99.9999%) or with CO_2 (Carbagas 99.998%) by sparging the solution under stirring for 20 min. CVs were carried out between -0.4 and -2.4 V vs. Fc^+/Fc at 100 mV s^{-1}, whereas linear sweep scans were carried out between the same potentials at 10 mV s^{-1}. Potential-stepping AC-impedance measurements were carried out using a BioLogic SP-300 between 1 MHz and 0.1 Hz.

Gas Measurements

Gas Measurements were carried out under 10 mL min^{-1} flow of CO_2 using the same equipment as described above. Blank tests were carried out, verifying that the counter-electrode in the cell produced negligible CO. Polarization was carried out using the potentiostats described above and the effluent gas was led into the sampling loop of a gas chromatograph after evaporated acetonitrile was condensed

out at - 25 °C. The gas chromatograph (Trace ULTRA, Thermo Scientific) was equipped with a ShinCarbon column (Restek) and a PDD detector (Vici). Helium was used as carrier gas.

Catalyst turnover numbers (TON) were calculated by integrating the amount of CO produced during the polarization test and comparing to the measured amount of catalyst.

Spectroelectrochemical measurements

Spectroelectrochemistry was carried out using the UV-Vis equipment and the custom-made test cell described above. An ocean-optics halogen lamp was used to illuminate transparent TiO_2 films on FTO, prepared as described above. A condenser lens behind the film collected the transmitted photons and fed them to an OceanOptics photodiode array by the means of a fiber optic cable. The potential was stepped from -0.4 to -2.4 V vs. Fc+/Fc using a Gamry Framework script. After 20 s equilibration time at each potential, a custom-made LabView software recorded a spectrum from the photodiode array.

References

1. Schreier, M. *et al.* Efficient and selective carbon dioxide reduction on low cost protected Cu_2O photocathodes using a molecular catalyst. *Energy Env. Sci* **8,** 855–861 (2015).
2. Kumar, B., Smieja, J. M. & Kubiak, C. P. Photoreduction of CO_2 on p-type Silicon Using Re(bipy-But)(CO)3Cl: Photovoltages Exceeding 600 mV for the Selective Reduction of CO_2 to CO. *J. Phys. Chem. C* **114,** 14220–14223 (2010).
3. Guerrero, A. *et al.* Organic photoelectrochemical cells with quantitative photocarrier conversion. *Energy Environ. Sci.* **7,** 3666–3673 (2014).
4. Costentin, C., Drouet, S., Robert, M. & Savéant, J.-M. Turnover Numbers, Turnover Frequencies, and Overpotential in Molecular Catalysis of Electrochemical Reactions. Cyclic Voltammetry and Preparative-Scale Electrolysis. *J. Am. Chem. Soc.* **134,** 11235–11242 (2012).
5. Cecchet, F., Alebbi, M., Bignozzi, C. A. & Paolucci, F. Efficiency enhancement of the electrocatalytic reduction of CO_2: fac-[Re(v-bpy)$(CO)_3$Cl] electropolymerized onto mesoporous TiO_2 electrodes. *Inorganica Chim. Acta* **359,** 3871–3874 (2006).
6. Windle, C. D. *et al.* Improving the Photocatalytic Reduction of CO_2 to CO through Immobilisation of a Molecular Re Catalyst on TiO_2. *Chem. – Eur. J.* **21,** 3746–3754 (2015).
7. Liu, C., Dubois, K. D., Louis, M. E., Vorushilov, A. S. & Li, G. Photocatalytic CO_2 Reduction and Surface Immobilization of a Tricarbonyl Re(I) Compound Modified with Amide Groups. *ACS Catal.* **3,** 655–662 (2013).
8. Dubois, K. D., He, H., Liu, C., Vorushilov, A. S. & Li, G. Covalent attachment of a molecular CO_2-reduction photocatalyst to mesoporous silica. *J. Mol. Catal. Chem.* **363–364,** 208–213 (2012).
9. Krawicz, A., Cedeno, D. & Moore, G. F. Energetics and efficiency analysis of a cobaloxime-modified semiconductor under simulated air mass 1.5 illumination. *Phys. Chem. Chem. Phys.* **16,** 15818–15824 (2014).
10. Krawicz, A. *et al.* Photofunctional Construct That Interfaces Molecular Cobalt-Based Catalysts for H_2 Production to a Visible-Light-Absorbing Semiconductor. *J. Am. Chem. Soc.* **135,** 11861–11868 (2013).
11. Seo, J., Pekarek, R. T. & Rose, M. J. Photoelectrochemical operation of a surface-bound, nickel-phosphine H_2 evolution catalyst on p-Si(111): a molecular semiconductor|catalyst construct. *Chem. Commun.* **51,** 13264–13267 (2015).
12. Nann, T. *et al.* Water Splitting by Visible Light: A Nanophotocathode for Hydrogen Production. *Angew. Chem. Int. Ed.* **49,** 1574–1577 (2010).
13. Kou, Y. *et al.* Visible light-induced reduction of carbon dioxide sensitized by a porphyrin–rhenium dyad metal complex on p-type semiconducting NiO as the reduction terminal end of an artificial photosynthetic system. *J. Catal.* **310,** 57–66 (2014).
14. Sahara, G. *et al.* Photoelectrochemical CO_2 reduction using a Ru(II)–Re(I) multinuclear metal complex on a p-type semiconducting NiO electrode. *Chem. Commun.* **51,** 10722–10725 (2015).
15. Sato, S. *et al.* Selective CO_2 Conversion to Formate Conjugated with H_2O Oxidation Utilizing Semiconductor/Complex Hybrid Photocatalysts. *J. Am. Chem. Soc.* **133,** 15240–15243 (2011).
16. Arai, T., Sato, S., Kajino, T. & Morikawa, T. Solar CO_2 reduction using H_2O by a semiconductor/metal-complex hybrid photocatalyst: enhanced efficiency and demonstration of a wireless system using $SrTiO_3$ photoanodes. *Energy Environ. Sci.* **6,** 1274–1282 (2013).
17. Arai, T., Sato, S. & Morikawa, T. A monolithic device for CO_2 photoreduction to generate liquid organic substances in a single-compartment reactor. *Energy Environ. Sci.* **8,** 1998–2002 (2015).
18. Tian, H. Molecular Catalyst Immobilized Photocathodes for Water/Proton and Carbon Dioxide Reduction. *ChemSusChem* **8,** 3746–3759 (2015).

19. Arai, T. *et al.* Photoelectrochemical reduction of CO_2 in water under visible-light irradiation by a p-type InP photocathode modified with an electropolymerized ruthenium complex. *Chem. Commun.* **46,** 6944–6946 (2010).
20. Torralba-Peñalver, E., Luo, Y., Compain, J.-D., Chardon-Noblat, S. & Fabre, B. Selective Catalytic Electroreduction of CO_2 at Silicon Nanowires (SiNWs) Photocathodes Using Non-Noble Metal-Based Manganese Carbonyl Bipyridyl Molecular Catalysts in Solution and Grafted onto SiNWs. *ACS Catal.* **5,** 6138–6147 (2015).
21. Arai, T. *et al.* Selective CO_2 conversion to formate in water using a CZTS photocathode modified with a ruthenium complex polymer. *Chem. Commun.* **47,** 12664–12666 (2011).
22. Schreier, M. *et al.* Efficient photosynthesis of carbon monoxide from CO_2 using perovskite photovoltaics. *Nat. Commun.* **6,** 7326 (2015).
23. Paracchino, A., Laporte, V., Sivula, K., Grätzel, M. & Thimsen, E. Highly active oxide photocathode for photoelectrochemical water reduction. *Nat. Mater.* **10,** 456–461 (2011).
24. Seger, B. *et al.* Using TiO_2 as a Conductive Protective Layer for Photocathodic H_2 Evolution. *J. Am. Chem. Soc.* **135,** 1057–1064 (2013).
25. Seger, B. *et al.* Silicon protected with atomic layer deposited TiO_2: durability studies of photocathodic H_2 evolution. *RSC Adv.* **3,** 25902–25907 (2013).
26. Ha, E.-G. *et al.* High-turnover visible-light photoreduction of CO_2 by a Re(I) complex stabilized on dye-sensitized TiO_2. *Chem. Commun.* **50,** 4462–4464 (2014).
27. Suzuki, T. M. *et al.* Direct assembly synthesis of metal complex–semiconductor hybrid photocatalysts anchored by phosphonate for highly efficient CO_2 reduction. *Chem. Commun.* **47,** 8673–8675 (2011).
28. Anfuso, C. L. *et al.* Covalent Attachment of a Rhenium Bipyridyl CO_2 Reduction Catalyst to Rutile TiO_2. *J. Am. Chem. Soc.* **133,** 6922–6925 (2011).
29. O'Regan, B. & Grätzel, M. A low-cost, high-efficiency solar cell based on dye-sensitized colloidal TiO_2 films. *Nature* **353,** 737–740 (1991).
30. Costentin, C., Robert, M. & Savéant, J.-M. Catalysis of the electrochemical reduction of carbon dioxide. *Chem. Soc. Rev.* **42,** 2423–2436 (2013).
31. Costentin, C., Drouet, S., Robert, M. & Savéant, J.-M. A Local Proton Source Enhances CO_2 Electroreduction to CO by a Molecular Fe Catalyst. *Science* **338,** 90–94 (2012).
32. Smieja, J. M. & Kubiak, C. P. Re(bipy-tBu)$(CO)_3Cl^-$ improved Catalytic Activity for Reduction of Carbon Dioxide: IR-Spectroelectrochemical and Mechanistic Studies. *Inorg. Chem.* **49,** 9283–9289 (2010).
33. Hawecker, J., Lehn, J.-M. & Ziessel, R. Electrocatalytic reduction of carbon dioxide mediated by Re(bipy)$(CO)_3Cl$ (bipy = 2,2′-bipyridine). *J. Chem. Soc. Chem. Commun.* **6,** 328–330 (1984).
34. Schreier, M. *et al.* Covalent Immobilization of a Molecular Catalyst on Cu_2O Photocathodes for CO_2 Reduction. *J. Am. Chem. Soc.* **138,** 1938–1946 (2016).
35. Ito, S. *et al.* Fabrication of thin film dye sensitized solar cells with solar to electric power conversion efficiency over 10%. *Thin Solid Films* **516,** 4613–4619 (2008).
36. Paracchino, A. *et al.* Ultrathin films on copper(I) oxide water splitting photocathodes: a study on performance and stability. *Energy Environ. Sci.* **5,** 8673–8681 (2012).
37. Zardetto, V. *et al.* Fully Plastic Dye Solar Cell Devices by Low-Temperature UV-Irradiation of both the Mesoporous TiO_2 Photo- and Platinized Counter-Electrodes. *Adv. Energy Mater.* **3,** 1292–1298 (2013).
38. Arakawa, H. *et al.* Efficient dye-sensitized solar cell sub-modules. *Curr. Appl. Phys.* **10,** S157–S160 (2010).
39. Blakemore, J. D., Gupta, A., Warren, J. J., Brunschwig, B. S. & Gray, H. B. Noncovalent Immobilization of Electrocatalysts on Carbon Electrodes for Fuel Production. *J. Am. Chem. Soc.* **135,** 18288–18291 (2013).
40. Keith, J. A., Grice, K. A., Kubiak, C. P. & Carter, E. A. Elucidation of the Selectivity of Proton-Dependent Electrocatalytic CO_2 Reduction by fac-Re(bpy)$(CO)_3Cl$. *J. Am. Chem. Soc.* **135,** 15823–15829 (2013).
41. Walter, M. G. *et al.* Solar Water Splitting Cells. *Chem. Rev.* **110,** 6446–6473 (2010).

42. Redmond, G. & Fitzmaurice, D. Spectroscopic determination of flatband potentials for polycrystalline titania electrodes in nonaqueous solvents. *J. Phys. Chem.* **97,** 1426–1430 (1993).
43. Takeda, H., Ohashi, M., Tani, T., Ishitani, O. & Inagaki, S. Enhanced Photocatalysis of Rhenium(I) Complex by Light-Harvesting Periodic Mesoporous Organosilica. *Inorg. Chem.* **49,** 4554–4559 (2010).
44. Won, D.-I. *et al.* Highly Robust Hybrid Photocatalyst for Carbon Dioxide Reduction: Tuning and Optimization of Catalytic Activities of Dye/TiO_2/Re(I) Organic–Inorganic Ternary Systems. *J. Am. Chem. Soc.* **137,** 13679–13690 (2015).
45. Fan, K. *et al.* Immobilization of a Molecular Ruthenium Catalyst on Hematite Nanorod Arrays for Water Oxidation with Stable Photocurrent. *ChemSusChem* **8,** 3242–3247 (2015).
46. Liu, R., Stephani, C., Han, J. J., Tan, K. L. & Wang, D. Silicon Nanowires Show Improved Performance as Photocathode for Catalyzed Carbon Dioxide Photofixation. *Angew. Chem. Int. Ed.* **52,** 4225–4228 (2013).
47. White, J. L. *et al.* Light-Driven Heterogeneous Reduction of Carbon Dioxide: Photocatalysts and Photoelectrodes. *Chem. Rev.* **115,** 12888-12935 (2015).

4 New Insights Into the Role of Imidazolium-based Promoters for the Electroreduction of CO_2 on a Silver Electrode

The chapter is adapted with permission from the peer-reviewed publication: ***Genevieve Lau‡ and Marcel Schreier‡****, Dmitry Vasilyev, Rosario Scopelliti, Michael Grätzel, Paul J. Dyson.* ‡ equal contribution
J. Am. Chem. Soc., 2016, vol. 25, 7820.

This work was carried out in collaboration with Dr. Genevieve Lau (LCOM, EPFL), whose previous work focused on the synthesis and application of ionic liquids in Dye Sensitized Solar Cells. The study was devised and pursued together, I set up the electrochemical testing equipment and introduced Dr. Lau to the relevant measurement techniques. Dr. Lau performed all syntheses and a majority of the electrochemical measurements. The publication was developed together.

Molecular catalysts such as shown in the previous chapters operate at inert catalyst surfaces, which are themselves inactive toward the reaction under investigation. However, a number of metals are intrinsically active toward the production of CO from CO_2. Interestingly, it has been shown that a number of organic cations, and in particular imidazolium, can promote this reaction on silver surfaces with the mechanism of this promoting effect being unclear. In this chapter, mechanistic insights are sought and obtained through the establishment of structure-activity relationships of various imidazolium cations. In contrast to previous literature, it is found that while the C2 proton is not relevant to the reaction, eliminating the C4 and C5 protons leads to a strong suppression of the promoting effect.

Introduction

The previous chapters introduced the electrochemical reduction of CO_2 to CO based on molecular rhenium catalysts, acting both as redox shuttles and catalytic center. These catalysts are coupled to the electrochemical process by being reduced on electrodes which are themselves inactive toward reducing CO_2. However, a number of electrode materials show significant intrinsic activity toward the electroreduction of CO_2 to CO, most notably gold and silver. Compared to immobilized molecular catalysts as shown in **Chapter 3**, these catalysts have the important advantage to show significantly better stability. Recently, a number of literature reports have appeared, which investigate tuning of the catalytic activity on these metal surfaces by the means of electrolyte constituents. These led to the discovery of the impact of electrolyte cations, anions, and their respective concentrations and also of different electrolyte additives.[1–10] Particular attention has been directed toward the activity of imidazolium-based ionic liquids, to both increase the solubility of CO_2 and, particularly intriguing, to change the catalytic activity of the metal electrode surface. Notably, it was recently shown that the addition of certain imidazolium-based ionic liquids, such as 1-ethyl-3-methylimidazolium tetrafluoroborate [EMIM][BF_4], resulted in a significant decrease in the overpotential required for the electrochemical reduction of CO_2 on silver electrodes, leading to a widely noted publication in Science (**Figure 4-1**).[5]

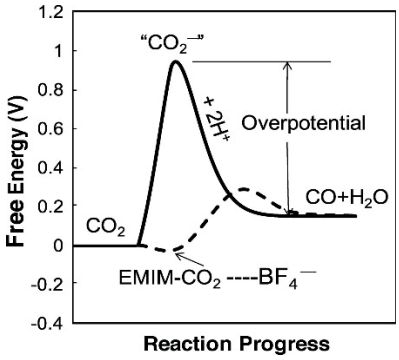

Figure 4-1: **Impact of EMIM on the CO_2 reduction pathway, as illustrated by Rosen and co-workers.** Adapted from Rosen et al.[5] Reprinted with permission from AAAS.

Subsequently, this favorable effect was independently demonstrated by numerous groups, and obtained in combination with a variety of electrocatalytic materials, including Ag,[10] Pb,[9] Sn,[11] and Bi[12] electrodes. The observed catalytic effect of these ionic liquid promoters has been studied by various groups in recent years,[8,13–18] nevertheless there remain a number of open questions regarding their mechanism of action. Particularly, it is not clear, whether a direct interaction of the imidazolium salt with the catalyst surface is taking place or whether the ions merely modify the charge density at the electrode surface.

In an attempt to make a step toward gaining more insight into these processes, Dr. Lau and I prepared a series of structurally related imidazolium-based salts and evaluated them as co-catalysts for the electrochemical reduction of CO_2. Moreover, through the examination of structure-activity relationships, we found that the C4- and C5-protons on the imidazolium ring are crucial for catalysis.

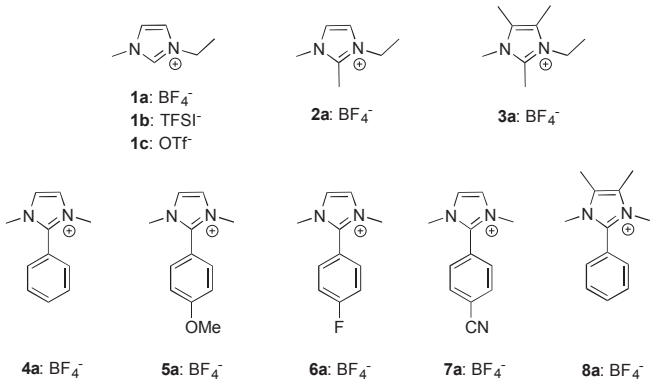

Figure 4-2: **Structures of the investigated imidazolium salts.** Adapted from Lau and Schreier et al.[19]

Results and Discussion

The structures of all imidazolium salts used in this study are presented in **Figure 4-2**, and their catalytic performance was evaluated via cyclic voltammetry, in an undivided gastight electrochemical cell, with a standard 3-electrode set-up (unless otherwise stated). In all experiments, an Ag/AgCl quasi-reference electrode was employed, which was calibrated using the ferrocene/ferrocenium redox couple. The working electrode was a 3 mm diameter Ag disk electrode. A flamed platinum wire was used as the counter electrode, and the supporting electrolyte consisted of a

0.1 M solution of tetrabutylammonium hexafluorophosphate [TBA][PF_6] in anhydrous acetonitrile (7 mL). Prior to all electrochemical measurements, the imidazolium salts were dried for 15 mins at 120 °C, and the electrolyte was purged with argon for 15 mins to remove any dissolved oxygen. All voltammograms were recorded at a potential sweep rate of 100 mV/sec, in an air-conditioned room (22 °C).

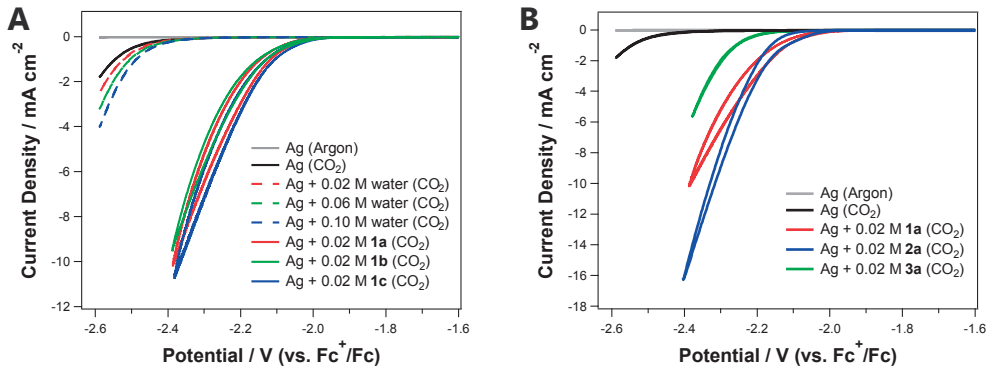

Figure 4-3: **Cyclic voltammograms recorded for electrolytes containing different additives.** (A) Effect of different anions and water concentrations on the electrochemical reduction of CO_2. (B) Effect of different cations (**1a**, **2a**, **3a**) on the electrochemical reduction of CO_2. Adapted from Lau and Schreier et al.[19]

It is well known that ionic liquids tend to be highly hygroscopic and may contain some residual water despite rigorous drying procedures.[20] The presence of water (a proton source) in the ionic liquid can potentially lead to enhanced reaction rates via proton-coupled electron transfer pathways.[21,22] The results here show, however, that the effect of adding 0.02M of **1a** is markedly different from that of adding water at the same concentration, **Figure 4-3A**. This suggests that the observed catalytic effect of **1a** does not stem from residual water in the ionic liquid. Furthermore, the contribution of the anion was also found to be rather small, with compounds **1a**, **1b**, and **1c** exhibiting very similar catalytic behavior, **Figure 4-3A**.

Based on these findings, the impact of the cation structure was investigated. Three different cations were investigated in the first instance, **1a**, **2a**, and **3a**, **Figure 4-3B**. Differences were observed in the catalytic activity of the three compounds, which decreased in the order **2a** > **1a** > **3a**. Numerous reports in the literature have suggested that the acidic proton at the C2-position of the imidazolium ring serves to stabilize a CO_2 anion radical intermediate, and is therefore a key site for

catalysis.[7,23] However, our findings are not entirely consistent with this proposed model. Instead, it would appear that the proton at the C2-position is not in fact essential for catalysis, as a methyl group at this position resulted in even higher current densities (**2a**). Further methylation of the imidazolium ring (**3a**), however, resulted in a sharp decrease in catalytic activity, as well as a negative shift in the onset potential, **Figure 4-3B**. Taken together, these results show that the catalytic activity of these imidazolium salts is highly sensitive to the chemical structure of the cation. Since **3a** is the least effective co-catalyst (among compounds **1a-3a**), the C4- and C5- protons on the imidazolium ring appear to be critical. It can be expected that these protons play an important role in the stabilization of a CO_2 anion radical intermediate via hydrogen bond interactions. Taking into account existing hypotheses in the literature,[14] we envision the following possible binding modes, **Figure 4-4**.

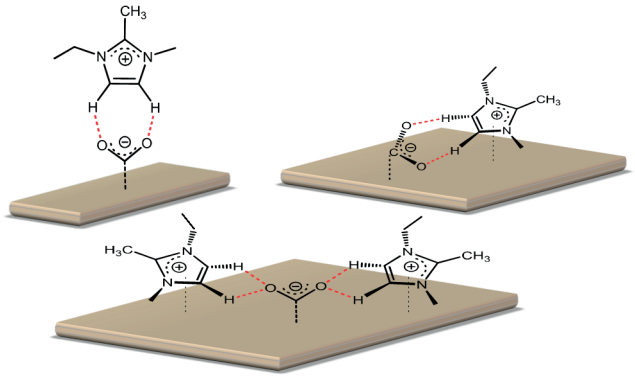

Figure 4-4: **Possible binding modes.** Potential configuration for the interaction of **2a** with an electro-generated CO_2 anion radical on a silver surface. Hydrogen bonds are represented by a dashed line (red). Adapted from Lau and Schreier et al.[19]

In order to test this hypothesis, we sought to synthesize a range of imidazolium salts bearing substituents at the C2-position with different electronic properties, so as to modulate the strength of the proposed hydrogen bond interactions. Compounds **4a-6a** were selected and synthesized, and likewise evaluated via cyclic voltammetry. (Note: imidazolium salts with strong electron-withdrawing groups directly attached to the imidazolium ring were found to decompose prior to CO_2 reduction, and were thus unsuitable for this study.)

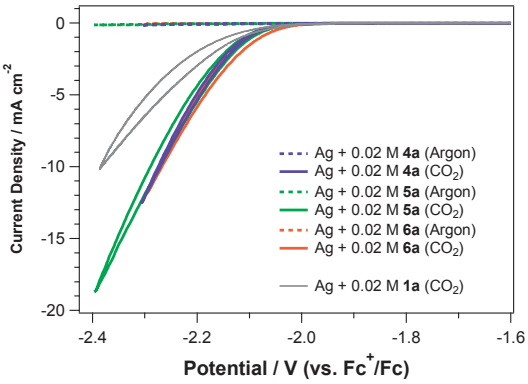

Figure 4-5: **Electrochemical characteristic of modified imidazolium cations.** Cyclic voltammograms recorded for electrolytes containing **4a**, **5a**, or **6a**. Adapted from Lau and Schreier et al.[19]

In general, the differences in the chemical structure of compounds **4a-6a** were found to have a negligible impact on their catalytic performance, resulting in very similar current responses, **Figure 4-5**. This result suggests that the different phenyl substituents are unable to significantly influence the electronic character of the C4- and C5- protons on the imidazolium ring. Such a behavior could be expected if the aromatic systems are not conjugated. Single crystal x-ray diffraction structures of **4a-6a** show that the imidazolium and phenyl rings lie on different planes, resulting in limited overlap of the π orbitals, **Figure 4-6**. In addition, the chemical shifts of the imidazolium protons in compounds **4a-6a** were found to be very similar, as determined by ^{1}H NMR spectroscopy and further indicates that their electronic properties do not differ greatly.[19]

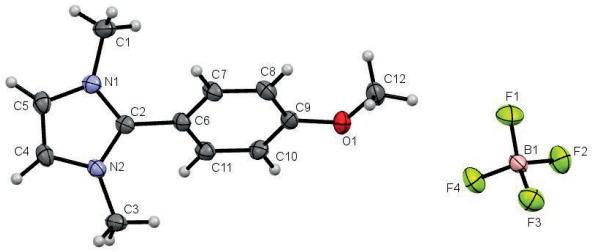

Figure 4-6: **Crystal structure of 5a.** ORTEP plot of the **5a** crystal structure shows the twisted configuration between the imidazole and penyl rings. Adapted from Lau and Schreier et al.[19]

Furthermore, it is also interesting to note that the steric bulk of these phenyl substituents does not appear to inhibit catalysis. Indeed, **4a-6a** displayed

exceptional activity as co-catalysts, significantly exceeding that of the benchmark [EMIM][BF_4] (**1a**) co-catalyst, under the same conditions, **Figure 4-5**. This again suggests that the C2- position is not the key site for CO_2 activation. Nevertheless, the different phenyl substituents had a remarkable impact on the cathodic limit of the imidazolium compounds. For example, compounds bearing electron-withdrawing substituents at the C2-position, **6a** and **7a**, were found to be more readily reduced, compared to their counterparts bearing electron-donating substituents, **5a**, **Figure 4-7**.

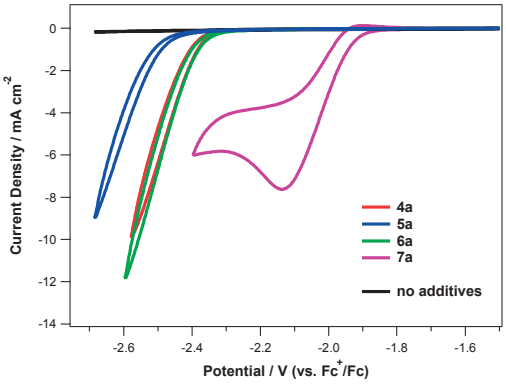

Figure 4-7: **Decomposition of 4-7a on a glassy carbon electrode in the presence of CO_2.** Voltammograms were recorded at a glassy carbon disk electrode (3 mm diameter), in CO_2 saturated electrolyte, with 0.02 M of additive. The last of 5 cycles is shown. Adapted from Lau and Schreier et al.[19]

In an argon-saturated environment, none of the imidazolium salts evaluated showed significant current flow prior to their respective cathodic limits, **Figure 4-5**. Under CO_2, however, catalytic currents were observed at much more positive potentials, where the imidazolium cation is not yet reduced. This serves as a strong indication of the CO_2-activating effect of the imidazolium salts, and points against them acting as an electron shuttle.

Since the electronic properties of the C4- and C5-protons on the imidazolium ring could not be modulated via different phenyl substituents at the C2-position, a different approach was adopted, leading to the synthesis of **8a** – an analog of **4a** with methylated C4- and C5-positions. In contrast to **4a**, a large cathodic shift in the onset potential for CO_2 reduction was observed when **8a** was employed in the electrolyte. This led to negligible catalytic activity in the working potential range, **Figure 4-8**. Beyond -2.3 V, reduction of **8a** starts to take place, which presumably

leads to undesirable side reactions. The significant inhibition of catalytic activity with the loss of the C4- and C5-protons on the imidazolium ring appears to be consistent with our hypothesis that these protons are likely involved in the stabilization of the CO_2 anion radical intermediate.

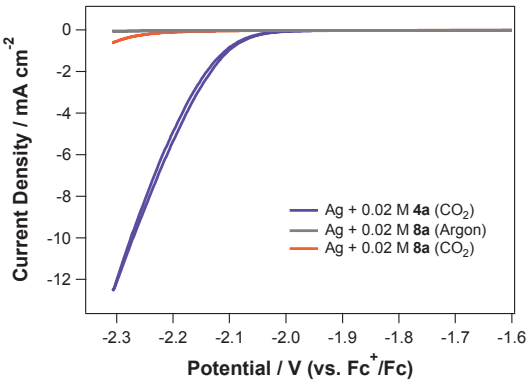

Figure 4-8: **Phenyl-modified imidazolium cations.** Cyclic voltammograms recorded for electrolytes containing **4a** or **8a**. Adapted from Lau and Schreier et al.[19]

That this effect is less pronounced in the case of **3a** suggests that other binding modes, which do not involve the C4- and C5-imidazolium protons, may also exist and play a role, accounting for the residual catalytic activity of **3a**.

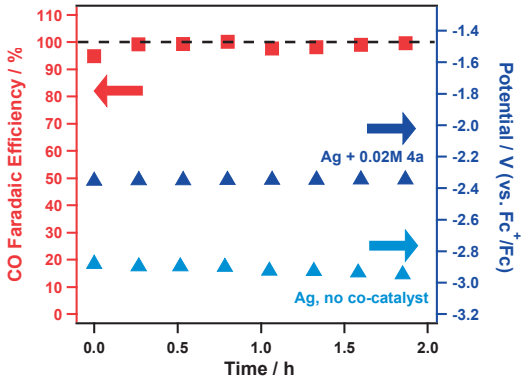

Figure 4-9: **Long term gas product measurements.** CO yields obtained with electrolyte containing 0.02 M **4a** (red squares, left axis) and the operating potential required to maintain 4.2 mA cm^{-2} current density (dark blue triangles, right axis) over the course of 2 hours. To facilitate comparison, the operating potential required to maintain the same current density on a bare Ag electrode without co-catalyst **4a** is also shown (light blue triangles, left axis). Adapted from Lau and Schreier et al.[19]

In order to verify that the irreversible reduction process observed on the voltammogram corresponds to the reduction of CO_2, preparative scale electrolysis

was performed under galvanostatic conditions in the presence and absence of **4a**, with on-line gas sampling, see **Figure 4-9**. On-line gas sampling at regular intervals during the chronopotentiometry (CP) experiment showed CO as the only gaseous product formed during the reaction, with quantitative yields obtained for all the tested compounds. As can be seen in **Figure 4-9**, the addition of **4a** results in a substantial and sustained shift to a more positive operating potential required for maintaining the selected current density, thus demonstrating the efficacy of the co-catalyst. Importantly, high-resolution ^{1}H and ^{13}C NMR spectroscopic analysis of the post-electrolysis electrolyte showed no evidence for the degradation of **4a**, thus affirming its role as a co-catalyst in the reaction. While a number of different pathways have been reported, given the absence of changes to the imidazolium-based co-catalyst, as well as to Bu_4N^+, it is likely that CO_2 serves as oxide acceptor in the reaction, yielding CO_3^{2-} as a by-product.[24–26]

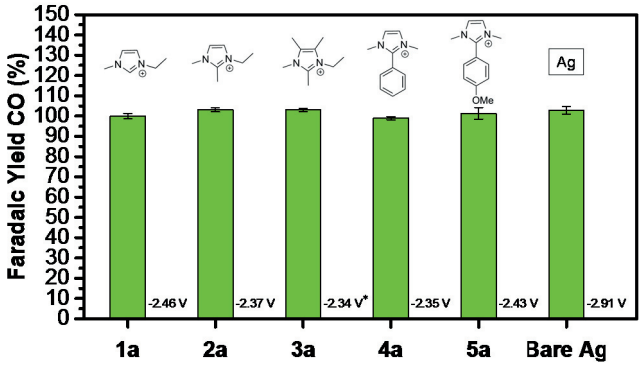

Figure 4-10: **Faradaic yield measurement of different promoters.** Tests were carried out at a Ag electrode in the presence and absence of imidazolium-based co-catalysts (**1a-5a**), at a current density of 4.2 mA cm^{-2}. *Compound **3a** was measured at 2.8 mA cm^{-2} due to its lower activity as described before. Adapted from Lau and Schreier et al.[19]

Gas product analysis was furthermore carried out for the other investigated imidazolium salts, leading to the observation of quantitative production of CO in all cases, as shown in **Figure 4-10**. For species **1a** and **4a**, the analysis was extended to a number of additional potentials, as shown in **Figure 4-11**, leading to the quantitative observation of CO under all the tested conditions. These measurements were carried out in galvanostatic mode using an Ag disk electrode. The data corresponds to the average over 1 to 4 h of continuous electrolysis, with a GC

injection every 15 min. The error bars designate the standard deviation of the measurements obtained. It can be observed that all the analyzed compounds produce quantitative yields in CO and that all co-catalysts led to a substantial and sustained positive shift in the required bias as compared to bare Ag.

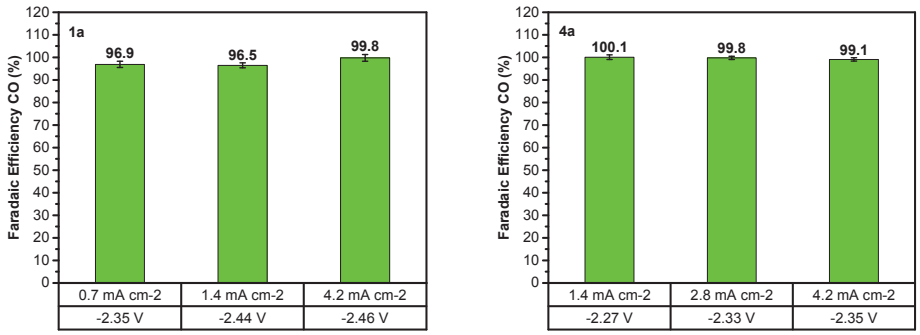

Figure 4-11: **Faradaic efficiency at different current densities.** Gas sampling analysis from electrolysis of CO_2 at different current densities in the presence of compound **1a** (left) and **4a** (right). Data was obtained as described above. It becomes clear that under all conditions, the yield in carbon monoxide is essentially quantitative. Adapted from Lau and Schreier et al.[19]

Conclusion and outlook

A series of structurally related imidazolium salts were prepared and evaluated as co-catalysts for the electrochemical reduction of CO_2 on a silver electrode. It was found that the co-catalytic effect primarily originates from the cation, and that the protons at the C4- and C5-positions are essential for efficient catalysis. Furthermore, our investigations led to the discovery of a novel imidazolium-based co-catalyst, **4a**, that could selectively produce CO with a higher activity than the well-established [EMIM][BF_4] co-catalyst. While the present study serves to highlight an important interaction between CO_2 and the C4- and C5-protons of the imidazolium cation, it must be emphasized that other binding modes for the stabilization of the CO_2 anion radical can be envisioned, and their contribution is likely to depend on the electrochemical system under investigation. Recent research has used computational and advanced spectroscopic techniques to investigate the role of imidazolium ions at the surface of electrodes. A computational study by Nørskov et al. concluded that under experimental conditions, the surface of Ag is covered by imdidazolium.[8] In another study, the same group suggested the presence

of imidazolium to have a significant impact on the electric field at the electrode surface,[27] thereby influencing the reaction kinetics. This seems to correlate with a notable study by Dlott and co-workers using sum frequency generation (SFG) spectroscopy. The authors found that the onset of CO_2 reduction coincided with a structural change of the imidazolium in the double layer as indicated by a change in the parabola of the SFG intensity (**Figure 4-12a**), suggested to lead to a change in local field strength, which was observed in the CO stark shift (**Figure 4-12b**).[18]

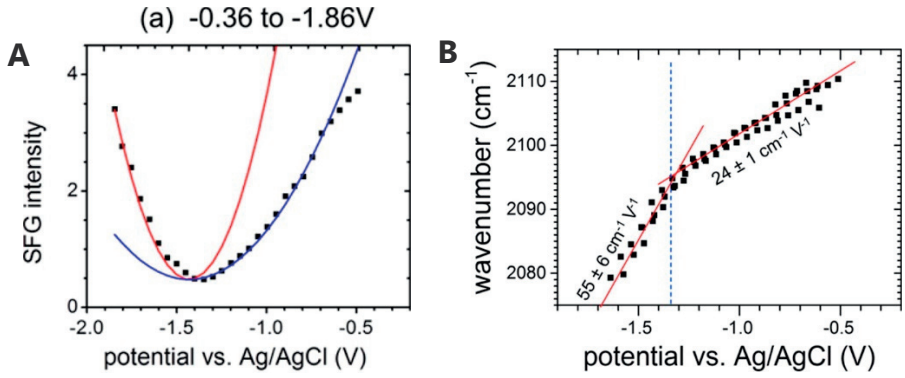

Figure 4-12: **SFG Intensity as function of potential.** (A) Sum frequency generation nonresonant intensity, showing a change in parabolic potential upon changing the bias on the silver electrode. (B) Stark shift observed from surface-adsorbed CO on Ag. Adapted with permission from García Rey et al.[18] Copyright 2015 American Chemical Society.

Further studies by Zhang and co-workers suggested that the role of the imidazolium was not only related to it modifying the double-layer. It was suggested that the imidazolium was electrochemically involved in the reaction and formed a direct adduct with CO_2,[6] however our data does not seem to support this.

These studies point the way to further investigations of the effects observed here. Carrying out SFG spectroscopy studies with C4 and C5 methylated imidazoliums will lead to insights on changes in reorientation and stark shift of the adsorbed CO. Such analysis is urgently needed to gain more understanding on the origin of the changed co-catalytic behavior upon imidazolium methylation. If reorientation is still observed with the modified co-catalyst, this could indicate that specific interactions between the imidazolium and CO are indeed taking place. *In-situ* FTIR and Raman studies could be able to directly identify a CO_2-imdiazolium adduct,

should it be long-lived enough.[28] Finally, computational studies may be able to guide further investigations and are needed.

It is hoped that the findings of the present study will serve as a basis for improved mechanistic understanding and lead to the development of even more efficient co-catalysts for this important reaction. Also, the work in this chapter marks a transition in the thesis toward investigations of electrocatalytically active surfaces as compared to inert electrodes, a trend which is to continue in the following chapters.

Methods

All reagents used were obtained commercially and used as received without further purification unless otherwise stated. Ar (99.9999 %), CO_2 (99.998 %) and He (99.9999 %) were obtained from Carbagas, Switzerland. Compounds **1a**, **1b**, and **1c**, were purchased from Iolitec GmbH, and compound **2a** was purchased from Sigma Aldrich. All imidazolium salts were dried in a 120 °C oven for 20 minutes prior to electrochemical experiments. ^{1}H-NMR spectra, ^{19}F-NMR, and proton-decoupled ^{13}C-NMR spectra were recorded on a Bruker Avance-400 (400 MHz) spectrometer, using Me_4Si as an external standard. ESI-MS were recorded on either a Waters Q-TOF Ultima or a Waters Autopurification system ZQ. High-resolution mass spectra (HR-MS) were recorded on a ThermoFinnigan LCQ Deca XP Plus quadrupole ion-trap instrument. Melting points were determined using a Stuart Scientific melting point apparatus SMP3. Microwave reactions were carried out in a Biotage Initiator+ microwave synthesizer.

Electrochemical measurements

Cyclic voltammetry (CV) measurements were carried out at controlled room temperature (22 °C) using a Gamry Interface 1000 potentiostat and a commercial electrochemical cell (Metrohm). 7 mL of 0.1 M Bu_4NPF_6 (Sigma-Aldrich) in anhydrous acetonitrile (99.9+ %, Extra Dry, Acros) was used as supporting electrolyte and the concentration of imidazolium salt was kept constant at 0.02 M for all tests. Commercial Ag and glassy carbon disk electrodes with a diameter of 3 mm were used as working electrode (Metrohm, Switzerland). Prior to each scan, the electrodes were polished with Al_2O_3 slurry (0.1 micron, Buehler USA 406361006), rinsed with water and dried in a stream of compressed air. An Ag/AgCl quasi-reference electrode was prepared by polarizing an Ag wire (0.5 mm diameter, 99.9 %, Sigma Aldrich) at 2 V against a Pt wire in a solution of 50 mM KCl and 0.1 M HCl for 5 minutes. This electrode was operated behind a ceramic diaphragm (6.1240.020, Metrohm) in supporting electrolyte and calibrated to the Ferrocene/Ferrocenium couple. A Pt wire within a small diameter glass tube was used as counter electrode. In order to keep ohmic losses in the cell constant, care was taken that the components were always at the same position in the cell. Prior

to conducting electrochemical experiments, the imidazolium compounds were dried at 120 °C for 15 min and the solution was sparged with gas for 15 min under stirring. CV scans were recorded at 100 mV/sec. During testing, the headspace of the cell was kept under a flow of gas.

Preparative electrolysis with gas sampling was carried out using a BioLogic SP-300 and a Gamry Interface 1000 potentiostat. Both a custom-made two-compartment test cell (PEEK), as well as a gastight electrochemical glass cell (Metrohm) were used, each with a liquid volume of 10 - 15 mL. The same concentrations of supporting electrolyte and imidazolium salt were used as described in the case of CV experiments. Also, the same working and reference electrode were used. The Pt wire counter electrode was kept in supporting electrolyte behind a glass frit. A mass flow controller (Bronkhorst High-Tech, F201CV) was used to supply CO_2 to the cell. During measurement, CO_2 was sparged at 20 mL min^{-1} and the outflowing gases directed into the sample loop of a gas chromaotraph (GC) (Thermo Trace ULTRA), after evaporated solvent was condensed out at -25 °C. Gas quantification measurements were carried out in galvanostatic mode to allow for better equilibration of the gas concentration in the headspace of the test cell. The gas chromatograph was equipped with a ShinCarbon column (Restek) and a PDD detector (Vici). Helium was used as carrier gas. Injections were carried out every ~15 min and data was reported after reaching equilibrium, commonly 30 min after start. The GC response was calibrated using a certified gas standard in CO_2 (Carbagas). By knowing the flowrate of CO_2, the measured concentration of CO, the current measured at the time of injection, Faraday's constant (96485 C mol^{-1}) and the number of electrons used to synthesize 1 molecule of CO from CO_2 (2), the faradaic efficiency could be calculated.

Compounds were synthesized by Dr. Genevieve Lau and Dmitry Vasilyev as follows:

Synthesis and characterization of compounds 3-9a

Synthesis of 1-ethyl-2,3,4,5-tetramethylimidazolium tetrafluoroborate, ***3a****:*

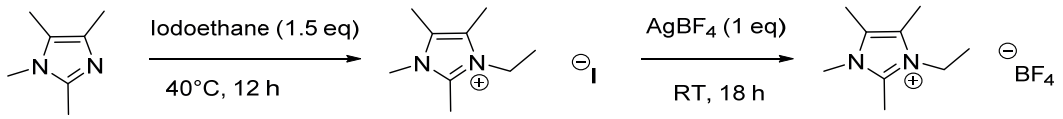

1,2,4,5-tetramethyl-imidazole (0.01 mol, 1.24 g) was reacted with iodoethane (0.015 mol, 2.34 g, 1.5 eq), neat, at 40 °C for 12 hours. The solution was allowed to cool to room temperature, and a yellow solid was obtained. The solid was repeatedly washed with diethyl ether(5 x 20 mL), then recrystallized from acetone to obtain transparent crystals of 1-ethyl-2,3,4,5-tetramethylimidaozlium iodide (Yield = 87 %, 2.44 g). A portion of the iodide salt (0.005 mol, 1.40 g) was reacted with silver tetrafluoroborate (0.005 mol, 0.97 g) in 10 mL of water. The mixture was stirred for 18 hours at room temperature in the dark. The yellow precipitate (AgI) was removed via centrifugation (6000 rpm, 25 minutes). The aqueous phase was transferred to a separating funnel and extracted with 50 mL of dichloromethane. The organic extracts were combined and dried over anhydrous Na_2SO_4. Removal of the solvents under reduced pressure at 40 °C gave **3a** as a colourless solid. Yield: 1.14 g, 95%. Melting point = 80 °C. ^{1}H NMR (400 MHz, DMSO-d_6, δ): 4.11 (q, J = 7.3 Hz, 2H; CH_2), 3.61 (s, 3H; CH_3), 2.60 (s, 3H; CH_3), 2.25 (s, 3H; CH_3), 2.21 (s, 3H; CH_3) 1.24 (t, J = 7.3 Hz, 3H; CH_3); ^{13}C NMR (100 MHz, DMSO-d_6, δ): 142.70, 125.93, 124.59, 32.08, 25.56, 14.98, 9.93, 8.52, 8.23; ^{19}F NMR (376 MHz, DMSO-d_6, δ): -148.29, -148.34; HR-MS (ESI) *m/z*: [cation]$^+$ calcd for $C_9H_{17}N_2$, 153.1386; found, 153.1384; [anion]$^-$ calcd for BF_4, 87.0024; found, 87.0029.

Synthesis of 1,3-dimethyl-2-phenyl-imidazolium tetrafluoroborate, ***4a****:*

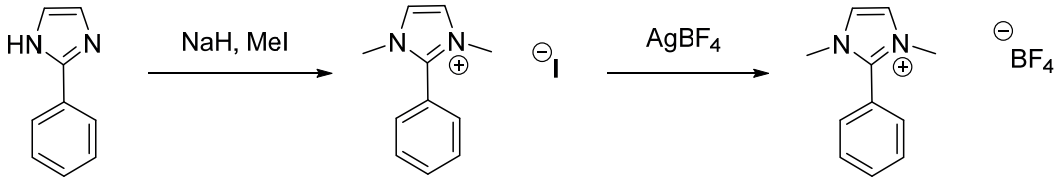

2-phenylimidazole (0.02 mol, 2.88 g) was reacted with NaH (0.08 mol, 1.92 g, 4 eq) in 10 mL of anhydrous tetrahydrofuran (THF). The mixture was stirred for 24 hours under an inert atmosphere at room temperature. Iodomethane (0.06 mol, 8.52 g, 3.74 mL) was added and the mixture was allowed to stir for a further 24 hours. Excess NaH was carefully neutralized by the slow addition of water. The solution was transferred to a separating funnel and extracted with dichloromethane (5 x 25 mL). The combined organic extracts were dried over anhydrous Na_2SO_4 and filtered. Removal of the solvents under reduced pressure at 40 °C gave a yellow residue. The yellow residue was re-dissolved in acetonitrile (approximately 40 mL) and transferred to a 100 mL single-neck round-bottom pressure flask. Iodomethane (0.04 mol, 5.68 g, 2.49 mL) was added to the solution. The flask was sealed with a PTFE plug and allowed to stir at 40 °C for 12 hours. At the end of the reaction, the solvent was reduced to half its original volume using a rotary evaporator and the flask was left at -18 °C for 4 days. Pale yellow crystals (*1,3-dimethyl-2-phenyl-imidazolium iodide*) were obtained after this time and collected via vacuum filtration. The crystals were washed with diethyl ether (4 x 10 mL) and dried under nitrogen for 5 hours. Yield = 5.10 g, 85 %. Melting point = 304 – 306 °C. ^{1}H NMR (400 MHz, DMSO-d_6, δ): 7.89 (s, 2H; Im H), 7.78 – 7.70 (m, 5H; Ar H), 3.70 (s, 6H; CH_3); ^{13}C NMR (100 MHz, DMSO-d_6, δ): 144.62, 132.79, 131.05, 129.88, 123.67, 121.67, 36.20; HR-MS (ESI) *m/z*: [cation]$^+$ calcd for $C_{11}H_{13}N_2$, 173.1073; found, 173.1071; [anion]$^-$ calcd for I, 126.9039; found, 126.9055.

A portion of the iodide salt (*1,3-dimethyl-2-phenyl-imidazolium iodide*) (0.01 mol, 3.00 g) was then reacted with silver tetrafluoroborate (0.01 mol, 1.95 g) in 5 mL of water. The mixture was stirred for 18 hours at room temperature in the dark. The yellow precipitate (silver iodide) was removed via centrifugation (6000 rpm, 25 minutes). The aqueous phase was transferred to a separating funnel and extracted with 50 mL of dichloromethane. The organic extracts were combined and dried over

anhydrous Na_2SO_4. Removal of the solvents under reduced pressure at 40 °C gave the crude product, which was recrystallized from ethanol to yield a white crystalline solid, **4a**. Yield: 2.05 g, 79%. Melting point = 228 °C. ^{1}H NMR (400 MHz, DMSO-d_6, δ): 7.87 (s, 2H; Im H), 7.78 – 7.69 (m, 5H; Ar H), 3.70 (s, 6H; CH_3); ^{13}C NMR (100 MHz, DMSO-d_6, δ): 144.63, 132.80, 131.03, 129.89, 123.67, 121.67, 36.17; ^{19}F NMR (376 MHz, DMSO-d_6, δ): -148.28, -148.33; HR-MS (ESI) *m/z*: $[cation]^+$ calcd for $C_{11}H_{13}N_2$, 173.1073; found, 173.1072; $[anion]^-$ calcd for BF_4, 87.0024; found, 87.0038.

*Synthetic route to obtain compounds **5-7a**:*

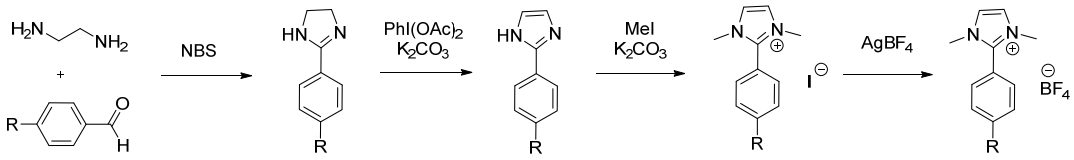

General procedure for the synthesis of 4,5-dihydro-2-arylimidazoles

Ethylenediamine (1.05 eq) was added to an ice-cooled (0°C solution of corresponding aldehyde (1.00 eq) in dry dichloromethane (1.6 ml per mmole) under inert atmosphere (N_2). After stirring for 30 min, N-bromosuccinimide (1.05 eq) was added in three portions and the mixture was left stirring for 18 hours at room temperature. The reaction was quenched with 10 wt % aqueous solution of NaOH (1.05 eq) and left stirring for 5 min. Water (equal volume) was added and the organic layer was separated. The aqueous layer was extracted with dichloromethane (2 x 30 mL). The combined organic fractions were dried over anhydrous Na_2SO_4 and the solvent was removed under reduced pressure. The product was recrystallized from ethyl acetate, affording the corresponding imidazoline as a crystalline solid.

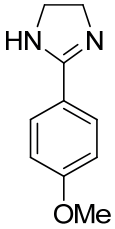

4,5-dihydro-2-(4-methoxyphenyl)imidazole: Yield: 52 %. ^{1}H NMR (400 MHz, $CDCl_3$, δ): 7.82 – 7.65 (m, 2H, Ar H), 6.97 – 6.79 (m, 2H, Ar H), 6.51 (s, 2H), 3.82 (s, 3H, OMe), 3.76 (d, J = 2.0 Hz, 4H, CH_2-N).; ^{13}C NMR (101 MHz, $CDCl_3$, δ): 164.44, 161.65, 128.69, 122.47, 113.78, 55.32, 49.93; mp = 129-130°C.

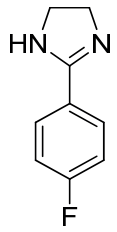

4,5-dihydro-2-(4-fluorophenyl)imidazole: Yield: 52 %. ^{1}H NMR (400 MHz, DMSO-d_6, δ): 7.96 – 7.80 (m, 2H, Ar-H), 7.33 – 7.20 (m, 2H, Ar-H), 6.95 (s, 1H, N-H), 3.60 (s, 4H, CH_2); ^{13}C NMR (101 MHz, DMSO-d_6, δ): 164.91, 163.07, 162.64, 129.88, 127.74, 115.63; ^{19}F NMR (376 MHz, DMSO-d_6, δ): -110.90; mp = 155-156°C.

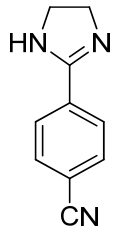

4,5-dihydro-2-(4-cyanophenyl)imidazole: Yield: 52 %. ^{1}H NMR (400 MHz, DMSO-d_6, δ): 8.05 – 7.95 (m, 2H, Ar-H), 7.94 – 7.83 (m, 2H, Ar-H), 7.14 (s, 1H, NH), 3.75 (s, 4H, N-CH_2); ^{13}C NMR (101 MHz, DMSO-d_6, δ): 162.83, 135.20, 132.69, 128.26, 118.96, 113.05, 50.24; mp = 202-203°C.

General procedure for the synthesis of 2-arylimidazoles

(Diacetoxyiodo)benzene (1.1 eq) was added to a suspension of corresponding imidazoline (1.0 eq) and K_2CO_3 (1.1 eq) in DMSO (1.25 ml per mmol) under N_2 atmosphere. The resulting suspension was left stirring for 18 hours at room temperature. The reaction was quenched with a saturated solution of $NaHCO_3$ (aq.) (1.1 eq), and an equivalent volume of ethyl acetate was added. The mixture was stirred for 5 min, and the organic layer was separated. The aqueous fraction was extracted with ethyl acetate (2 x 30 mL). The combined organic fractions were washed with brine, and stirred for 2 hours with anhydrous Na_2SO_4 and activated

charcoal. The mixture was then filtered through celite and the solvent was removed under reduced pressure. The resulting product was purified by recrystallization from ethyl acetate. In the case of *2-(4-methoxyphenyl)-imidazole*, purification via column chromatography (40-63 μm silica, ethyl acetate/hexane (4:1) to pure ethyl acetate) was employed.

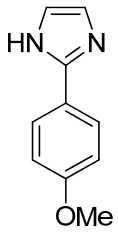

2-(4-methoxyphenyl)-imidazole: Yield: 32 %. ^{1}H NMR (400 MHz, $CDCl_3$, δ): 7.83 – 7.73 (m, 2H, Ar-H), 7.11 (s, 2H, Im-H), 6.98 – 6.88 (m, 2H, Ar-H), 3.83 (s, 3H, OMe); ^{1}H NMR (400 MHz, DMSO-d_6, δ): 7.87 (d, J = 8.5 Hz, 2H, Ar-H), 7.31 – 6.79 (m, 4H, Ar-H +Im-H), 3.79 (s, 3H, OMe); ^{13}C NMR (101 MHz, DMSO-d_6, δ): 159.54, 146.08, 126.66, 124.23, 114.53, 55.62; mp = 158-160°C; HRMS (ESI) *m*/*z*: $[M + H]^+$ calcd for $C_{10}H_{10}N_2O$: 175.0793; found, 175.0871.

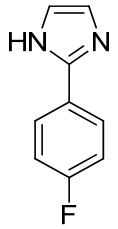

2-(4-fluorophenyl)-imidazole: Yield: 49 %. ^{1}H NMR (400 MHz, DMSO-d_6, δ): 8.17 – 7.83 (m, 2H, Ar-H), 7.47 – 7.14 (m, 3H, Ar-H +Im-H), 7.16 – 6.90 (m, 1H, Im-H); ^{13}C NMR (101 MHz, DMSO-d_6, δ): 163.52, 161.09, 145.19, 129.40, 128.02, 127.99, 127.31, 127.23, 118.17, 116.20, 115.98; ^{19}F NMR (376 MHz, DMSO-d6, δ): -114.05; mp = 194-195°C.

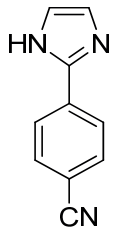

2-(4-cyanophenyl)-imidazole: Yield: 45 %. ^{1}H NMR (400 MHz, DMSO-d_6, δ): 8.18 – 8.04 (m, 2H, Ar-H), 7.97 – 7.85 (m, 2H, Ar-H), 7.38 (s, 1H, Im-H), 7.13 (s, 1H,

Im-H); ^{13}C NMR (101 MHz, DMSO-d_6, δ): 144.35, 135.24, 133.27, 125.62, 119.66, 119.32, 110.36; mp = 193-195°C.

General procedure for the synthesis of 2-arylimidazolium iodides

Iodomethane (5 eq) was added to a suspension of corresponding 2-arylimidazole (1 eq) and K_2CO_3 (2 eq) in acetonitriile (3.5 ml per mmol) under inert atmosphere (N_2). The reaction mixture was refluxed for 24 hrs. The mixture was allowed to cool to room temperature, filtered through a glass frit, and concentrated in vacuo. The residue was re-dissolved in dichloromethane and filtered through celite. The solvent was removed in vacuo, and the resulting product was washed with diethyl ether, yielding pure iodide salt.

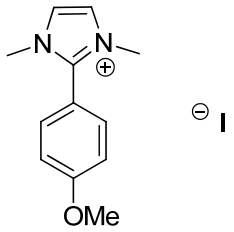

1,3-dimethyl-2-(4-methoxyphenyl)-imidazolium iodide: . Yield: 96 %. ^{1}H NMR (400 MHz, $CDCl_3$, δ): 7.81 (s, 2H, Im-H), 7.68 – 7.63 (m, 2H, Ar-H), 7.14 – 7.08 (m, 2H, Ar-H), 3.88 (s, 3H, OMe), 3.84 (s, 6H, Me); ^{13}C NMR (101 MHz, $CDCl_3$, δ): 162.84, 145.11, 132.53, 123.46, 115.45, 111.95, 55.75, 36.90; HRMS (ESI) *m*/*z*: [Cation]$^+$ calcd for $C_{12}H_{15}N_2O^+$: 203.1179; found: 203.1188; [Anion]$^-$ calcd for I^-: 126.9050; found: 126.9045.

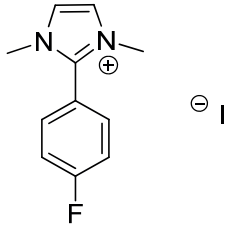

1,3-dimethyl-2-(4-fluorophenyl)-imidazolium iodide: Yield: 96 %. ^{1}H NMR (400 MHz, DMSO-d_6, δ): 7.88 (m, 4.6 Hz, 4H, Ar-H+Im-H), 7.68 – 7.50 (m, 2H, Ar-H), 3.69 (s, 6H, Me); ^{13}C NMR (101 MHz, DMSO-d_6, δ): 143.83, 134.09, 134.00, 123.67, 117.31, 117.09, 91.68, 36.15; ^{19}F NMR (376 MHz, DMSO-d6, δ): -106.94; mp = 250°C (dec); HRMS (ESI) *m*/*z*: [Cation]$^+$ calcd for $C_{11}H_{12}FN_2^+$: 191.0979; found: 191.0983; [Anion]$^-$ calcd for I^-: 126.9050; found: 126.9045.

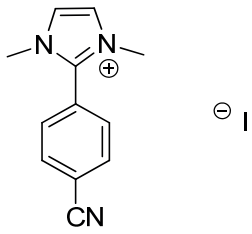

1,3-dimethyl-2-(4-cyanophenyl)-imidazolium iodide: Yield: 95%. ^{1}H NMR (400 MHz, DMSO-d_6, δ): 8.25 – 8.18 (m, 2H, Ar-H), 8.08 – 8.02 (m, 2H, Ar-H), 7.95 (d, J = 1.2 Hz, 2H, Im-H), 3.72 (s, 6H, Me); ^{13}C NMR (101 MHz, DMSO-d_6, δ): 142.92, 133.62, 132.39, 126.14, 124.15, 118.36, 115.29, 36.34; mp = 211°C (dec); HRMS (ESI) *m*/*z*: [Cation]$^{+}$ calcd for $C_{12}H_{12}N_3^{+}$: 198.1026; found: 198.1030; [Anion]$^{-}$ calcd for I^{-}: 126.9050; found: 126.9042.

General procedure for the synthesis of 2-arylimidazolium tetrafluoroborates

Corresponding 2-arylimidazolium iodide (1 eq) was mixed with $AgBF_4$ (1 eq) in water (5 mL). The reaction mixture was stirred for 18 hours in the dark, after which the mixture was filtered through celite. The celite plug was washed with ethanol. The solvent was removed under reduced pressure, and the product was recrystallized from ethanol.

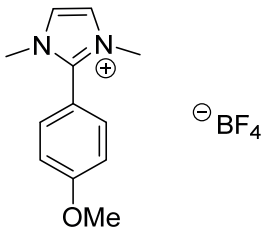

1,3-dimethyl-2-(4-methoxyphenyl)-imidazolium tetrafluoroborate, ***5a***: . Yield: 50 %. ^{1}H NMR (400 MHz, DMSO-d_6, δ): 7.83 (s, 2H, Im-H), 7.76–7.63 (m, 2H, Ar-H), 7.30–7.18 (m, 2H; Ar-H), 3.89 (s, 3H; O-CH3), 3.68 (s, 6H, Me); ^{13}C NMR (101 MHz, DMSO-d_6, δ): 162.47, 144.81, 132.73, 123.42, 115.38, 113.26, 56.09, 36.08; ^{19}F NMR (376 MHz, DMSO-d_6, δ): -148.30, -148.35; mp = 121-122°C; HRMS (ESI) *m*/*z*: [Cation]$^{+}$ calcd for $C_{12}H_{15}N_2O^{+}$: 203.1179; found: 203.1184; [Anion]$^{-}$ calcd for BF_4^{-}: 87.0035; found: 87.0023.

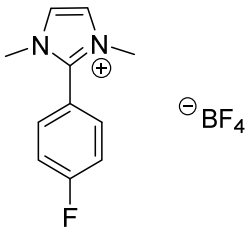

1,3-dimethyl-2-(4-fluorophenyl)-imidazolium tetrafluoroborate, ***6a***: . Yield: 52 %. ^{1}H NMR (400 MHz, DMSO-d$_6$, δ): 7.96–7.78 (m, 4H, Ar-H+Im-H), 7.66–7.49 (m, 2H, Ar-H), 3.69 (s, 6H, Me); ^{13}C NMR (101 MHz, DMSO-d$_6$, δ): 165.92, 163.42, 143.87, 134.04, 133.95, 123.68, 118.11, 118.08, 117.31, 117.09, 36.10; ^{19}F NMR (376 MHz, DMSO-d$_6$, δ): -106.93, -148.31, -148.37; mp = 231-232°C; HRMS (ESI) *m*/*z*: [Cation]$^+$ calcd for $C_{11}H_{12}FN_2^+$: 191.0979; found: 191.0984; [Anion]$^-$ calcd for BF_4^-: 87.0035; found: 87.0029.

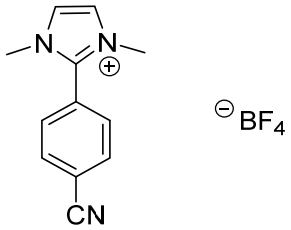

1,3-dimethyl-2-(4-cyanophenyl)-imidazolium tetrafluoroborate, ***7a***: . Yield: 57 %. ^{1}H NMR (400 MHz, DMSO-d$_6$, δ): 8.33–8.15 (m, 2H, Ar-H), 8.11–7.96 (m, 2H, Ar-H), 3.71 (s, 6H, Me); ^{13}C NMR (101 MHz, DMSO-d6, δ): 142.96, 133.63, 132.28, 126.18, 118.36, 115.34, 36.20; ^{19}F NMR (376 MHz, DMSO-d$_6$, δ): -148.33, -148.38; mp = 151-152°C; HRMS (ESI) *m*/*z*: [Cation]$^+$ calcd for $C_{12}H_{12}N_3^+$: 198.1026; found: 198.1031; [Anion]$^-$ calcd for BF_4^-: 87.0035; found: 87.0023.

Synthesis of 1,3,4,5-tetramethyl-2-phenyl-imidazolium tetrafluoroborate ***8a****:*

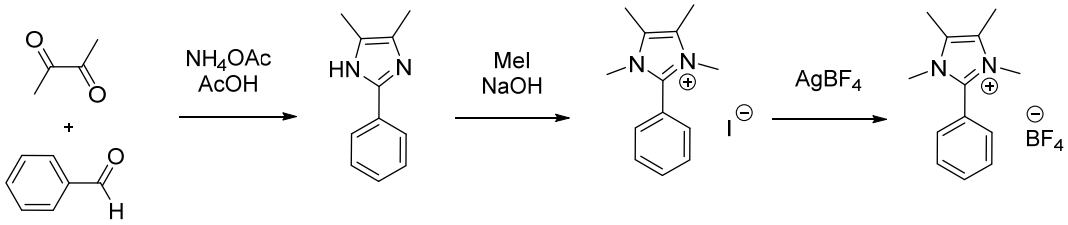

2,3-butadiaone (0.26 mL, 0.003 mol), benzaldehyde (0.30 mL, 0.003 mol), and ammonium acetate (2.31 g, 0.03 mol) were dissolved in 15 mL of acetic acid. The solution was then transferred to a 20 mL microwave reaction vial containing a magnetic stirrer bar. The reaction vial was sealed and heated in a microwave reactor

for 5 minutes at 180 °C, after which it was cooled to 30 °C and removed from the reactor. The reaction mixture was transferred dropwise to an ice cold solution of 25 % aqueous NH_4OH (50 mL). The aqueous solution was then extracted with ethyl acetate (4 x 20 mL), dried over anhydrous Na_2SO_4, and concentrated on a rotary evaporator to obtain a brown solid (2-phenyl-4,5-dimethyl-imidazole). The brown solid was then transferred to a 100 mL single-neck round-bottomed pressure flask. Sodium hydroxide (0.48 g, 0.012 mol), iodomethane (1.3 mL, 0.02 mol) and a solution of acetonitrile/methanol (1:1) (25 mL) were added, and the flask was sealed with a PTFE plug. The solution was heated in an oil bath at 50 °C for 12 hours. At the end of the reaction, the organic solvents were removed under reduced pressure and replaced with 30 mL of distilled water. The aqueous solution was extracted with dichloromethane (4 x 20 mL) and dried over anhydrous Na_2SO_4. The solvent was removed under reduced pressure and an orange solid was obtained. The solid was recrystallized twice from ethanol to obtain a pale-white solid (1,3,4,5-tetramethyl-2-phenyl-imidazolium iodide). A portion of the iodide salt (0.39 g, 0.0012 mol) was then mixed with $AgBF_4$ (0.23 g, 0.0012 mol) in 5 mL of distilled water, and allowed to stir at room temperature for 18 hours in the dark. The yellow precipitate (AgI) formed during the reaction was removed via centrifugation (6000 rpm, 25 mins) and the solvent was removed under reduced pressure at 40 °C. The crude product was then recrystallized from ethanol to yield **8a** as an off-white solid. Overall yield: 32 %, 0.277 g. Melting point: 117 °C; ^{1}H NMR (400 MHz, $CDCl_3$, δ): 7.73-7.56 (m, 5H; Ar H), 3.56 (s, 6H; CH_3), 2.34 (s, 6H; CH_3); ^{13}C NMR (100 MHz, $CDCl_3$, δ): 143.21, 132.34, 130.49, 129.80, 127.06, 122.04, 32.77, 8.70; ^{19}F NMR (376 MHz, $CDCl_3$, δ): -154.98, -155.03; HRMS (ESI) *m*/*z*: [cation]$^+$ calcd for $C_{13}H_{17}N_2$, 201.1420; found, 201.1383; [anion]$^-$ calcd for BF_4, 87.0024; found, 87.0031.

References

1. Singh, M. R., Kwon, Y., Lum, Y., Ager, J. W. & Bell, A. T. Hydrolysis of Electrolyte Cations Enhances the Electrochemical Reduction of CO_2 over Ag and Cu. *J. Am. Chem. Soc.* **138,** 13006–13012 (2016).
2. Murata, A. & Hori, Y. Product Selectivity Affected by Cationic Species in Electrochemical Reduction of CO_2 and CO at a Cu Electrode. *Bull. Chem. Soc. Jpn.* **64,** 123–127 (1991).
3. Thorson, M. R., Siil, K. I. & Kenis, P. J. A. Effect of Cations on the Electrochemical Conversion of CO_2 to CO. *J. Electrochem. Soc.* **160,** F69–F74 (2013).
4. Yoshihara, N., Arita, M. & Noda, M. Electrolyte Dependence for the Electrochemical CO_2 Reduction Activity on Cu(111) Electrodes. *Chem. Lett.* **46,** 125–127 (2017).
5. Rosen, B. A. *et al.* Ionic Liquid–Mediated Selective Conversion of CO_2 to CO at Low Overpotentials. *Science* **334,** 643–644 (2011).
6. Zhao, S.-F., Horne, M., Bond, A. M. & Zhang, J. Is the Imidazolium Cation a Unique Promoter for Electrocatalytic Reduction of Carbon Dioxide? *J. Phys. Chem. C* **120,** 23989–24001 (2016).
7. Niu, D., Wang, H., Li, H., Wu, Z. & Zhang, X. Roles of ion pairing on electroreduction of carbon dioxide based on imidazolium-based salts. *Electrochimica Acta* **158,** 138–142 (2015).
8. Urushihara, M., Chan, K., Shi, C. & Nørskov, J. K. Theoretical Study of EMIM+ Adsorption on Silver Electrode Surfaces. *J. Phys. Chem. C* **119,** 20023–20029 (2015).
9. Sun, L., Ramesha, G. K., Kamat, P. V. & Brennecke, J. F. Switching the Reaction Course of Electrochemical CO_2 Reduction with Ionic Liquids. *Langmuir* **30,** 6302–6308 (2014).
10. Salehi-Khojin, A. *et al.* Nanoparticle Silver Catalysts That Show Enhanced Activity for Carbon Dioxide Electrolysis. *J. Phys. Chem. C* **117,** 1627–1632 (2013).
11. Medina-Ramos, J., DiMeglio, J. L. & Rosenthal, J. Efficient Reduction of CO_2 to CO with High Current Density using in-situ or ex-situ Prepared Bi-based Materials. *J. Am. Chem. Soc.* **136,** 8361–8367 (2014).
12. DiMeglio, J. L. & Rosenthal, J. Selective Conversion of CO_2 to CO with High Efficiency Using an Inexpensive Bismuth-Based Electrocatalyst. *J. Am. Chem. Soc.* **135,** 8798–8801 (2013).
13. Asadi, M. *et al.* Robust carbon dioxide reduction on molybdenum disulphide edges. *Nat. Commun.* **5,** 4470 (2014).
14. Matsubara, Y., Grills, D. C. & Kuwahara, Y. Thermodynamic Aspects of Electrocatalytic CO_2 Reduction in Acetonitrile and with an Ionic Liquid as Solvent or Electrolyte. *ACS Catal.* **5,** 6440–6452 (2015).
15. Zhou, F. *et al.* Highly selective electrocatalytic reduction of carbon dioxide to carbon monoxide on silver electrode with aqueous ionic liquids. *Electrochem. Commun.* **46,** 103–106 (2014).
16. Wang, Y. *et al.* Activation of CO_2 by ionic liquid EMIM–BF_4 in the electrochemical system: a theoretical study. *Phys. Chem. Chem. Phys.* **17,** 23521–23531 (2015).
17. Rosen, B. A. *et al.* In Situ Spectroscopic Examination of a Low Overpotential Pathway for Carbon Dioxide Conversion to Carbon Monoxide. *J. Phys. Chem. C* **116,** 15307–15312 (2012).
18. García Rey, N. & Dlott, D. D. Structural Transition in an Ionic Liquid Controls CO_2 Electrochemical Reduction. *J. Phys. Chem. C* **119,** 20892–20899 (2015).
19. Lau, G. P. S. *et al.* New Insights Into the Role of Imidazolium-Based Promoters for the Electroreduction of CO_2 on a Silver Electrode. *J. Am. Chem. Soc.* **138,** 7820–7823 (2016).
20. Maiti, A., Kumar, A. & Rogers, R. D. Water-clustering in hygroscopic ionic liquids—an implicit solvent analysis. *Phys. Chem. Chem. Phys.* **14,** 5139–5146 (2012).
21. Schreier, M. *et al.* Efficient and selective carbon dioxide reduction on low cost protected Cu_2O photocathodes using a molecular catalyst. *Energy Env. Sci* **8,** 855–861 (2015).
22. Oh, Y. & Hu, X. Ionic liquids enhance the electrochemical CO_2 reduction catalyzed by MoO_2. *Chem. Commun.* **51,** 13698–13701 (2015).
23. Wang, Y. *et al.* Activation of CO_2 by ionic liquid EMIM–BF_4 in the electrochemical system: a theoretical study. *Phys. Chem. Chem. Phys.* **17,** 23521–23531 (2015).

24. Amatore, C. & Saveant, J. Mechanism and Kinetic Characteristics of the Electrochemical Reduction. *J. Am. Chem. Soc.* **103,** 5021–5023 (1981).
25. Bolinger, C. M. *et al.* Electrocatalytic reduction of CO_2 based on polypyridyl complexes of rhodium and ruthenium. *J. Chem. Soc., Chem. Commun.* **12,** 796–797 (1985).
26. Gennaro, A. *et al.* Mechanism of the electrochemical reduction of carbon dioxide at inert electrodes in media of low proton availability. *J. Chem. Soc., Faraday Trans.* **92,** 3963–3968 (1996).
27. Chen, L. D., Urushihara, M., Chan, K. & Nørskov, J. K. Electric Field Effects in Electrochemical CO_2 Reduction. *ACS Catal.* **6,** 7133–7139 (2016).
28. Santos, V. O., Leite, I. R., Brolo, A. G. & Rubim, J. C. The electrochemical reduction of CO2 on a copper electrode in 1-n-butyl-3-methyl imidazolium tetrafluoroborate (BMI.BF4) monitored by surface-enhanced Raman scattering (SERS). *J. Raman Spectrosc.* **47,** 674–680 (2016).

5 PHOTOSYNTHESIS OF CARBON MONOXIDE FROM CO_2 USING PEROVSKITE PHOTOVOLTAICS AND WATER AS ELECTRON SOURCE

The chapter is adapted with permission from the peer-reviewed publication: ***Marcel Schreier****, Laura Curvat, Fabrizio Giordano, Ludmilla Steier, Antonio Abate, Shaik M Zakeeruddin, Jingshan Luo, Matthew T Mayer, Michael Grätzel. Nature Communications, 2015, vol. 6, 7326.*

The studies introduced in the previous chapters have been carried out in nonaqueous electrolytes. The anode reaction in such systems is not sustainable and involves the decomposition of electrolyte constituents. To enable the sustainable conversion of CO_2 into CO and O_2, water has to be used as an electron source, in combination with a CO_2 reduction catalyst that is able to suppress the competing hydrogen evolution reaction. In this chapter, gold and iridium oxide were used as cathode and anode, respectively, in a water based electrolyte and driven by three methylammonium lead halide perovskite solar cells, setting the world record for the solar-driven splitting of CO_2 into CO and O_2.

Introduction

The studies presented in the previous chapters led to very relevant insights into the charge transfer dynamics at semiconductor interfaces, showed substantial novelty in the design of hybrid homogeneous-heterogeneous CO_2 reduction devices and led to the discovery of new mechanistic parameters for the CO_2 reduction with imidazolium based co-catalysts. However, these studies suffer, as do most studies carried out in nonaqueous electrolytes, from involving an uncontrolled anode reaction, which entails the irreversible oxidation of the electrolyte to serve as an electron source for CO_2 reduction. As a consequence, devices operating under these conditions are intrinsically unsustainable for prolonged use. Also, in both photo-driven systems the light contributes only part of the total energy and a large additional bias voltage is required for the reaction to take place. The present chapter is dedicated to solving these two problems, thereby achieving an efficient and unassisted device, able to effectuate the solar-driven reduction of CO_2 without requiring an additional bias voltage.

As described before, "artificial photosynthesis",[1] has been mainly directed toward sunlight-driven splitting of water to generate H_2 and O_2, and solar-to-hydrogen energy conversion efficiencies up to 30% have been demonstrated.[2–5] Producing oxygen and hydrogen from water benefits from the substrate (H_2O, H^+ or OH^-) to be present in very large concentration in the electrolyte. Furthermore, unless exotic electrolytes are being employed or the electrodes are corroding, the resulting current corresponds to the production of H_2 and O_2. No selectivity issues are therefore encountered and only limited product characterization is required. The same consideration is largely true for the electroreduction of CO_2 in stable nonaqueous solvents, which makes them an excellent choice for studies carried out predominantly using potentiodynamic measurements, as is the case for **Chapter 2**, **3** and **4**. However, a complete process for the light-driven synthesis of carbon monoxide must be based on a sustainable and balanced reaction, consuming only CO_2. To match the reduction of CO_2 at the cathode, an oxidation reaction must occur at the anode, which supplies the electrons consumed in the reduction and regenerates the protons used to accept oxygen from CO_2. Combustion of a fuel

involves its reaction with O_2, leading to CO_2 and H_2O. The only sustainable anode process for fuel production, enabling a closed cycle, is therefore the oxidation of water to lead to the production of oxygen. To tackle this challenge, in contrast to the studies in the previous chapters, an aqueous system is employed here, where water oxidation leads to the evolution of oxygen and continuously provides a proton source to accept oxygen from CO_2, leading to the reactions defined by **Equation 5-4**.

Reactions	**Standard electrode potentials (V vs. RHE*)**	
CO_2 (g) + 2 H^+ + 2 e^- ↔ CO (g) + H_2O (l)	–0.11	(Eq. 5-1a)
H_2O ↔ ½ O_2 (g) + 2 H^+ + 2 e^-	+1.23	(Eq. 5-2b)
CO_2 (g) ↔ CO (g) + ½ O_2 (g)	ΔE = 1.34 V	(Eq. 5-3c)

* RHE: reversible hydrogen electrode

Equation 5-4: **Sustainable electrolysis of CO_2 into CO and O_2 in the presence of water.** The electrochemical cathode (top) and anode reactions (bottom) lead to the overall transformation shown below the line.

While providing an abundant source of electrons, carrying out CO_2 reduction in aqueous solutions leads to a number of new challenges which complicate the experimental setup. The substrate for the cathode reaction, dissolved CO_2, is present at only 34 mmol L^{-1} at 25°C and 1 atm,[6] which is small compared to the substrates for the hydrogen evolution reaction. This leads to hydrogen evolution being a constant accompanying effect of CO_2 reduction in aqueous environments. For successful reduction of CO_2 in an aqueous electrolyte to be possible, the employed electrode material has to exhibit good selectivity for reducing CO_2, which is only the case for few elements and leads to substantial requirements with respect to the cleanliness of all system components, as many common impurities can enhance the hydrogen evolution reaction.[7] Furthermore, the presence of a hydrogen source extends the spectrum of products obtainable from reducing CO_2 to all species involving carbon, hydrogen and oxygen. As a consequence, electrochemical measurements can no longer provide much insight into the electrocatalytic processes which are taking place. Reactions in aqueous electrolytes therefore require comprehensive characterization of the liquid and gaseous reaction products.

The combination of these effects makes sunlight-driven CO_2 reduction difficult to achieve a desirable product with high efficiency,[8] a challenge which is addressed in this chapter with the help of metal halide perovskite solar cells.

The emergence of metal halide perovskites has attracted great attention in the photovoltaic community due to a combination of advantages, such as low-cost synthesis, abundant materials, and rapidly climbing efficiencies, presently certified at 21%, competing with the commercially available silicon solar cells.[9–11]

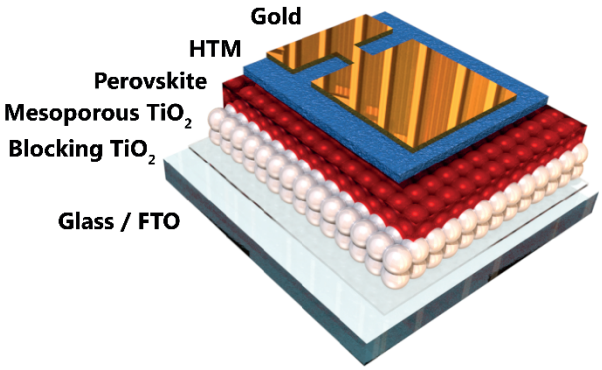

Figure 5-1: **Schematic of a perovskite solar cell.** The stucture is deposited on a conductive glass slide, followed by a blocking and a mesoporous TiO_2 layer. The organic-inorganic perovskite is deposited on top and into the mesoporous layer, followed by a hole transport material and a counter electrode. The device is illuminated from the bottom. *own work*

Perovskite solar cells in their simplest realization, are based on methylammonium lead iodide, a hybrid organic-inorganic semiconductor with the chemical structure $CH_3NH_3PbI_3$. This material, which has a direct bandgap of 1.55 eV[9] is deposited in and onto a mesoporous TiO_2 scaffold to serve as a light absorber. In addition to its high extinction coefficient, it has very beneficial properties to serve as a light absorber for photovoltaic applications, including a weak exciton binding energy, leading to the rapid separation of charges and high carrier mobility for both electrons and holes.[9,12] A typical device architecture is shown in **Figure 5-1** and a large number of designs are currently being investigated. Very notable progress has also been made in recent months on the stability of the resulting cells.[13] Perovskite solar cells tend to exhibit a good utilization of their bandgap, getting close to the entropic limit, and leading to very high open circuit voltages.[14]

Building on their high voltage properties, in collaboration with colleagues, I was able to demonstrate a simple system, achieving a striking 12.3% solar to hydrogen efficiency by the use of perovskite photovoltaics, thereby showing a promising path toward the realization of high-efficiency solar-to-fuel conversion devices.[3]

Here, extending this work in an attempt to get closer to carbon-based photosynthesis and taking advantage of the high open-circuit voltage of perovskite photovoltaics, the efficient reduction of CO_2 to carbon monoxide (CO) is being investigated, driven solely by simulated sunlight and using water as the electron source.

The production of CO from CO_2 requires 259 kJ mol^{-1} of free energy (22 kJ mol^{-1} greater than water electrolysis), corresponding to a voltage of 1.34 V. However, both the cathodic and anodic half reactions suffer significant kinetic overpotentials (η) which must be overcome to drive the reaction at meaningful rates. These overpotentials depend largely on the nature of the electrodes, and on the constraint that electrochemical CO_2 reduction must be performed at near-neutral pH, as discussed below. Gold (Au) is known to be the best catalyst in terms of overpotential for selective cathodic CO evolution.[7,15] However, a number of different products can be generated by reduction processes on Au, including hydrogen from aqueous proton reduction. This creates a potential-dependent product selectivity, which must be accounted for when defining the cathode operating potential. Substantial progress has been made by the group of Matthew Kanan, through the electrochemical oxidation and subsequent reduction of gold to serve as a CO_2 reduction catalyst, leading to substantial improvements in both overpotential and selectivity.[16] This material was therefore chosen to serve as a CO-producing cathode in this study.

On the anode side, iridium oxide (IrO_2) is known to be a top performer for the oxygen evolution reaction, but suffers an overpotential increase in near-neutral conditions.[17] As represented schematically in **Figure 5-2** and described below, considering the thermodynamic voltage and the overpotentials for both electrodes, a voltage of at least 2 V is demanded to drive efficient and selective CO evolution from CO_2.

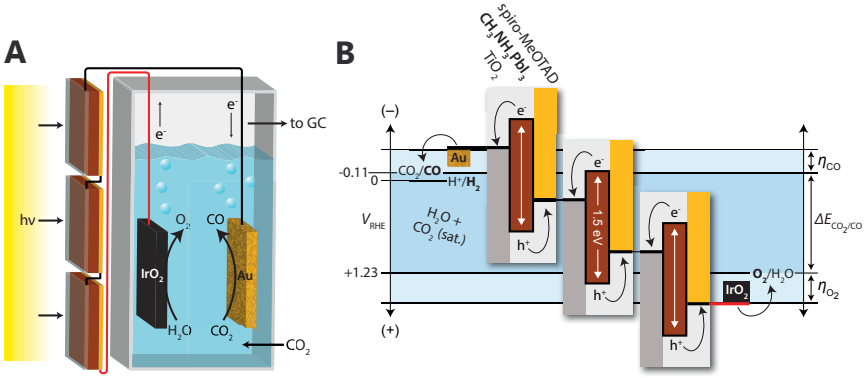

Figure 5-2: **Sunlight-driven CO_2 reduction device**. (A) Schematic of the device combining photovoltaics with an electrochemical cell. (B) Generalized energy diagram for converting CO_2 into CO with three perovskite solar cells. The series connected photovoltaics produce a voltage sufficient to overcome the sum of the reaction free energy (ΔE) and the reaction overpotentials (η) at the electrodes. Adapted from Schreier et al.[18]

Results and Discussion

Preparation and characterization of catalyst electrodes

To achieve the best possible performance from Au, oxidized cathodes were prepared by electrochemical anodization as mentioned above.[16] After exposure to reaction conditions and reduction, these electrodes exhibit a highly porous structure of metallic Au with an increased surface area (**Figure 5-3a**) and XRD analysis showed the successful transformation of Au_2O_3 into metallic gold (**Figure 5-3b**). The electrocatalytic performance of this material was assessed at various potentials in a three-electrode configuration in CO_2-saturated 0.5 M $NaHCO_3$ aqueous electrolyte (pH 7.2), and gas chromatography analysis was performed in situ to monitor the product. In **Figure 5-4a**, the cathodic current density and Faradaic efficiency of CO production are reported as a function of electrode potential versus the reversible hydrogen electrode (RHE). Carbon monoxide production starts to be observed at 90 mV overpotential (-0.20 V vs RHE), confirming the impressive activity of gold toward this reaction. The CO selectivity peaks at around -0.4 V vs RHE, exceeding 90% Faradaic efficiency toward CO, then decreases again at more negative potentials. The remaining balance of current primarily goes to the reduction of aqueous protons to generate hydrogen. Due to this potential-dependent

product selectivity, an effective overpotential for optimal CO yield is around 300 mV on this cathode.

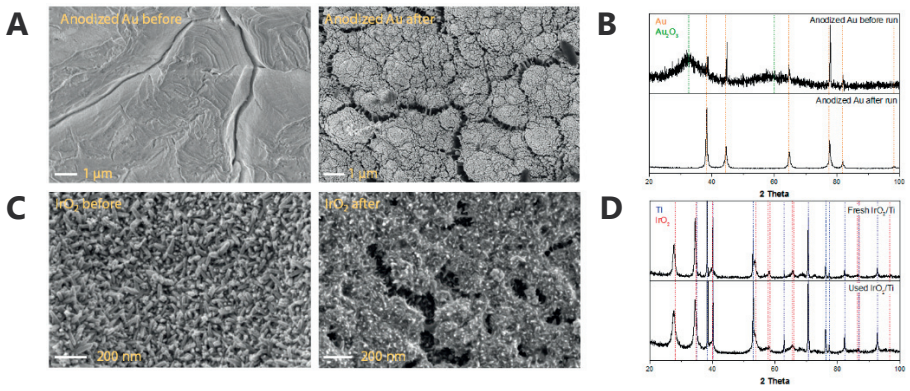

Figure 5-3: **SEM micrographs and XRD analysis of anodized Au cathodes and IrO_2 anodes before and after CO_2 photolysis.** (A) During the photolysis experiment, the anodized Au cathodes develop a highly porous structure. (B) Anodized Au cathodes. It can clearly be seen that anodization of gold has led to Au_2O_3 which is entirely reduced to metallic Au during the photolysis experiment. Au reference from JCPDS card #04-0784. Au_2O_3 reference from [2]. (C) The structure of the IrO_2 anodes stays relatively similar before and after operation. (D) The presence of IrO_2 can be seen from the diffraction pattern. Only few differences are observed before and after testing, confirming the impressive stability of anodes based on IrO_2. Ti reference from JCPDS card #44-1294, IrO_2 reference from JCPDS card #15-0870. Weak lines were omitted for clarity. Adapted from Schreier et al.[18]

As mentioned above, aqueous carbon dioxide reduction processes are constrained to near-neutral environments. This is because in acid, most known CO_2 reduction catalysts favor H_2 evolution over reducing carbon dioxide, whereas in base, dissolved CO_2 spontaneously converts to carbonate, which is unreactive as a substrate in electrochemical CO evolution.[15] In a complete system, the anode and cathode must be operated in the same solution to avoid introducing chemical bias based on concentration gradients, masking the true operating voltage. Commonly, CO_2 reduction is carried out in aqueous bicarbonate electrolytes, which, upon saturation with CO_2, results in a solution buffered at pH 7.2. This presents a challenge for the anodic reaction, since although many electro-catalysts have demonstrated high catalytic activity toward the oxygen evolution reaction,[17] they are typically most efficient in either strongly alkaline or acidic solutions. Oxygen evolution from near-neutral solutions has received less attention,[19,20] but nonetheless plays an important role in complete CO_2 reduction cells. In an ideal

case, an oxygen evolution catalyst should be selected which is based on low cost and earth abundant materials. However, since experiments with anode materials based on nickel-iron layered double hydroxides (NiFeLDH) led to poisoning of the Au cathode (**Figure 5-5**), IrO_2 was selected as anode material here because of its great stability and excellent performance toward the oxygen evolution reaction.[17]

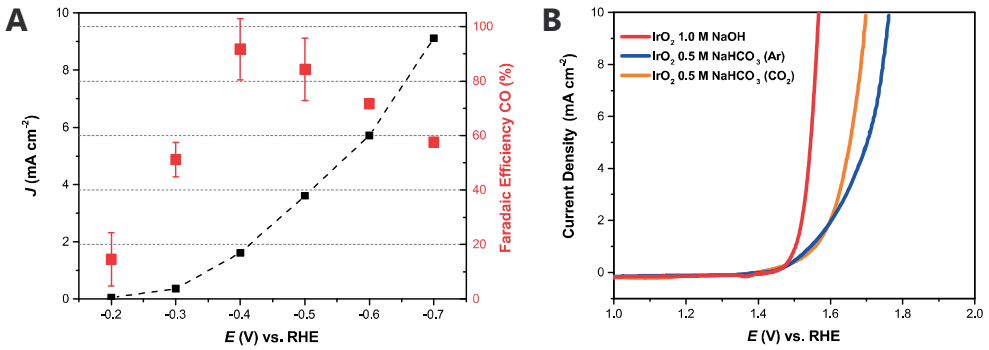

Figure 5-4: **Characterization of CO_2 reduction and H_2O oxidation electrodes.** (A) Electrochemical performance and Faradaic efficiency toward CO production of oxidized Au electrodes in CO_2-saturated aqueous solution of 0.5 M $NaHCO_3$. Error bars correspond to the standard deviation of repeated gas measurements. (B) Electrochemical performance of IrO_2 toward water oxidation in solutions of 1.0 M NaOH and 0.5 M $NaHCO_3$ under Ar and CO_2 saturation, respectively. Adapted from Schreier et al.[18]

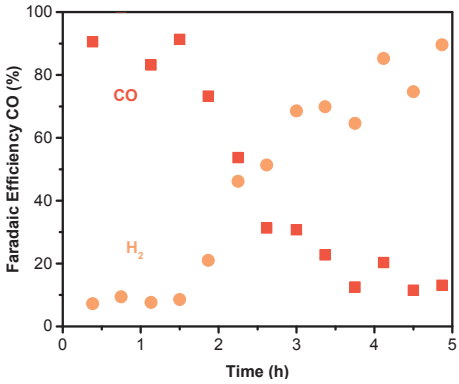

Figure 5-5: **Early test of the solar-driven operation of an oxide-derived Au catalyst combined with a NiFeLDH anode.** The rapid decrease of the production of CO in favor of almost quantitative production of H_2 can be observed. Adapted from Schreier et al.[18]

IrO_2 electrodes were prepared by thermal decomposition of H_2IrCl_6 on Ti foil, resulting in the structure and XRD pattern shown in **Figure 5-3c** and **Figure 5-3d**, respectively. Current-voltage curves are shown in **Figure 5-4b**. In alkaline solutions (1 M NaOH), these electrodes show comparable performance to previous reports.[21]

In 0.5 M $NaHCO_3$ the onset is shifted to slightly more positive values and it was found that the catalyst showed better performance in a CO_2-saturated electrolyte than under Ar. Under CO_2 photolysis conditions, the anode reaches 5 mA cm^{-2} at an overpotential of 400 mV.

Integrated device characterization

Considering the performance of both electrodes, an overall overpotential of about 700 mV is expected for selective production of CO, therefore necessitating a driving force of 2 V or more. This is visualized in their current-voltage response in a two-electrode configuration (**Figure 5-6a**), where additional ohmic losses are taken into account. Driving this reaction with sunlight requires a device producing voltages considerably higher than conventional photovoltaics. In this study three perovskite cells connected in series were employed, producing an open circuit voltage of 3.1 V and a short circuit current density of 6.15 mA cm^{-2} (**Figure 5-6a**, red).

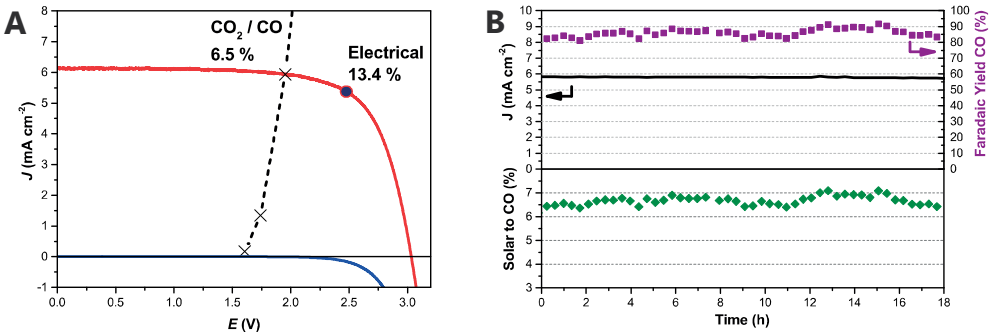

Figure 5-6: **Characterization of the complete device.** (A) J-V curves of three series-connected perovskite cells under simulated AM 1.5G 1 Sun solar irradiation and in the dark, overlaid with the matched J-V characteristics of the CO_2-reduction and oxygen evolution electrodes. The maximum power point of the photovoltaics is designated with a dot. (B) Current density, CO yield, and solar to CO conversion efficiency of the device during an 18-hour stability test. Adapted from Schreier et al.[18]

The operating point of the complete device can be predicted by the intersection of the electrode and photovoltaic curves,[3,22] which, in this case, falls on the outer end of the plateau current of the photovoltaic – not far from the maximum power point for solar-to-electric energy conversion. Intersecting in this relatively flat region of the perovskite J–V characteristics enables a stable system with respect to small perturbations such as fluctuations in the light intensity and performance fluctuations of the catalysts. The data predict a device current density of approximately 5.93 mA

cm^{-2} (normalized to the total illuminated area of the photovoltaics), which is close to the value observed on the complete assembled device.

For long-term testing of the complete device, a CO_2-saturated solution of 0.5 M $NaHCO_3$ was used as electrolyte, and the PV cells were kept in a transparent chamber under a constant flow of argon. Upon exposure to simulated sunlight, the series connected perovskite tandem cell produced an absolute current of 1.65 mA (for a total illuminated area 0.285 cm^2). In order to establish the cathode operating potential at -0.4 V vs. RHE, at which CO yield on Au is maximal, the cathode area was adjusted to 1.0 cm^2 to achieve the desired current density as defined by the catalyst behavior shown in **Figure 5-4a**. After initial equilibration of both the catalyst and the PV cells, the system was allowed to run without any external bias under constant illumination for more than 18 h (**Figure 5-6b**). The experimental setup is shown in **Figure 5-7**. Over the time of the experiment, the solar current density remained constant at about 5.8 mA cm^{-2} and the minimal change in observed photocurrent verifies the excellent stability of not only the anode and cathode, but also of the three perovskite photovoltaics which are transferring power to the catalyst load. At the time of carrying out the experiments, this was one of the first studies of extended testing of $CH_3NH_3PbI_3$ perovskite photovoltaics under actual load conditions, confirming that stable operation of these devices can be achieved, which was a finding of considerable importance.

Evolved gases were periodically analyzed by gas chromatography, and the CO signal was related to the measured currents to determine the Faradaic efficiency (FE) of sunlight-driven CO_2 reduction to CO. As shown in **Figure 5-6b**, during the 18 h period of operation, the FE varies between 80% - 90%. The energy conversion efficiency for solar-to-CO is defined by **Equation 5-5**:

$$\eta_{CO} = \frac{E^0_{CO_2/CO} \cdot J \cdot FE_{CO}}{I_{solar}}$$

Equation 5-5: **Solar to CO efficiency calculation.** $E^0_{CO_2/CO} = 1.34\ V$ is the thermodynamic energy stored in the CO_2/CO couple, J is the observed current density, FE_{CO} is the faradaic efficiency toward CO formation and I_{solar} is the solar power density.

The measured current and FE combine to yield a CO_2 reduction efficiency greater than 6.5%, a new benchmark exceeding greatly the efficiencies previously reported on systems driven by Si photovoltaics.[23,24] Additionally, considering hydrogen that is formed as a secondary product at an average faradaic yield of 10.5% over the whole experiment, a solar to fuel efficiency exceeding 7% was achieved using this system. While this study focuses on gas-phase products, anodized gold catalysts have been reported to also produce liquid-phase products, albeit in very small amounts.[16]

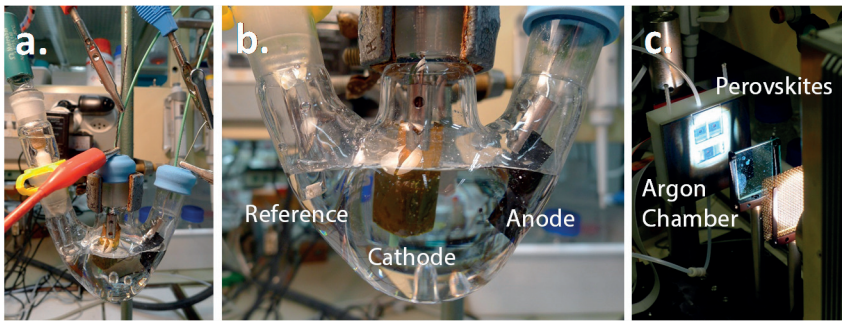

Figure 5-7: **Experimental setup.** (A) A three-neck round-bottom flask was used for electrocatalysis. PEEK tubing was used to bring in CO_2 and remove gases for continuous analysis by gas chromatography. Various electrical contacts are used to connect the catalysts to the PV device and to log the potentials of all system constituents which are related to the potential of a Ag/AgCl (KCl sat.) reference electrode. (B) Anode, cathode and reference electrodes can be seen in the three-neck round bottom flask. Kapton® was used to mask the electrodes. (C) A gastight box was used to keep three perovskite cells under an argon atmosphere. Adapted from Schreier et al.[18]

To understand the behavior of each component, the potentials of the anode, cathode, and each photovoltaic cell were monitored over time, as plotted in **Figure 5-8a**. It can be seen that a distinct equilibrium takes place between the three series connected photovoltaic cells, whereas the potentials at the anode and cathode remain fairly constant during the course of the experiment. J−V curves of the series-connected PV before and after testing are shown in **Figure 5-8b**. Since the perovskite photovoltaics are tested over an extended amount of time, and the efficiency is defined by the actual current density during operation (Eq. 2), hysteretic behavior does not affect the determination of the CO_2 reduction efficiency.[25] In this configuration, the performance of the device is largely dictated by the interplay between the Au cathode and photovoltaic current-voltage behavior,

since the anode shows a very steep J–V behavior compared to the other system components and thus only negligibly influences the operating voltage. Chopped light experiments carried out after the long term test give insight into the dynamic processes occurring between anode and cathode (**Figure 5-9**).

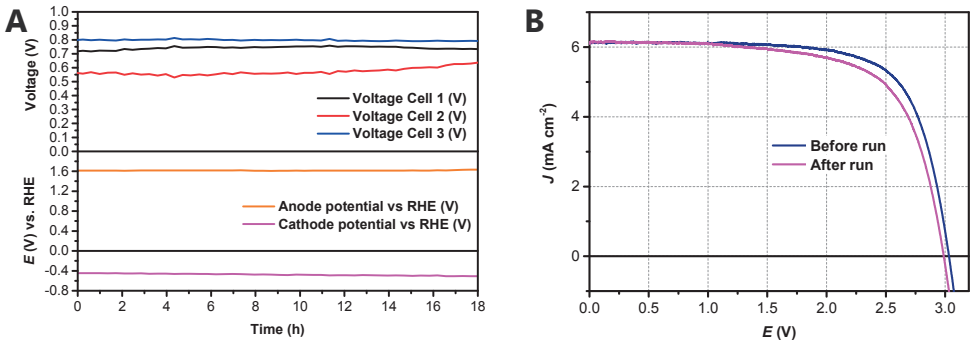

Figure 5-8: **Performance of system components during long term test**. (A) Evolution of each cell voltage and cathode and anode potential over the course of the experiment and (B) JV scans of the series-connected perovskite cells before- and after the run. The perovskite solar cells behave in a distinct equilibrium to each other. The potentials of the electrodes stay fairly constant over time, however a slight increase in cathode potential can be observed. Adapted from Schreier et al.[18]

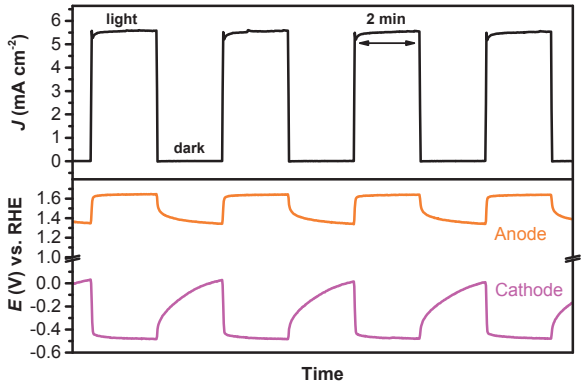

Figure 5-9: **Chopped light test.** Chopped illumination (2 minutes interval) with simultaneous measurement of the system current as well as cathode- and anode potentials vs. RHE. It can be seen that in the dark, no currents are observed. The equilibration of the system is slow, with the two minute interval not allowing for complete equilibration. The IrO_2 anode reaches its equilibrium much more quickly than the cathode. Adapted from Schreier et al.[18]

Conclusion and outlook

With the goal of going beyond CO_2 reduction in nonaqueous electrolytes, this chapter introduced a highly efficient and unassisted photolytic system for the

reduction of carbon dioxide to carbon monoxide using water as electron source, reaching benchmark solar-to-CO efficiencies over 6.5%. This system, driven by three perovskite photovoltaics, was shown to be stable over 18 h. Remarkably, the extended operation under load demonstrated the ability of the photovoltaics to maintain the necessary voltage for selective photolytic synthesis of CO from CO_2 in the long term, encouraging further work on perovskite stability. Their large open circuit voltage constitutes a major strength of perovskite photovoltaics. As a consequence of this, three of these in series connected cells were more than sufficient for CO production to be driven with high efficiency, whereas conventional photovoltaics like Si, on the other hand, require at least four cells to achieve voltages sufficient to drive water splitting and CO_2 reduction efficiently.[4]

Despite the remarkable efficiencies that were observed here, there is still room for improvement. The use of more abundant electrode materials will benefit the applicability of this catalytic approach to industrial implementation. For instance, transition metal or mixed metal cathodes have shown promise toward CO evolution, although their performances are still less desirable than for gold.[26] Additionally, alternative anode materials for the oxygen evolution reaction in near-neutral pH, such as Co-Pi and Ni-Bi,[19,20] should be examined, keeping in mind that metal contaminants in solution present the risk of poisoning the activity of the CO_2-reducing cathode.[15] Since this photovoltaic system produces a slight excess photovoltage, this design could accommodate the use of higher-overpotential but cheaper electrode materials and provide great potential for the selective synthesis of other products. Developing a low cost and all earth-abundant catalytic system for achieving both the CO_2 reduction and water oxidation reaction will therefore be the focus of the next chapter.

Side-reactions due to crossover of dissolved products (for instance, re-oxidation of CO at the anode) constitute a loss channel in this single-compartment system, as is shown in **Figure 5-10**. Further efficiency improvements can be expected upon incorporating a separator to prevent product diffusion between electrode compartments. The use of a membrane can, however, impart a significant overpotential because of the buildup of a pH gradient, as has been previously reported.[27,28] Such a gradient and overpotential buildup would be detrimental to the

operation of a CO_2 reduction cathode which exhibits a pH- and potential-dependent product distribution. The development of an effective membrane for neutral electrolysis could enable even higher efficiencies in such a system and will likewise be addressed in the next chapter. Nevertheless, the solar-to-CO efficiency reported here is unaffected from crossover since it is derived from real-time measurements of the evolved gases.

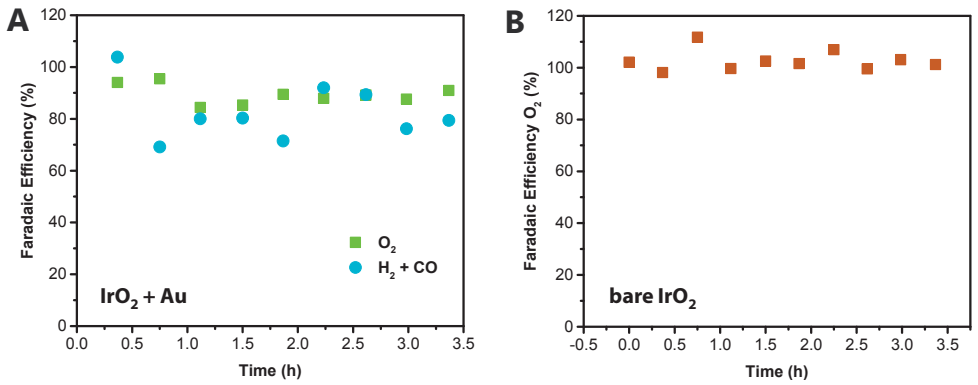

Figure 5-10: **Faradaic yields of anode and cathode products.** (A) In order to elucidate the efficiency of the anode process, in a separate experiment, in addition to CO and H_2, the concentration of O_2 was quantified in the outlet stream by gas chromatography. During this experiment, the cathode was polarized at -0.4 V vs. RHE while IrO_2 was used as anode in the same compartment. (B) In a different experiment, the IrO_2 electrode was characterized in a two-compartment cell, separated by a gastight diaphragm, leading to quantitative O_2 evolution. Adapted from Schreier et al.[18]

The concept presented here shows that record performance can be reached through simple device design. It is therefore meant to carry a strong encouragement toward simplifying systems for solar fuel generation and opens up a new path toward the efficient storage of solar energy in carbon based fuels.

Methods

Electrode preparation and characterization

Oxidized gold cathodes were prepared with a modified method as described in [20]. Gold foil (99.97%, Chempur, Germany) was cleaned in aqua regia mixed with DI water (18.2 MΩ) and subsequently oxidized in 0.5 M H_2SO_4 (96%, "extra pure", Acros Organics) by applying square pulses between 1.183 V and 3.183 V vs. Ag/AgCl (KCl sat.) at 500 Hz using a potentiostat (Interface 1000, Gamry USA). IrO_2 anodes were prepared as follows: Titanium foil (99.7%, 0.25 mm, Sigma Aldrich) was etched for 60 min in boiling 1 M oxalic acid (≥97%, anhydrous, Fluka). Subsequently, 30 uL of 0.2 M H_2IrCl_6 (99.9%, hydrate, ABCR) in isopropanol (ACS Reagent, Merck) were drop cast on the foil. This was followed by drying at 70 °C for 10 min and calcination at 500 °C for 10 min in air. The step was repeated 3 times on each side of the Ti foil. 6.3 mg of IrO_2 were deposited on each side. Both electrodes were characterized before and after photolysis experiments by scanning electron microscopy (SEM) and X-ray diffraction (XRD). SEM micrographs were recorded using a Zeiss Merlin high resolution SEM. XRD measurements were performed on a Bruker D8 Discover X-ray diffractometer in the Bragg-Brentano Geometry using a CuK_α source (1.540598 Å) and a Ni β filter. A linear silicon strip detector was used (Lynx Eye). Scans were acquired from 2θ = 15° - 110° with a step width of 0.03° and scan rates between 2 and 10 seconds $step^{-1}$. The diffraction patterns were matched to the PDF-4+ database (ICDD) and to literature reports.[29]

Photovoltaic cell preparation

Perovskite photovoltaic cells were prepared by Dr. Fabrizio Giordano and Dr. Antonio Abate using a similar procedure as described in the literature.[30] Different from the previous method, the perovskite precursor solution was prepared dissolving 1.1 M of lead iodide and methyl ammonium iodide in dimethylsulfoxide. The perovskite film was deposited by spin coating, using chlorobenzyl as antisolvent to control the crystallization. 2,2',7,7′-tetrakis-(*N*,*N*-di-*p*-methoxyphenylamine)-9,9′-spirobifluorene (*spiro*-OMeTAD) was used as hole

transporting layer and it was doped with bis(trifluoromethylsulfonyl)imide lithium salt and tris(2-(1H-pyrazol-1-yl)-4-tert-butylpyridine)- cobalt(III) tris(bis(trifluoromethylsulfonyl)imide).[31,32]

Electrochemical device testing

Electrocatalytic testing was performed in CO_2-saturated 0.5 M $NaHCO_3$ (99.7%, Sigma Aldrich) at pH 7.2. Anode I-V curves were recorded in 1 M NaOH (Reactolab, Switzerland) and in 0.5 M $NaHCO_3$ under Ar (Carbagas, Switzerland) and CO_2 (Carbagas, Switzerland) using a potentiostat (Interface 1000, Gamry USA). A Luggin capillary was used to minimize the iR-drop between the working- and reference electrodes, therefore eliminating the need for applying iR correction which is a common source of performance overestimation. The gold cathode performance was assessed by testing at different potentials in CO_2 saturated 0.5 M $NaHCO_3$ aqueous electrolyte (pH 7.2), each point for 2 hours, and the product was monitored at the same time by gas chromatography. These tests were performed in a 25 mL three-neck flask with an Ag/AgCl (KCl sat.) reference electrode (Metrohm, Switzerland) and sealed by septa (Suba Seal®, Sigma Aldrich). A flamed Pt wire was used as counter electrode. CO_2 was sparged into the electrolyte at 20.00 mL min^{-1} using a mass flow controller (Bronkhorst EL-Flow, Netherlands) and the product gas was analyzed in a gas chromatography apparatus (Trace ULTRA, Thermo USA) equipped with a ShinCarbon Column (Restek, USA) and a PDD detector (Vici, USA), which was calibrated with respect to certified gas standards (Carbagas, Switzerland). Combined J–V characteristics of the anode and cathode were derived from the data obtained on both electrodes, considering the series resistance of the cell and 4.5 cm^2 as the surface area of the anode and adjusting the surface area of the cathode to match the PV current at 2 V at -0.4 V vs RHE as described below. During testing, perovskite cells were kept in a custom-made chamber, which was constantly flushed with argon gas (90 mL min^{-1}). This chamber was illuminated using a 450 W Xe arc lamp (Lot Oriel) with a KG3 filter (Edmund Optics, USA). The total illuminated area of the perovskite cells was 0.285 cm^2. The intensity of the light source was adjusted to match standard AM 1.5G sunlight at 100 mW cm^{-2} intensity. J–V curves of the cells were recorded from 3.1 V to 0 V at

a scan rate of 10 mV sec^{-1}. Electrocatalysis was performed as described above but with the Pt anode replaced by IrO_2/Ti. Before the test, the cathode was activated at -0.4 V vs. RHE until reaching a steady current. Similarly, the series-connected PV cells were activated at 2 V. No external bias was applied for the whole duration of the stability test. For the Au cathode to yield a maximum selectivity for CO, its surface area was adjusted to 1.0 cm^2, which binds it to operate at -0.4 V vs. RHE at the current supplied by the photovoltaic (as described above and seen in the catalyst J–V curve in Fig. 2a). The surface area of the anode was left constant at 4.5 cm^2. The stable device current density of 5.8 mA cm^{-2} (normalized by illuminated area) corresponded to a net current of 1.65 mA and therefore electrode current densities of 1.65 mA cm^{-2} and 0.37 mA cm^{-2} on the cathode and anode, respectively. The faradaic efficiency data was smoothed to correct for variations due to bubble formation and bubble breaking. Chopped illumination experiments were conducted to confirm the light dependence of current and electrode potentials. During testing, the current and voltage on each cell and on each electrode as well as on the Ag/AgCl (KCl sat.) electrode were monitored using a Keithley 197 multimeter connected to an A/D converter (USB 6211, National Instruments, USA) and the data recorded using LabView (National Instruments, USA). The series resistance between the anode and cathode was evaluated by potentiostatic AC-impedance measurements between 1 MHz and 0.2 Hz at 2 V cell voltage and 10 mV perturbation, using the same potentiostat as above, and determined to be 22 ohms.

References

1. Marshall, J. Solar energy: Springtime for the artificial leaf. *Nature* **510,** 22–24 (2014).
2. Khaselev, O., Bansal, A. & Turner, J. A. High-efficiency integrated multijunction photovoltaic/electrolysis systems for hydrogen production. *Int. J. Hydrog. Energy* **26,** 127–132 (2001).
3. Luo, J. *et al.* Water photolysis at 12.3% efficiency via perovskite photovoltaics and Earth-abundant catalysts. *Science* **345,** 1593–1596 (2014).
4. Cox, C. R., Lee, J. Z., Nocera, D. G. & Buonassisi, T. Ten-percent solar-to-fuel conversion with nonprecious materials. *Proc. Natl. Acad. Sci.* **111,** 14057–14061 (2014).
5. Jia, J. *et al.* Solar water splitting by photovoltaic-electrolysis with a solar-to-hydrogen efficiency over 30%. *Nat. Commun.* **7,** 13237 (2016).
6. The Solubility of Carbon Dioxide in Water at Low Pressure. *J. Phys. Chem. Ref. Data* **20,** 1201–1209 (1991).
7. Kuhl, K. P. *et al.* Electrocatalytic Conversion of Carbon Dioxide to Methane and Methanol on Transition Metal Surfaces. *J. Am. Chem. Soc.* **136,** 14107–14113 (2014).
8. Kumar, B. *et al.* Photochemical and Photoelectrochemical Reduction of CO_2. *Annu. Rev. Phys. Chem.* **63,** 541–569 (2012).
9. Grätzel, M. The light and shade of perovskite solar cells. *Nat. Mater.* **13,** 838–842 (2014).
10. Gao, P., Grätzel, M. & Nazeeruddin, M. K. Organohalide lead perovskites for photovoltaic applications. *Energy Environ. Sci.* **7,** 2448–2463 (2014).
11. NREL Solar Cell Efficiency Chart. Available at: http://www.nrel.gov/pv/assets/images/efficiency-chart.png. (Accessed: 21st January 2017)
12. Zhang, W., Eperon, G. E. & Snaith, H. J. Metal halide perovskites for energy applications. *Nat. Energy* **1,** 16048 (2016).
13. Saliba, M. *et al.* Incorporation of rubidium cations into perovskite solar cells improves photovoltaic performance. *Science* **354,** 206–209 (2016).
14. Polman, A., Knight, M., Garnett, E. C., Ehrler, B. & Sinke, W. C. Photovoltaic materials: Present efficiencies and future challenges. *Science* **352,** aad4424 (2016).
15. Hori, Y. in *Handbook of Fuel Cells* (John Wiley & Sons, Ltd, 2010).
16. Chen, Y., Li, C. W. & Kanan, M. W. Aqueous CO_2 Reduction at Very Low Overpotential on Oxide-Derived Au Nanoparticles. *J. Am. Chem. Soc.* **134,** 19969–19972 (2012).
17. McCrory, C. C. L., Jung, S., Peters, J. C. & Jaramillo, T. F. Benchmarking Heterogeneous Electrocatalysts for the Oxygen Evolution Reaction. *J. Am. Chem. Soc.* **135,** 16977–16987 (2013).
18. Schreier, M. *et al.* Efficient and selective carbon dioxide reduction on low cost protected Cu_2O photocathodes using a molecular catalyst. *Energy Env. Sci* **8,** 855–861 (2015).
19. Dincă, M., Surendranath, Y. & Nocera, D. G. Nickel-borate oxygen-evolving catalyst that functions under benign conditions. *Proc. Natl. Acad. Sci.* **107,** 10337–10341 (2010).
20. Kanan, M. W. & Nocera, D. G. In Situ Formation of an Oxygen-Evolving Catalyst in Neutral Water Containing Phosphate and $Co2^{+}$. *Science* **321,** 1072–1075 (2008).
21. Lee, Y., Suntivich, J., May, K. J., Perry, E. E. & Shao-Horn, Y. Synthesis and Activities of Rutile IrO_2 and RuO_2 Nanoparticles for Oxygen Evolution in Acid and Alkaline Solutions. *J. Phys. Chem. Lett.* **3,** 399–404 (2012).
22. Brillet, J. *et al.* Highly efficient water splitting by a dual-absorber tandem cell. *Nat. Photonics* **6,** 824–828 (2012).
23. White, J. L., Herb, J. T., Kaczur, J. J., Majsztrik, P. W. & Bocarsly, A. B. Photons to formate: Efficient electrochemical solar energy conversion via reduction of carbon dioxide. *J. CO_2 Util.* **7,** 1–5 (2014).
24. Sugano, Y. *et al.* Crucial role of sustainable liquid junction potential for solar-to-carbon monoxide conversion by a photovoltaic photoelectrochemical system. *RSC Adv.* **5,** 54246–54252 (2015).
25. Snaith, H. J. *et al.* Anomalous Hysteresis in Perovskite Solar Cells. *J. Phys. Chem. Lett.* **5,** 1511–1515 (2014).

26. DiMeglio, J. L. & Rosenthal, J. Selective Conversion of CO_2 to CO with High Efficiency Using an Inexpensive Bismuth-Based Electrocatalyst. *J. Am. Chem. Soc.* **135,** 8798–8801 (2013).
27. Hernández-Pagán, E. A. *et al.* Resistance and polarization losses in aqueous buffer–membrane electrolytes for water-splitting photoelectrochemical cells. *Energy Environ. Sci.* **5,** 7582–7589 (2012).
28. Jin, J. *et al.* An experimental and modeling/simulation-based evaluation of the efficiency and operational performance characteristics of an integrated, membrane-free, neutral pH solar-driven water-splitting system. *Energy Environ. Sci.* **7,** 3371–3380 (2014).
29. Hore, S. *et al.* Carbonization of polyethylene on gold oxide. *J. Mater. Chem.* **18,** 5589–5591 (2008).
30. Jeon, N. J. *et al.* Solvent engineering for high-performance inorganic–organic hybrid perovskite solar cells. *Nat. Mater.* **13,** 897–903 (2014).
31. Abate, A. *et al.* Lithium salts as 'redox active' p-type dopants for organic semiconductors and their impact in solid-state dye -sensitized solar cells. *Phys. Chem. Chem. Phys.* **15,** 2572–2579 (2013).
32. Burschka, J. *et al.* Tris(2-(1H-pyrazol-1-yl)pyridine)cobalt(III) as p-Type Dopant for Organic Semiconductors and Its Application in Highly Efficient Solid-State Dye-Sensitized Solar Cells. *J. Am. Chem. Soc.* **133,** 18042–18045 (2011).

6 Atomic Layer Modification of CuO electrocatalysts

The chapter is adapted from the 1st revision of the publication: ***Marcel Schreier****, Florent Héroguel, Ludmilla Steier, Jeremy S. Luterbacher, Matthew T. Mayer, Jingshan Luo, Michael Grätzel.*
Submitted to Nature Energy

Previous research on the unassisted solar-driven reduction of CO_2 has focused on the use of precious metal catalysts such as gold, iridium, palladium and ruthenium. In this chapter, the modification of CuO nanowires by atomic layer deposition of very thin layers of SnO_2 is investigated. It is found that this modifies the wide product selectivity of CuO to the predominant production of CO, leading to a low-cost catalyst for the selective production of CO in aqueous electrolytes. The catalyst is also found to enable the oxidation of water to oxygen and therefore allows for the design of a bifunctional system, employing the same catalyst both as cathode and anode. Separated by a bipolar membrane which enables the sustainable operation with different catholytes and anolytes, the all earth-abundant electrolysis device was driven by a 3-junction photovoltaic, leading to a solar-to-CO efficiency peaking at 13.4%.

Introduction

In addition to the production of CO, shown in **Chapter 5**, a number of other products have been successfully synthesized by the electrochemical reduction of CO_2 in aqueous electrolytes, most notably formic acid (HCOOH).[1,2] However, as described before, copper is the only catalyst able to produce large amounts of methane (CH_4)[3], ethylene (C_2H_4)[4] and ethanol (CH_3CH_2OH).[5] This list is non-exhaustive and a large number of other compounds have also been observed from this material.[6,7] Due to the numerous possible reaction pathways, selectively targeting one specific product at high yield has remained a challenge, which, to the present day, has only been achieved for CO and formic acid in aqueous electrolytes. Unfortunately, selective electroreduction of CO_2 to these products either relies on precious metals (Au, Ag, Pd),[8–11] requires operation at considerable overpotentials[12] or the use of electrolyte additives such as ionic liquids.[13] This becomes obvious when considering that the catalysts employed in **Chapter 5** consist of gold and iridium, both of which being very rare and expensive metals. Developing inexpensive, selective, stable and scalable catalysts operating at low overpotentials is therefore a crucial requirement.

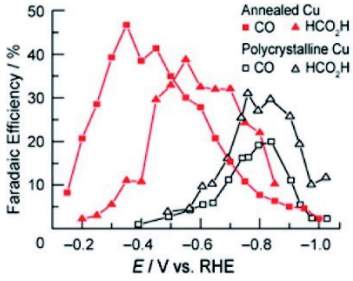

Figure 6-1: **Selectivity of oxide-dervide copper catalysts.** The peak selectivities for formate and CO were increased and shifted to lower overpotentials. Adapted with permission from Li et al.[14] Copyright 2012 American Chemical Society.

On the way to addressing this challenge, Kanan and co-workers made substantial progress toward decreasing the overpotential of copper-based electrodes by employing catalysts derived from copper oxides, an effect which they related to an increase of grain boundary density in these catalysts (**Figure 6-1**). However, the insufficient selectivity remained an issue, with the catalyst producing CO, H_2 and formic acid at comparable selectivities.[14] Following up on this work, Watanabe and

co-workers have demonstrated that by electrochemically reducing copper oxide in the presence of indium ions, the selectivity toward producing CO could be substantially enhanced.[15,16] More recently, the same group demonstrated tin to have a similar effect.[17] Though adding sources of metal ions during the catalyst reduction process is effective in tuning the selectivity, it is difficult to control and may not guarantee uniform coating. The need for effective ways toward tuning the selectivity of CO_2 reduction electrocatalysts asks for further investigations into the precise surface modification of materials, wherein lies tremendous potential toward effective catalyst design.

In this chapter, the surface modification of CuO nanowire electrodes with SnO_2 using atomic layer deposition (ALD) is demonstrated, leading to a highly selective catalyst for the electrochemical reduction of CO_2 to CO. Atomic Layer Deposition is a technique for depositing thin films, based on the sequential gas phase adsorption and reaction of two precursors. In a typical ALD process, a deposition and oxidation cycle is repeated numerous times under the constant flow of a carrier gas.[18] As an example, the deposition of SnO_2 is carried out as follows.

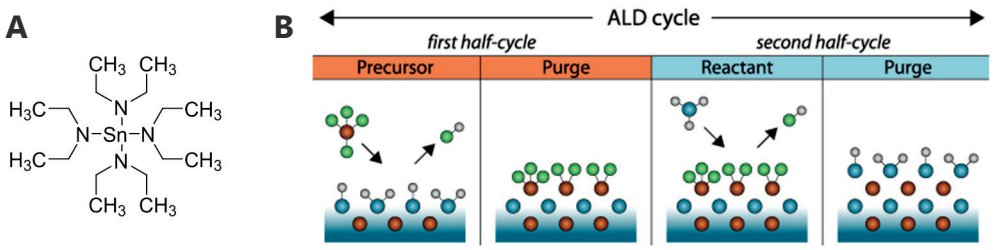

Figure 6-2: **Atomic Layer Deposition (ALD).** (A) Molecular Structure of Tetrakis(diethylamido)tin(IV), precursor for the deposition of SnO_2. (B) Illustration of the sequence of steps involved in an ALD cycle. Adapted from Langereis et al.[19] © IOP Publishing. Reproduced with permission. All rights reserved.

Under a continuous flow of nitrogen and under vacuum, a precursor, here Tetrakis(diethylamido)tin(IV) (**Figure 6-2a**), is exposed to the samples heated to 185°C. At the same time, the valve to the vacuum pump is closed and the precursor left to adsorb on the surface of CuO. After a fixed amount of time, the precursor source is closed and residual precursor is evacuated from the deposition chamber until the only precursor remaining is surface bound. Next, the sample is exposed to ozone which serves to oxidize the surface-bound molecular precursor and thereby

leads to the deposition of a layer of SnO_2. This process, as illustrated in **Figure 6-2b**, is repeated until the desired layer thickness has been reached. Key advantages of this method are the good uniformity of the deposited films, as well as the possibility to uniformly coat samples with very high aspect ratios.

By this approach, it is possible to control the deposited amount of SnO_2 at monolayer level precision, changing the very broad product selectivity of CuO to lead to the sole production of CO at selectivities up to 97% of all observed products. Later in the chapter, efforts are described to understand the changes in catalyst selectivity. Furthermore, in addition to the reduction of CO_2, the catalyst was investigated for the oxygen evolution reaction, opening up the novel possibility of designing a bifunctional system, employing SnO_2-coated CuO as an electrode for both the reduction and oxidation reaction. This is highly beneficial because it eliminates the need to introduce elements foreign to the cathode, which can lead to its poisoning after extended operation as shown above. However, running the electrode in a bifunctional configuration requires the presence of different electrolytes in each compartment. To satisfy this requirement in a sustainable manner, the operation of bipolar membranes was investigated, culminating in a system driven by a 3-junction photovoltaic, reaching the record efficiency for solar driven CO_2 reduction at the time the experiments were carried out. As this new efficiency record for solar driven CO_2 reduction to CO is achieved with one single Earth-abundant catalyst it offers practical advantages over the system described in **Chapter 5** and further previously reported high efficiency sunlight-driven CO_2 reduction systems, where noble metal cathode materials such as gold, palladium and ruthenium have been employed along with IrO_2 to catalyze the OER.

Results and Discussion

Catalyst Preparation and Characterization

Electrodes were prepared by sputter deposition of 1.5 μm films of Cu on glass slides, followed by anodization in 3 M KOH to yield $Cu(OH)_2$ nanowires. These were subsequently dehydrated for 1 h at 150 °C in air to transform $Cu(OH)_2$ into CuO while retaining the nanowire morphology (**Figure 6-3**).

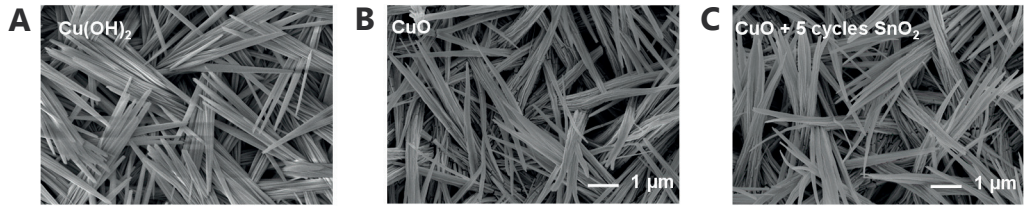

Figure 6-3: **Morphologies at different preparation steps.** SEM micrographs of $Cu(OH)_2$, CuO and 5 cycle SnO_2 coated CuO nanowires.

Modification with SnO_2 was carried out using atomic layer deposition, employing tetrakis(dimethylamido)tin(IV) as a metal precursor and O_3 as an oxidant, wherein sequential pulses of precursor and oxidant led to the layer-by-layer buildup of tin dioxide. The morphology of the samples and their phase composition were verified by scanning electron microscopy (SEM), scanning transmission electron microscopy combined with energy-dispersive X-Ray spectroscopy (STEM-EDX), X-Ray diffraction (XRD), X-Ray photoemission spectroscopy (XPS) and Raman spectroscopy (**Figure 6-4**).

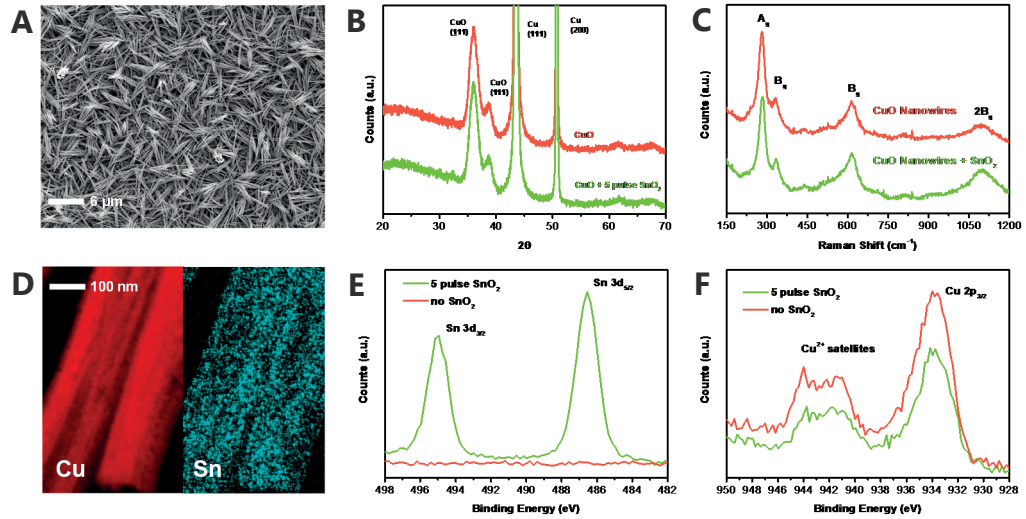

Figure 6-4: **Structural and compositional characterizations of CuO nanowires with and without SnO_2 surface modification.** (A) SEM micrograph of as-prepared CuO nanowires. (B) X-Ray diffraction pattern of SnO_2-modified and unmodified samples. From the annotated reflections, the presence of CuO can be observed but no reflections corresponding to SnO_2 were detected. (C) Raman spectrum of SnO_2-modified and unmodified samples. The characteristic modes of CuO were observed; however, no modes relative to SnO_2 were detected. (D) STEM-EDX mapping of a CuO nanowire after coating with 5 ALD cycles of SnO_2. Sn is uniformly distributed on the nanowire. (E) Sn 3d XPS spectrum, confirming the presence of Sn after modification of CuO nanowire samples with 5 cycles of SnO_2. (F) Cu 2p XPS spectrum, showing the features of Cu^{2+} satellites, which confirm the presence of CuO.

Electron microscopy confirmed the nanowire morphology of the CuO samples (**Figure 6-4a**), and the morphology remained unchanged after modification with five ALD cycles of SnO_2 (**Figure 6-3**). XRD patterns of bare and SnO_2-modified samples show the presence of the CuO-phase,[20] as well as of metallic Cu, which is present underneath the nanostructure (**Figure 6-4b**). These findings were supported by Raman measurements (**Figure 6-4c**), detecting peaks at 282 cm^{-1}, 333 cm^{-1} and 613 cm^{-1}, as well as a broad peak at 1095 cm^{-1}, characteristic of CuO A_g, B_g and $2B_g$ modes, respectively.[21] The absence of any peak below 282 cm^{-1} indicates that no significant amount of Cu_2O was present on the surface. Interestingly, in the case of ALD-coated samples, no SnO_2 could be detected by XRD or Raman, which can likely be attributed to the ultrathin character of the SnO_2 surface layer. To verify that Sn was successfully deposited, surface elemental analysis was carried out by STEM-EDX and XPS. EDX measurements showed that Sn coated the CuO nanowires homogenously (**Figure 6-4d**). XPS measurements further confirmed the presence of Sn at the surface with Sn 3d core level peaks locating at binding energies of 495.0 and 486.6 eV (**Figure 6-4e**). The peak position of Sn, together with the presence of a shoulder at 531 eV at the oxygen 1s edge, indicats that Sn is likely in its +4 oxidation state.[22] In contrast, no peaks corresponding to Sn could be observed in the case of an unmodified CuO sample. Cu 2p XPS showed a peak at 933.8 eV as well as strongly visible Cu^{2+} satellites between 939 and 946 eV, attributed to the presence of Cu in a +2 oxidation state (**Figure 6-4f**). A similar spectrum was obtained for a sample modified with SnO_2.

Electrochemical performance

To evaluate the catalyst's electrochemical performance for CO_2 reduction, the electrodes were tested in a Nafion-separated two-compartment cell. The electrolyte was CO_2-saturated 0.1 M $NaHCO_3$ (pH 6.75), which had been treated with an ion exchange resin (Chelex) to minimize the concentration of transition metal impurities. Such impurities were previously shown to negatively interfere with precise CO_2 reduction studies by contaminating the cathode surface, as can also be seen in **Chapter 5**.[23,24] Inductively Coupled Plasma Mass Spectrometry (ICP-MS) analysis of the resulting electrolyte found all measured impurities to be below the

detection limit (**Table 6-1**). Prior to polarization at the stated potential, the samples were subjected to a cathodic current of -2.0 mA cm^{-2} under CO_2 saturation to reduce the oxides until the potential reached -0.5 V vs. RHE, thereby activating the catalyst. A typical reduction curve of a CuO sample modified with 2 cycles of SnO_2 is shown in **Figure 6-5**.

Fe (ppm)	Ni (ppm)	Co (ppm)	Pb (ppm)	Pt (ppm)
< 0.1	< 0.1	< 0.1	< 0.01	< 0.01

Table 6-1: **ICP-MS measurements of fresh electrolyte.** All measured species were below the detection limit.

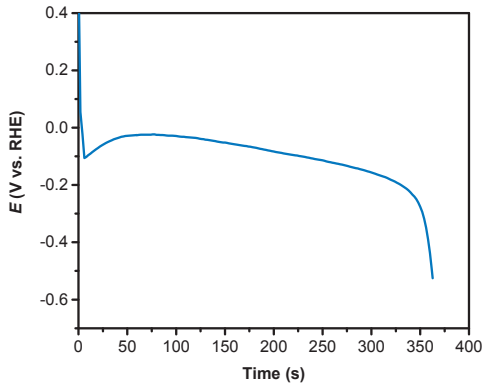

Figure 6-5: **Reduction at -2.0 mA cm^{-2} of a CuO nanowire sample, coated with 2 ALD cycles of SnO_2.** It can be seen that substantial charge is passing before the desired potential can be reached. This current is attributed to the reduction of the oxides.

At this point, the desired potential was applied. In the case of Sn-containing samples, the reduction step was followed by 1 h polarization at -0.7 V vs. RHE before applying the desired potential. **Figure 6-6** shows the resulting electrochemical behavior and CO_2 reduction product distribution for samples tested at different potentials. Each data point in **Figure 6-6 a**, **b**, **c** and **Figure 6-12 a**, **b** corresponds to the average of results obtained from two to three independent and freshly prepared samples. Each individual data point can be found in the publication cited at the beginning of this chapter.

As expected from the literature on copper-based catalysts, a large range of CO_2 reduction products was observed on bare CuO samples.[14,25,26] CO production was found to peak at -0.6 V vs. RHE, reaching a selectivity of 36%. At lower potentials,

the production of hydrogen was dominant, whereas at more negative bias, in addition to hydrogen, the production of more reduced carbon-containing species such as ethylene, ethanol and 1-propanol was also observed.

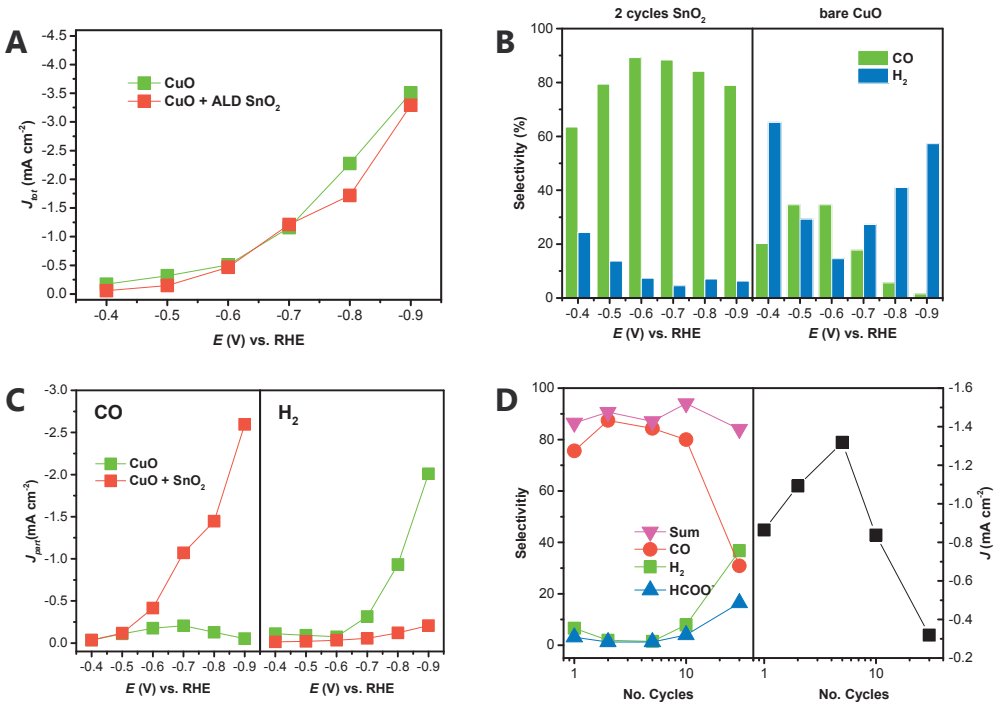

Figure 6-6: **Electrochemical CO_2 reduction performance.** (A) Current density of SnO_2-modified and unmodified samples. (B) Faradaic selectivity toward CO and H_2 for samples modified with 2 ALD cycles of SnO_2 (left) and for unmodified samples (right). (C) Partial current densities toward CO (left) and H_2 (right) from SnO_2-modified samples (2 ALD cycles) and unmodified samples. (D) Impact of the amount of deposited SnO_2 (by ALD cycles) on the electrocatalytic performance and selectivity at -0.7 V vs. RHE. Current densities have been calculated using the geometric surface area of the samples.

After ALD modification with 2 pulse cycles of SnO_2 using tetrakis(dimethylamido)tin(IV) as precursor and ozone as oxidizer, the observed current densities changed little compared to the unmodified samples (**Figure 6-6a**). At the same time, the product distribution was strongly altered (**Figure 6-6b**), which is reflected by the relative partial current densities for CO and H_2 on modified and unmodified samples (**Figure 6-6c**). With the modified samples, the dominant product was CO for all potentials, reaching a selectivity as high as 97% of all the observed products. Furthermore, even at high bias, virtually no C2 or C3 products were observed, suggesting that further reduction is inhibited in the presence of Sn. The highest yields of carbon monoxide were obtained at -0.6 V vs. RHE and a broad

plateau of high CO yields was observed between -0.5 and -0.9 V vs. RHE. The sum of observed products varied between 85-100%. The SnO_2-modified samples showed good stability upon extended testing as shown in **Figure 6-7.**

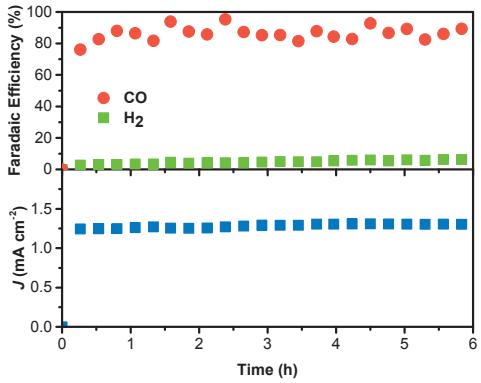

Figure 6-7: **Representative chronoamperometry test of a CuO sample with 2 cycles of SnO_2.** The sample was biased at -0.7 V vs. RHE in 0.1 M $NaHCO_3$. The performance stays stable over extended amounts of time.

To confirm whether indeed gaseous CO_2 was the source of carbon leading to the production of CO, control experiments with $^{13}CO_2$ as substrate and $NaH^{13}CO_3$ as supporting electrolyte were carried out. In a first set of tests using gas phase Fourier Transform Infrared Spectroscopy (FTIR), the change in product isotope was analysed upon switching the substrate from $^{12}CO_2$ to $^{13}CO_2$ in 0.1 M $NaH^{12}CO_3$ at -0.7 V vs. RHE (**Figure 6-8**). It could be seen that under $^{12}CO_2$ (indicated as a blue surface under the chronoamperometric data) and in the presence of $NaH^{12}CO_3$, the product is solely ^{12}CO, as seen by the appearance of the rovibrational signature corresponding to ^{12}CO in spectrum no. 1. Upon changing the substrate to $^{13}CO_2$, indicated as a green surface in the figure, the production of ^{13}CO appeared and subsequently became the only observed product as characterized by the shift to lower wavenumbers of the CO-rovibrational signature in spectrum no. 3. In the absence of current, no product was detected under either CO_2 isotope. This confirms that indeed gaseous CO_2 serves as the substrate for the electrosynthesis of CO.

In a second set of experiments, a similar test was carried out at -1.295 V vs. Ag/AgCl (KCl sat.) with 0.1 M $NaH^{13}CO_3$ as supporting electrolyte (**Figure 6-9**). Polarizing in the absence of substrate CO_2 gas led to low currents and no substantial observation of CO. Only traces of ^{13}CO could be observed as seen in FTIR spectrum

no. 1. Starting the flow of $^{12}CO_2$ leads to a rapid increase of current and to the rapid appearance of ^{12}CO. Switching the substrate gas to $^{13}CO_2$ again leads to the observation of solely ^{13}CO as a product, further confirming that the carbon source is indeed the gaseous CO_2 and indicating that it is most likely acting as a substrate in the form of dissolved CO_2 in the electrolyte. The small amount of ^{13}CO observed from polarization under He could in this case potentially be attributed to a small amount of $^{13}CO_2$ released from the bicarbonate water equilibrium and subsequently reacting at the electrode.

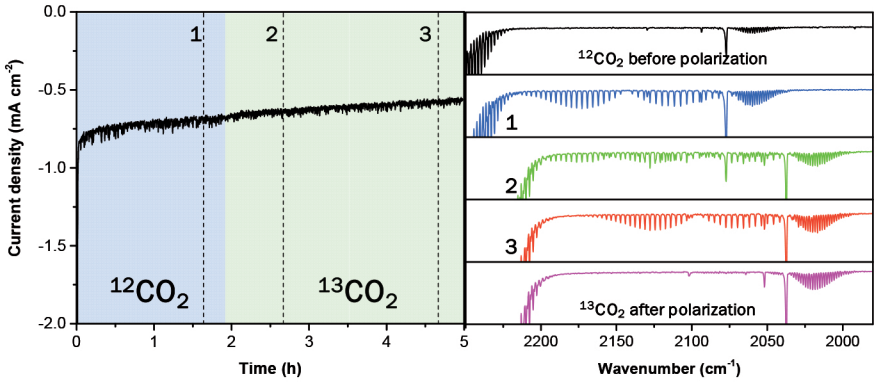

Figure 6-8: **Isotopic CO_2 test in 0.1 M $NaH^{12}CO_3$ at -0.7 V vs. RHE.** The lines labelled with 1, 2 and 3 in the chronoamperometric plot (left) designate the measurement times of the FTIR spectra shown in the right side of the graph. All infrared spectra are shown at the same scale.

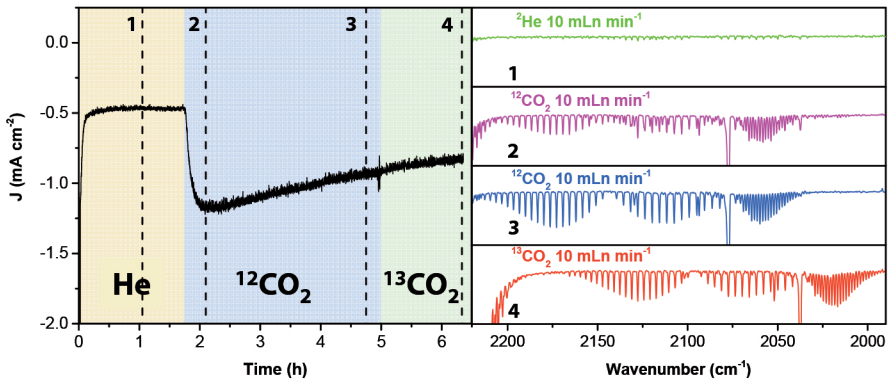

Figure 6-9: **Isotopic CO_2 test in 0.1 M $NaH^{13}CO_3$.** Polarization was carried out at -1.295 V vs. Ag/AgCl (KCl sat.) for the whole experiment. All infrared spectra are shown at the same scale.

Like previously discussed in **Chapter 4**, the composition of the electrolyte was also found to play a role on the product selectivity, as is influenced e.g. by the nature of the alkali cation in bicarbonate based electrolytes. CuO nanowire samples modified

with two ALD cycles of SnO_2 were therefore also tested in 0.1 M $KHCO_3$ and in 0.1 M $CsHCO_3$ at -0.7 V vs. RHE. The results are depicted in **Figure 6-10** and show that while the trend of increasing the CO selectivity in the presence of SnO_2 is maintained, the absolute CO selectivity is even further enhanced for K and Cs containing electrolytes. What is more, at constant bias, the current densities were found to increase in the order of Na < K < Cs, in agreement with the literature.[27] This effect, which has previously also been observed on silver and bare copper surfaces, has been attributed to the pKa of the hydrated cations, modifying the pH at the electrode surface under operation.[27]

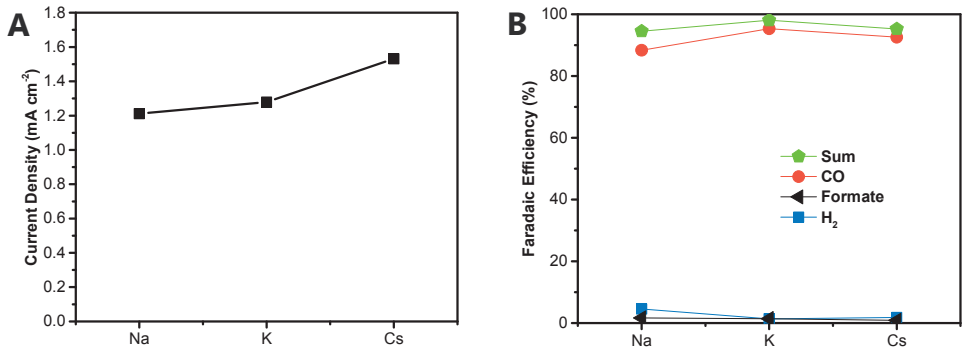

Figure 6-10: **Impact of electrolyte cation on catalytic activity and selecitvity.** (A) Current density and (B) Faradaic efficiencies observed at -0.7 V vs. RHE on CuO nanowire samples, modified with 2 ALD cycles SnO_2 in 0.1 M bicarbonate electrolyte with different alkali cations.

Sn and SnO_2 are known to normally lead to the production of formate as well as CO in the electrochemical reduction of CO_2.[12,28,29] In view of the particularly high selectivity for CO observed from the samples in the present study, it was hypothesized that a cooperative effect between CuO and SnO_2 is taking place, altering the selectivity from what was observed on the two phases separately. To gain insight into this effect, a series of CuO cathodes with varied amounts of SnO_2 on the surface was examined, testing each at a potential of -0.7 V vs. RHE (**Figure 6-6d**). It was found that modification with 1 cycle of SnO_2 already led to a pronounced change in selectivity, and optimum selectivity was achieved between 2 and 5 cycles. For larger cycle numbers, the selectivity for CO decreased while that of H_2 and formate increased. Interestingly, the current density was also affected by the amount of deposited SnO_2 (**Figure 6-6d**), reaching a peak value for samples

modified with 5 ALD cycles, then decreasing for larger amounts of SnO_2 as the surface approaches the state of pure SnO_2. These measurements show that a specific amount of SnO_2 is required to achieve the desired effect of modifying the product distribution to maximize the generation of CO. Changes in the catalyst structure upon testing will be discussed below, giving further insight into the interaction between SnO_2 and CuO.

To optimize the deposition of SnO_2, the impact of precursor dose (exposure time) on sample performance was investigated. As expected for an ALD process, the selectivity toward CO was found to depend on the precursor dose when small amounts of precursor were used, but reached a plateau at higher precursor doses (**Figure 6-11**). It is notable, that relatively large precursor doses (10 s exposure) were needed to reach complete surface saturation with precursor. This exposure time was therefore kept for all depositions carried out for this study.

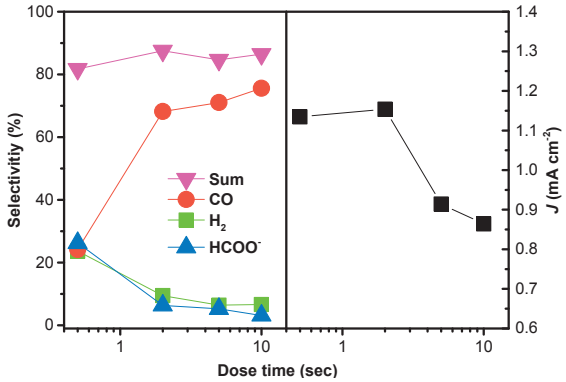

Figure 6-11: **Impact of ALD precursor dose on catalytic activity product selectivity.** On ALD cycle of (Tetrakis(dimethylamido)tin(IV)) was deposited at different exposure times. Tested at -0.7 V vs. RHE in 0.1 M $NaHCO_3$ for 3h. It can be seen that a plateau performance is achieved with increasing precursor dose time.

Mechanistic investigation

In **Figure 6-12a** and **b**, the formation rates of CO and H_2, corresponding to the respective partial current densities are being analyzed. This allows for understanding the reasons leading to the pronounced modification in product distribution upon ALD coating with SnO_2. It must be mentioned that due to potential sharing of catalytic sites by the HER and CO evolution reaction, the calculation of Tafel parameters lacks a theoretical basis and hence was avoided

here. After modification with SnO_2, the nanowire electrodes were found to exhibit a linear trend in a plot of overpotential vs. the logarithm of the partial current density going toward the production of CO. In the case of unmodified CuO nanowires, an overlapping trend could be seen in the low overpotential region, hinting at a similar mechanism for CO formation on modified and unmodified CuO nanowires. On unmodified samples, however, the production of CO substantially decreased at higher overpotentials, while the yield of H_2 and other CO_2 reduction products increased concomitantly. The production of these other products was successfully suppressed on SnO_2-modified samples, leading to a linear slope of the CO formation rate. The performance of unmodified CuO nanowires is in agreement with previous reports on oxide-derived copper catalysts.[14,15] In contrast, the production rate of H_2 was reduced by roughly an order of magnitude by the SnO_2-modified catalyst over almost the entire potential range indicating that the increased selectivity toward CO production is due to the suppression of H_2 production. Analysis of the partial current density for H_2 production (**Figure 6-12a**) reveals substantial changes in mechanism for hydrogen production, which can be attributed to a change in the adsorption strength of key reaction intermediates on the surface. To test this hypothesis experimentally, chemisorption measurements were carried out.

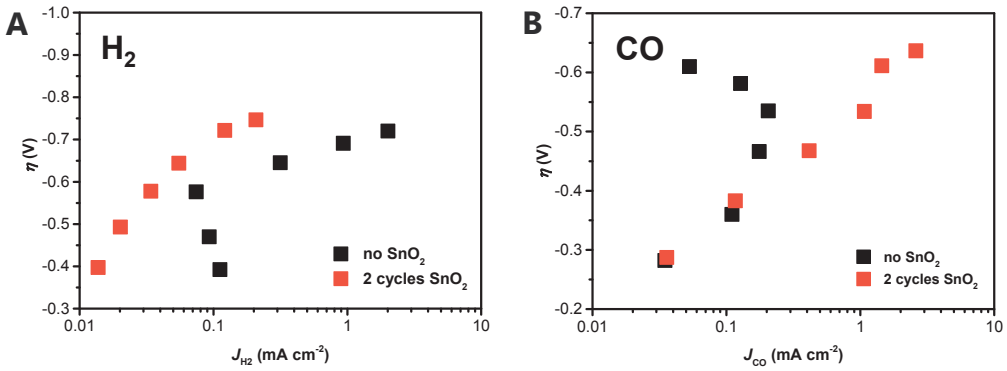

Figure 6-12: **Partial current density analysis.** IR-corrected logarithmic plots of the current densities for (A) H_2 and (B) CO from SnO_2-modified (2 ALD cycles) and unmodified CuO nanowire samples.

Gas-phase adsorption measurements were carried out on CuO nanoparticle samples, reduced *in-situ* under H_2, which has been shown to lead to catalytic activity comparable to that obtained by electrochemical reduction.[30,31] Particles

were chosen for these measurements because their high surface area and small size are more amenable to the study in conventional chemisorption equipment, such as the Micromeritics 3 Flex used here. SnO_2 ALD coating of the particles was carried out by Beneq in a fluidized bed reactor and confirmed by STEM-EDX (**Figure 6-13a**). Reduction of the particles was confirmed by temperature programmed reduction (TPR, **Figure 6-13b**) and their modification with SnO_2 was confirmed to lead to the same trend of selectivity changes as observed when modifying CuO nanowires (**Figure 6-14**).

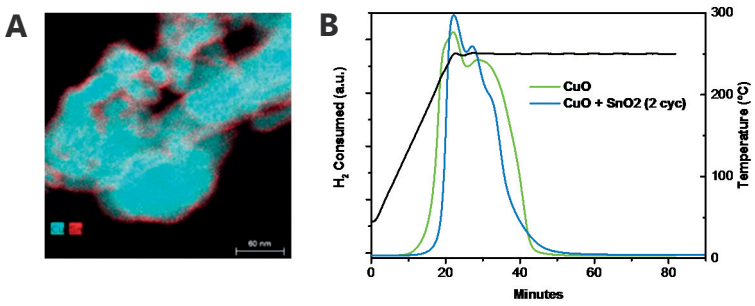

Figure 6-13: **Characterization of the CuO particle model system.** STEM-EDX of FBR-ALD-Coated CuO particles (2 cycles of SnO_2) (A) and (B) TPR of the same particles compared to untreated CuO particles, confirming complete reduction by H_2 before chemisorption measurements.

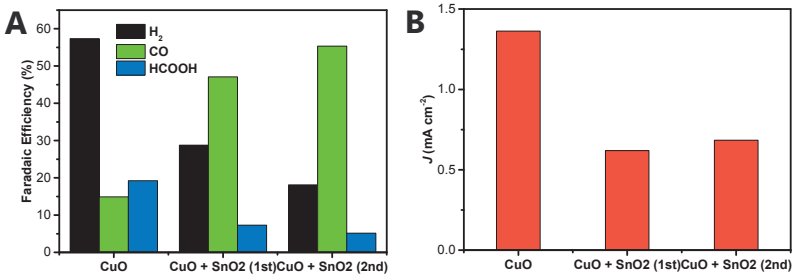

Figure 6-14: **Electrochemical performance of CuO nanoparticle model system.** Product selectivity (A) and current density (B) for CuO and CuO nanopowder (modified with 5 ALD cycles SnO_2) on roughened Ti substrate. The substrate itself showed only a current density of 85 µA cm^{-2}. Tested at -0.7 V vs. RHE. It can be seen that, similar to the case of CuO nanowires, the yield in CO is substantially enhanced upon FBR ALD SnO_2 modification of CuO nanopowder. CuO and CuO + SnO_2 (2^{nd}) were measured for 3h, whereas CuO + SnO_2 (1^{st}) was measured for 10 h.

The resulting adsorption isotherms show that, upon modification with SnO_2, the binding strength of both CO and adsorbed hydrogen (H*) is significantly decreased (**Figure 6-15c**, **d**), as confirmed by Langmuir fits (**Table 6-2**).

H_2 and CO adsorption isotherms were fitted with single or dual Langmuir isotherms according to **Equation 6-1** and **Equation 6-2** below.

$$Q_{ads} = \frac{Q_2 K_2 P}{1 + K_2 P}$$

Equation 6-1: **Single Langmuir Isotherm**

$$Q_{ads} = \frac{Q_1 K_1 P}{1 + K_1 P} + \frac{Q_2 K_2 P}{1 + K_2 P}$$

Equation 6-2: **Dual Langmuir Isotherm**
K_i (1, 2) are the adsorption equilibrium constants. K_1 accounts for strong chemisorption observed in the low pressure range (0-50 mbar) (K_1 >1) while K_2 accounts for weak chemisorption (K_2<0.01)
Q_i are the respective quantities adsorbed at saturation.

$$S_0 = \sum Q_i$$

Equation 6-3: **Total amount adsorbed at saturation.**

N_2 physisorption isotherms at 77 K for Cu_2O and 2 cycle SnO_2 modified Cu_2O were quasi-identical with comparable surface areas (8.27 and 8.54 m^2/g, respectively). The chemisorption data discussed here can hence be attributed solely to the nature of the surface, excluding any effects due to differing surface areas.

For better comparison, **Figure 6-15a** and **b** show the data and Langmuir fits normalized to the amount adsorbed at saturation (S_0, **Equation 6-3**). In fact, while the H_2 and CO adsorption isotherms from CuO after SnO_2 deposition are fitted using a single Langmuir isotherm with a small equilibrium constant (K < 0.01, low binding strength), a dual Langmuir isotherm including an additional large equilibrium constant (K > 1, high binding strength) was required to fit the data from unmodified CuO. Based on the volcano-relationship between hydrogen binding energy and HER performance as shown in **Figure 6-16a**, decreasing the binding strength of H on Cu will move Cu to the lower-activity region of the volcano plot and thus lead to a decreased hydrogen evolution activity, in agreement with the electrochemical results observed in the previous section.[32] Furthermore, this would decrease the equilibrium concentration of H* on the catalyst surface, thereby inhibiting the further reduction of CO to alcohols and hydrocarbon species at higher bias. Interestingly, it was found that for SnO_2-coated samples, the binding strength

of CO was also decreased. Similar to the case of H_2, when considering the volcano relationship for CO_2 reduction activity versus CO binding strength,[7] decreasing the CO binding strength of copper should shift its catalytic performance closer to that of Au and Ag, both known to be excellent catalysts for CO electrosynthesis (**Figure 6-16b**).

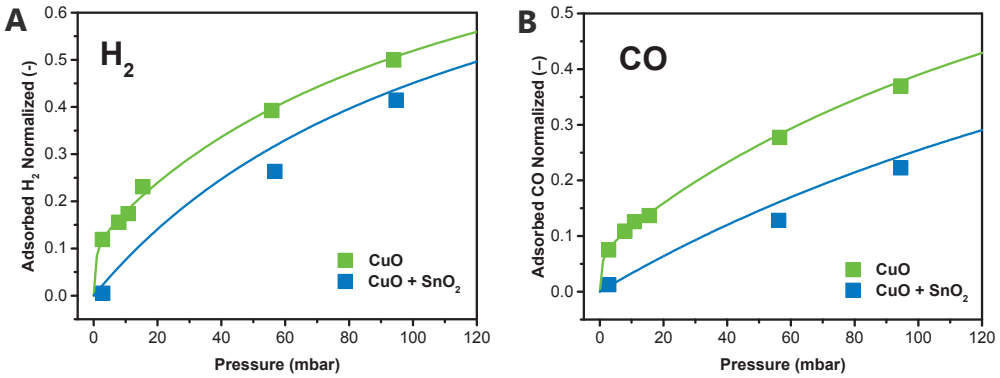

Figure 6-15: **Chemisorption analysis.** Chemisorption measurements for (A) H_2 and (B) CO from SnO_2-modified (2 ALD cycles) and unmodified CuO nanopowder. The solid lines correspond to the Langmuir fit of the data. For better comparison of affinities, the data has been normalized to the quantity adsorbed at saturation (S_0), as obtained from Langmuir fits.

	H_2		CO	
	CuO	CuO / SnO_2	CuO	CuO / SnO_2
K_1	2.1		2.25	
K_2	0.0084	0.0082	0.0052	0.0034
Q_1	0.63		0.99	
Q_2	4.896	2.81	12.45	3.37
Q_{tot}	5.53	2.81	13.44	3.37

Table 6-2: **Results from gas adsorption measurements.** The parameters pertaining to the double-Langumir fits on the chemisorption data point to a stronger adsorption in the absence of SnO_2.

At the same time, the decreased binding strength of CO will likely also inhibit further reduction, by decreasing its surface concentration, as was observed in the

partial current density analysis. Even though these results have been obtained from studies on solid-gas interfaces, they provide useful thermodynamic insight into changes in binding strength under electrochemical testing conditions, as has been proposed previously.[31] They therefore offer a plausible explanation for the observation that increased selectivity toward CO production for SnO_2 modified CuO is due to the suppression of production of H_2.

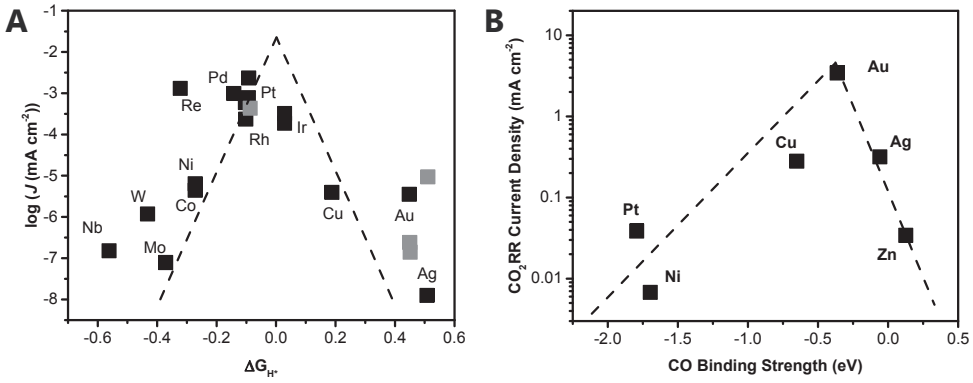

Figure 6-16: **Interpreation of chemisorption measurements.** (A) Volcano plots of HER current vs. H binding strength, adapted from reference 32 and (B) CO_2 reduction current vs. CO binding strength, adapted from reference 33. Grey data points represent single crystal data.

Structural change upon electrochemical testing

SnO_2 coated and uncoated nanowires had to be reduced before products were observed, indicating that the reduced, metallic form of the material constitutes the active catalyst, in agreement with earlier studies.[14,17,29] Similarly, electron energy loss spectroscopy (EELS) analysis before and after testing confirms the transformation of the bulk of copper from a Cu(II) oxide to the metallic form (**Figure 6-17**).

XPS sputtering profile analysis of samples before and after testing at -0.7 V vs. RHE for 3 h showed that while Sn predominantly occurs at the surface of the structure before testing, it was found to be more evenly distributed after completion of the electrochemical runs (**Figure 6-18a**). After testing, the peak of Sn was observed at a smaller binding energy (486.19 eV) (**Figure 6-18b**), indicating reduction of its oxidation state from to +4 to +2. The XPS sputtering profile shows a changed distribution of Sn after electrochemical operation. However, due to the

nanostructured nature of the sample, interpretation of these data are not straightforward.

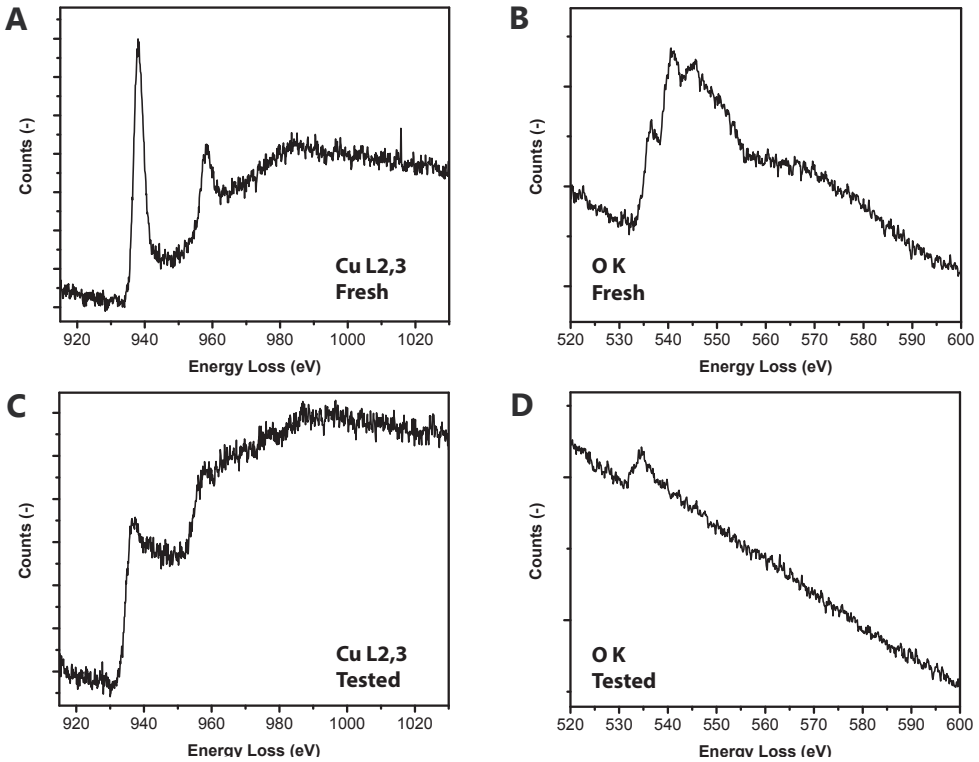

Figure 6-17: **Electron Energy Loss Spectroscopy (EELS).** Cu L2,3 edge (A, C) and O K edge spectra (B, D) of 2 cyc. ALD SnO_2 / CuO samples fresh (top) and tested at -0.7 V vs. RHE for 3h (bottom). The spectra clearly show that after testing the majority of the copper in the sample has been reduced from Cu(II) oxide to Cu(0).[34] This conclusion is also supported by the EELS O edge, which initially shows three peaks, indicative of Cu(II) oxide and the intensity of which is substantially decreased after testing.[34]

To get more insight into this intriguing effect, aberration corrected high resolution STEM-EDX measurements (**Figure 6-19**) were carried out with a FEI Titan Themis microscope, eventually providing further support for the mixing of Cu and Sn. These measurements showed that before testing, Sn was mainly found on the perimeter of the CuO structure, giving way to a more uniform distribution after the catalytic reaction. This indicates that despite having been deposited at the surface, Sn redistributes during the electrocatalytic reaction, potentially leading to the formation of an alloy.[17]

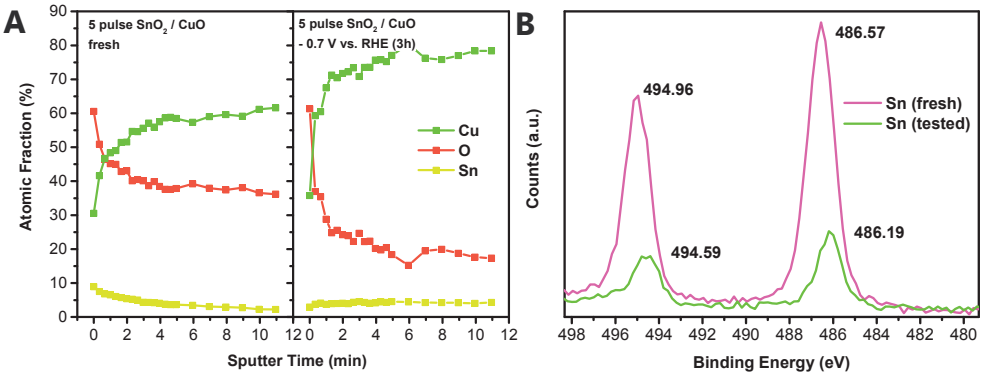

Figure 6-18: **XPS analysis before and after electrochemical testing.** (A) XPS Sputtering Depth profile (Ar gun, 2kV, 2x2 mm, 9 nm/min on flat sample). In the case of untested samples, more Sn can be found at the surface of the structure. In the case of tested samples, Sn is more distributed toward the interior of the structure. Also, tested samples contain much less oxygen than untested ones, while oxygen is interestingly still present to deep within the structure. (B) Sn 3d surface XPS spectrum of fresh and tested samples with 5 cycles SnO_2 on CuO. After reaction, Sn is found in a more reduced state. The peak energy is indicated.

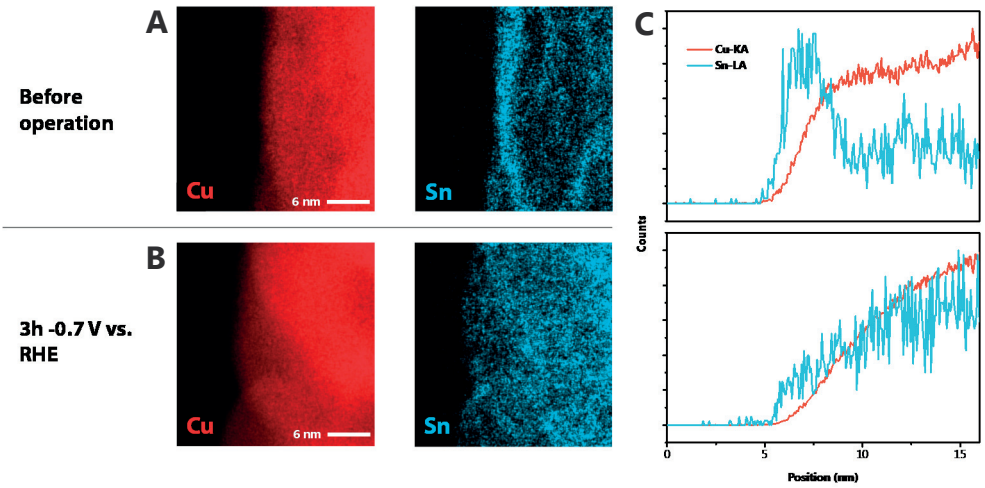

Figure 6-19: **High-resolution STEM-EDX maps before and after electrochemical testing.** Data was recorded with an aberration corrected FEI Titan Themis Microscope, equipped with a 4-quadrant SDD EDX detector (Bruker). Data has been analysed using the "Esprit" software package (Bruker). (A) Edge of a pristine CuO nanowire after deposition of 2 cycles of SnO_2. (B) Same sample after operation at -0.7 V vs. RHE in 0.1 M $NaHCO_3$ for 3 h. It can be seen that while originally Sn is predominantly found at the surface of the structure, it was found more evenly distributed in the structure after electrochemical operation. (C) The same trend becomes evident from EDX line scans on both samples, where the more uniform nature of the Sn distribution becomes evident.

After testing, SEM analysis of the unmodified CuO samples showed the appearance of a large number of cracks in the nanowire structure, which otherwise appeared to

stay intact. However, in contrast to neat CuO, the SnO_2 modified samples showed a slightly different morphology which was characterized by the appearance of fiber-like extensions at the tips of the nanowires (**Figure 6-20**).

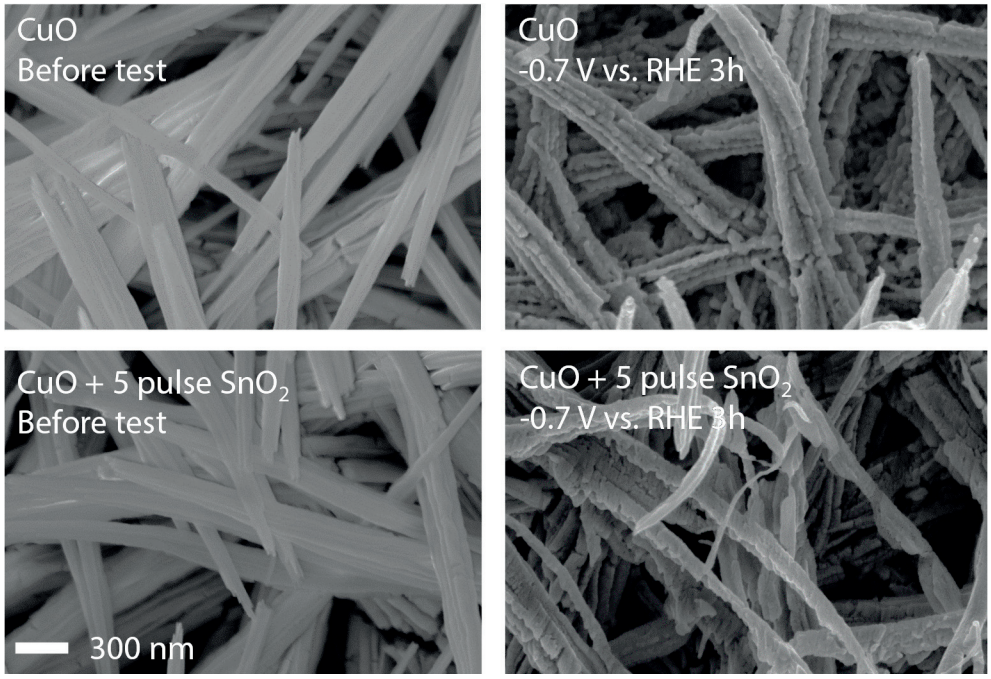

Figure 6-20: **Morphology change during electrochemical operation.** SEM micrographs of uncoated and ALD-coated CuO nanowires before- and after electrocatalytic testing at -0.7 V vs. RHE for 3h. After operation, the structures show more cracks, and in the case of SnO_2-coated samples, showed the appearance of fibre-like extensions at the nanowire tips.

STEM-EDX measurements of these fibers showed that they contain both Cu and Sn in a ratio similar to the rest of the structure. ICP-MS analysis of the electrolyte after electrochemical tests showed both Cu and Sn below the detection limit. From all of these data it can be concluded that the catalyst nanowire structure remains largely intact upon long-term testing, after electrolysis the Sn is found to be uniformly distributed and is present mainly in the +2 oxidation state with the appearance of some Cu(I) in contrast to the initial state where it is predominantly found as Sn(IV) at the surface. It has to be noted that post-electrolysis *ex situ* analysis is sensitive to surface oxidation in air which may occur during sample transfer, and may not necessarily reflect on the catalytically active species. Previous literature suggested that SnO_2 only led to a good performance as a CO_2 reduction catalyst when present in a metastable oxide state beyond its reduction potential.[35]

In addition, the question of whether residual oxides play a role in CO_2 reduction catalysis on oxide-derived catalysts is still under debate in the community.[14,36–38] The oxidation states of both Sn and Cu in the active catalyst thus remain uncertain and work to address this question will be needed to gain improved understanding of these systems. Such insight will likely come from *in-situ* measurements which should be able to reliably assess the metal oxidation states during catalytic operation.

Bifunctional catalysis

An overall electrochemical system, affecting the splitting of CO_2 into CO and O_2, requires a cathode for CO_2 reduction and an anode for water oxidation. Improving on the Au and IrO_2-based design introduced in **Chapter 5** requires the introduction of earth-abundant electrode materials and the use of a membrane for product separation. Numerous Earth-abundant catalysts have been developed for the oxygen evolution reaction, most of them consisting of transition metals such as Ni and Fe, which are prone to dissolve and redeposit on the CO_2 reducing cathode. As shown in **Chapter 5**, this leads to poisoning of the electrode,[23] a problem which may be averted by avoiding the use of elements foreign to the cathode. It was therefore decided to investigate OER electrodes which are made from the same elements as the cathode, leading to a bifunctional catalyst configuration that has the additional benefit of making the device simpler and more cost effective, which is a truly novel concept and particularly interesting for the field of CO_2 reduction. Though Ni, Fe and Co based compounds dominate the literature on OER catalysis,[39–41] a number of recent reports have demonstrated the activity of CuO toward the oxygen evolution reaction, making it a viable bifunctional electrode for both CO_2 reduction and OER.[42–45] To assess the activity of the CuO nanowire samples for OER, linear sweep voltammetry measurements were carried out in a three-electrode setup using 0.25 M KOH as electrolyte. Oxygen evolution was observed at an overpotential of 320 mV with a current density of 0.1 mA cm^{-2}, the value being similar with and without ALD SnO_2 coating (**Figure 6-21a**). Gas chromatography (GC) measurements confirmed that the observed current leads to quantitative oxygen evolution under these conditions, pointing to the absence of anode corrosion

(**Figure 6-21b**). However, in 1.0 M KOH, the electrode was found to rapidly deactivate. From these results it can be inferred that SnO_2-coated CuO nanowires represent efficient catalysts for both the reduction of CO_2 to CO and the electrochemical oxidation of water to produce O_2, which enables the conception of a bifunctional system, using the same electrode for both reactions.

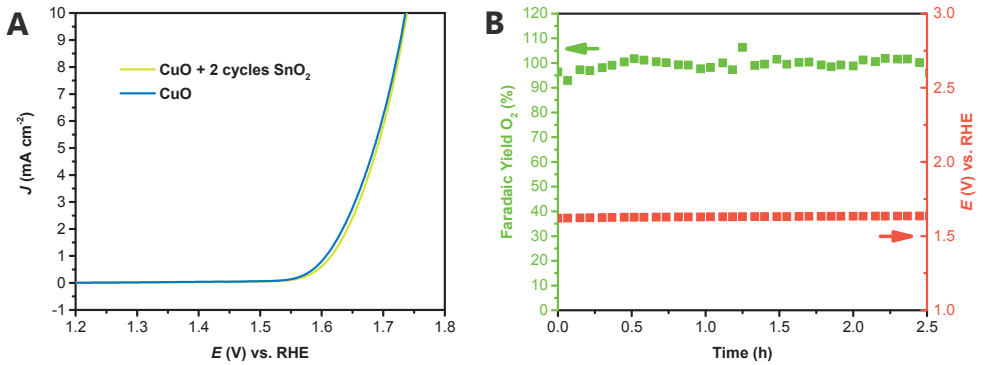

Figure 6-21: **OER activity of SnO_2-coated CuO nanowires.** (A) J-V curves characterizing the OER performance of bare and ALD-coated CuO nanowires in 0.25 M KOH. (B) Quantification of oxygen produced at 1.25 mA cm^{-2} from a SnO_2-coated CuO nanowire sample in 0.25 M KOH. A near-quantitative Faradaic yield in oxygen was observed.

In setting up a system for sustained CO_2 electrolysis, a key challenge is the electrolyte. In contrast to the oxygen evolution reaction which is most efficient when run under alkaline conditions, electrochemical CO_2 reduction tends to work best under neutral conditions.[12] If SnO_2 coated CuO electrodes are to be employed, these requirements become mandatory, as described before. Using a catholyte that differs from the anolyte would address these problems but challenges arise from the need of using an ion exchange membrane to keep the two electrolytes apart. During operation, OH^- ions are consumed at the anode while protons are consumed at the cathode, producing a pH gradient that will ultimately arrest the reaction. At the same time, the current carrying ions are unlikely to be OH^- or H^+ since in the case of a cation exchange membrane, the positively charged electrolyte cation, present in large excess, will flow from the anode to the cathode compartment, building up a cation concentration gradient since these ions are not electroactive. A similar phenomenon would occur for anion exchange membranes, where HCO_3^- ions are to be expected to carry the current. Furthermore, passive exchange of ions will occur

across the membrane as long as their concentration is different in the two compartments (shown later).

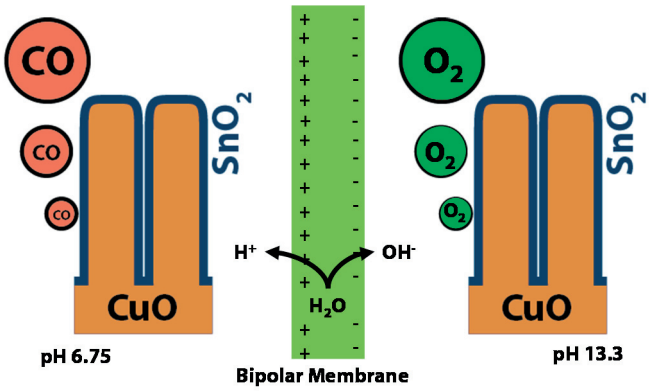

Figure 6-22: **Bifunctional catalysis.** Schematic representation of a bifunctional CO_2 electrolysis setup, involving a bipolar membrane which enables the use of all earth-abundant catalysts.

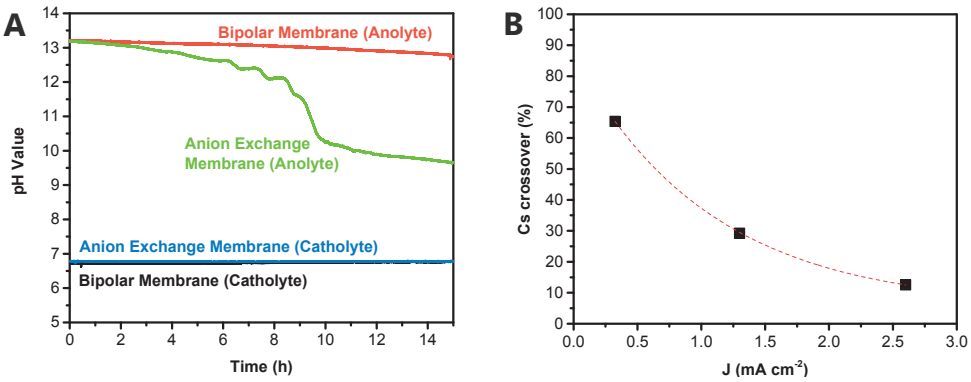

Figure 6-23: **Performance of bipolar membrane.** (A) Measurement of pH in anode and cathode compartments upon application of 0.5 mA cm^{-2} (membrane area) to two Pt electrodes in 0.25 M KOH (Anode) and 0.1 M $NaHCO_3$ (Cathode). It can be seen that a substantial change in pH is observed when using an anion exchange membrane, whereas only a weak change was observed in presence of a bipolar membrane. The catholyte pH stays virtually unchanged in the case of the anion exchange membranes, because any OH^- reaching this CO_2-saturated compartment will be transformed into HCO_3^-. (B) The selectivity of the bipolar membrane toward the transport of Cs^+ cations decreases at larger current densities. Tested with a 10 cm^2 membrane, Pt wire as anode and cathode. Catholyte: 0.1 M CsHCO3, Anolyte: 0.25 M CsOH.

Bipolar membranes offer an elegant solution to these problems, enabling the sustainable use of distinct electrolyte compositions, exhibiting different pH values in two separate compartments, as has been demonstrated previously for the case of water electrolysis.[46–49] They therefore are the key piece enabling the design of a bifunctional electrolysis device, as is depicted in **Figure 6-22**. Bipolar membranes

overcome the above mentioned challenges by using a double-layer membrane, consisting of an anion exchanger on the anode side and a cation exchanger on the cathode side of the cell. These block the straight-through transport of both cations and anions. However, water is able to penetrate between the two layers, where it is dissociated into OH^- and H^+ which are each transported through their respective ion exchange layer to their respective compartment, carrying the ionic current. Under these conditions, the current carrying ions consumed at the electrode in the Faradaic reactions are replenished, avoiding the buildup of a pH or ion gradient, as well as avoiding passive ion exchange, as is demonstrated in **Figure 6-23a**.

It has to be noted, however, that bipolar membranes are not yet perfect. While they show a good selectivity toward the desired water dissociation process at high current density, ions in the electrolyte still carry a certain amount of current, which becomes particularly relevant at low current densities, as is depicted in **Figure 6-23b**. Further research on this type of membrane is therefore necessary for them to be used widely in electrolysis applications.

Sustained photo-driven CO_2 reduction using water as electron source

Exploiting the properties of bipolar membranes and the bifunctional nature of the SnO_2-modified CuO catalysts, a 20 cm^2 sized prototype electrolysis cell was designed consisting exclusively of Earth-abundant materials. To optimize catalyst performance according to the findings with different electrolytes as detailed above, solutions of 0.1 M $CsHCO_3$ (pH 6.75) and 0.25 M CsOH (pH 13.3) were used as catholyte and anolyte, respectively (see schematic in **Figure 6-24a**). The resulting dark load of the catalytic system, composed of cathode, anode and bipolar membrane, is depicted by the black curve with symbols in **Figure 6-24b**, whereas the individual potentials of the cell components as a function of the current density are depicted in **Figure 6-25**. Driven by a single 3-junction GaInP/GaInAs/Ge PV device, illuminated with standard AM 1.5G solar light at room temperature and 1000 W/m^2 (1 sun) intensity, the unassisted solar-driven reduction of CO_2 was achieved. Overlaid with the *J*-V curve of the PV device, the predicted operating point of the overall solar driven system is expected at ~2.38 V. In agreement with

this prediction, long term operation of the coupled system showed an operating voltage of 2.39 V, producing a photo-current density of 11.57 mA cm^{-2} at room temperature (**Figure 6-24b**).

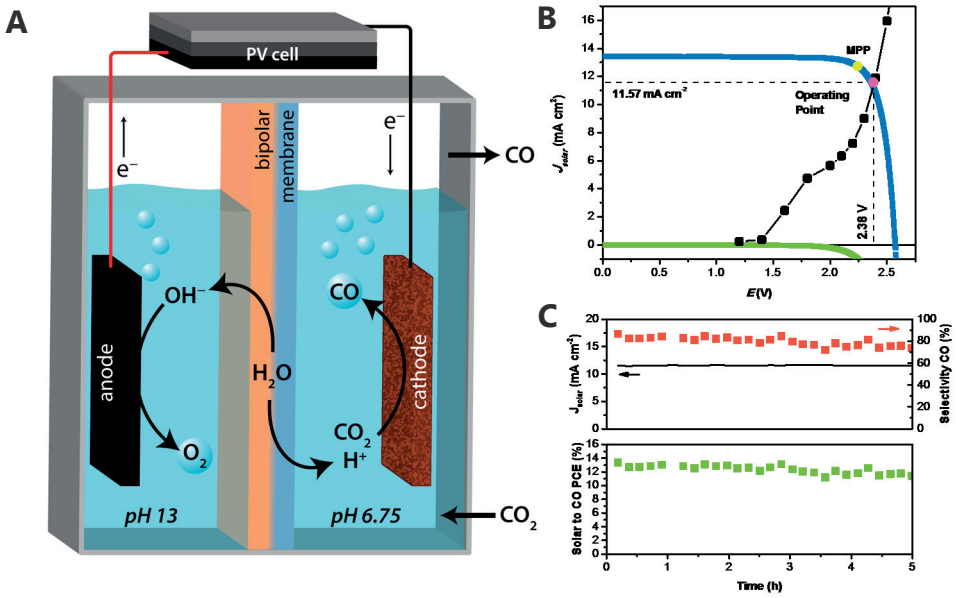

Figure 6-24: **Photoelectrolysis of CO_2.** (A) Schematic of the solar-driven CO_2 reduction device. (B) Photovoltaic and electrocatalytic J-V behaviors. The observed long term operating point of the device is marked by a pink dot, whereas the PV MPP is indicated by a yellow dot.. We observed good agreement between the calculated intersection and the measured operating point for the device. (C) Selectivity toward carbon monoxide, solar current density and solar-to-CO efficiency as a function of photoelectrolysis time.

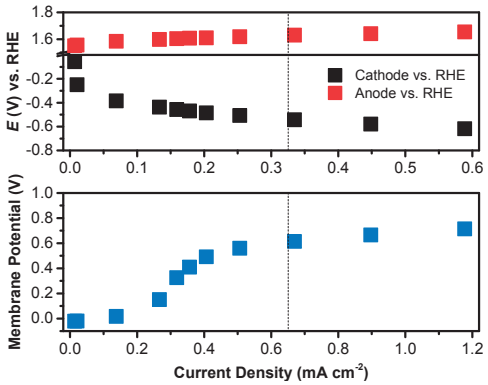

Figure 6-25: **Potential distribution in the electrolysis cell.** Steady-state J-V data for each cell component using 0.25 M CsOH as anolyte and CO_2-saturated 0.1 M $CsHCO_3$ as catholyte, recorded with the same electrodes as used for the long-term solar-driven CO_2 electrolysis experiment. The long-term operation point is designated by a dashed line.

The measured cathode potential remained constant at -0.55 V vs. RHE over the test period of 5 h and the observed Faradaic efficiency in CO of 81% led to a solar-to-CO free energy conversion efficiency peaking at 13.4%. On average, the solar-to-CO efficiency reached 12.4%, whereas the average total solar-to-fuel efficiency was found to be 13.8%. At the same time, the anode potential remained constant at +1.61 V vs. RHE. The evolution of the system potentials is shown in **Figure 6-26**. Overpotential losses at the anode and cathode were η_a = 380 mV and η_c = 440 mV, respectively, whereas the membrane potential was found to be 606 mV which exceeds the 370 mV protomotive force between the two compartments due to the pH gradient. Thus, the overpotential loss on the membrane is 236 mV.

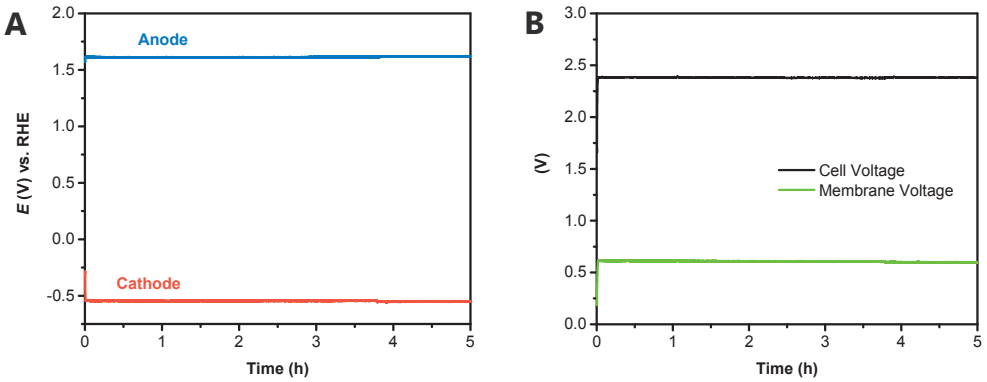

Figure 6-26: **Evolution of system potentials with time.** (A) Anode and cathode potentials, relative to the RHE scale in their respective compartment. (B) Cell voltage and potential drop over the bipolar membrane as a function of time.

Over the course of the experiment, the yield in hydrogen increased slightly and concurrently with the sum of all observed products, which peaked at 14.4% for overall solar to fuel conversion efficiency. The SFE increases to ~16% if the higher heating values of CO and H_2 are considered. These observed solar to CO efficiencies establish a new record efficiency doubling the one reported in **Chapter 5**[46] of 6.5 % for this key photo-driven CO_2 splitting reaction, which is gaining increasing attention both from academia and industry.[50]

Perspective

To the best of my knowledge, this is the first demonstration of the use of atomic layer deposition in the field of CO_2 reduction electrocatalysis.[18] The results show impressive and tunable changes in selectivity upon ALD modification of CuO. Of

the 2-electron products accessible from CO_2, CO is an interesting candidate due to its gaseous character and versatility as a vector in well-established processes leading to bulk chemicals and transportation fuels.[51] In the future, direct production of other reduction products such as ethylene or alcohols in an electrochemical process remains a very important objective since it may provide a way to produce commodity chemicals and fuels directly from electrical power and abundant CO_2. In this context, the ability of ALD to modify the surface of CO_2 reduction catalysts with fine control of product selectivity and reproducibility is a promising and very powerful tool toward the future design of CO_2 reduction catalysts. The broad range of materials accessible by ALD will likely prove particularly helpful in the framework of designing catalysts able to overcome scaling relations, which will be crucial when targeting CO_2 reduction products other than CO and HCOOH.[52]

The catalyst system demonstrated herein is the first demonstration of an all Earth-abundant CO_2 to CO electrolyzer working in aqueous electrolyte. In addition, the SnO_2-modified CuO cathode remains selective over a large potential range, enabling stable operation at various power levels. This will become crucial for implementing solar driven fuel generating systems, which have to cope with sunlight intensity fluctuations during the day. A solar to fuel catalyst must be able to tolerate this fluctuation at constant selectivity. As an additional strong point, the introduction of a bipolar membrane into an electrochemical CO_2 reduction system is likely to provide a solution to the issue of maintaining pH and ion gradients, which constitutes a major issue for the field. During the experiments for this chapter, some ion crossover was found to occur due to imperfections of the bipolar membrane, with the percentage depending on the operating current density as described before. Further membrane development will thus be crucial to tackle this issue for sustained long term operation.

Finally, it has to be emphasized that deposition of ultrathin layers of SnO_2 on the surface of the catalyst led to pronounced changes in selectivity. This serves as a good example for the exceptionally high degree of susceptibility of CO_2 reduction catalysts to trace elements in the system, whether by design or by accident during the catalyst synthesis procedure or from impurities in the electrolyte. This sensitivity is a likely culprit for the broad variations of CO_2 reduction activity

reported in the literature but at the same time also opens a large parameter space options for catalyst modifications.

Conclusion

It has been demonstrated that ALD modification of CuO nanowires with small amounts of SnO_2 successfully directs the selectivity toward producing CO in the electroreduction of CO_2. Furthermore, it has been shown that the same catalyst can be applied toward the OER, which led to the design of a bifunctional, intrinsically non-poisoning and all Earth-abundant system using SnO_2-coated CuO as both CO_2 reduction and water oxidation catalyst. To allow for the sustainable operation under different catholyte and anolyte, a bipolar membrane was successfully employed. This system was driven by a 3-junction photovoltaic using simulated AM 1.5G illumination, achieving a new record solar-to-CO efficiency peaking at 13.4%. Accounting for all reduction products, the total solar to fuel efficiency peaks at 14.4%. The SFE increases to ~16% if the higher heating values of CO and H_2 are considered.

Methods

Unless stated otherwise, 18.2 MΩ water was employed and experiments were carried out in an air-conditioned room at 22 °C.

Preparation of catalyst samples

TEC 15 fluorine-doped tin oxide (FTO) glass was treated with Zn powder and 10% HCl solution to remove the conductive coating, followed by rinsing with water. Removal was confirmed by the absence of electrical conductivity. Subsequently, 1.5 µm of Cu (99.995%) were deposited on the glass side of the substrate using a DP 650 sputter coater (Alliance-Concept, France). These samples (3.3×7 cm) were subsequently anodized in 3 M KOH (technical grade, Reactolab, Switzerland). The counter electrode was a sheet of FTO, coated with 500 nm of Au. Anodization was carried out at a constant room temperature of 22 °C at 8 mA cm^{-2} until reaching a potential of 2 V, at which point the sample was removed and copiously rinsed with H_2O. Subsequently, the sample was left to dry on a sheet of household paper.

After drying, the samples were cut to the size of 3.3×1 cm and dehydrated at 150 °C for 1 h in a box furnace (Lenton, UK). Heating and cooling rates were set to 10 °C min^{-1}.

ALD deposition was carried out using a home-made ALD system that has been described in detail elsewhere.[53] SnO_2 was deposited at 118 °C from tetrakis(dimethylamino)-tin(IV) (TDMASn, 99.99% Sn, Strem Chemicals, USA). Ozone served as oxidizer and was generated by an ozone generator (AC-2025, IN USA Incorporated) supplied with oxygen (99.9995%, Carbagas, Switzerland) and producing a concentration of 13% ozone in O_2. N_2 (99.9999%, Carbagas, Switzerland) was used as carrier gas at a flow rate of 10 mln min^{-1}. Prior to deposition, the sample was pretreated with 7×0.01 sec ozone pulses under vacuum. The precursor, heated to 65 °C was pulsed under exposure mode for 10 s, unless stated otherwise. After 15 additional seconds, the chamber was set under vacuum. After waiting for 60 s, the sample was exposed for 15 s to a 0.015 s pulse of ozone in O_2. This sequence was repeated until reaching the desired amount of cycles. Before deposition, the system was left to equilibrate for ~30 min. A constant

growth/cycle of 0.15 nm/cycle was measured by ellipsometry (Sopra GES 5E) on Si wafers for depositions with Sn pulse durations of 10 s.

ALD coating of CuO nanopowders for chemisorption measurements (<50 nm, Sigma-Aldrich) was carried out by Beneq using a fluidized bed ALD reactor (Beneq, Finland). Tetrakis(dimethylamino)-tin(IV) was used as precursor and H_2O as oxidizer. The precursor was held at 100 °C and deposition was carried out at 180 °C. In order to reach complete saturation with precursor, micropulsing was used. Two cycles of SnO_2 were deposited.

Ti slides (Sigma Aldrich) were etched for 1 h in boiling 1 M oxalic acid (Sigma Aldrich), followed by copious rinsing with water. 18.8 mg of powder were transformed into a slurry by adding 400 µL of H_2O. Subsequently, 20 µL of this slurry were drop casted on etched Ti substrates. The non-covered area was inactivated with Kapton tape and the samples tested as described below.

Electrocatalytic testing

The non-anodized part of the samples was masked with Kapton tape (Eurostat Group, France). Subsequently, the surface area was measured and the sample was fixed in the cathode compartment of a custom-made gastight electrochemical cell (PEEK, as described in **Chapter 1**), containing 15 mL of electrolyte. A membrane (Nafion 117N, Ion Power, USA), was used to separate the anode compartment, which was exposed to air. A double-junction of ceramic diaphragms (Metrohm, Switzerland) was used to separate the reference electrode (Ag/AgCl KCl sat., Metrohm, Switzerland) from the cathode compartment. Potential values were transformed to the RHE scale as follows: $V_{RHE} = V_{Ag/AgCl\ (KCl\ sat.)} + 0.197\ V + 0.059\ V \times pH$.

The electrolyte was prepared as follows. 20 g of Chelex® 100 (100–200 mesh, Fluka, Switzerland) was added to a 0.5 M solution of $NaHCO_3$ (99+%, Sigma Aldrich), stirred for several days and stored in this form. From this stock solution, 0.1 M $NaHCO_3$ was prepared by dilution with high purity H_2O. Prior to adding to the cell, the electrolyte was sparged with CO_2 (99.998%, Carbagas, Switzerland) for several hours. Before use, the ion exchange resin was removed using a syringe filter (Filtropur S 0.2 µm, Sarsted, Germany).

A SP-300 (BioLogic, France) and an Interface 1000 (Gamry, USA) potentiostat were used to polarize the sample. Until reaching -0.5 V vs. RHE, the samples were reduced galvanostatically at -2 mA cm^{-2}, followed by polarization at the desired potential for 3 h. The resulting current was recorded every 0.5 s. For potential variations on SnO_2-coated samples, samples were held at -0.7 V vs. RHE for 1 h before 6 h polarization at the desired potential.

CO_2 was sparged into the cell at 10.00 mLn min^{-1} using a mass flow controller (Bronkhorst High-Tech, F201CV, Bronkhorst, Netherlands) and at the cell outlet passed into the sample loop of a gas chromatograph (Trace ULTRA, Thermo), equipped with a ShinCarbon column (Restek, USA) and a PDD detector (Vici, USA). Helium (99.9999%, Carbagas, Switzerland) was used as carrier gas and injections were carried out approximately every 15 min. The gas analysis was calibrated using a certified gas standard containing all relevant gases in CO_2 (Carbagas, Switzerland), which was flown through the sample loop at the same flow rate as during the experiment.

To substantiate that gaseous CO_2 is the source of carbon for the synthesis of carbon monoxide, experiments using isotopic $^{13}CO_2$ as reagent and $NaH^{13}CO_3$ as supporting electrolyte were carried out. The presence of ^{12}CO and ^{13}CO in the product gas was assessed by Fourier Transform Infrared (FTIR) spectroscopy of the product gas in a spectroscopic gas cell, equipped with two KBr windows. FTIR rovibrational spectra of ^{12}CO and ^{13}CO are distinct and characterized by a shift to lower wavenumbers for ^{13}CO.[54] The product gases from the electrochemical test cell were passed through the IR gas cell after residual water was condensed out at -25 °C to avoid damaging the KBr windows. During a typical chronoamperometric test of a SnO_2-modified CuO sample, the substrate gas, flowing at 10 mLn min^{-1}, was switched from $^{12}CO_2$ to $^{13}CO_2$. At the times indicated in **Figure 6-8** and **Figure 6-9**, FTIR spectra were recorded, demonstrating the shift to the exclusive production of ^{13}CO in the presence of $^{13}CO_2$ and confirming gaseous CO_2 as the source of carbon in the reaction.

Liquid analysis was performed on the electrolyte after each polarization experiment by NMR spectroscopy using a presaturation technique to suppress the signal of water. An Avance 500 Spectrometer (Bruker, Switzerland), equipped with

CryoProbe (Bruker, Switzerland) was used. 100 µL of 143 µM DMSO in D_2O were added as internal standard to 500 µL of sample in a high-field NMR tube (Wilmad Labglass, USA). In order to account for differences in T1, calibration curves were recorded for each quantified species, while keeping the acquisition parameters constant for all experiments. A typical NMR spectrum is shown in **Figure 6-27**.

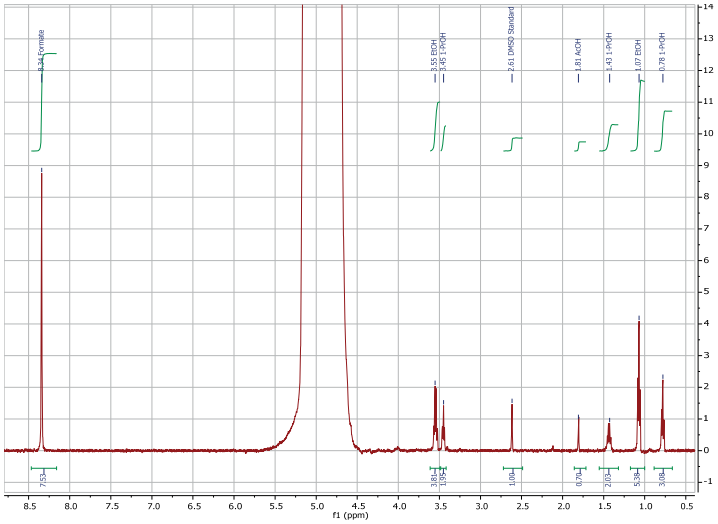

Figure 6-27: **Liquid product analysis.** Representative NMR spectrum for a CuO nanowire sample measured at -0.9 V vs. RHE for 3h.

Faradaic efficiencies were calculated as follows. The molar flow of gas from the test cell was calculated using the concentration of species k measured by GC (x_k [mol mol^{-1}]) and the CO_2 flow rate (F_{CO2} [mol s^{-1}]). Knowing the number of exchanged electrons to produce species k from CO_2 (n_k [-]) and the Faraday constant (96485 [C mol^{-1}]), the partial current toward species k (i_k [A]) was calculated. Comparing the partial current to the total current (i_{tot}) yielded the Faradaic efficiency for species k (FE_k):

$$FE_k = \frac{i_k}{i_{tot}} = \frac{x_k \cdot F_{CO_2} \cdot n_k \cdot 96485[C\ mol^{-1}]}{i_{tot}}$$

For liquid samples, NMR spectra were Fourier-transformed without apodization and baseline corrected using Whittaker Smoother in MestReNova. The concentration of each product was calculated from the relative peak area between DMSO, the formate singlet, ethanol triplet and 1-propanol triplet, based on calibration curves for each species. A representative NMR spectrum is shown in

Figure 6-27. The concentration of species l in the test cell (c_l [mol L^{-1}]) was multiplied with the electrolyte volume in the cell (V_{cell} [L]), the number of exchanged electrons (n_l [-]) and the Faraday constant (96485 [C mol^{-1}]) and subsequently compared to the total charge passed (q_{tot}) to yield the Faradaic efficiency (FE_l):

$$FE_l = \frac{q_l}{q_{tot}} = \frac{c_l \cdot V_{cell} \cdot n_l \cdot 96485[C\ mol^{-1}]}{q_{tot}}$$

The relevant potential drop for I-V correction of the Tafel plots was determined by using hybrid electrochemical impedance spectroscopy between 1 MHz and 100 mHz, 10 points/dec, 10 mV perturbation at -0.7 V vs. RHE in CO_2-saturated 0.1 M $NaHCO_3$ electrolyte. The measurement was carried out at the end of a test using a representive CuO nanowire sample, coated with 2 cycles of ALD SnO_2. The IR-drop was determined to be 81 Ω and this value was used to correct the potentials in the Tafel plot.

Overpotentials were calculated as follows:

$$\eta_{CO_2/CO} = \left|E_{Cathode} - E^0_{CO_2/CO}\right|$$

$$\eta_{O_2/H2O} = \left|\mathrm{E}_{Anode} - E^0_{O_2/H2O}\right|$$

where $\eta_{CO_2/CO}$, $E_{Cathode}$, $E^0_{CO_2/CO}$ and $\eta_{O_2/H2O}$, E_{Anode}, $E^0_{O_2/H2O}$ designate the overpotentials, operating potentials of the respective electrode and themodynamic equilibrium potentials (-0.11 V vs. RHE for CO_2/CO and +1.23 V vs. RHE for O_2/H_2O) for the CO and O_2 formation half-reactions, respectively.

Solar-driven CO_2 reduction

Solar-driven CO_2 reduction experiments were carried out in a large scale prototype cell, using a bipolar membrane (Fumasep® FBM). 0.25 M CsOH was used as anolyte and CO_2-saturated 0.1 M $CsHCO_3$ as catholyte. Both anode and cathode were CuO nanowires, coated with 2 ALD cycles of SnO_2. The anode and cathode surface area were both 20.0 cm^2 and the membrane 10 cm^2. The system was driven using an unmasked commercial 3-junction GaInP/GaInAs/Ge solar cell (photo shown in **Figure 6-28**), illuminated with a simulated AM1.5G spectrum at 1 sun

intensity from an Oriel LCS-100 Class ABB solar simulator (Newport, USA) and achieving a maximum electrical power conversion efficiency of 28.5% at 2.24 V. During operation, the potential of anode, cathode, reference electrodes in both the anode and cathode compartments and PV cell were monitored using an NI USB-6211 A/D converter and a custom-made LabView program. Before start, the system was activated at -0.7 V vs. RHE and then connected to the illuminated PV device, leading to an operating current of 6.51 mA, corresponding to 0.33 mA cm^{-2} for the anode and cathode and 0.66 mA cm^{-2} for the membrane. The stated photocurrent density is based on the illuminated surface area of the GaInP/GaInAs/Ge multijunction solar cell.

Solar to fuel efficiencies were calculated as follows:

$$Eff_{CO} = \frac{P_{CO}}{P_{Solar}} = \frac{E^0_{CO/CO_2} \cdot J_{Solar} \cdot FE_{CO}}{P_{Solar}}$$

where P_{CO} is the power going toward the production of carbon monoxide from CO_2, P_{Solar} is the incident solar power on the solar cell, $E^0_{CO/CO_2} = 1.34\,V$ is the equilibrium potential for the reaction $CO_2 + 2e^- \rightarrow CO + ½\,O_2$, J_{Solar} is the current density at the solar absorber and FE_{CO} is the Faradaic efficiency of CO production.

The potential distribution in the system was measured by applying a series of currents to the cell. After stabilizing for 5 minutes at each current, the cathode and anode operating potential, as well as the membrane voltage were recorded against Ag/AgCl reference electrodes in each compartment.

Sample characterization

X-Ray diffraction was carried out on a D8 DISCOVER diffractometer (Bruker, Germany), equipped with a silicon strip detector LynxEye (Bruker, Germany) and a monochromated Cu K-α source. Patterns were recorded in locked-coupled mode between 2θ = 10 to 70°, at 0.1° min^{-1} with a step size of 0.02.

Raman scattering experiments were carried out using an XploRA ONE™ Raman microscope (Horiba, Japan), equipped with a 532 nm doubled Nd:YAG DPSS laser. The laser power was set to 25%, acquisition time was 3 s and 200 spectra were recorded for each sample. X-Ray photoelectron spectroscopy and profile analysis

was carried out using a PHI VersaProbe II XPS microprobe. Scanning electron microscopy was carried out on a MERLIN high resolution SEM (Zeiss, Germany).

Transmission electron microscopy was carried out on a Technai Osiris electron microscope (FEI), and elemental mappings were obtained from energy-dispersive X-ray (EDX) spectra obtained in scanning transmission electron microscopy (STEM) mode. Aberration-corrected STEM was carried out on a Titan Themis (FEI).

Volumetric measurements of H_2 and CO adsorption isotherms were carried out at 35 °C between 2 and 300 mbar on a Micromeritics 3 Flex instrument. The sample (300 mg) was loaded into a U-shaped cell and reduced *in-situ* under H_2 flow (50 mL $min^{-1)}$ at 250 °C (5 °C min^{-1}) for 1 h and adsorbed H_2 was removed by vacuum (< 10^{-3} mbar) at 250 °C for 30 min. After cooling down to 35 °C under vacuum, a leak test was performed prior to analysis.

H_2 Temperature programmed reduction (H_2-TPR) experiments were carried out on a Micromeritics Autochem 2920 instrument. The sample (300 mg) was loaded into a U-shaped cell and dried under He flow (50 mL min^{-1}) at 120 °C (5 °C min^{-1}) for 30 min. After cooling down to 40 °C, the flow was switched to a H_2/Ar mixture (10/90 vol.) and the sample was ramped to 250 °C (10 °C min^{-1}) while H_2 consumption was quantified using a calibrated thermal conductivity detector (TCD). An isopropanol/liquid N_2 cold bath was used between the sample and the TCD to trap water produced during TPR, the absence of which was verified by monitoring mass 18 on a MKS Cirrus 2 mass spectrometer placed after the TCD.

Inductively Coupled Plasma Mass Spectrometry (ICP-MS) measurements were carried out on a Perkin-Elmer DRC II. A plasma torch in axial position was run under argon 99.99998%. Calibration was carried on each of the measured elements between 1 and 50 µg/l over 6 points. Prior to analysis, samples were diluted 10'000 times in order to avoid saturation due to excess sodium ions from the electrolyte.

Bipolar membrane characterization was carried out by running a 10 cm^2 bipolar membrane using two Pt wire electrodes with CO_2-saturated 0.1 M $NaHCO_3$ catholyte and 0.25 M CsOH anolyte at various current densities until reaching ~125 Coulombs of passed charge. Electrolyte composition analysis of the initial and final

state was subsequently performed by ion chromatography using a Dionex™ Integrion™ HPIC™ System (Thermo Fisher Scientific). Samples were diluted 100x with water in order to avoid saturation.

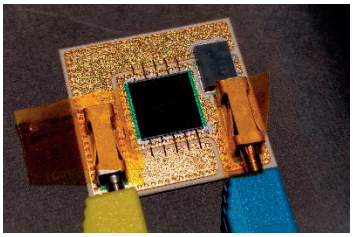

Figure 6-28: **Illustration of the 3-junction photovoltaic cell.**

References

1. Schreier, M. *et al.* Efficient and selective carbon dioxide reduction on low cost protected Cu_2O photocathodes using a molecular catalyst. *Energy Env. Sci* **8,** 855–861 (2015).
2. Schreier, M. *et al.* Covalent Immobilization of a Molecular Catalyst on Cu_2O Photocathodes for CO_2 Reduction. *J. Am. Chem. Soc.* **138,** 1938–1946 (2016).
3. Zhang, S. *et al.* Polymer-supported CuPd nanoalloy as a synergistic catalyst for electrocatalytic reduction of carbon dioxide to methane. *Proc. Natl. Acad. Sci.* **112,** 15809–15814 (2015).
4. Ren, D. *et al.* Selective Electrochemical Reduction of Carbon Dioxide to Ethylene and Ethanol on Copper(I) Oxide Catalysts. *ACS Catal.* **5,** 2814–2821 (2015).
5. Qiao, J., Liu, Y., Hong, F. & Zhang, J. A review of catalysts for the electroreduction of carbon dioxide to produce low-carbon fuels. *Chem. Soc. Rev.* **43,** 631 (2014).
6. Kuhl, K. P., Cave, E. R., Abram, D. N. & Jaramillo, T. F. New insights into the electrochemical reduction of carbon dioxide on metallic copper surfaces. *Energy Environ. Sci.* **5,** 7050–7059 (2012).
7. Kuhl, K. P. *et al.* Electrocatalytic Conversion of Carbon Dioxide to Methane and Methanol on Transition Metal Surfaces. *J. Am. Chem. Soc.* **136,** 14107–14113 (2014).
8. Chen, Y., Li, C. W. & Kanan, M. W. Aqueous CO_2 Reduction at Very Low Overpotential on Oxide-Derived Au Nanoparticles. *J. Am. Chem. Soc.* **134,** 19969–19972 (2012).
9. Feng, X., Jiang, K., Fan, S. & Kanan, M. W. Grain-Boundary-Dependent CO_2 Electroreduction Activity. *J. Am. Chem. Soc.* **137,** 4606–4609 (2015).
10. Min, X. & Kanan, M. W. Pd-Catalyzed Electrohydrogenation of Carbon Dioxide to Formate: High Mass Activity at Low Overpotential and Identification of the Deactivation Pathway. *J. Am. Chem. Soc.* **137,** 4701–4708 (2015).
11. Lu, Q. *et al.* A selective and efficient electrocatalyst for carbon dioxide reduction. *Nat. Commun.* **5,** 3242 (2014).
12. Hori, Y. in *Handbook of Fuel Cells* (John Wiley & Sons, Ltd, 2010).
13. DiMeglio, J. L. & Rosenthal, J. Selective Conversion of CO_2 to CO with High Efficiency Using an Inexpensive Bismuth-Based Electrocatalyst. *J. Am. Chem. Soc.* **135,** 8798–8801 (2013).
14. Li, C. W. & Kanan, M. W. CO_2 Reduction at Low Overpotential on Cu Electrodes Resulting from the Reduction of Thick Cu_2O Films. *J. Am. Chem. Soc.* **134,** 7231–7234 (2012).
15. Rasul, S. *et al.* A Highly Selective Copper–Indium Bimetallic Electrocatalyst for the Electrochemical Reduction of Aqueous CO_2 to CO. *Angew. Chem. Int. Ed.* **54,** 2146–2150 (2015).
16. Watanabe, M., Shibata, M., Kato, A., Azuma, M. & Sakata, T. Design of Alloy Electrocatalysts for CO_2 Reduction III . The Selective and Reversible Reduction of on Cu Alloy Electrodes. *J. Electrochem. Soc.* **138,** 3382–3389 (1991).
17. Sarfraz, S., Garcia-Esparza, A. T., Jedidi, A., Cavallo, L. & Takanabe, K. Cu–Sn Bimetallic Catalyst for Selective Aqueous Electroreduction of CO_2 to CO. *ACS Catal.* **6,** 2842–2851 (2016).
18. O'Neill, B. J. *et al.* Catalyst Design with Atomic Layer Deposition. *ACS Catal.* **5,** 1804–1825 (2015).
19. Langereis, E. *et al.* In situ spectroscopic ellipsometry as a versatile tool for studying atomic layer deposition. *J. Phys. Appl. Phys.* **42,** 073001 (2009).
20. Luo, J. *et al.* Cu_2O Nanowire Photocathodes for Efficient and Durable Solar Water Splitting. *Nano Lett.* **16,** 1848–1857 (2016).
21. Wang, W., Wang, L., Shi, H. & Liang, Y. A room temperature chemical route for large scale synthesis of sub-15 nm ultralong CuO nanowires with strong size effect and enhanced photocatalytic activity. *CrystEngComm* **14,** 5914 (2012).
22. Szuber, J., Czempik, G., Larciprete, R., Koziej, D. & Adamowicz, B. XPS study of the L-CVD deposited SnO_2 thin films exposed to oxygen and hydrogen. *Thin Solid Films* **391,** 198–203 (2001).

23. Wuttig, A. & Surendranath, Y. Impurity Ion Complexation Enhances Carbon Dioxide Reduction Catalysis. *ACS Catal.* **5,** 4479–4484 (2015).
24. Lum, Y. *et al.* Trace Levels of Copper in Carbon Materials Show Significant Electrochemical CO_2 Reduction Activity. *ACS Catal.* **6,** 202–209 (2016).
25. Gattrell, M., Gupta, N. & Co, A. A review of the aqueous electrochemical reduction of CO_2 to hydrocarbons at copper. *J. Electroanal. Chem.* **594,** 1–19 (2006).
26. Ma, M., Djanashvili, K. & Smith, W. A. Selective electrochemical reduction of CO_2 to CO on CuO-derived Cu nanowires. *Phys Chem Chem Phys* **17,** 20861–20867 (2015).
27. Singh, M. R., Kwon, Y., Lum, Y., Ager, J. W. & Bell, A. T. Hydrolysis of Electrolyte Cations Enhances the Electrochemical Reduction of CO_2 over Ag and Cu. *J. Am. Chem. Soc.* **138,** 13006–13012 (2016).
28. Chen, Y. & Kanan, M. W. Tin Oxide Dependence of the CO_2 Reduction Efficiency on Tin Electrodes and Enhanced Activity for Tin/Tin Oxide Thin-Film Catalysts. *J. Am. Chem. Soc.* **134,** 1986–1989 (2012).
29. Zhang, S., Kang, P. & Meyer, T. J. Nanostructured Tin Catalysts for Selective Electrochemical Reduction of Carbon Dioxide to Formate. *J. Am. Chem. Soc.* **136,** 1734–1737 (2014).
30. Li, C. W., Ciston, J. & Kanan, M. W. Electroreduction of carbon monoxide to liquid fuel on oxide-derived nanocrystalline copper. *Nature* **508,** 504–507 (2014).
31. Verdaguer-Casadevall, A. *et al.* Probing the Active Surface Sites for CO Reduction on Oxide-Derived Copper Electrocatalysts. *J. Am. Chem. Soc.* **137,** 9808–9811 (2015).
32. Nørskov, J. K. *et al.* Trends in the Exchange Current for Hydrogen Evolution. *J. Electrochem. Soc.* **152,** J23-J26 (2005).
33. Kuhl, K. P. *et al.* Electrocatalytic Conversion of Carbon Dioxide to Methane and Methanol on Transition Metal Surfaces. *J. Am. Chem. Soc.* **136,** 14107–14113 (2014).
34. Leapman, R. D., Grunes, L. A. & Fejes, P. L. Study of the L 23 edges in the 3d transition metals and their oxides by electron-energy-loss spectroscopy with comparisons to theory. *Phys. Rev. B* **26,** 614 (1982).
35. Dutta, A., Kuzume, A., Rahaman, M., Vesztergom, S. & Broekmann, P. Monitoring the Chemical State of Catalysts for CO_2 Electroreduction: An In Operando Study. *ACS Catal.* **5,** 7498–7502 (2015).
36. Eilert, A., Roberts, F. S., Friebel, D. & Nilsson, A. Formation of Copper Catalysts for CO_2 Reduction with High Ethylene/Methane Product Ratio Investigated with In Situ X-ray Absorption Spectroscopy. *J. Phys. Chem. Lett.* **7,** 1466–1470 (2016).
37. Lee, S., Kim, D. & Lee, J. Electrocatalytic Production of C3-C4 Compounds by Conversion of CO_2 on a Chloride-Induced Bi-Phasic Cu_2O-Cu Catalyst. *Angew. Chem. Int. Ed.* **54,** 14701–14705 (2015).
38. Mistry, H. *et al.* Highly selective plasma-activated copper catalysts for carbon dioxide reduction to ethylene. *Nat. Commun.* **7,** 12123 (2016).
39. Luo, J. *et al.* Water photolysis at 12.3% efficiency via perovskite photovoltaics and Earth-abundant catalysts. *Science* **345,** 1593–1596 (2014).
40. Burke, M. S., Enman, L. J., Batchellor, A. S., Zou, S. & Boettcher, S. W. Oxygen Evolution Reaction Electrocatalysis on Transition Metal Oxides and (Oxy)hydroxides: Activity Trends and Design Principles. *Chem. Mater.* **27,** 7549–7558 (2015).
41. McCrory, C. C. L. *et al.* Benchmarking Hydrogen Evolving Reaction and Oxygen Evolving Reaction Electrocatalysts for Solar Water Splitting Devices. *J. Am. Chem. Soc.* **137,** 4347–4357 (2015).
42. Deng, Y., Handoko, A. D., Du, Y., Xi, S. & Yeo, B. S. *In Situ* Raman Spectroscopy of Copper and Copper Oxide Surfaces during Electrochemical Oxygen Evolution Reaction: Identification of Cu^{III} Oxides as Catalytically Active Species. *ACS Catal.* **6,** 2473–2481 (2016).
43. Liu, X., Cui, S., Qian, M., Sun, Z. & Du, P. In situ generated highly active copper oxide catalysts for the oxygen evolution reaction at low overpotential in alkaline solutions. *Chem Commun* **52,** 5546–5549 (2016).
44. Liu, X. *et al.* Self-Supported Copper Oxide Electrocatalyst for Water Oxidation at Low Overpotential and Confirmation of Its Robustness by Cu K-Edge X-ray Absorption Spectroscopy. *J. Phys. Chem. C* **120,** 831–840 (2016).

45. Liu, X. *et al.* Nanostructured copper oxide electrodeposited from copper(II) complexes as an active catalyst for electrocatalytic oxygen evolution reaction. *Electrochem. Commun.* **46,** 1–4 (2014).
46. Luo, J. *et al.* Bipolar Membrane-Assisted Solar Water Splitting in Optimal pH. *Adv. Energy Mater.* **6,** 1600100 (2016).
47. Vargas-Barbosa, N. M., Geise, G. M., Hickner, M. A. & Mallouk, T. E. Assessing the Utility of Bipolar Membranes for use in Photoelectrochemical Water-Splitting Cells. *ChemSusChem* **7,** 3017–3020 (2014).
48. Vermaas, D. A., Sassenburg, M. & Smith, W. A. Photo-assisted water splitting with bipolar membrane induced pH gradients for practical solar fuel devices. *J Mater Chem A* **3,** 19556–19562 (2015).
49. Sun, K. *et al.* A Stabilized, Intrinsically Safe, 10% Efficient, Solar-Driven Water-Splitting Cell Incorporating Earth-Abundant Electrocatalysts with Steady-State pH Gradients and Product Separation Enabled by a Bipolar Membrane. *Adv. Energy Mater.* **6,** 201600379 (2016).
50. Schreier, M. *et al.* Efficient photosynthesis of carbon monoxide from CO_2 using perovskite photovoltaics. *Nat. Commun.* **6,** 7326 (2015).
51. Dry, M. E. The Fischer–Tropsch process: 1950–2000. *Catal. Today* **71,** 227–241 (2002).
52. Li, Y. & Sun, Q. Recent Advances in Breaking Scaling Relations for Effective Electrochemical Conversion of CO_2. *Adv. Energy Mater.* **6,** 1600463 (2016).
53. Steier, L. *et al.* Low-Temperature Atomic Layer Deposition of Crystalline and Photoactive Ultrathin Hematite Films for Solar Water Splitting. *ACS Nano* **9,** 11775–11783 (2015).
54. Tidwell, E. K. P., Lamdin R.Blaine, Eugene D. Infrared absorption and emission spectra of carbon monoxide in the region from 4 to 6 microns. *J. Res. Natl. Bur. Stand.* **55,** 183 (1955).

7 General Conclusions and Summary

The studies in this thesis represent early examples of the integration of CO_2 reduction catalysts with photoabsorbers, both in the form of photoelectrodes and distinct PV-driven systems.

The operation of a homogeneous molecular rhenium bipyridyl catalyst was investigated on the surface of TiO_2-protected Cu_2O photocathodes. This led to the appearance of unexpected charge transfer limitations, making the 2nd catalyst reduction impossible. Adding protic additives such as methanol to the electrolyte allowed for overcoming these limitations by changing the catalytic pathway, enabling the long-term light-assisted reduction of CO_2 to CO with unity faradaic efficiency.

In a next step, phosphonate binding groups were introduced on the bipyridyl ligand, allowing for the covalent immobilization of the catalyst on the TiO_2 surface of the photocathode. However, the flat photocathode did not provide surface for enough catalyst to be adsorbed, showing the need for introducing a nanostructure at its surface. This was achieved in a low temperature process, culminating in the deposition of mesoporous TiO_2 on the protected Cu_2O photocathode. This design achieved photocurrents exceeding 2.5 mA cm^{-2}, leading to high faradaic efficiency for CO production from CO_2. After extended testing, ~60% of the initial rhenium was still found on the photocathode but the diffuse reflectance significantly changed. The continuous decrease of photocurrent was therefore ascribed to likely changes in catalyst structure upon operation.

Imidazolium cations were investigated in nonaqueous solutions to serve as promotors for the electroreduction of CO_2 to CO on silver electrodes. Contrary to previous reports, it was found that the C2 proton was not crucial for the promoting effect, as its replacement by a methyl group led to an improved performance. If a phenyl substituent was present in the C2 position, an even more significant improvement over $EMIM^+$ was observed. In contrast, replacing the C4 and C5 protons suppressed the promoting effect of the imidazolium, indicating that these protons may play an important role in the process.

With the goal of achieving the unassisted and sustainable solar-driven conversion of CO_2 to CO and O_2, a system was designed incorporating porous Au electrodes as selective cathodes for CO evolution from CO_2 and IrO_2 anodes for effectuating the oxygen evolution from water. This system was operated in a bicarbonate electrolyte and driven by three perovskite photovoltaics in series, which were chosen for their large photovoltages. Sustained operation for 18 h achieved a solar to CO conversion efficiency exceeding 6.5 %, setting the world record at the time the work was published.

To decrease the reliance on expensive electrode materials, CO_2 reduction on CuO nanowire electrodes was studied. ALD modification of these electrodes with small amounts of SnO_2 achieved a substantial modification of the selectivity from a wide product distribution characteristic of copper-based catalysts, toward the predominant production of CO with high selectivity. Partial current density measurements and chemisorption analysis suggested that the change of selectivity is due to a decreased binding strength of hydrogen upon modification with SnO_2. A cooperative effect between Cu and Sn is believed to be in play, based on the observation that thick SnO_2 films did not show the same CO selectivity. Exploiting the fact that SnO_2-coated CuO also serves as an oxygen evolution catalyst, a bifunctional electrolysis system was set up, with the two half-cells separated by a bipolar membrane, allowing for the sustained operation with different electrolyte and pH in the anode and cathode chamber. Driven by a 3-junction photovoltaic under 1 sun illumination, this device achieved a solar-to-CO efficiency peaking at 13.4%, again breaking all previous records.

During the time research for this thesis was conducted, a global race was underway for the solar-driven production of fuels from CO_2. As can be seen in **Figure 7-1**, I managed to keep ahead of the competition, contributing the highest efficiencies to this race and keeping EPFL and LPI on the map.

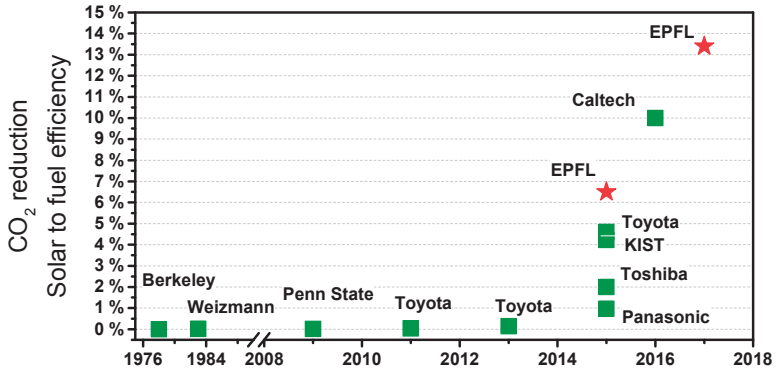

Figure 7-1: **The CO_2 to solar fuel efficiency race.** The two marks denoted by EPFL correspond to the studies in this thesis.

The potential applications for CO_2 reduction technology are manifold. Various scenarios have been suggested. The most obvious ones include the production of high value chemicals such as ethylene from cheap CO_2 and inexpensive surplus renewable electricity, as well as the production of high density solar fuels for transport applications.

It has widely been argued that such fuels could serve to store electricity for later use in the electrical grid. However, despite being mentioned in the introduction, there might be illusions pertaining to the need of storage in the electrical energy system. As Fares and Webber have put it in a recent analysis, energy storage is an energy consumer and not an energy producer[1] and will in the worst case simply increase energy use. This is due to the fact that all storage technologies have a roundtrip efficiency of less than 100%, with an estimated overall average around 70%,[2] meaning that a significant amount of energy has to be invested in order to be able to store energy in the first place. For the production of synthetic natural gas from renewable electricity for example, a roundtrip efficiency as low as 30 to 38% has been estimated.[2] A study by the German think tank *Agora Energiewende* points in a similar direction, arguing that electrical storage will be required only at very high shares of renewable energy.[3] There is still a long way before this becomes a

necessity. However, the same study reaches the conclusion that a new market is emerging for storage technologies relevant to *transportation* and to the *chemical sector*, which concerns precisely the technologies described in this thesis, underlines their relevance, as well as the considerable likelihood that they will find an industrial application.

The studies presented in this thesis represent small steps toward the real, industrial feasibility of reducing CO_2 to fuels and chemicals and closing the human carbon cycle. Many challenges still have to be addressed for these technologies to become reality. Retrieving CO_2 from the atmosphere may itself present a challenge, with the cost estimated at up to 1000 \$ t^{-1},[4] as compared with the current ethanol prize of 488 \$ t^{-1}.[5] Also, while the production of CO starts to be understood to a point where the design of industrial electrolyzers becomes possible, numerous challenges related to the engineering of such electrolyzers also have to be overcome, particularly related to mass transport. The large scale electrosynthesis of products different from CO remains out of reach to the present day due to excessive overpotentials[6] and unstable catalysts[7] in the case of formic acid production and also insufficient selectivity in the case of hydrocarbons and oxygenates.[8–11] Additionally, problems related to product separation may need more consideration.[12] Substantial progress is therefore required in the fundamental understanding and improvement of the processes involved in CO_2 electroreduction.

The way to further improve the solar-driven reduction of CO_2 to fuels lies in the optimization of the catalyst and electrolyzer design, making them both robust to the inherent fluctuation of solar light. The state of the art catalysts are only insufficiently able to maintain their selectivity in face of varying light intensity and therefore varying potential, which is inherent to solar and other renewables as energy sources. The problem is particularly acute when copper catalysts are used to produce hydrocarbons and oxygenates, the selectivity of which has been shown to be highly sensitive to the electrochemical potential. This requirement persists even if DC-DC converters are used because the incoming solar power will still be fluctuating and a DC-DC converter will not be able to satisfy the constraints imposed by the narrow operation conditions of CO_2 reduction catalysts, without requiring substantial curtailment.

It also remains important to keep in view the scale of the problem at hand. The 20 cm^2 electrolyzer shown in **Chapter 6** operates at a power of 15.6 mW, whereas a typical nuclear powerplant produces 1000 MW_{el}, 10 orders of magnitudes more. The average power used in 2014 for transportation alone amounted to almost 3000 GW, which is another 3000 times larger. For the electrosynthesis of fuels and chemicals to become possible, scale-up has to be envisioned early in the process. Two avenues of future research can therefore be distinguished. One of them leading in the industrial direction, toward the improvement of electrodes capable of achieving large current densities, predominantly toward the production of CO. The other direction will go into the depth of the study of catalyst materials, leading to the understanding of the origins of selectivity and activity on catalysts such as copper, which are able to produce highly relevant products like ethylene. With sufficient investment in these research efforts, the selective production of ethylene should be possible but may require innovative strategies for electrode and reactor design.

Despite the challenges mentioned here, the production of carbon based fuels from CO_2 will allow for establishing a valuable link between the electrical and petrochemical energy system, allowing for the versatile utilization of renewable energy. This prospect will likely lead to sustained funding of these interesting research efforts.

It is my hope that future efforts toward the more efficient electrochemical conversion of CO_2 will, as a welcome byproduct, also lead to an improved understanding of the fundamental processes involved in electrocatalysis. This knowledge should prove widely useful in a large amount of fields relevant to humanity.

References

1. The impacts of storing solar energy in the home to reduce reliance on the utility. *Nat. Energy* **2,** 17001 (2017).
2. IEC. *Electrical Energy Storage*. (2011) Available at: http://www.iec.ch/whitepaper/pdf/iecWP-energystorage-LR-en.pdf (Accessed: 2nd February 2017)
3. Agora Energiewende - Electricity Storage in the German Energy Transition. *Electricity Storage in the German Energy Transition* (2017). Available at: https://www.agora-energiewende.de/en/topics/-agothem-/Produkt/produkt/62/Electricity+Storage+in+the+German+Energy+Transition/. (Accessed: 5th February 2017)
4. House, K. Z. *et al.* Economic and energetic analysis of capturing CO_2 from ambient air. *Proc. Natl. Acad. Sci.* **108,** 20428–20433 (2011).
5. Today in Energy - Daily Prices - Prices - U.S. Energy Information Administration (EIA). Available at: https://www.eia.gov/todayinenergy/prices.php. (Accessed: 26th January 2017)
6. Hori, Y. in *Handbook of Fuel Cells* (John Wiley & Sons, Ltd, 2010).
7. Min, X. & Kanan, M. W. Pd-Catalyzed Electrohydrogenation of Carbon Dioxide to Formate: High Mass Activity at Low Overpotential and Identification of the Deactivation Pathway. *J. Am. Chem. Soc.* **137,** 4701–4708 (2015).
8. Chen, C. S. *et al.* Stable and selective electrochemical reduction of carbon dioxide to ethylene on copper mesocrystals. *Catal. Sci. Technol.* **5,** 161–168 (2014).
9. Chen, C. S., Wan, J. H. & Yeo, B. S. Electrochemical Reduction of Carbon Dioxide to Ethane Using Nanostructured Cu $_2$ O-Derived Copper Catalyst and Palladium(II) Chloride. *J. Phys. Chem. C* **119,** 26875–26882 (2015).
10. Kas, R., Kortlever, R., Yılmaz, H., Koper, M. T. M. & Mul, G. Manipulating the Hydrocarbon Selectivity of Copper Nanoparticles in CO_2 Electroreduction by Process Conditions. *ChemElectroChem* **2,** 354–358 (2015).
11. Kas, R. *et al.* Electrochemical CO_2 reduction on Cu_2O-derived copper nanoparticles: controlling the catalytic selectivity of hydrocarbons. *Phys. Chem. Chem. Phys.* **16,** 12194–12201 (2014).
12. Singh, M. R. & Bell, A. T. Design of an artificial photosynthetic system for production of alcohols in high concentration from CO_2. *Energy Env. Sci* **9,** 193–199 (2016).

Acknowledgements

When I was young, one of my biggest fear was that one day I would have reached the limit of knowledge and learnt everything that there is to learn. After four years of Ph.D. research, my fear has changed to the opposite – that I can never get anywhere close to understand nature and the dynamics of our planet. Despite this reckoning, I want to keep learning and generate new knowledge. The thrill in doing research is the discovery of unexpected results and I am keen to experience more of that.

I look back to four very instructive, challenging and exciting years which I would not want to miss.

My biggest thank goes to my thesis director Prof. Michael Grätzel. During my entire tenure under his supervision, I never stopped regarding it as a fantastic privilege to be able to do a Ph.D. with one of the most respected physical chemists of our time and I was thoroughly aware that only few people are given such a chance in any generation. In lengthy discussions with Prof. Grätzel, I was allowed time and again to gain insight and learn from his deep scientific knowledge and his experience in life, derived from an extraordinary biography. These experiences stay engrained in my memories and will continue to serve me as a reference for the time to come.

His wife, Dr. Carole Grätzel was very nice to me during my stay at LPI.

I also want to thank my colleagues Dr. Matthew Mayer and Dr. Jingshan Luo. Matt was instrumental in teaching me how to transform a research project into a scientific publication, a key lesson of the Ph.D. studies and I feel very thankful for this. I was able to collaborate with him on a large number of projects and I thoroughly felt this to be a mutually beneficial and rewarding experience. Matt also recommended the application for the IPMI Student Award, which I was awarded. Together we were travelling around the world, sharing wonderful experiences and creating more CO_2 emissions than our discoveries will be able to offset in the foreseeable future.

Jingshan also helped my Ph.D. work. He brought the motivation and intensity that I was searching at the beginning of my Ph.D. We spent evenings and nights in the office and laboratory together, trying to fix problems which often had nothing to do with deep scientific insight, but rather with how to make an electrode work of which

we already knew that it should work. I also owe him the idea for the subtitle of this thesis. We travelled a lot together and shared (endless) discussions on scientific topics and the state of the world.

I did not tell my parents much about the work that I was doing during my Ph.D. but still got a lot of help from them. I also have to thank them for their help and support.

Dr. Minkyu Son helped and listened to me in moments of difficulty for which I am very thankful.

Dr. Genevieve Lau contacted me asking for a project in CO_2 reduction research, which led to the data shown in **Chapter 4**. Working with her was great and made my Ph.D. a more pleasant experience overall. I would also like to thank Genevieve's supervisor, Prof. Paul Dyson for his support.

The same is true for the students who worked with me during my Ph.D. Sylvain Gros, Laura Curvat and Aufar Kari brought new air into my lab and allowed me to make substantial progress. I hope (and believe) that they also were able to learn a lot.

I also would like to thank my fellow Ph.D. students, Ludmilla Steier, Linfeng Pan, Norman Pellet, Aravind Chandiran, Amita Ummadisingu, Julian Burschka, Amalie Dualeh, Maurin Cornuz and Konrad Domanski for the time we shared in and outside of the lab. I also shared interesting discussions with Dr. Michael Saliba and other postdoctoral scholars in our group, including Dr. Thomas Moehl who helped me with electrochemical questions in my first projects. Dr. Juan Pablo Correa Baena and Dr. Xiong Li are also thanked.

Dr. Nicolas Tetreault handled my admission into LPI and my initial financing and I owe him great thanks for this. Also, I would like to thank the postdocs who welcomed me to the lab, Prof. David Tilley and Prof. Morgan Steffik.

I would also like to thank the people of the solar fuels community with whom I enjoyed the privilege to discuss and spend time. This includes among others Prof. Avner Rothschild (Technion), Prof. Roel van de Krol (Helmholtz Berlin), Prof. Erwin Reisner (Cambridge), Prof. Matthew Kanan (Stanford), Prof. Alex Bell (Berkeley), Prof. Yogesh Surendranath (MIT), Dr. Joel Ager (Berkeley) and Dr. Artur Braun (EMPA).

So many people contributed to making the results presented in this thesis possible. As a Ph.D. student at EPFL, I could profit from an excellent infrastructure. I would like to thank to everyone who is providing this infrastructure and since so many people are involved, I fear that I might forget some of them. Thanks go to Dr. Pascal Miéville for providing an incredible NMR platform, to André Fattet, Guillaume Francey, Gil Corbaz, Christophe Clement and everyone else of the mechanical workshop who helped me to transform my ideas for electrochemical test cells, photoelectrochemical setups, gas processing devices and other pieces into tactile reality. Frédéric Gumy helped me to set up LabView controlled equipments and A/D converters. I also would like to thank all the members of the ISIC electronic workshop, Supardi, Harald, Grégoire, for many reparations, modifications and pieces. Karine Vernez and Sylvain Coudret carried out numerous elemental analyses for me and were a pleasure to talk to as well. The same is true for Jacques Gremaud and Dr. Marie Jirousek who run the chemical store in our building.

I also would like to thank the people involved in the ISIC council and in the council of the faculty of basic science at EPFL for the interesting deliberations.

Dr. Véronique Amstutz was a good friend and a strong support during my Ph.D. Being more than a year in advance on me, she helped me to put the challenges I encountered into perspective and also helped me brainstorming ideas. Due to her work on large scale systems, we shared numerous interesting discussions on visions for a realistic future energy system. I also have to thank her supervisor, Prof. Hubert Girault for similar discussions and his taking time to read and comment my first publications.

Prof. Anders Hagfeldt who joined us half-way through my Ph.D. invited me to dinners with his group and we shared numerous interesting discussions on science and the world.

I want to thank Dr. Jonas Milani for the time we shared together during our Ph.D. studies. I will remember our march in the dark.

Prof. Kevin Sivula, my co-advisor, always was a valuable source of advice for which I would like to thank him.

Heidi Francelet and Carmen Biagini, the administrators of LPI, were a great help with many administrative affairs and I would like to thank them for their patience and understanding.

Great thanks go to Siemens and in particular to Prof. Maximilian Fleischer, Dr. Günter Schmid and Dr. Kerstin Wiesner for funding my Ph.D., for many productive and pleasant meetings and for welcoming me to Munich and Erlangen.

Furthermore, I would like to thank IPMI for awarding me the IPMI Student Award in 2015.

Matt and Véronique corrected my thesis for which they deserve my gratitude.

I also would like to thank to all visitors to LPI who crossed my way during the Ph.D. for the great times and discussions.

Last but not least I would like to thank 张晓瑜. 谢谢你.

8 Curriculum Vitae Marcel Schreier

Personal data

Family / First Name	Schreier Marcel
Day of birth	September 29, 1986
Nationality	Swiss
Address	Moosackerweg 4, CH-4148 Pfeffingen
Contact	www.linkedin.com/in/schreier-marcel

Ph.D. with **Prof. Michael Grätzel** at **EPFL**
"Solar-driven reduction of CO_2: From homogeneous to heterogeneous catalytic systems"

Education

Swiss Federal Institute of Technology (EPFL)
Ph.D. in Physical Chemistry
(11/2012 – 04/2017)

Swiss Federal Institute of Technology (ETH Zurich)
MSc in Chemical Engineering
(09/2010 – 10/2012)

California Institute of Technology (Caltech)
Master Thesis, "Matching of scales in nanostructured solid acid electrodes by the means of carbon nanotubes"
(09/2011 – 05/2012)

Swiss Federal Institute of Technology (EPFL)
BSc in Chemistry and Chemical Engineering
(09/2006 – 08/2009)

Awards

IPMI Student Award 2015
20'000 USD award for research on precious metals

Pelet Prize EPFL 2009
Best Grade Point Average over Bachelor cycle in Chemistry and Chemical Engineering

Graduate School Fellowship offers from UC Berkeley, Stanford University and California Institute of Technology

Member of the BASF European Talent Pool

Languages

German (native), French (proficient), English (proficient, TOEFL iBT: 111), Mandarin (beginner)

Publication List

(ordered by date and importance)
(Google Scholar: http://go.epfl.ch/ms-scholar)

1. Covalent Immobilization of a Molecular Catalyst on Cu_2O Photocathodes for CO_2 Reduction
   Marcel Schreier, Jingshan Luo, Peng Gao, Thomas Moehl, Matthew T. Mayer, and Michael Grätzel
   J. Am. Chem. Soc., 2016, 138 (6), 1938–1946
2. Efficient photosynthesis of carbon monoxide from CO_2 using perovskite photovoltaics
   Marcel Schreier, Laura Curvat, Fabrizio Giordano, Ludmilla Steier, Antonio Abate, Shaik M Zakeeruddin, Jingshan Luo, Matthew T Mayer, Michael Grätzel
   Nature Communications, 2015, 6, 7326
3. Efficient and selective carbon dioxide reduction on low cost protected Cu_2O photocathodes using a molecular catalyst
   Marcel Schreier, Peng Gao, Matthew T Mayer, Jingshan Luo, Thomas Moehl, Mohammad K Nazeeruddin, S David Tilley, Michael Grätzel
   Energy Environ. Sci., 2015, 8, 855–861
4. Solar conversion of CO_2 to CO using earth-abundant electrocatalysts prepared by atomic layer modification of CuO
   Marcel Schreier, Florent Heroguel, Ludmilla Steier, Jeremy Luterbacher, Matthew T. Mayer, Jingshan Luo, Michael Grätzel
   Nature Energy, accepted
5. New Insights Into the Role of Imidazolium-based Promoters for the Electroreduction of CO_2 on a Silver Electrode
   (Genevieve P. S. Lau, **Marcel Schreier)**[‡], Dmitry Vasilyev, Rosario Scopelliti, Michael Grätzel, Paul J. Dyson
   J. Am. Chem. Soc., 2016, *138* (25), 7820–7823

   [‡] equal contribution
6. Molecular Engineering of Potent Sensitizers for Very Efficient Light Harvesting in Thin-Film Solid-State Dye-Sensitized Solar Cells
   (Xiaoyu Zhang, Yaoyao Xu)[‡], Fabrizio Giordano*, **Marcel Schreier***, Norman Pellet, Yue Hu, Chenyi Yi, Neil Robertson, Jianli Hua*, Shaik M. Zakeeruddin*, He Tian, Michael Grätzel*
   J. Am. Chem. Soc., 2016, 138 (34), 10742–10745

   * corresponding author
7. Water photolysis at 12.3% efficiency via perovskite photovoltaics and Earth-abundant catalysts
   Jingshan Luo, Jeong-Hyeok Im, Matthew T Mayer, **Marcel Schreier**, Mohammad Khaja Nazeeruddin, Nam-Gyu Park, S David Tilley, Hong Jin Fan, Michael Grätzel
   Science, 2014, 6204 (345), 1593–1596

8. Transparent Cuprous Oxide Photocathode Enabling a Stacked Tandem Cell for Unbiased Water Splitting
Paula Dias, **Marcel Schreier**, S David Tilley, Jingshan Luo, João Azevedo, Luísa Andrade, Dongqin Bi, Anders Hagfeldt, Adélio Mendes, Michael Grätzel, Matthew T Mayer
Adv. Energy Mater., 2015, 5, 1501537

9. Ruthenium Oxide Hydrogen Evolution Catalysis on Composite Cuprous Oxide Water-Splitting Photocathodes
S David Tilley, **Marcel Schreier**, João Azevedo, Morgan Stefik, Michael Graetzel
Adv. Funct. Mater., 2014, 24, 303–311

10. Scaling up magnetic filtration and extraction to the ton per hour scale using carbon coated metal nanoparticles
Michael Rossier, **Marcel Schreier**, Urs Krebs, Beat Aeschlimann, Roland Fuhrer, Martin Zeltner, Robert N Grass, Detlef Günther, Wendelin J Stark
Sep. Purif. Technol., 2012, 96, 68–74

11. Lithium-ion conductivity of radiation grafted membranes
Lorenz Gubler, **Marcel Schreier**, Petr Novák
PSI ECL Jahresbericht, 2011, 43, doi:10.3929/ethz-a-007047464

12. A copper nickel mixed oxide hole selective layer for Au-free transparent cuprous oxide photocathodes
Min-Kyu Son, Ludmilla Steier, **Marcel Schreier**, Matthew T Mayer, Jingshan Luo, Michael Grätzel
Energy Environ. Sci., 2017, 10, 912–918

13. Tin oxide as stable protective layer for composite cuprous oxide water-splitting photocathodes
João Azevedo, S David Tilley, **Marcel Schreier**, Morgan Stefik, Célia Sousa, João Pedro Araújo, Adélio Mendes, Michael Grätzel, Matthew T Mayer
Nano Energy, 2016, 24, 10–16

14. Hybrid organic-inorganic H_2-evolving photocathodes: understanding the route toward high performances organic photoelectrochemical water splitting
Francesco Fumagalli, Sebastiano Bellani, **Marcel Schreier**, Silvia Leonardi, Hansel Comas Rojas, Alì Ghadirzadeh, Gabriele Tullii, Alberto Savoini, Gianluigi Marra, Laura Meda, Michael Grätzel, Guglielmo Lanzani, Matthew T Mayer, Maria Rosa Antognazza, Fabio Di Fonzo
J. Mater. Chem. A, 2016, 4, 2178–2187

15. Cu_2O nanowire photocathodes for efficient and durable solar water splitting
Jingshan Luo, Ludmilla Steier, Min-Kyu Son, **Marcel Schreier**, Matthew T Mayer, Michael Grätzel
Nano Lett., 2016, 16 (3), 1848–1857

16. Low-Temperature Atomic Layer Deposition of Crystalline and Photoactive Ultrathin Hematite Films for Solar Water Splitting
Ludmilla Steier, Jingshan Luo, **Marcel Schreier**, Matthew T Mayer, Timo Sajavaara, Michael Grätzel
ACS Nano, 2015, 9 (12), 11775–11783

17. Solution Transformation of Cu_2O into $CuInS_2$ for Solar Water Splitting
Jingshan Luo, S David Tilley, Ludmilla Steier, **Marcel Schreier**, Matthew T Mayer, Hong Jin Fan, Michael Grätzel
Nano Lett., 2015, 15 (2), 1395–1402

18. Targeting Ideal Dual-Absorber Tandem Water Splitting Using Perovskite Photovoltaics and $CuIn_xGa_{1-x}Se_2$ Photocathodes
Jingshan Luo, Zhen Li, Shiro Nishiwaki, **Marcel Schreier**, Matthew T Mayer, Peter Cendula, Yong Hui Lee, Kunwu Fu, Anyuan Cao, Mohammad Khaja Nazeeruddin, Yaroslav E Romanyuk, Stephan Buecheler, S David Tilley, Lydia Helena Wong, Ayodhya N Tiwari, Michael Grätzel
Adv. Energy Mater., 2015, 5: 1501520
19. High-Surface-Area Porous Platinum Electrodes for Enhanced Charge Transfer
Yelin Hu, Aswani Yella, Stefan Guldin, **Marcel Schreier**, Francesco Stellacci, Michael Grätzel, Morgan Stefik
Adv. Energy Mater., 2014, 4, 1400510
20. Carbon nanotubes as electronic interconnects in solid acid fuel cell electrodes
Áron Varga, Moritz Pfohl, Nicholas A Brunelli, **Marcel Schreier**, Konstantinos P Giapis, Sossina M Haile
Phys. Chem. Chem. Phys., 2013, 15, 15470–15476
21. Polymer-based photocathodes with a solution-processable cuprous iodide anode layer and a polyethyleneimine protective coating
Hansel Comas Rojas, Sebastiano Bellani, Francesco Fumagalli, Gabriele Tullii, Silvia Leonardi, Matthew T Mayer, **Marcel Schreier**, Michael Grätzel, Guglielmo Lanzani, Fabio Di Fonzo, Maria Rosa Antognazzadoi
Energy Environ. Sci., 2016, 12, 3710–3723

Conference Presentations

1. Materials Research Society (MRS) Fall Meeting 2016, Boston, MA, USA
Talk: "Molecular and Heterogeneous Catalysis for the Sunlight-Driven Reduction of CO_2 to Fuels"
(11/2016)
2. Gordon Research Conference Renewable Energy: Solar Fuels, Tuscany, Italy
Poster: "Efficient sunlight-driven reduction of CO_2 to fuels based on Cu_2O and perovskite absorbers"
(02/2016)
3. 66th Annual Meeting of the International Society of Electrochemistry, Taipei, Taiwan
Talk: "Efficient sunlight-driven reduction of CO_2 to fuels based on Cu_2O and perovskite absorbers"
(10/2015)
4. SFN International Discussion: "Solar Fuels: Moving from Materials to Devices", London, UK
Poster: "Efficient sunlight-driven reduction of CO_2 to fuels based on Cu_2O and perovskite absorbers"
(07/2015)
5. IPMI 39th Annual Conference, San Antonio, TX, USA
Prize Acceptance Speech: "Storage of solar energy in carbon-based fuels"
(06/2015)
6. 65th Annual Meeting of the International Society of Electrochemistry, Lausanne, Switzerland
Poster: "Reduction of carbon dioxide using Cu_2O photocathodes"
(09/2014)
7. 20th International Conference on Photochemical Conversion and Storage of Solar Energy, Berlin, Germany
Talk: "Reduction of carbon dioxide using Cu_2O photocathodes"
(07/2014)

8. 3rd International Conference on New Advances in Materials Research for Solar Fuels Production, Montreal, Canada
   Poster: "Reduction of carbon dioxide using Cu_2O photocathodes"
   (06/2014)
9. 30th One-Day-Symposium on Electrochemistry, PSI, Villigen, Switzerland
   (05/2014)
10. 28th One-Day-Symposium on Electrochemistry, PSI, Villigen, Switzerland
    (05/2012)
11. 27th One-Day-Symposium on Electrochemistry, PSI, Villigen, Switzerland
    (05/2011)

Research Experience

1. Ph.D. Thesis (Photo- / Electrochemical reduction of CO_2; Prof. Michael Grätzel) at EPFL, Switzerland
   (01.11.2012 – 10.04.2017)
2. Master Thesis (SAFC Electrodes; Prof. Sossina Haile) at California Institute of Technology, Pasadena, USA
   (12.09.2011 – 01.05.2012)
3. Research Project (Membranes for Lithium Sulfur Batteries; Prof. Petr Novák) at PSI, Villigen, Switzerland
   (02.05.2011 – 20.05.2011)
4. Internship (Mechanism of SPA Catalysis; Prof. A. de Klerk, Prof. Eric Rivard) at University of Alberta, Edmonton, Canada
   (12.04.2010 – 14.06.2010)
5. Research Assistant (Magn. Nanoparticle Engineering; Prof. Wendelin Stark) at ETH Zurich, Zurich, Switzerland
   (12.10.2009 – 26.03.2010)
6. Internship (Lithium Ion Batteries) at BASF SE, Ludwigshafen, Germany
   (06.07.2009 – 06.09.2009)
7. Internship (Chemical Engineering) at Siegfried AG, Zofingen, Switzerland
   (24.08.2008 – 13.09.2008)
8. Vacation stand-in during High School at DSM Pentapharm, Aesch, Switzerland
   (07-08/2005, 07-08/2006)
9. High School Research Internship (Biotechnology) Novartis, Basel, Switzerland
   (10/2005)
10. High School Research Project (Building a Fuel Cell) Gymnasium Munchenstein, Munchenstein, Switzerland
    (Spring semester 2004)

Teaching

1. Teaching Assistant "Introduction to practical Redox Chemistry", EPFL, Lausanne, Switzerland
   (Fall semester 2014, spring semester 2015)
2. Teaching Assistant „Electrochemical Engineering", EPFL, Lausanne, Switzerland
   (Spring semester 2013, spring semester 2014)
3. Teaching Assistant „Transport Phenomena", EPFL, Lausanne, Switzerland
   (Fall semester 2013)
4. Teaching Assistant „Chemical Structure Analysis", EPFL, Lausanne, Switzerland
   (Fall semester 2008)

Media Experience

1. Newspaper interview on danger of lithium ion batteries, "Le Lithium est partout", Le Matin, Switzerland
   (01.04.2014)
2. TV Interview about Prof. Michael Grätzel for presentation at Samson Awards, recorded by NBC
   (14.11.2014)

Skills and Techniques

- *Expert in:* Electrochemistry, Photoelectrochemistry, Electrocatalysis, Cyclic voltammetry, Gas Chromatography, High-field NMR spectroscopy with CryoProbe, Scanning electron microscopy, Design of laboratory equipment and measurement setups
- *Skilled in:* Thin film deposition, X-Ray diffraction, IR Spectroscopy, UV-Vis spectroelectrochemistry, LabView programming and computer communication protocols, Basic chemical synthesis
- *Skilled user:* Microsoft Office, Sharepoint Administration, OriginLab, Adobe Illustrator

Academic and Political Activities

- Member of the council of the Institute of Chemical Science and Engineering at EPFL
- Elected Member of the council of the Faculty of Basic Science at EPFL
- Peer-reviewer for: *Chemical Science, Nano Energy, Electrochimica Acta, Electrochemistry Communications, International Journal of Hydrogen Energy*

Areas of Interest

- Electrocatalysis, CO_2 reduction, Photoelectrochemistry, Interphases, Surface properties, Macroscopic energy systems, Relationship of science and society

28th of April 2017